High-pressure hydrogen storage tank rupture in confined space

Wulme Puoru Dery
(BSc, MSc)

Faculty of Computing, Engineering and the Built Environment
Ulster University

Thesis submitted for the degree of
Doctor of Philosophy

November 2020

I confirm that the word count of this thesis is less than 100,000.

Thesis outline

Acknowledgements

There are a large number of people responsible for me starting and finishing this thesis, too many to do justice by only acknowledging them on a piece of paper. Nevertheless, here goes.

Principally, to Prof. Vladimir Molkov for acting as my primary supervisor, the guidance needed to steer me the right way not a trivial task: add a lot of education, mentoring, patience and a few anecdotes to lighten the mood, it only accounts for a fragment of the efforts made, for which I am grateful for. To my second supervisor, Dr. Dmitriy Makarov, for always being available for supervision and sound advice, and embarking on the tumultuous task of providing feedback on the written work. To my third supervisor, Dr. Volodymyr Shentsov, for not only properly introducing me into the world of CFD, but having the endurance of teaching me day after day the complexities of it all.

To my fellow colleagues (who I consider co-co supervisors) Dr. Sergii Kashkarov and Dr. Donatella Cirrone, I am gracious of our discussions and collaboration. I am grateful to the people I shared an office with, both from HySAFER and FireSERT, for excellent companionship during the good and bad (weather) days.

I would like to give a special shout out to Linda Hooper, Zora Sashkova and Issac "Jojo" Ampomah, from our first encounter as fellow doctoral researchers to our regular lunches, which will be immensely cherished. Together with all other people encountered and befriended during this period, the friendships made assuredly preserved in perpetuity.

It goes without saying that without the endless love, support and encouragement from my parents I would not be here and for that, I am forever in your debt. To Taume, who should be acknowledged not only for being my brother, but for the continuous support given in all forms. Last but not least, I would like to my thank my dearest Christiane, for your unmeasurable care and cheerfulness.

#Linje3

Abstract

This doctoral study investigates and closes a few knowledge gaps within the hydrogen safety engineering associated with the rupture of a stored hydrogen tank in an open atmosphere and a tunnel. Using contemporary numerical methods such as computational fluid dynamics (CFD), the development of a model for simulation of blast wave and fireball dynamics after a high-pressure hydrogen tank rupture in a fire has been outlined. This includes understanding the effect of different sub-models, numerical methods and insights into blast wave propagation and fireball dynamics. The validation of the model against experiments was attained in an open atmosphere, confirming the models' capability as a predictive tool for assessment of tank rupture in fire consequences. The isolated effect of fire surrounding a stand-alone hydrogen tank prior to rupture was investigated, towards creating a more accurate consequence analysis and harmful criteria. The presence of fire as it may enhance the process towards a conceivable tank rupture, was found to have an adverse effect on the hazard consequences of the generated blast wave and fireball. The validated CFD model was applied to observe the direct effect of a blast wave after hydrogen tank rupture between open atmosphere and the close-in effects of a tunnel confinement. A three-dimensional blast wave decay pattern in open atmosphere was found, vastly different to the more one-dimensional blast wave propagation in a tunnel. Accordingly, numerical experiments were performed in a wide range of tunnels of various cross-section areas including tank ruptures of various volumes and pressures. A novel correlation for blast wave decay in tunnel was proposed using methods of similitude analysis. This resulted in a near linear fit between the two dimensionless parameters, able to predict blast wave decay across various stored hydrogen and tunnel dimensions. In the absence of experiments on hydrogen tank rupture in a tunnel fire, the developed correlation is the only tool available to stakeholders for hazards and associated risk assessment.

Keywords: CFD, hydrogen safety, fire, tank rupture, blast wave, fireball, tunnel, correlation

Nomenclature

Acronyms

BCD	Bounded Central Differencing
CFD	Computational Fluid Dynamics
CFL	Courant-Friedrichs-Lewy
CFRP	Carbon Fibre Reinforced Plastic
CNG	Compressed Natural Gas
CPU	Central Processing Unit
CV	Control Volume
DNS	Direct Numerical Simulation
DO	Discrete Ordinates
DOE	Department Of Energy
ECF	Energy Concentration Factor
EDC	Eddy Dissipation Concept
EDM	Eddy Dissipation Model
FRC	Finite Rate Chemistry
HRR	Heat Release Rate
HSE	Health and Safety Executive
INERIS	French Institute of Industrial Environment and Risks

ISO	International Organization for Standardization	
LFL	Lower Flammability Limit	
LPG	Liquefied Petroleum Gas	
NWP	Nominal Working Pressure	
PISO	Pressure-Implicit with Splitting of Operators	
RANS	Reynolds-Averaged Navier Stokes	
SAE	Society of Automotive Engineers	
SGS	Sub-Grid Scale	
TNT	Trinitrotoluene	
TPRD	Thermally-activated Pressure Relief Device	
URF	Under Relaxation Factors	

Greek letters

α	Mechanical coefficient	
α	Thermal diffusivity	m^2/s
α_W	Ratio of the explosive diameter to the tunnel hydraulic diameter	
β	Chemical energy coefficient	
β_{max}	Limiting angle in degrees for Mach stem	
ϵ	Turbulent dissipation rate	m^2/s^3
η	Empirical explosion efficiency	
γ	Gas ratio of specific heats	
κ	von Kármán constant	
μ	Dynamic viscosity	Pa s
ν	Kinematic viscosity	m^2/s
ω_v	Tensile strength of material	Pa

ϕ	Azimuthal angle	
π	"pi" constant	
ρ	Density	kg/m^3
σ	Stefan-Boltzmann constant	W/(m^2 K^4)
σ_s	Scattering coefficient	
τ	Time scale	s
θ	Polar angle	
ξ	Length scale of turbulent structures	

Latin letters

ΔP	Blast wave overpressure	Pa
Δt	Time step	s
Δx	Cell size	m
$\dot{m}$	Mass flow rate	kg/s
$\dot{Q}$	Heat release rate	W
$\overline{I}$	Dimensionless impulse	
$\overline{L}$	Dimensionless distance	
$\overline{L}_{D_T}$	Dimensionless tunnel hydraulic diameter	
$\overline{P}$	Dimensionless pressure	
$\overline{Z}$	Dimensionless distance from explosive charge/vessel	
$\vec{r}$	Position vector	
$\vec{s}$	Direction vector	
A	Cross-section area	m^2
a_g	Speed of sound in compressed gas	m/s
a_s	Speed of sound in surrounding gas	m/s

A_T	Tunnel cross-section area	m^2
A_t	Temperature dependent pre-exponential factor	
AR	Width-to-height aspect ratio	
b	Co-volume constant	m^3/kg
C_τ	Time scale constant	
C_ξ	Volume fraction constant	
c_p	Specific heat capacity	J/K
C_s	Homogeneous isotropic turbulence	J/K
D, d	Diameter	m
d_0	Outer diameter of cylinder	m
d_h	Hydraulic diameter of the tunnel	m
d_w	Wall thickness	m
D_T	Hydraulic diameter of tunnel	m
E	Energy	J
E_a	Activation energy	J/kmol
E_C	Heat of combustion of flammable material	kJ/kg
E_m	Total mechanical energy	J
E_{ch}	Total chemical energy	J
E_{TNT}	Heat of combustion of TNT	kJ/kg
F	Force	kg m/s^2
f	Friction factor	
g	Gravity	m/s^2
H	Height	m
h	Enthalpy	J/kg

H_C	Heat of combustion	J/kg
I	Impulse	Pa s
I	Radiation intensity	W/m^2
k	Thermal conductivity	(W K)/m
k	Turbulence kinetic energy	J
L	Length/distance	m
L_s	Mixing length sub-grid scale	m
M	Mach number	
m	Mass of flammable material	kg
m_g	Mass of compressed gas	kg
M_m	Molecular mass	kg/mol
M_x	Mach number of the incident shock wave	
M_{sh}	Mach number of the shock wave	
n	Refractive index	
N_ϕ	Phi division	
N_θ	Theta division	
P	Pressure	Pa
p	Partial pressure	Pa
P_g	Gas pressure	Pa
P_s	Surrounding pressure	Pa
Pe	Peclet number	
R	Global reaction rate constant	
R	Universal gas constant	J/(K mol)
r	Distance from energy source/vessel	m

R^2	Goodness-of-fit coefficient of determination	
r_b	Volume of hemisphere occupied by products of complete combustion	m
R_m	Rate of species production/consumption source term	kg/(s m^3)
R_n	Net rate of production of species	
r_{sh}	Ratio of volume of hemisphere behind the shock	m
Re	Reynolds number	
s	Displacement distance	m
S_E	Source term of energy	J/(s m^3)
S_{c_t}	Turbulent dynamic viscosity	Pa s
T	Temperature	K or °C
t	Time	s
U, u	Velocity	m/s
V	Volume	m^3 or L
V_T	Volume of tunnel enclosure	m^3 or L
V_{ideal}	Ideal gas volume	m^3 or L
V_{real}	Real gas volume	m^3 or L
W	Quantity of explosive	kg
W_T	Width of tunnel enclosure	m
W_{TNT}	Equivalent weight of TNT	kg
wp	Wetted perimeter of a cross-section area	m
Y_m	Mass fraction of m-th specie	
Z	Compressible factor	
Z	Scaled distance from explosive charge/vessel	m/kg$^{1/3}$
Z_{TR}	Scaled transitional zone distance	m/kg$^{1/3}$

Subscripts and superscripts

b	Burned
C	Flammable material
ch	Chemical
f	Fireball
g	Gas pressure
H	Height
$ideal$	Ideal gas
m	Mechanical
max	Maximum
min	Minimum
n	Fireball mass constant
o	Outer
op	Operating pressure
$real$	Real gas
s	Surrounding gas
sh	Shock wave
st	Starting shock
T	Tunnel
TR	Transition zone
w	Wall
x	Incident shock

Publications

Journal papers

Molkov, V. and Dery, W. (2020), The blast wave decay correlation for hydrogen tank rupture in a tunnel fire, *International Journal of Hydrogen Energy*.

Molkov, V., Cirrone, D., Shentsov, V., Dery, W., Kim, W. and Makarov, D. (2020), Dynamics of blast wave and fireball after hydrogen tank rupture in a fire in the open atmosphere, *International Journal of Hydrogen Energy*.

Conference papers

Dery, W., Shentsov, V., Kashkarov, S., Molkov, V. and Makarov, D. (2019), Numerical study on effect of fire on strength of blast wave after stand-alone hydrogen tank rupture, *Conference proceedings of the 14th International Postgraduate Research Conference 2019: contemporary and future directions in the Built Environment*, December 16–17, Manchester, UK.

Shentsov, V., Makarov, D. and Dery, W. (2019), Stand-alone hemisphere-tank rupture in tunnel fire: effect of hydrogen inventory on blat wave strength in far field, *Proceedings of the 9th International Seminar on Fire and Explosion Hazards*, April 21–26, St. Petersburg, Russia.

Molkov, V., Cirrone, D., Shentsov, V., Dery, W. and Makarov, D. (2019), Contribution of combustion to the blast wave strength after high-pressure hydrogen tank rupture in a fire, *27th International Colloquium on the Dynamics of Explosions and Reactive Systems*, July 28–August 2, Beijing, China.

Molkov, V., Cirrone, D., Shentsov, V., Dery, W., Kim, W. and Makarov, D. (2018), Blast wave and fireball after hydrogen tank rupture in a fire, *11th International Colloquium on Pulsed and Continuous Detonations (ICPCD)*, September 17–21, St. Petersburg, Russia.

List of Tables

List of Figures

Chapter 1

Introduction

1.1 Project background

As the demand for global energy increases, uncertainty regarding fossil and hydrocarbon energy supply sources and long-term effects on the environment are of major concern. Various combustion products such as CO_2 and NO_x released into the atmosphere cause air pollution and contribute to the global temperature increase. An industry-led effort in aims to steer away from fossil-fuelled energy carrier dependencies is therefore gaining vast interest. Hydrogen is specifically targeted in the energy evolution with it representing a clean fuel with high energy content. This initiative coined as the hydrogen economy is part of a growing movement towards a more environmentally friendly and sustainable energy for the coming decades.

Formerly, the use of hydrogen was limited to industrial areas dealing with petroleum refineries processes, and otherwise for aerospace applications. Presently, utilisation of hydrogen as a commercial energy carrier is being veered onto private and public automotive domains, such as in the transportation sector (e.g. cars and buses). Major automobile manufacturers such as Honda, Mercedes Benz and Toyota have hydrogen-powered vehicles available for the public in select markets, with hydrogen filling stations growing steadily. The aim of offering an adequate driving range is of great importance, as alternatively powered vehicles such as those powered by hydrogen, are subject to comparison with petrol and gasoline-powered vehicles. This requires the usage of gaseous hydrogen stored in composite vessels of pressures up to 700 times above the atmospheric (surrounding) pressure.

Hydrogen can be used either for internal combustion engine or fuel cell vehicles. The commercial breakthrough has however tilted towards the latter option, similar to the electrical vehicles. To power vehicles, hydrogen is fused chemically with oxygen from air in a fuel cell and in the process electricity is released used to power the electric motor(s). When hydrogen is used as a fuel, its by-product is essentially water vapour. Remarkably, the quality of air coming out of a hydrogen-powered vehicle may in some cities be cleaner than the air going in.

A parameter particularly important for vehicle manufactures in order to bring hydrogen-powered vehicles into the mainstream market is costs. The challenge of keeping costs down in terms of high-pressure hydrogen storage systems with the undergarment of high safety guarantee is inescapable. Ideally, inexpensive storage vessels with durable material structures would be employed with favourable weight, in addition to having the ability to store large volumes of compressed hydrogen. However, a significant incident involving a hydrogen project whereby safety is compromised would negatively impact the public perception, and clean alternatives to conventional energy systems may never experience commercial deployment successfully.

Continuous research and understanding of emerging alternative energy-based vehicles must go hand-in-hand, as to not create uncertainness in terms of safety. Before hydrogen can be used as a common energy carrier, there must be widely accepted standards, methodologies, mitigations techniques and regulations in place ensuring at least the same level of safety and reliability as today's fossil fuels. This involves covering different aspects of vehicle conduct in day-to-day activities, anticipating accidents and accounting for unforeseen consequences. This is accomplished by creating validated engineering models and tools for reliable prediction of an accident.

Hydrogen-powered cars and buses are already operating on roads in different countries around the globe. If an accident whereby the hydrogen tank is exposed to fire occurs, the current fire resistance of modern composite tanks is limited, which may in certain cases lead to a catastrophic rupture. A blast wave and fireball following the high-pressure tank rupture in a fire represent its major pressure and thermal hazards, threatening both life and property losses. Besides some rudimentary activities, little dedicated research has been done on the hazards of accidents involving hydrogen-powered vehicles in critical infrastructures such as in tunnels. For instance, tunnels represent a structure strong enough to withstand tremendous pressure. Therefore, hazards of a tank rupture in a tunnel are distinguished from those established in an unconfined space.

These specific hazards and associated risks in a tunnel are largely unknown and thus, prevention and mitigation strategies are neither developed nor validated. Several parameters such as the amount and condition of the hydrogen stored, the tunnel's flow field and surrounding atmospheric conditions will all have a significant influence on characteristics of blast wave and fireball dynamics in a tunnel. These knowledge gaps and technological bottlenecks in hydrogen safety hamper the further inherently safer deployment of hydrogen-powered vehicles and public acceptance of the technology.

To shed some light at the end of the tunnel, this thesis is part of a pre-normative research project aiming to improve safety and reduce risks in the use of hydrogen and fuel cell cars and hydrogen delivery transport in underground transportation systems. Outcomes of this project will inform car original equipment manufacturers, health and safety authorities, fire and rescue services about hazards of potential fire accidents with hydrogen-powered vehicles in tunnels. The research results will feed the development of engineering methodology to assess blast wave overpressure and fireball size in the event of catastrophic tank rupture, towards the development of appropriate prevention and mitigation strategies.

1.2 Aim and objectives

This study aims to understand the hazards of a high-pressure hydrogen tank rupture in a tunnel and characterise the blast wave propagation and fireball dynamics. To realise this aim, the following objectives will be addressed:

- Perform a critical literature review on hazards associated with hydrogen storage and consequences from high-pressure tank rupture in an open atmosphere and a tunnel.
- Develop models and validate CFD simulations of blast wave and fireball dynamics from rupture of a tank in a fire.
- Explore the effect of tunnel confinement on the blast wave propagation and fireball dynamics of a high-pressure hydrogen tank rupture using the validated CFD model.
- Introduce an engineering tool enabling prediction of blast wave in a tunnel after a tank rupture.

1.3 Structure of the thesis

A short description of how the thesis is organised is presented below as follows:

Chapter 2 consists of the literature review, synthesizing previous work conducted within the realm of onboard hydrogen storage, accidents and statistics, blast wave and fireball dynamics of high-pressure tank rupture in an open atmosphere and a tunnel – both experimentally and computationally.

Chapter 3 describes the development of the CFD model, sub-models and computation domain, and includes the preliminary results of blast wave formation and fireball dynamics.

Chapter 4 presents the obtained results from numerical simulations, and the validation process when compared against experimental values.

Chapter 5 explores the effect of two fire sizes engulfing a stand-alone tank prior to rupture, with regards to the generated blast wave strength and fireball dynamics.

Chapter 6 provides the insight of a blast wave in an experimental tunnel compared to in an open atmosphere and explores the effect of tank orientation in tunnel prior to rupture.

Chapter 7 proposes a blast wave decay in a tunnel following a parametric study involving 14 tank ruptures of various parameters in three tunnels of different cross-section areas.

Chapter 8 concludes the current study including its scientific novelty and further work.

Chapter 2

Literature review

2.1 Onboard hydrogen storage

Hydrogen is a gas at essentially all normal use and storage temperatures as the atoms naturally combine into pairs and exist under normal conditions formed by diatomic molecules, H_2 (Yang et al., 2010). The fact that hydrogen molecules are very small and lightweight (2.016 g/mol) makes the construction of storage tanks challenging. At high pressures, hydrogen interaction with materials is a present issue. Hydrogen embrittlement causes a significant deterioration in the mechanical properties, posing a careful selection of structural material (Molkov, 2012). For many metals at high pressures absorb hydrogen, and it affects the strength and ductility of the material. This happens by permeating through the metal atomic, recombining to molecules on the external surface of storage to diffuse into surrounding gas afterwards. Therefore, carbon fibre reinforced plastic vessel materials are utilised for onboard hydrogen storage (Hwang and Varma, 2014). It accounts for a lightweight, inexpensive and sufficiently strong enough material to meet the required stress, strain and safety specifications. Standards for tanks include limitations on the acceptable permeation rates, 1.0 Ncm^2/hr per litre internal volume of a container for the settled pressure at 15°C (HySAFE, 2009). Technically, the main issues related to hydrogen gas storage are the weight of the storage tank and the volume needed. All various hydrogen storage mechanisms have fundamental limitations: as gas, it requires a relatively large volume; as liquid, it evaporates easily; as hydrides, with metal the added weight is undesirable and as an adsorbent does not hold enough hydrogen to be practically viable (Durbin and Malardier-Jugroot, 2013). The energy density of hydrogen is relatively high by weight, whereby 1 kg of hydrogen contains approximately 2.5 times more energy than 1 kg of natural gas (Verfondern, 2008). However, it exhibits a very low volumetric density characteristic (0.0899 g/L), making it 3000 times smaller than gasoline. The aim of condensing as much hydrogen as possible by using as little additional material as possible is a materials science challenge yet to be completely overcome.

In terms of storage applications, the capacity of a hydrogen-sorption giving the amount

of electricity produced for any given weight is measured as the wt.%: the weight percent capacity or the gravimetric storage density of a material. The gravimetric storage capacity in which the hydrogen is stored within a bulk of the material is calculated as the ratio of the mass of hydrogen stored within the vessel to the mass of the host material including the hydrogen (Zheng et al., 2012). The latest target made by the US Department of Energy declared in 2015, interpolating between the ultimate target and current state-of-the-art compressed hydrogen systems yielded values of 1.5 wt.% and 1.8 wt.% for the year 2020 and 2025 respectively, with an ultimate value of 2.2 wt.% (Harrison et al., 2015). The system volumetric capacity (amount of hydrogen stored per unit volume) is for the year 2020 and 2025 at 30 g H_2/L and 40 g H_2/L respectively. The ultimate value is at 50 g H_2/L, taking into account the properties of the entire storage system. Presented in Figure 2.1 is the volumetric density of a hydrogen cylinder with regards to gas pressure. It increases with the pressure depending on the material and its tensile strength, with the trade-off of decreasing gravimetric density (Züttel, 2003).

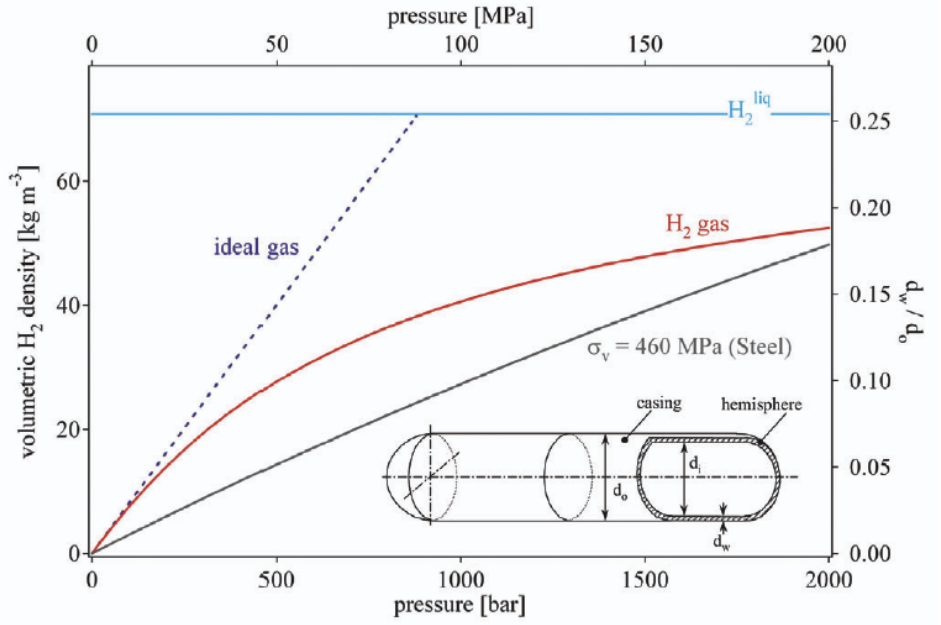

Figure 2.1: Volumetric density of hydrogen as a function of pressure, and the ratio of wall thickness of the pressure cylinder on the right (Züttel, 2003).

Considering an average range of 400–600 km for gas vehicles, around 5.6 kg of usable H_2 is required, representing a volumetric capacity of 18 g H_2/L and 28 g H_2/L for 35 MPa (350 bar) and 70 MPa (700 bar) respectively (Hwang and Varma, 2014). These values are based on base system performance and cost suitable for automotive applications. Technically, a further increase of the pressure of 70 MPa is not advised as the effect leads to a counter-productive effect on the compressibility of the hydrogen with it diminishing as the pressure rises (Maus et al., 2008). The tanks used are optimally in cylindrical shapes to provide proper integrity under the pressure, putting restraints in vehicle designs (Hordeski, 2009).

There are four standard types of cylinder developed and used for the transport and storage of hydrogen: Type I, all-metal cylinders, Type II, hoop-wrapped composite cylinders, Type III, fully wrapped composite cylinders with metallic liners and Type IV, fully wrapped composite cylinders with non-load-bearing non-metallic liners (Jorgensen, 2011). All the above mentioned cylinder types are listed in Figure 2.2. Type I and II, although relatively cheap storage options are not suitable for automotive applications due to its considerable weights and sizes (strength-to-weight limitation for all metal). Equipped with lighter and with thinner walls, Type III and IV vessel can withstand pressures up to 100 MPa and are preferably used for automotive applications. Type IV, in particular, is of full composite structure, most desirable with regards to capabilities of high gravimetric storage densities (Sinha and Yang, 2010).

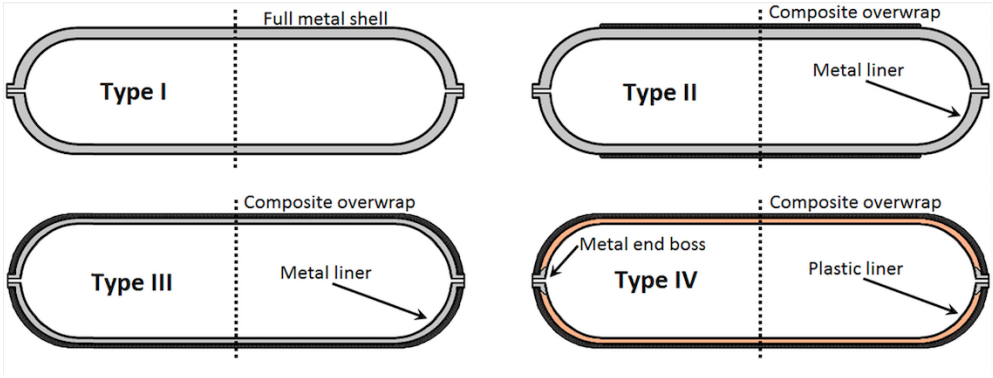

Figure 2.2: Standards of high-pressure cylinders currently utilized for hydrogen storage (Fowler et al., 2016).

2.2 Relevant accidents and statistics

Vehicles equipped with hydrogen storage tanks are held up to the highest standards, undergoing extensive testing to ensure performance and safety requirements according to the Society of Automotive Engineers (SAE). With many types demonstrated in several prototype fuel cell vehicles with worldwide certification, the safety record of these tanks have been excellent. Tanks are subjected to rigorous testing involving pressure and depressurization, 2 m drops, shots by rifles, burned and exposed to road hazards such as acids and salts before being installed in vehicles (Department for Communities and Local Government et al., 2010). Probability of storage vessel rupture reported by LaChance et al. (2009) stated an annual cylinder rupture frequency to be 5.0×10^{-7}, and a generic annual cylinder rupture frequency of 2.1×10^{-6}, using among other methods a Bayesian analysis[1]. Another method of quantifying the risks related to hydrogen-powered vehicles employed the event tree/fault method, using a one-tank hydrogen storage system as the main source of risk (Rodionov

[1]Bayesian analysis, a method of statistical inference (named for English mathematician Thomas Bayes) that allows one to combine prior information about a population parameter with evidence from information contained in a sample to guide the statistical inference process (Berger, 2013).

et al., 2011). Three initiating events were considered: crash accidents, fire accidents without crash (no other cars involved) and hydrogen leakages followed by ignition. These events were then developed taking into account the environment (geometry, wind etc.), and accident sequences assumptions made justified by extracting the data from the hydrogen incidents and accidents database (Galassi et al., 2012). The study concluded in an estimated hydrogen explosion frequency of 7.35×10^{-5} per car per year, under 2% compared to the total amount of traffic accidents per car per year (5.24×10^{-3}). Furthermore, 98.8% of the risks were related to an explosion in open and semi-confined environments, comparable with the consequences of normal traffic accidents. Although this methodology proves useful when there is a limited amount of data available, there may be bias in the data resulting in an underpredicted value. A risk matrix [2] also suggested a worst-case risk profile to be *Low*, based on probabilities alone (Post et al., 2015). It was argued in the report that "*this event is not reasonably credible under most normal operating scenarios*" (Post et al., 2015, p. 147).

A review covering the USA and European sources were reported by Waite (2012), including vessels of storage tanks, LPG, oil gas and chemical industries. Up to 27% of all releases were classified as catastrophic, found in the historical incident databases including statistical analysis. Verfondern (2008) reported a significantly high probability (96%) of gaseous hydrogen released leading to an explosion, with hot surfaces or open fire representing the ignition source. This was concluded after an evaluation of 287 occurrences of accidental hydrogen releases caused by leakage or insufficient purging or venting, independent of the state of the hydrogen. The UK Health and Safety Executive (HSE) conducted a review of HSE data and frequencies used in the Netherlands focusing on the size of defect or hole from a scale of a small hole to total failure of the vessel. In approximate terms, it was listed as shown in Table 2.1 (Nussey, 2006). The values for total failure remained the same when updated a few years later (HSE, 2012).

Table 2.1: Failure frequencies for pressure vessels (Nussey, 2006).

Type of failure	HSE failure freqency, cpm[3]
Sudden total failure	2–6
Large hole	5
Small hole	55
All types	62–66

The current drawback of investigating hydrogen storage tank failure frequencies is the lack of statistics due to its limited usage. It can, however, be argued that experience exists with compressed natural gas (CNG) vehicles (22.3 million CNG's worldwide since large-scale use began in the early 1980s in North America), providing a glance into the future concerning safety incidental and accidental occurrences (Gambone and Wong, 2007). CNG is a fossil fuel composed mainly of methane, but also contain small concentrations of other gases such

[2] A risk used during risk assessment helps identify the level of risk by considering the category of probability or likelihood of their occurrence and the category of consequence severity impact (Cox, 2009).

[3] cpm = chance per million per vessel per year: 1 cpm = 1×10^{-6} per vessel per year.

as ammonia, hydrogen and carbon dioxide. It is usually stored in a fuel tank with an internal pressure of 20–25 MPa. Wong (2009) has been testing CNG storage systems since 1983, maintaining a failure database limiting major leaks and catastrophic ruptures of cylinders. With a total of 81 reported incidents, see Figure 2.3, observations from the data reveal that vehicle localized fires account for 25% of the failures, originating from Type IV vessels.

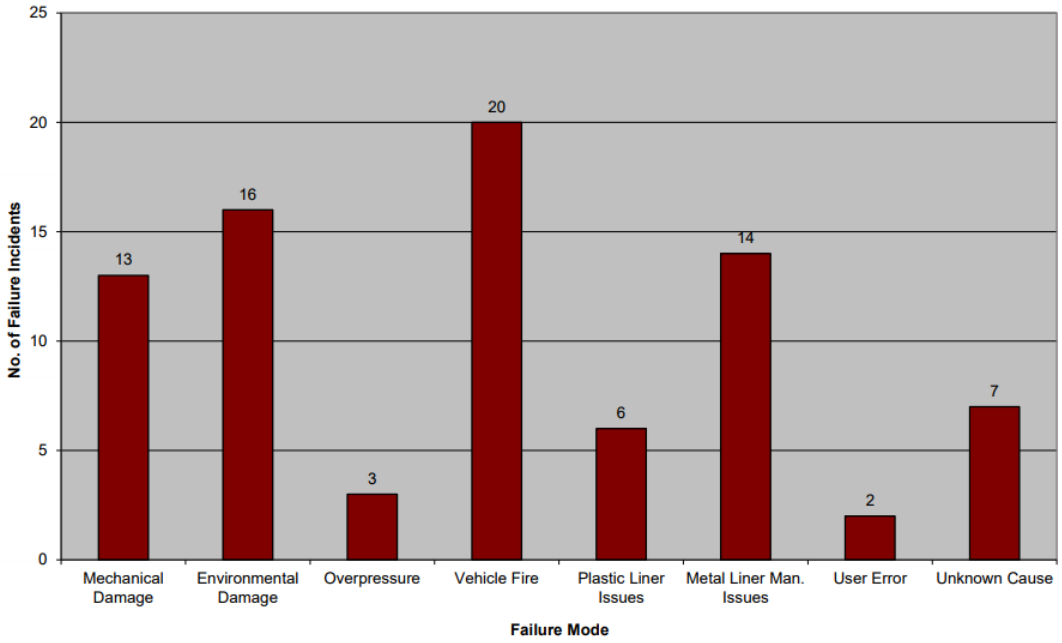

Figure 2.3: CNG failure incidents by failure type (Wong, 2009). Mechanical Damage: external abrasion and/or impact; Environmental Damage: external environment assisted; Overpressure: faulty fuelling equipment or faulty CNG cylinder valves; Vehicle Fire: faulty TPRD or lack of TPRDs of localized fires; Plastic Liner Issues: defects including cracking; Metal Liner Issues: defects including pinhole leaks; User Error: test facility error; Unknown Cause: limited or no data available.

A rupture of a high-pressure hydrogen tank is considered viable via two failure modes. First, when the internal pressures exceed the strength of the container. For instance, this could occur when excessive heat transfer into the hydrogen increases the internal pressure following refilling of the tank with a pressure supply source connection not designed for that tank. Mitigations against this are enforced by ISO[4] and SAE standards, preventing the refilling interface from connecting to vehicles with a higher working pressure than that of the vehicle tank (Kumar et al., 2009). Secondly, cases relating to factors reducing the strength of the container. This includes a chemical exposure or mechanical damage by the presence of fire or other external mechanisms leading to a unfavourable high vessel temperature. These

[4]ISO (International Organization for Standardization) is an independent, non-governmental international organization that give specifications for products, services and systems, to ensure quality, safety and efficiently.

type of cases are mitigated as the solution of venting the contents are considered to be less hazardous than a catastrophic rupture (Rodionov et al., 2011). Explosive failures of a vessel should be rare due to precautions normally taken including adherence to consensus design, fabrication and test codes and standards. High-pressure hydrogen tanks onboard vehicles are required by the European Regulations to be equipped with thermally-activated pressure relief devices (TPRD). These are designed to release some or all of the contents of the tank following an event of high temperatures and/or high pressures (Sunderland, 2008). However, a weakness with TPRD design is localized flame exposure going unnoticed. The abilities of the insulating composite material used in the tanks suppress a majority of the temperature increase, simultaneously degrading the material leading to a catastrophic rupture (Gambone and Wong, 2007). Furthermore, it is noted that all tanks are susceptible to rapid degradation once a localized fire has occurred regardless of the working pressure. With regards to pressure, compressed hydrogen is less vulnerable to temperature increase in terms of pressure rise, adding to the ineffectiveness of an activated relief device being governed by pressure. This is an issue that needs further research to be resolved, in order to gain public acceptance of this emerging use of high pressured hydrogen as an energy carrier.

To assess a specific case, a quantitative risk assessment (QRA) investigating a sequence of series for an accident of an onboard hydrogen-powered vehicle storage rupture due to fire exposure has been recently explored (Dadashzadeh et al., 2018). Of a low-frequency high consequence scenario, excluding that of other hazards such as projectiles and jet fires, the key identified hazard relevant to an accident scene such as blast wave and fireball were considered. A flowchart of the QRA methodology used is presented in Figure 2.4, with the output value of risks in terms of human fatality per vehicle per year. In this case, the tank rupture frequency was a product of three independent parameters – the initiating event frequency, TPRD failure probability and the probability of emergency operations failing to extinguish the fire. The initiating events were identified as a vehicle fire due to an accident, a fire caused by leaking high-pressure fittings, valves or piping connection and fire while filling hydrogen/tow away. A value of 3.14×10^{-3} was assumed the risk of human life lost in an accident, whereby a tank would rupture after an accident had escalated to a fire (Dadashzadeh et al., 2018). Over two magnitudes higher than the acceptable level of risk of 1.00×10^{-5} found elsewhere (LaChance et al., 2011), it demonstrates that the risk of hydrogen-powered vehicles is not at a negligible level.

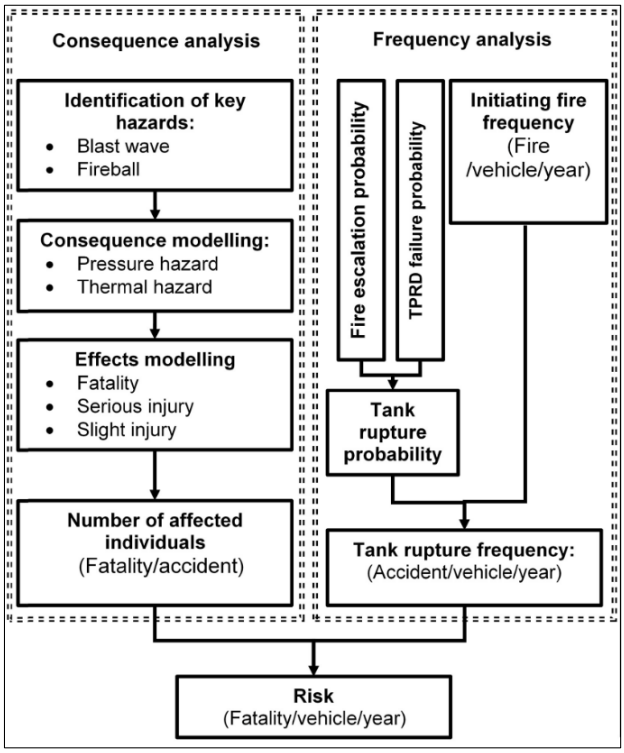

Figure 2.4: QRA methodology flowchart describing risk in terms of fatality per vehicle per year (Dadashzadeh et al., 2018).

2.3 Conducted experiments of high-pressure hydrogen tank rupture

2.3.1 Physical experiments

There are relatively few conducted experiments on high-pressure hydrogen tank induced ruptures in the open literature. One instance was carried out by Weyandt (2005), to examine the catastrophic failure of a high-pressure hydrogen tank and the corresponding extent and magnitude of the subsequent blast wave and fireball. A cylinder Type IV, 74.2 L (1.64 kg hydrogen) and had an internal pressure of 34.3 MPa at the beginning of the experiment. To ensure a catastrophic rupture, the tank was altered to exclude a TPRD. The cylinder was set 20 cm above a propane fire of 370 kW heat release rate, and it was exposed to the fire for 6 minutes and 27 seconds, after which it failed catastrophically as the integrity eradicated initially fracturing through the bottom. The maximum pressure was recorded at 1.9 m was 300 kPa. An estimated 10.8 MJ in mechanical energy was released when the tank burst, with a corresponding 197 MJ in chemical energy released in total as combustion occurred (Weyandt, 2005). Recorded using a high-speed video camera, a fireball was observed instantly after the tank burst. The initial shape of the fireball is captured with rapid expanding flame is specific directions, before becoming more hemispherical after 45 seconds, see Figure 2.5. Another experiment carried out with the tank placed under (28 cm above the ground)

a typical SUV vehicle kept the same mission of inducing a catastrophic failure of a Type III hydrogen tank (Weyandt, 2006). A propane fire with 265 kW heat release rate was installed, using 12 minutes and 18 seconds for the tank to burst. An estimated 12.8 MJ in mechanical energy was released when the tank burst, and up to 220 MJ in chemical energy released, based on the heat of combustion of hydrogen. In this case, the projectiles were more significant as the vehicle body frame moved 22.3 m. At a distance of 1.22 m is where the maximum pressure was recorded of 140 kPa.

Figure 2.5: Fireball formation after tank rupture of a stand-alone tank at 10 ms (left), 45 ms (middle) and 997 ms (right) (Zalosh and Weyandt, 2005).

Another experiment was conducted by Tamura et al. (2006), whereby two high-pressure hydrogen tanks, Type III (36 L) and Type IV (35 L) respectively, were rupture-induced by a bonfire. The former tank was filled to a nominal pressure of 70.69 MPa prior to being engulfed in fire. The internal pressure measured by a pressure transducer measured a pressure upsurge of almost 30% to 99.47 MPa before catastrophically rupturing. The blast wave measured at 5 m perpendicular to the tank was 74.3 kPa, with a fireball diameter measured at *"about 20 m"*. For the Type IV tank and its rupture, the pressure upsurge before it burst measured was almost the same as for tank III, from 70.23 MPa to 94.54 MPa, a 25% increase. However, the blast wave measured closer to the tank at 5 m was measured higher at 110.5 kPa with a similar maximum measured fireball diameter. The rupture time for tank Type III and Type IV was 654 s and 1281 s (i.e 10 min 54 s and 21 min 21 s) respectively. Last, and fairly recently, two experiments of high-pressure hydrogen storage tank rupture in fire were conducted by Shen et al. (2018), to assess the consequences following a catastrophic explosion. The explosion process consisted of having a Type III tank with an internal volume of 165 L. The nominal working pressure was 35 MPa with an allowable working pressure of up to 43.75 MPa. The tank was subjected 100 mm above a fire source and in both experiments the failure of TPRD to activate resulted in explosions. In the first test, onwards denoted as Test 1, the internal pressure of the tank increase to 44 MPa, and in the second experiment (Test 2) increased to 43.74 MPa. The internal temperature of the gas was not measured. The fireball size in both experiments was measured to be around 7–8 m. Various projectiles as a function of the rupture occurred distinctively for both cases.

2.3.2 Numerical experiments

The use of CFD enables governing equations and combustion models to gain insight into physical phenomena and simulate results resembling the trends of relevant experimental data. Furthermore, it allows sequences of unwanted events to be carried out, without the need to perform expensive and sometimes non-applicable experiments. However, to have confidence in the results, a comprehensive set of best practice guidelines are to be followed, for fuel cells and hydrogen applications (Tolias et al., 2018). For CFD tools to be an integrated part of the risk assessment methodology, the procedure starts with a worst-case evaluation. It is then followed by a realistic worst-case evaluation, and ultimately a probabilistic risk evaluation. Throughout the procedure, if the consequences are seen unacceptable, modifications of the design are and evaluated, and mitigation methods considered (Hansen and Middha, 2008). A high-pressure tank rupture is a complicated explosion process, which as opposed to a hydrogen leak or deflagration, is difficult to recreate in simulations. Several attempts have been used in developing a validated model for high-pressure tank rupture using various models based on the experimental data in (Weyandt, 2005). In the earliest work by Shentsov, Kim, Makarov and Molkov (2016), the applied CFD model used to compare against experimental data was the renormalization group theory (RNG) k-epsilon model for turbulence. It was found more accurate than the standard k-epsilon model, as it features significant improvement in accuracy for rapidly strained and swirling flows. Combustion was incorporated using 37 elementary chemical reactions with the eddy dissipation model (EDC) as the sub-model, which had been confirmed with its predictive power to reproduce numerical simulations of spontaneous ignition of hydrogen (Bragin et al., 2013). A polyhedral mesh was used to resolve stiff evaluation of high gradients of velocity and pressure observed in tetrahedral mesh, with a total number of control volumes (cells) of 172 199. The obtained results from simulations overestimated the blast wave pressure in the near field (1.9 m), with better reproduction at the two latter sensors at 4.2 m and 6.5 m (see Figure 2.6). To explain the overprediction of close to 100 kPa at the first sensor, lack of energy not displaced in to ground cratering and with the converse effect of ground reflection was reasoned. The maximum fireball size was found to be between 10.5 m and 12 m, corresponding better to the value of 11.8 m, found using an analytical model. Furthermore, at 45 ms the fireball size measured in the experiment of 7.7 m corresponded well with size found in simulation at similar time duration. Some initial measurements and geometric features required for simulations were not readily available, constricting the accuracy of input information in the simulations. Therefore, some assumptions based on calculations were inferred adding to a systematic uncertainty of the simulations results.

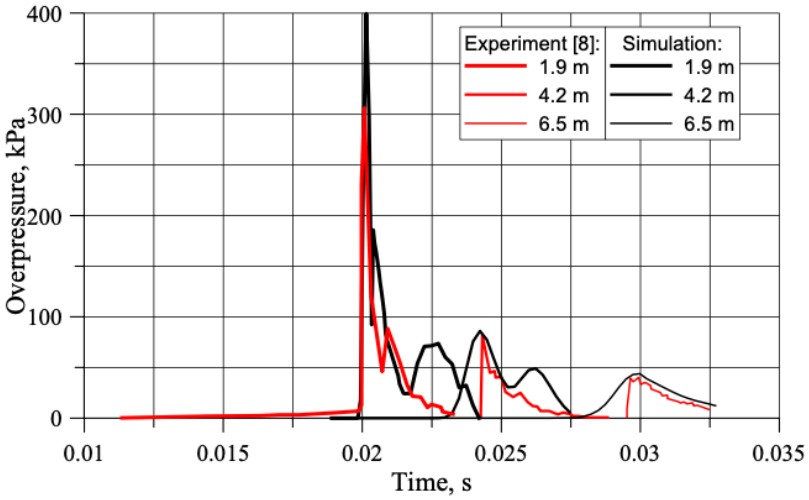

Figure 2.6: Comparison between blast wave overpressure between developed simulation and experiment (Shentsov, Kim, Makarov and Molkov, 2016).

Most studies neglected the hazards generated by the fireball. Therefore, a study was later conducted to investigate hazards distances determined by the blast wave and also fireball, and the effect of radiation sub-model was implemented (Shentsov, Cirrone, Makarov and Molkov, 2016). With radiation heat transfer included, the EDC model was coupled with discrete ordinates. The hazard distances were then determined by the pressure, but also by the generated thermal dose observed to be relatively less hazardous. An attempt by Kim et al. (2017) used the realizable k-epsilon model for turbulence, with combustion obtained from eddy dissipation sub-model. The domain was meshed using tetrahedral control volumes with a total number of 944 868 cells. These simulations again overestimated the overpressure at the first sensor, while underestimating the overpressure at 4.2 m and 6.5 m sensors. This was partly due to insufficient combustion intensity provided by the combustion sub-model, not contributing to the overall pressure. This was also evident in the obtained maximum fireball size of only 5.3 m, compared to the measured fireball size of 7.7 m of the experiment after 45 ms. To conclude, further iterations of a CFD model is required, to validate the model order for it to be used as a predictive tool. And with the inclusion of other available experimental studies available of hydrogen gaseous storage tank rupture, a more rigorous validation process can be ascertained.

2.4 Blast wave and fireball dynamics

2.4.1 Blast waves characteristics

A common definition of a blast wave is given by Zalosh (2003, p. 375): *"A blast wave generated by an explosion consists of a shock front in which the pressure rises virtually instantaneously, followed by an explosion wave in which the pressure returns to its ambient*

value". Blast waves are not always caused or created by an explosion. A rapid release of energy from a source such as a bursting pressure vessel from which compressed air expands or a rapid transition from liquid to gas can create a blast wave. In any case, as long as the vessel pressure is above two atmospheres at failure and the pressure is released abruptly, the resultant blast will be a shock wave (i.e. suddenly applied) (Dusenberry, 2010). An almost instantaneous abrupt change in pressure, shock waves are high-pressure blast waves that travel through air (or other media) at a velocity faster than the speed of sound. Below the speed of sound, blast pressure waves are characterized by a more gradual increase in pressure than a shock wave, with a decay of pressure much slower than a shock wave. The characteristics identified to describe a blast wave starts with the initial shock intensity. Depending on the explosion energy release, the initial shock pressure at a location creates a vacuum, which is usually followed with a decrease with a positive and negative phase impulse as the pressure overexpands below ambient pressure. The impulse describes the change in momentum and is projected as the area under the pressure-time curve with dimensions of the force-time product. The blast wave impulse which depends on the blast wave peak overpressure in the shock front and the duration of the wave is an important aspect of the damage-causing ability of the blast. The blast loads in the positive phase are generally more consequential than negative phase loads, the latter of which is often ignored (Crowl, 2010). The negative phase pressure is generally lower in magnitude (absolute value), but longer in the duration than the positive phase, see Figure 2.7.

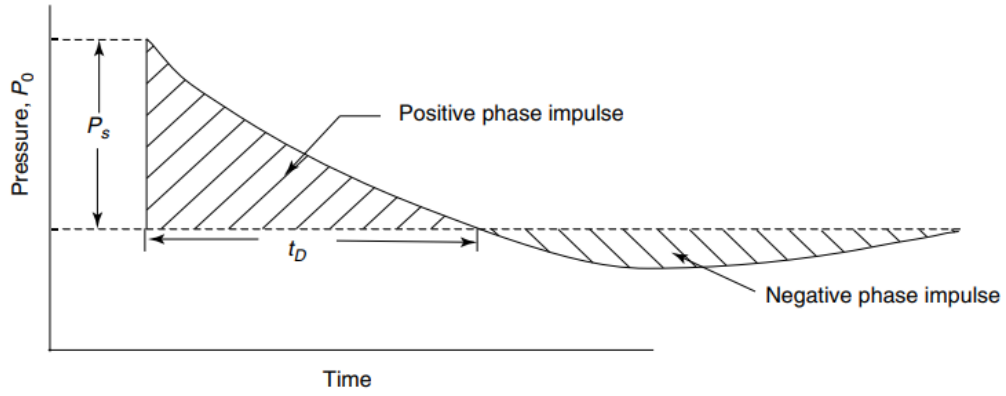

Figure 2.7: Ideal blast wave characteristics generated by a an explosion, adapted from (Zalosh, 2003).

2.4.2 Blast wave reflections

Once a blast wave is formed and hits a surface, e.g. the ground, it reflects and bounces back. The reflected wave travels through hotter and denser air than the primary wave, where the sonic speed is greater. This reflected wave may eventually catch up to the incident (or primary blast wave). Once the incident and reflected wave coalesces, they form a single reinforced shock front known as the Mach stem. The formation of the Mach stem with an associated triple point is a consequence of the inability of the (detached) reflected shock to

redirect the stream completely back to its original direction (Kinney and Graham, 2013). That is, the maximum possible angle of re-deflection for the detached reflected shock is less than the actual angle of deflection for the incident shock. Therefore, the velocity above the Mach stem is directed slightly toward the surface, and as a result, the triple point moves out from that surface (Baker et al., 1983). This will cause the region of the Mach stem to grow with time and it increases with height, as seen in Figure 2.8. The formation of a Mach stem may also be regarded as occurring when the reflected shock, unable to adjust to the requirements for stability, encroaches on the incident shock and the two shocks fuse into one. As encroachment by the reflected shock and the resulting fusion proceeds, the Mach stem grows and the triple point advances along the plane of the incident shock.

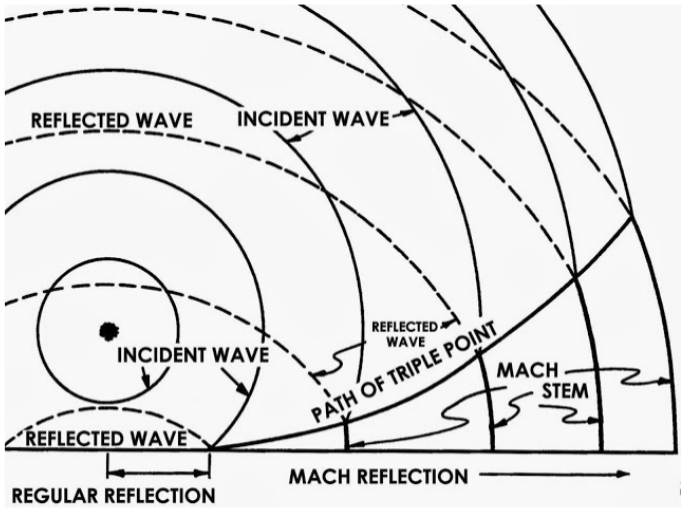

Figure 2.8: The formation and trajectory of the Mach stem, after an initial explosion (Staff, 2017).

2.4.3 Blast wave energy

The exact amount of energy distribution is dynamic throughout the explosion, pinpointing the proportion of available energy distribution difficult to determine. The energy release, if sudden and rapid enough, will cause a localisation of energy dissipated by a blast wave, propulsion of fragments and surrounding material and in many cases thermal radiation (Cullis, 2001). Once a failure of a pressurized vessel has occurred, either at or near the operating pressure of the vessel or at elevated pressures, the energy allocation is normally distributed as follows (Center for Chemical Process Safety, 1994):

- vessel stretch and tearing
- kinetic energy of fragments
- energy in shock wave

- *"waste"* energy (heating of surrounding air)

A schematic representation of energy distribution of a blast wave, subject to the nature of the explosion process itself shows distinct forms of energy behaviour at various times and locations as the explosion process proceeds, illustrated in Figure 2.9. The radiated energy is seen to quickly conform to a constant value, after initial loss to the rest of the explosion system. The propagating wave contains a fraction of its energy in the far-field, as the potential energy is redistributed in various forms and parts of the total system. The kinetic energy is primarily thermally stored in the fragments and source material, and eventually dissipates by mixing relatively slowly compared to the blast wave propagation process.

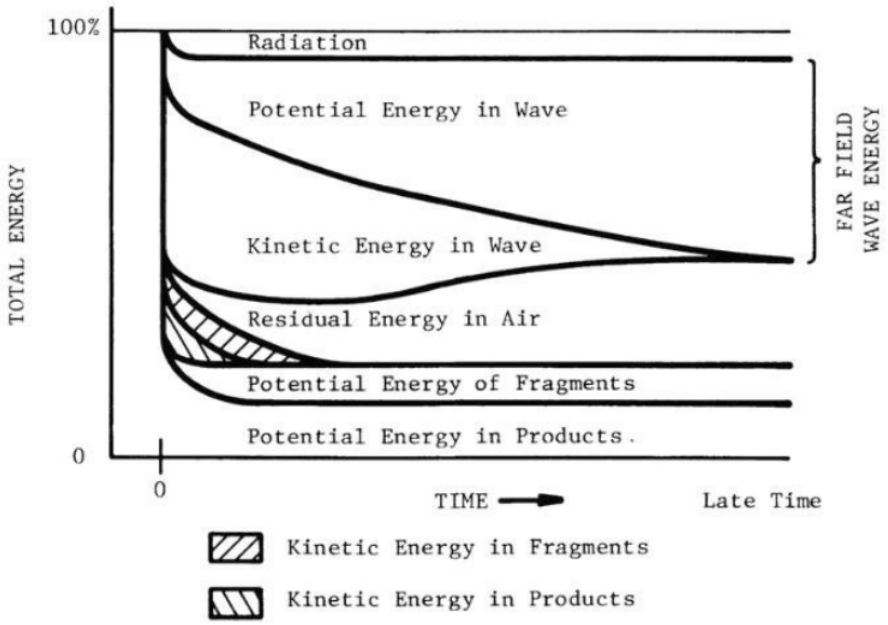

Figure 2.9: Energy distribution in a blast wave of a spherical source material as a function of time (Baker et al., 1983).

The energy of an explosion of a pressure vessel is often needed to pressurize the initial volume of the vessel from ambient pressure, with the internal energy of the system being the sum of kinetic, potential and intermolecular energy in the system. For an ideal gas, the blast wave energy based on an isobaric expansion, E, generated from compressed gas in a pressure vessel during a rupture is given by Brode (1959) as:

$$E = \frac{V(P_g - P_s)}{\gamma - 1}, \tag{2.1}$$

where V is the volume, P_g and P_s the gas and ambient (surrounding) pressure respectively, and γ the gas ratio of specific heats. Based on isentropic expansion of an ideal gas,

this originated after considering the energy of the high-temperature product gases of the combustion of a spherical trinitrotoluene (TNT) charge in a fixed volume. However, this equation is conservative, as it gives energies slightly higher than energies calculated with more precise models of the gas expansion process. The intensity of a blast wave from a bursting vessel also depends on the ideal gas assumptions inferred. In real situations, the blast wave energy released by the vessel failure is less than that of the theoretical value obtained, with real gas effects reduce the energy released as compared to an ideal gas. Hydrogen in particular exhibits significant deviation behaviourally from ideal gas when sufficiently compressed (10–20 MPa), acting more like a non-ideal gas (Molkov, 2012). The chief differences between ideal and real gasses arise from the variation of specific heat with temperature and, at higher temperatures and pressures, from the processes of dissociation and ionization. This is an important application to consider due to overestimation of parameters such as mass flow rate, overpressure, temperature etc. when the ideal gas law is applied.

Quantifying the energy allocated to blast wave strength is intricate and based upon material characteristics (e.g., fracture toughness, material flaws, and mode of vessel failure), which would result in varying rates of energy released. Energies required to rupture the vessel and launch the fragments of the containment vessel may amount from 20% up to 50% of the total internal energy ideally calculated (Baker et al., 1983). High (1989) proportioned the total amount of available energy used in generating a shock wave from a ruptured cylinder conservatively around 40%, with energy losses in connection with non-ideal behaviour and providing fragment kinetic energy. Elsewhere, it is suggested a value up to 60% could be allocated to the fragment kinetic energy for brittle type failures (Center for Chemical Process Safety, 1999).

2.4.4 Prediction of a blast wave

The non-ideal early depressurization of a pressure vessel is still a phenomenon not readily accounted for. Due to real accounts of the walls of the vessel not instantaneously disappearing, the acceleration of the shock wave is often overestimated. Some authors have proposed different zones, whereby the near field and far-field calculations are tailored (INERIS, 2012). In the near field when an idealized sphere bursts, the air shock overpressure is assumed at its maximum right at the contact surface between the gas and the surrounding air. These two regions of initial high and low pressure acts like a piston in a shock tube, with the high-pressure region driving into the expansion area without mixing, neglecting diffusion (Liepmann and Roshko, 2001). This relationship between the bursting pressure ratio and shock pressure is therefore used to calculate the pressure of the shock. Although it is assumed in the case of a vessel that the explosion energy is distributed uniformly, in reality, this is rarely the case (American Institute of Chemical Engineers, 1994). Far-field blast waves are easier to predict, as they resemble those induced by an instantaneous release of energy that occurs with high explosives such as TNT. Therefore, overpressure decay in relation to distance is a more straightforward approximation. For the prediction of the blast effects from bursting vessel, the key parameters include the volume and composition of the volume in

the vessel, the failure pressure and temperature of the contents. Data is usually presented as peak overpressure versus distance per unit weight of TNT. There are several mathematical models and data correlations for ideal blast waves, showing that the blast wave pressure and impulse both are proportional to the distance. The most common approach to taking into account the effect of the explosion (either by the quantity of the explosive W, or the energy of gas expansion, E), is known as the 'cube root', reported by Baker et al. (1983) as the Hopkinson-scaled distance:

$$Z = \frac{r}{E^{1/3}} \; or \; \frac{r}{W^{1/3}}. \tag{2.2}$$

The pressure field history is identical for both the actual and reduced scale and the application times are multiplied by the scale radio of the experiment. Shock wave characteristics of a catastrophic rupture using an equivalent weight of known TNT has been utilized in the literature, e.g. (Henrych, 1979; High, 1989), on the bases of the theory of model similarity attained from experiments. This approach is conveniently used since significant data exists on TNT explosions and the resulting blast wave (Coleman et al., 1988). There are some limitations of the TNT equivalent method with regards to pressurized vessels, as they are based on the power of an explosion of a gas is proportional to a charge of equivalent TNT energy. However, the pressure developed by a TNT explosion confined within the boundaries of the charge is of the order of up to 50000 MPa (Mannan, 2005). Generally compared to TNT, a bursting vessel has usually a much lower initial overpressures with slower decay in terms of distance, with longer positive phase durations and larger negative phases and strong secondary shocks (Stoffen, 2005). Predictions of the shock wave overpressure of an explosion in the near field due to the high complexity of shock wave formation and gasses expanding erratically lower the accuracy compared to far-field overpressure predictions (Neto et al., 2017). Furthermore, some of these methods are limited into taking directional effects, asymmetric explosions or effects due to partial confinements considerations, pointed out by Hansen et al. (2010). It is therefore only reasonable to use TNT as a reference when the result sought after are of far enough range, which definition is correctly related to the explosion energy. Usually, this far range is a minimum distance of 10 to 20 times the vessel diameter. Nevertheless, it was found after experimental work presenting overpressure versus distances curves comparing pressure vessel and TNT blast waves a non-correspondence, due to among other things lack of allocated energy loss expended in vessel tearing and fragment acceleration (Dusenberry, 2010).

To further describe the overpressure behaviour after a burst, other methods are employed based on the principles of thermodynamics. Using the shock tube method, the mass of gas proposed as the differentiating parameter originates from Brode (1959). Assuming air surrounding the tank, the near field is defined within 10 times the radial distance of the explosive charge. In the far-field assuming the blast wave characteristics are only dependent on the source energy, the blast wave is simplicity estimated using an extrapolated overpressure produced graphs based on a load of TNT as a function of Z, referred to as TM 5-1300 graphs. This method has since been proposed some modifications known as the PROJEX method can be found elsewhere (INERIS, 2012). The blast wave produced

of different weights could be scaled once detonated in atmospheric conditions. However, this is true only for varying distances and not varying initial pressure, which was found to give inconsistencies with regards to impulse in particular. Therefore, the Sachs-scaling is used by Baker et al. (1975), which takes into regards the surrounding pressure, adaptable to change in both blast distance and corresponding pressure. A dimensionless distance of a target from the energy release centre is accordingly given as:

$$\overline{Z} = r\left(\frac{P_s}{E}\right)^{1/3}, \tag{2.3}$$

where r is the distance from the energy source, $\overline{Z}$ is the non-dimensional distance, and E is the blast wave energy. Baker et al. (1978) proposed both near field and far-field pressure versus distance relationship based on the results of numeric calculations of bursts of tanks containing perfect gasses, air assumed surrounding the vessels. The effects of the containing vessel and its fragments were all disregarded with no loss of kinetic energy, with all of the energy within the gas vessel put into the flow field. For far-field, an overpressure decline similar to a high condensed explosive, pentolite, was used with similar properties to that of TNT. These correlations have been standardized as one of the few methods for predicting blast wave from vessel rupture (Center for Chemical Process Safety, 2010). It was previously instated that combustion contribution to blast waves was kept at a minimal, due to different time-scales between the propagation of blast wave and corresponding reaction rate of combustion and its products. However, and especially for hydrogen known for its spontaneous ignition and high flame speed, the omission of combustion energy contributing to the blast was updated (Molkov and Kashkarov, 2015). Indeed, existing models used to predict the blast wave strength and decay excluding combustion were debunked – a newly developed model which takes into account real gas effects and combustion of the flammable gas released into the air (chemical gas). Based on the dimensionless distance expressed in Equation (2.3), the model was redefined as:

$$\overline{Z} = r\left(\frac{P_s}{\alpha \cdot E_m + \beta\left(\frac{r_{sh}}{r_b}\right)^3 \cdot E_{ch}}\right)^{1/3}, \tag{2.4}$$

with E_m and E_{ch} being the total mechanical and chemical energy of the vessel respectively. Including an empirical mechanical energy coefficient to account for ground effects, α, it also introduces a chemical energy coefficient β, indicating the fraction of combustion energy contributing to the blast wave strength. It also accounts for losses on radiation from the flame. $(r_{sh}/r_b)^3$ describes the ratio between the volume of hemisphere behind the shock, r_{sh}, and the volume of the hemisphere that could be occupied by products of complete combustion of hydrogen released, r_b. This unfixed ratio was to account for the physics of gradual combustion of products, as opposed to α, as a rupture and release of the mechanical energy is considered instantaneous. This updated model, as seen in Figure 2.10, was able to

reproduce experimental data with increased accuracy, both stand-alone and under-vehicle stored hydrogen tank rupture. In the latter experiment, the fraction of stored combustion energy released in the experiments feeding the shock wave was found much larger than the total mechanical energy of the compressed gas.

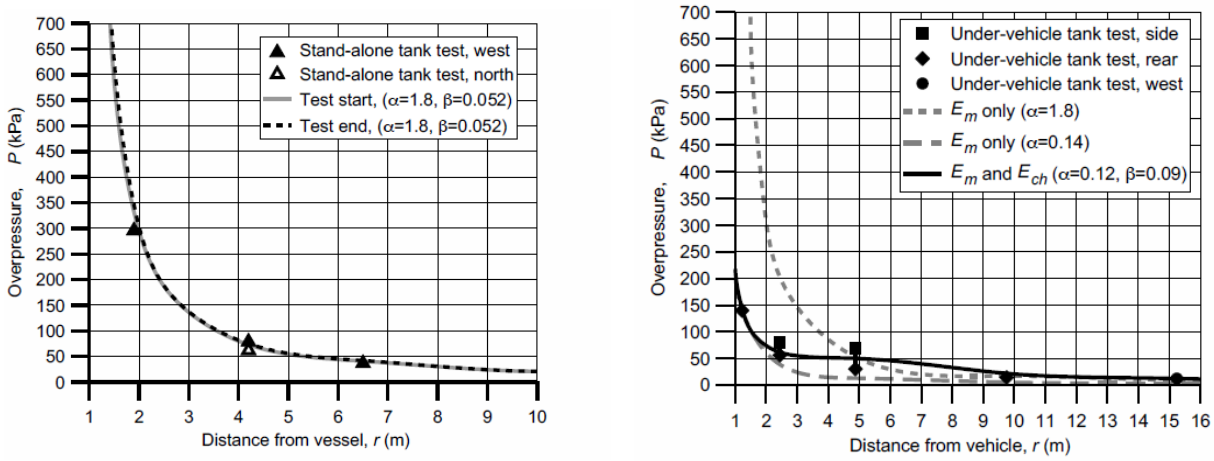

Figure 2.10: Experimental data on blast wave decay in stand-alone (left) and under-vehicle (right) taken from Weyandt (2005, 2006), and calculations with and without combustion contribution using the real gas model (Molkov and Kashkarov, 2015).

Cylindrical effects

Charges with geometrical characteristics (spherical, cylindrical or block) are often not considered when TNT equivalence method is carried out, which is based on data for spherical charges. Time, orientation and directional effects are therefore not only varied, but the effects may also be inherently enhanced (Knock and Davies, 2012). Most real blast sources such as cylindrical or block-shaped are non-spherical and can be quite complex, presented in Figure 2.11. The shock fronts have highly directional properties, with a decay that is quite different from a near-field spherical wave. The pattern, unlike being proportionate in all directions, from a cylindrical vessel reflects off each other and creates bridging waves as the shock waves collide and coincide.

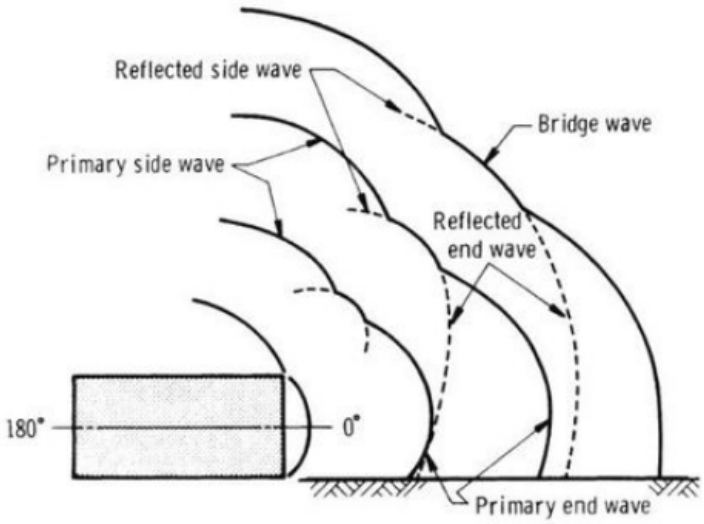

Figure 2.11: Schematic wave development of a cylindrical charge (Baker et al., 1983).

There are several pressure/impulse multipliers suggested for bursts of a cylindrical vessel as a function of $\overline{Z}$ listed in the literature, see Table 2.2. Most of these relations are based on experimental data, and often restrained to extrapolation within the range of the correlation provided. Empirical in nature, these constraints are one of the limitations of these methods, using correlations based on dimensional or dimensionless groups (Birk et al., 2007). Additionally, the energy of explosion assuming it stems from a specific point source is rarely the case in real life process equipment explosions (Geng et al., 2011). Therefore, these multipliers for a cylindrical vessel may not be representative in giving accurate results at large distances. Directional blast effects are observed to diminish with increasing distance, with the load gaining even distribution in all directions. Due to dependence on the experiments used to extract from which these factors were derived, their scope of accuracy are very limited. In conclusion, a simple correlation using parameters such as pressure ratio and cylindrical vessel aspect ratio due to their unpredictable nature development of adjustment factors are found unattainable.

Table 2.2: Adjustment factors for pressure and impulse for cylindrical vessels of various dimensionless parameters (Baker et al., 1975, 1983).

$\overline{Z}$	Multiplier for	
	$\overline{P}$	$\overline{I}$
< 0.3	4	2
$\geq 0.3 \leq 1.6$	1.6	1.1
$> 1.6 \leq 3.5$	1.6	1
> 3.5	1.4	1

Ground effects

It was observed by Henrych (1979), that with a ground explosion the corresponding shock wave energy from the charge was concentrated, as opposed to an explosion in an unlimited atmosphere and therefore; *"all relations derived before for an explosion in an unlimited atmosphere are valid here too, except the energy of the charge, E, must be substituted with* $2 \times E$*"*. For instance, take a configuration as shown in Figure 2.12(a), whereby an explosive charge with diameter, d, is located on the ground shown both axial and perpendicular direction. Consider a half of the explosive charge containing the same weight as the original explosive charge, within the same tunnel with hydraulic diameter, d_H, showed in Figure 2.12(b). If the wall is assumed perfectly smooth and rigid with no irregularities the blast wave would be reflected in its entirety without any energy loss. This is similar to the case in which the explosive is located at the middle point of the tunnel geometry with double dimensions, as shown in 2.12(c). Although a simple factor of 2 would be sufficient, Baker et al. (1983) suggested to multiply the effective source energy by a factor of 1.8, as in actuality some energy ($\approx 10\%$) is lost due to partial reflection and/or cratering.

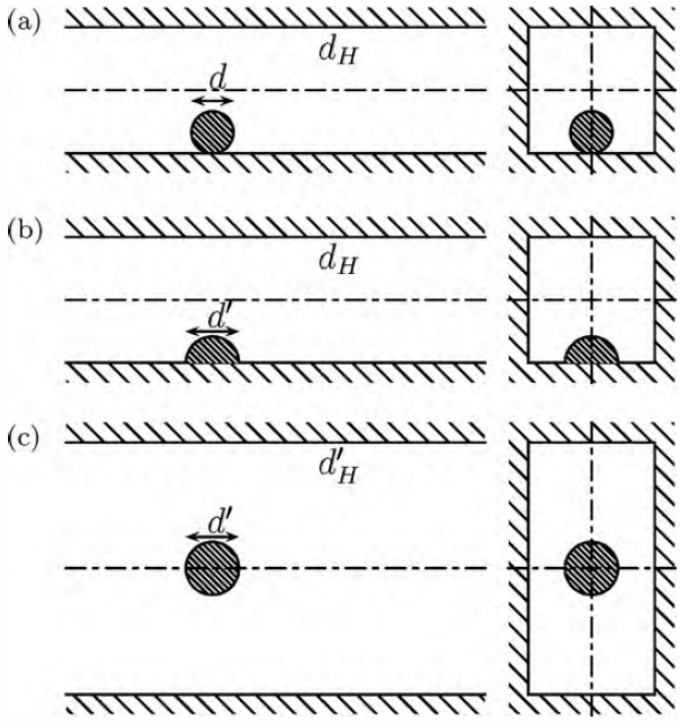

Figure 2.12: Ground effects demonstrated for an explosive charge on the ground (a), the explosive charge half the geometrical size on the ground (b), and the equivalent half envisaged centred (c) (Benselama et al., 2010).

2.4.5 Fireball dynamics

It could be apparent that blast wave severity is far greater than that of thermal radiation which follows with a fireball. Generally, a fireball is a dynamic phenomenon, an extremely hot and highly luminous spherical mass of air and gaseous weapon residues, that grows rapidly after its formation (Martinsen and Marx, 1999). Illustrated in Figure 2.13 is the life cycle of a fireball. It is normally relatively short (up to a 2 s), and during its duration passes through various distinctive stages chronologically: growth, steady burning and burnout (Mannan, 2005). During the growth stage, as rapid mixing and combustion occur, there lacks a distinct shape whereas in the steady burning stage the fireball is roughly spherical and conforms into a mushroom shape. The fireball later decreases in temperature due to the increase in mass and rises with buoyancy effects. Here, it may reach its maximum diameter and the limited fuel supply eventually consumed causing the fireball to burnout.

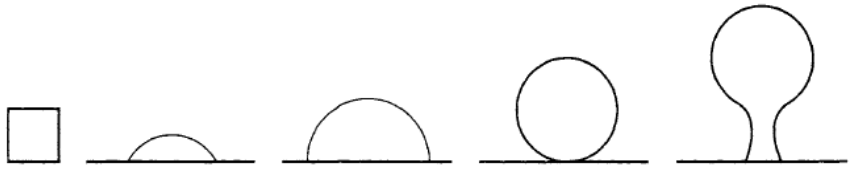

Figure 2.13: Development of a typical fireball from a source at ground level (Mannan, 2005).

Current models of fireballs despite its dynamic behaviour are mostly treated as a static event, assuming when it reaches its maximum diameter maintains that size for the full duration of the fireball (Martinsen and Marx, 1999). The calculation of the fireball diameter is done by relating the fireball diameter to the fuel mass, contributing in its entirely to the fireball formation as $D_f = k \cdot m^n$, where D_f the maximum fireball diameter, m the mass of fuel involved and k and n constants depending on the model derived of specific fuel or mass. It is also assumed that the ignition occurs when the mixture is in stoichiometric ratio and all available fuel is burned (Roberts, 1981). Following this simple empirical equation, Hord (1978) developed the following hydrogen-based fireball diameter model based on tests with hydrogen-air and rocket bi-propellants:

$$D_f \approx 7.93 \cdot m^{1/3}. \tag{2.5}$$

The fireball duration, t_f, relating the duration or lifetime of the fireball to the mass of fuel invoked in the fireball was estimated as:

$$t_f = 0.47 \cdot m^{1/3}. \tag{2.6}$$

Zalosh and Weyandt (2005) suggested that the fireball duration correlation, Equation (2.6), was better suited when the fireball was momentum-dominated, and to better correlate

fireball with buoyancy effects using:

$$t_f = 2.6 \cdot m^{1/6}. \tag{2.7}$$

These models are however very restrained in understanding the phenomena associated with combustion of fuel and flame structure inside the fireball, and the transient growth of a fireball analytically is an approach not universally determined yet.

2.5 Blast wave and fireball dynamics in a tunnel

The potential hazards associated with hydrogen vehicles in road tunnels was internally identified and investigated by a project called HyTunnel (Kumar et al., 2009). Mainly non-instantaneous hydrogen release (i.e. through vents) were illustrated through reviewing current hydrogen designs, tunnel design practice and a programme of experiments and CFD modelling performed for selected scenarios. Despite specifying a simultaneous release of a large mass of hydrogen found to be more hazardous compared to when the same mass being released through a single vent, a study extended to examine this particular issue was left unattended. There are only two studies performed experimentally or numerically (to the author's knowledge) looking into the hazards of high-pressure hydrogen tank rupture in a tunnel of natural provenance. The first was conducted by Shentsov et al. (2018), numerically investigating the blast wave dynamics after a 140 L (5.5 kg) 70 MPa hydrogen tank rupture in a 150 m tunnel with a cross-section of 40 m^2. The generated maximum blast wave overpressure within the first 50 m was presented (see Figure 2.14). During a fast decrease of blast wave overpressure up to 10 m, a higher overpressure as a function of height was observed. The overpressure within the tunnel cross-section was uniform after 40 m, with a relatively slow decay pattern as a function of distance thereafter.

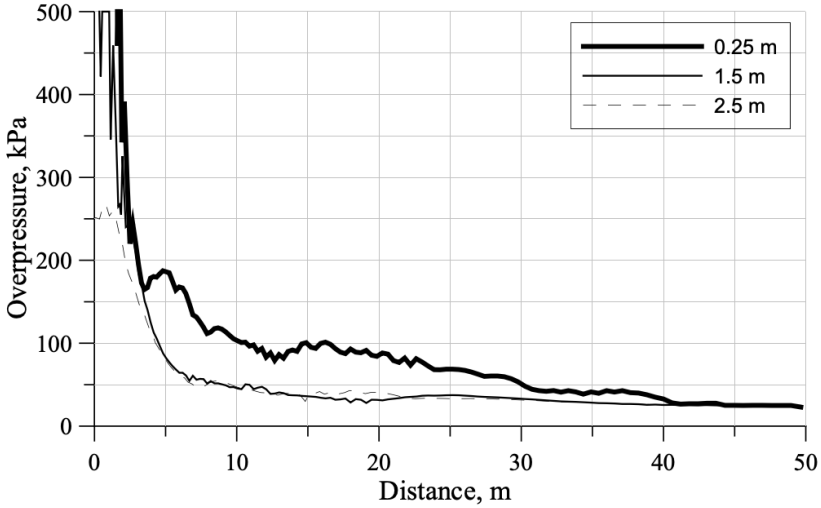

Figure 2.14: The maximum blast wave overpressure in a tunnel after a high-pressure hydrogen tank rupture, shown for various heights (Shentsov et al., 2018).

The second study found on high-pressure hydrogen tank rupture in a tunnel was conducted by (Li, 2019). Here, explosion hazards of alternative fuel vehicle in tunnels were investigated including high-pressure hydrogen tank rupture. For hydrogen tanks (2–6 kg) in a 50 m^2 cross-section tunnel, results showed a peak overpressure rapidly decreasing within the first 50 m, after which a significantly reduced rate of decay ensued up towards the 250 m tunnel exit. However, with the use of an one-dimensional CFD model, the accuracy in the near field was deemed reduced as the model would not be able to properly attain secondary shocks that initially appear. For the development of fireball in a tunnel, a model was developed for a general hydrocarbon fuel, interpreting the volume produced of stoichiometric combustion (Li, 2018). The length within a tunnel of a certain cross-sectional area was proposed as:

$$L_{max} = 102\frac{m}{A}, \tag{2.8}$$

where A is the tunnel cross-section area, and m the mass of fuel. Not validated against experimental data yet, it alludes to the fireball propagation being one-dimensional in contrast to the three-dimensional fireball in an open atmosphere. The model for open atmosphere and tunnel differs proportionally to the amount of fuel. For instance, for a 10 kg fuel, the maximum fireball diameter is calculated to be 10 m for open atmosphere and 20 m in a tunnel (50 m^2 cross-section). Correspondingly, for a 30 kg fuel mass, the maximum fireball diameter is calculated to be 19 m in an open atmosphere, and 60 m in the same aforementioned tunnel, a significant increase.

2.5.1 Blast wave propagation in a tunnel

Despite the paucity of research of high-pressure tank rupture in a tunnel, there are other studies conducted of various explosives in tunnels, which can be used to analyse the general blast wave and fireball characteristics. For instance, in a scenario whereby a burst centred in a tunnel occurs, an initial formation of a Mach stem on either side of the tunnel wall appears. Each follow a symmetric triple point trajectory and the position where they coalesce, and the whole tunnel may be subjected to the same overpressure, see Figure 2.15. In fact, Kinney and Graham (2013) found it possible to define an empirical hyperbolic equation describing the critical angle separating the region of oblique reflection and Mach stem formation:

$$\theta_{max} = \frac{1.75}{M_x - 1} + 39 \; for \; M > 1, \tag{2.9}$$

where θ_{max} is the limiting angle in degrees for Mach stem formation and M_x is the Mach number for the incident shock. Once the Mach stem is established, it has a uniform pressure propagating profile and may then be enforced by reflected shock waves.

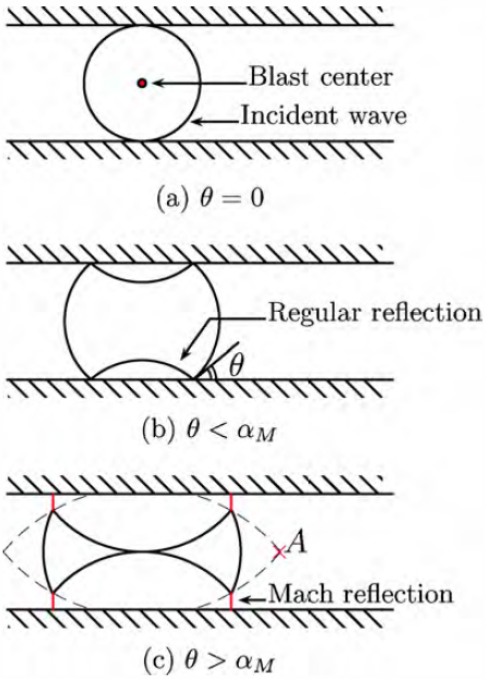

Figure 2.15: Illustration depicting the wall reflections from a blast wave according to the incident angle θ. A refers to the position whereby both Mach reflections coalesce (Benselama et al., 2010).

A numerical and reduced-scale experimental investigation of blast wave pattern reliance on the geometrical condition was performed by Pennetier et al. (2015). TNT masses of range between 0.53 to 11.69 kg in a tunnel with a constant square section of 5 m $\times$ 5 m with a length of 30 m was considered with one side near the explosive closed and the opposite side open in numerical simulations. The experimental set-up was identical in aspect ratio, although at a reduced scaled model of 1:30 the size. Instead of using TNT masses, a propane-oxygen stoichiometric mixtures corresponding to the aforementioned TNT masses were used, with bubble radius between 25 mm and 70 mm. Figure 2.16 highlights the arrival time of the blast wave shock waves using one example of the numerical and experimental results. Points (a), (b), and (c) correspond to the overpressure peaks from the initial, reflected and the coalesced blast wave, respectively. The coalesced blast wave that occurs when both the initial and reflected waves converge, denoted as (I), (II) and (III), causes the maximum overpressure peak and highlights the commencement of a uniform pressure propagation within a tunnel behind the shock.

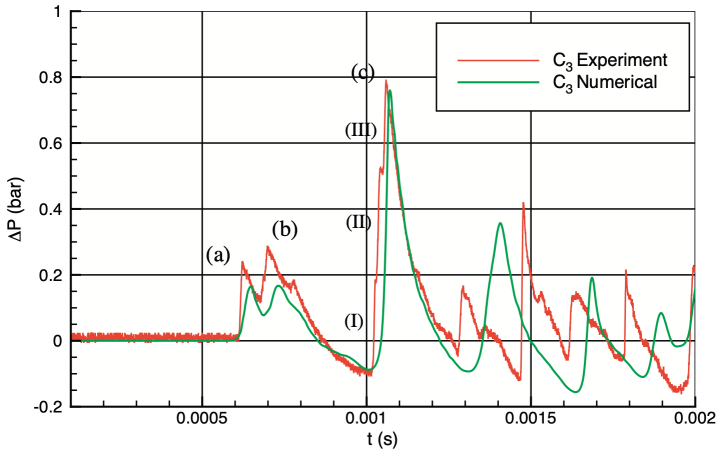

Figure 2.16: Experimental and numerical pressure evolution of a sensor located 30 cm and 11.5 m away from the scaled numerical and experimental case respectively (Pennetier et al., 2015).

One method of predicting the blast wave of explosives (expressed as Z) in a tunnel is by adapting free-field decay laws, e.g. (Henrych, 1979; Kinney and Graham, 2013), into one that considers geometry. Introduced as the energy concentration factor, it is the ratio between the volume of the expanding blast wave hemisphere in an open atmosphere and the volume of tunnel (Silvestrini et al., 2009). This reduction of volume available for the blast wave to expand in a confined space is taken into account with this geometrical factor, as the spatial density is subsequently increased. The evolution of blast wave decay in a tunnel was found to have two distinguishing patterns (Benselama et al., 2010). Initially, a free-propagating three-dimensional (3D) blast wave was established before reaching the close-in effect of the tunnel walls. Once this occurs, a transitional period whereby the blast wave becomes a quasi-one-dimensional pattern. Using different quantities of TNT charges centred inside a tunnel, various simulations were conducted, each explosive weight corresponding to a parameter, α_W: the ratio of the equivalent TNT explosive quantity to the tunnels hydraulic diameter. A proposed fitting law to determine the transition zone was offered as:

$$Z_{TR} = \frac{0.0509}{(\alpha_W/100)^{13/9}}. \tag{2.10}$$

The illustration of an initial free-field decay blast wave, the transition point and the following one-dimensional decay pattern are shown in Figure 2.17. It was ascertained that the shape of the blast wave and transition zone would differ significantly in a rectangular cross-sectional tunnel where the transversal and vertical reflections do not occur simultaneously (Uystepruyst and Monnoyer, 2015). A two-dimensional (2D) pattern after the first vertical reflection (in the direction of the height) was singled out, a pattern initially occurring after the free-field pattern and before the one-dimensional (1D) pattern in the direction of the width. Following, a 3D–2D–1D pattern was proposed based on numerical experiments.

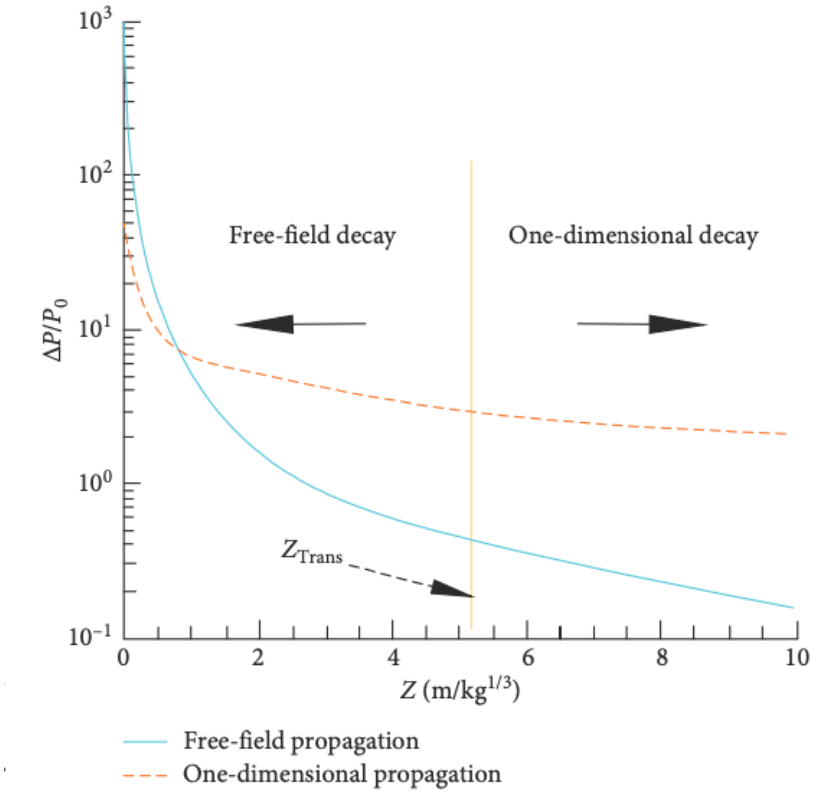

Figure 2.17: The use of the free field decay lay, transition zone and one-dimensional decay synthesized, illustrated by Fang et al. (2019).

Earlier forms of blast wave decay law established was derived by Curran et al. (1966), indicating the dependence of the peak overpressure, P, on the ratio of charge weight, m, to the volume of enclosure or tunnel, V, as $P \propto A \cdot (m/V)^b$, where b represents the decay pattern of maximum blast wave overpressure. There are various parameters found for A and b, depending on the tunnel and explosive charge found by other authors (C. Smith and J. Sapko, 2005; Skacel et al., 2013; Rodríguez et al., 2010). The isolated effect of friction from a straight wall is mostly omitted in decay laws found in this review, with substantially limited applicability found elsewhere (Ning and Bin, 2012). Despite the notion that its influence on the blast wave decay is non-negligible, roughness factors and determining friction coefficients is a fickle matter to tamper with, with little comprehensive parameters generally established (Skjeltorp, 1975). Performing hydrodynamic calculations of a blast wave propagating in a long conduit, it was carried out for both smooth and rough wall, whereby surface perturbations were inferred with an amplitude of 50 mm (Kivity, 2012). Results showed an effect of a shock front pressure reduced up to 50% at certain distances.

2.5.2 Fireball dynamics in a tunnel

Within a tunnel, confinements effects lead to a higher and wider temperature range, in addition to a longer duration compared to in open space. Additionally, the heat release rate may be quadrupled (Beard and Carvel, 2012). Chen et al. (2017) investigated the dynamic thermal environment inside a tunnel after an explosion, with the presence of explosion fireball radiation. The explosive used was a 100 kg thermobaric explosive, a new subcomponent of volumetric explosives with higher thermal characteristics and duration up until 10 times more than traditional explosives i.e. TNT. Simulating an open ended tunnel case, the results showed, after the preliminary period, a concentration of high-temperature at the top of the tunnel near to the explosion source, see Figure 2.18. The confinement of the tunnel forced forward a natural convection process whereby the hot air rose with direction towards the exits, with *"cold"* air gradually concentrating at the bottom.

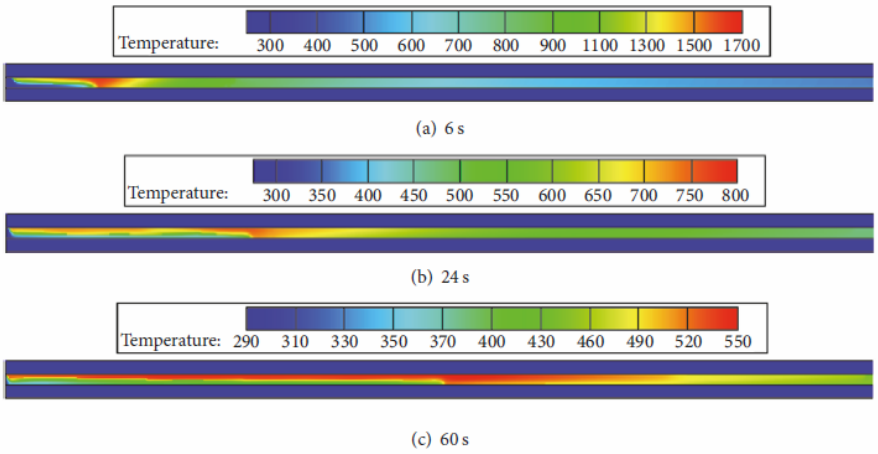

Figure 2.18: Temperature variation in the tunnel after the explosion of 100 kg TBX (Chen et al., 2017).

Figure 2.19 shows the maximum temperature curves, measured at a height of 20 cm below the tunnel ceiling. The temperature curves are seen to initially display high values before attenuating spatially. More noticeable are times after 240 s, a relatively high temperature sustained up until 840 s (14 min) at $\approx$ 300 K – close to atmospheric (surrounding) air temperature. This long duration time was pointed out to be dangerous, as with regards to its potential source of a secondary fire once a flammable gas mixture was still present.

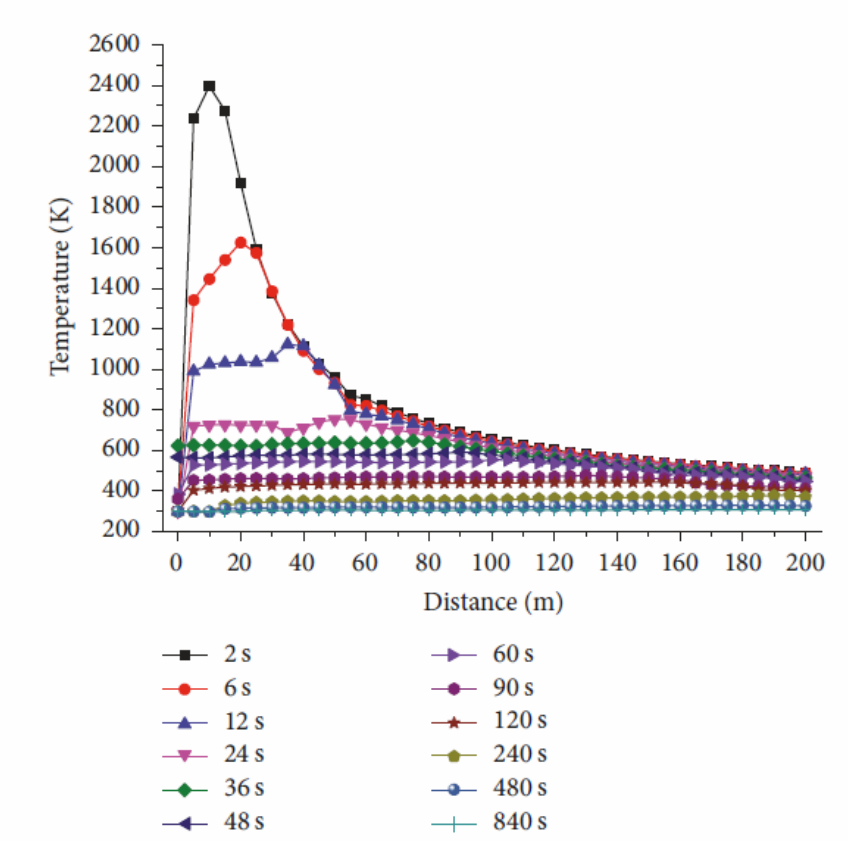

Figure 2.19: Spatial variation of the temperature at different times after explosion in the tunnel at a 20 cm height below the ceiling (Chen et al., 2017).

2.6 Pressure and thermal hazards

2.6.1 Blast effect on humans and structures

Blast damage caused by the shock wave generated from an explosion has various primary effects on humans and structures alike, depending not only on the strength of the incident, reflected and dynamic overpressure, but also on the duration of the blast wave (Baker et al., 1983). Pressure effects on humans depend primarily on the duration of the blast wave, indicative of the primary effects [5], on the body stemming from a combination of overpressure and impulse. If the duration of the overpressure is long, this external pressure will have ample time to push the chest wall inwards cause injury. Contrariwise if the blast wave passage is relatively short, the impulse will cause the primary injury effects (American Institute of Chemical Engineers, 1994). In the event of an explosion, it is however typically defined as a function of peak overpressure, as the exposure time is usually very short (under 100 ms). Time to react or take shelter does not pragmatically enter into the relationship.

[5]Primary effects are referred to as fragments originating directly from the explosion source such a pressure vessel (American Institute of Chemical Engineers, 1994).

Injury to the body is mostly subjected to the lung, as it has a relatively large void between its tissues (air), thus most susceptible to primary blast damage such as haemorrhage. The ear, although not a vital organ, is extremely sensitive to pressure effects and can easily cause a rupture of the eardrums, designated therefore as the threshold for the initial injury (Baker et al., 1975). Secondary effects, defined as impact by accelerated missiles originating after interaction with the blast wave, may involve skin laceration, blunt trauma and head impacts from buildings and other structures being disintegrated. These injuries followed are typical causes for fatality, as the human body can survive fairly strong blast wave direct from the explosion. A third category, tertiary effects, involves whole-body displacements due to the explosion wind. In these cases with the displacement acceleration relative to the size, shape and mass of the person, the head is the most vulnerable part of the body (UK HSE, 2010). Another significant factor that determines the severity of the injuries inflicted is the orientation of the person relative to the blast front, as seen in Figure 2.20. Besides, a person standing next to a wall orthogonal to the blast wave will be subjected to a reflected blast wave, increasing the overpressure cultivated. These are all parameters that ensure determining an undisputed harm criteria cumbersome.

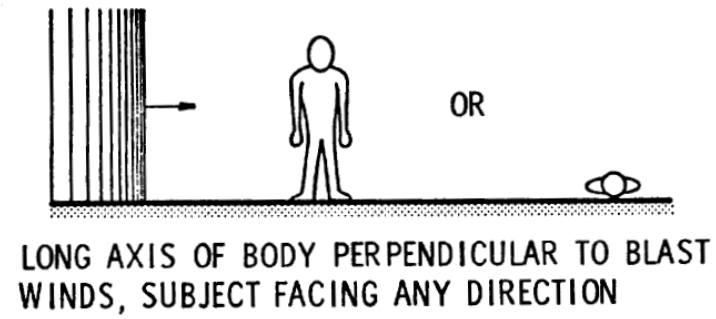

Figure 2.20: Human body position subject to blast wave (Baker et al., 1975).

The choice of harm criteria and assessment for humans and structures varies in the published material. Early criteria from 1968 are presented in Figure 2.21, reconstructed by calculating scaled incident overpressure and scaled specific impulse (Baker et al., 1983). Although antiquated, it is a novel approach to access survivability applying to all altitudes with different atmospheric pressure and all masses of human bodies.

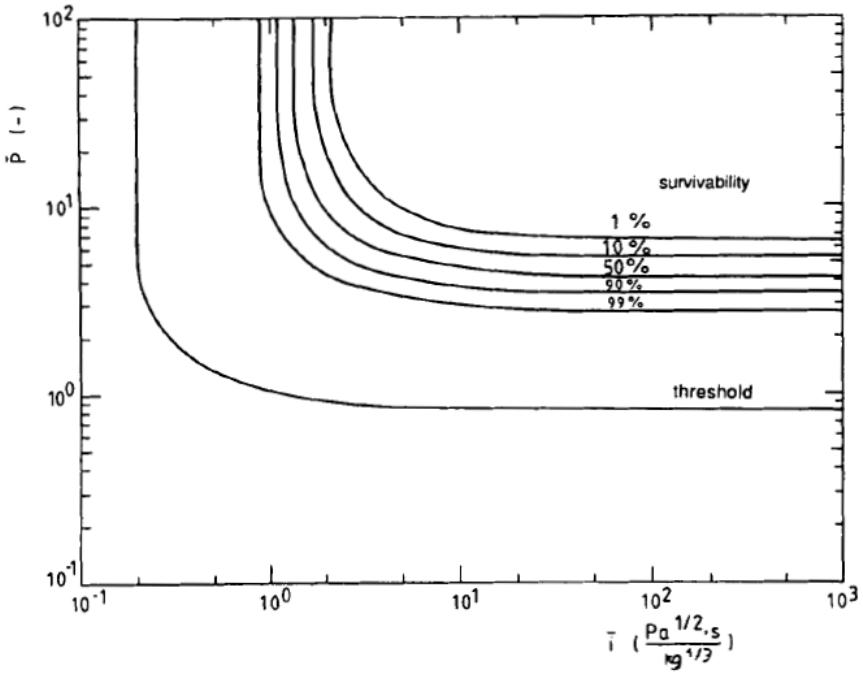

Figure 2.21: Pressure vs impulse diagram for lung injury, with the scaled parameters for pressure and impulse (Baker et al., 1983).

An updated harm criteria and assessment for humans are found elsewhere, (Jeffries et al., 1997; Zalosh, 2003; Malhotra et al., 2017), with scattered values of pressure depending on the harm criteria. For instance, the threshold for eardrum rupture is between 13.8–35 kPa, and the threshold for lung damage between 210–280 kPa. When the overpressure duration is longer, the effect on humans and structures are summarised in Table 2.3.

Table 2.3: Long duration overpressure and the corresponding effect on structures and humans (Zipf and Cashdollar, 2015).

Overpressure, kPa	Effect on structures	Effect on human body
6.9	Window glass shatters	Light injuries from fragments occur
13.8	Moderate damage to houses (windows and doors blown out and severe damage to roofs)	Serious injuries are common, fatalities may occur
20.6	Residential structures collapse	Serious injuries are common, fatalities may occur
34.5	Most buildings collapse	Injuries are universal, fatalities are widespread
68.9	Reinforced concrete buildings are severely damaged or demolished	Most people are killed
137.9	Heavily built concrete buildings are severely damaged or demolished	Fatalities approach 100%

After validating an analytical model from experiments whereby the chemical energy contribution was included, the overpressure distances for stand-alone and onboard tank were investigated (Molkov and Kashkarov, 2015). Four tanks, a 100 MPa pressure stand-alone tank similar to a refuelling station vessel and three on-board with typical volumes typical for hydrogen-powered vehicles, 170 L (35 MPa), 33 L (70 MPa) and 12 L (70 MPa), was chosen to determine the deterministic hazard distances, see Table 2.4. Hazard distance is a recent term to describe the distance from the source of hazard to a determined physical effect, leading to a harm condition i.g. no and maximum harm to people, equipment or environment. The values for harm and damage criteria were subjectively selected by the authors involved as 1.35 kPa, 16.5 kPa and 100 kPa for *"no harm"*, *"injury"* and *"fatality"* respectively, and are disposed to alternative interpretations. It is however evident that the distance needed to avoid injury or worst for refuelling stations at 470 m is distance noteworthy. Likewise in a tunnel, the blast wave harm assessment based on conducted simulation found a no *"no-harm"* zone within the tunnel length of 150 m (Shentsov et al., 2018). For distances 5–50 m away from the tunnel after tank rupture for various heights, a 1% *"fatality"* threshold of 100 kPa was overcome close to the tank rupture location, most distances within a 1% *"injury"* threshold of 16.5 kPa.

Table 2.4: Calculated hazard distances for four typical hydrogen application, relating to humans and buildings (Molkov and Kashkarov, 2015). a: (Baker et al., 1983); b: (Mannan, 2005).

Object	Criterion for seperation	Hazard distance, m			
		Stand-alone		Onboard	
		10 m^3	170 L	33 L	12 L
		100 MPa	35 MPa	70 MPa	
Humans	No harm[a]	470	90	57	35
	Injury[b]	78	16	11	7.5
	Fatality[b]	23	2	1.4	1
Building[b]	Minor damage	190	36.5	25.5	18
	Partial damage	136	29	20.6	14.5
	Almost total destruction	49	9.7	6.7	4.8
Building[a]	Minor damage	115	-		
	Major damage	42			
	Partial demolition	25			

2.6.2 Thermal exposure and radiation

Reported in (UK HSE, 2010), elevated ambient temperatures effect on humans based on tests are listed in Table 2.5. It indicates that 149 °C is the maximum survivable breathing air temperature based on full-scale tests. Furthermore, temperatures below 70 °C are considered the *"no-harm"* temperature limit for humans (Hadjisophocleous et al., 1998).

Table 2.5: Elevated temperature response on the human body.

Temperature, °C	Physiological Response
127	Difficult breathing
140	5 min tolerance limit
149	Mouth breathing difficult, temperature limit for escape
160	Rapid, unbearable pain with dry skin
182	Irreversible injury in 30 seconds
203	Respiratory systems tolerance time less than four minutes with wet skin

Once a fireball has emerged, it is the thermal radiation energy that may last for several seconds that causes body damage such as skin burns and eye injuries, see Table 2.6. More relevant to occupancy within a generation of a fireball, thermal radiation is defined as the electromagnetic radiation emitted from a material that is due to the heat of the material, the characteristics of which depend on its temperature (Crowl, 2010). Thermal radiation depending on the material may be reflected, partially absorbed or even pass through objects.

Material such as steel may fail due to yield stress, whereas wood-based construction may fail due to combustion.

Table 2.6: Effects of thermal radiation on personnel and materials (Crowl, 2010).

Radiation intensity, kW/m^2	Observed effect
37.5	Damage to process equipment
25.0	Minimum energy required to ignite wood at indefinitely long exposure unpiloted
12.5	Minimum energy required for piloted ignition of wood, melding plastic tubing
9.5	Pain threshold reached after 8 seconds, second degree burns after 20 seconds
4.0	Sufficient to cause pain to personnel if unable to reach cover within 20 seconds; however blistering of the skin (second degree burns) is likely; 0% lethality
1.6	Will cause no discomfort for long exposure

2.7 Concluding remarks

This research seeks the ability to explore, pin down and mitigate hazards associated with the current understanding of onboard hydrogen storage applications. With a non-zero probability of a high-pressure hydrogen storage tank rupturing catastrophically, this phenomenon is pivotal to have gained a complete overview over, prior to an incident and its aftermath. Methods of predicting effects of the blast wave and fireball from a pressurised vessel were found in the literature not straightforward – especially the former catering for intricate rupture dynamics and geometrical effects of the tank. The hazards following such an event are significant, not only in the near vicinity of the blast source but also in the far-field for both humans and structures. The conducted insight into the literature gives the sense that some key issues of the effects following a hydrogen tank rupture has been left untended, particularly confinements effect of those found in a tunnel, and will be the noble objective to address going forward in this study.

Chapter 3

Development of the CFD model

In this chapter, a CFD model is to be developed able to simulate complex phenomena arising from a high-pressure hydrogen tank rupture such as blast wave and fireball. An experiment on hydrogen tank rupture in a fire with initial pressure in a tank of 35 MPa is used as the basis, outlined when needed and details published elsewhere (Weyandt, 2005; Zalosh and Weyandt, 2005; Zalosh, 2007). Simulations applied in this study were performed using the commercially available ANSYS Fluent 16.2 software as the computational engine. This chapter was conducted in conjunction with a collective effort at the HySAFER centre with synthesized contributions from a total of six researchers (Molkov et al., 2018, 2020). Outlined in this chapter, it details the work conducted by the author unless stated otherwise by referring to the above papers.

3.1 Setting up the model

All of computational fluid dynamics (CFD), in one form or another, is established on the fundamental physical principles of fluid dynamics – the continuity, momentum and energy equations whereby the following are true:

1. Mass is conserved.
2. Newton's second law, $F = ma$.
3. Energy is conserved.

There are two ways of modelling a flow when the objective is to apply fundamental physical principles on a moving fluid. For a continuum fluid, a finite region of the flow may be defined as a control volume; a control surface defined as the closed surface which bounds the volume. The control volume may be fixed in space as the fluid moves through it, or moving correspondingly with the fluid with the no change in the particles inside it. In either case, the control volume may have the fundamental physical principles applied, without *"attention"* limited to the control volume instead of the whole field (Anderson, 1995). If the finite control volume is fixed in space, the governing equations are applied in an integral

form which is directly obtained. These integral forms of the governing equations can be manipulated to indirectly obtain partial differential equations. Both instances of forms are called the conservation form of the governing equations. Non-conservation form of the governing equations, either integral or partial differential form, are equations obtained from the finite control volume moving with the fluid. Conservation equations in its sense ensure that the mass, momentum and energy sum of fluxes that enter a cell is equal in leaving, calculated at a specific moment using the discrete method. This method entails calculating a cell centre value, which in turns determines the boundary values of that cell by interpolation with the centre values of surrounding cells.

3.1.1 Turbulence model

Three main turbulence models are used in CFD: Reynolds-averaged Navier-Stokes (RANS), large eddy simulation (LES) and direct numerical simulation (DNS), in order of decreasing filter scale. Whereas RANS solves mean flow quantities and models all the scales of turbulence, DNS thoroughly solves all the fluctuations at all scales using the Navier-Stokes equations. Navier-Stokes equations are extensions of Euler equations, describing the motion of viscous fluid substances. With regards to the advantages and disadvantages in RANS versus DNS, i.e. pragmatism versus accuracy, LES acts as a midpoint solution. Its approach separates the large scale turbulent motions, where the majority of the energy is contained, and the small-scale motions known as the Kolmogorov scale when the Reynolds number becomes small enough, resolving the former and modelling the latter.

Governing equations

Using LES, the conservation equations are obtained for LES by filtering the three-dimensional instantaneous conservation equations for mass, momentum and energy. By setting a filter width or grid spacing in computations, the filtering process weeds out the eddies smaller than the threshold set, for the equations to govern only the dynamics of the large eddies. For compressible Newtonian fluid the mass, momentum and energy equations are respectively expressed as (Molkov, 2012):

$$\frac{\partial \overline{\rho}}{\partial t} + \frac{\partial}{\partial x_j}(\overline{\rho}\widetilde{u}_j) = 0, \tag{3.1}$$

$$\frac{\partial \overline{\rho}\widetilde{u}_i}{\partial t} + \frac{\partial}{\partial x_j}(\rho\widetilde{u}_j\widetilde{u}_i) = \frac{\partial \overline{p}}{\partial x_i} + \frac{\partial}{\partial x_j}\left((\mu+\mu_t)\left(\frac{\partial \widetilde{u}_i}{\partial x_j} + \frac{\partial \widetilde{u}_j}{\partial x_i} - \frac{2}{3}\frac{\partial \widetilde{u}_k}{\partial x_k}\delta_{ij}\right)\right) + \overline{\rho}g_i, \tag{3.2}$$

$$\frac{\partial}{\partial t}(\overline{\rho}\widetilde{E}) + \frac{\partial}{\partial x_j}(\widetilde{u}_j(\overline{\rho}\widetilde{E}+\overline{p})) = \frac{\partial}{\partial x_j}\left(\left(k+\frac{\mu_t c_p}{Pr_t}\right)\frac{\partial \widetilde{T}}{\partial x_j} - \sum_m \widetilde{h}_m\left(-\rho D_m \frac{\mu_t}{Sc_t}\frac{\partial \widetilde{Y}_m}{\partial x_j}\right)\right.$$
$$\left. + \widetilde{u}_i(\mu+\mu_t)\left(\frac{\partial \widetilde{u}_i}{\partial x_j} + \frac{\partial \widetilde{u}_j}{\partial x_i} - \frac{2}{3}\frac{\partial \widetilde{u}_k}{\partial x_k}\delta_{ij}\right)\right) + S_E, \tag{3.3}$$

where ρ is the density, t is time, $u_{i,j,k}$ are the velocity components, $x_{i,j,k}$ are the spatial coordinates, g_i is the vector of gravity acceleration in x_i axis direction, E is the total energy, S_E the source term in energy conservation equation, m the specie index, p is the pressure, μ is the dynamic viscosity, c_p is the specific heat capacity of mixture, Pr_t is the the energy turbulent Prandtl number equal to 0.85, Y_m is the mass fraction of m-th specie, Sc_t is the turbulent Schmidt number equal to 0.7, h is enthalpy, δ is the Kronecker symbol, μ_t is the turbulent dynamic viscosity, D_m is the molecular diffusivity of the specie m, k is the thermal conductivity, h is the enthalpy of specie m and T is the temperature. Through the solution of a convection-diffusion equation for the m-specie, the general form of specie m mass fraction conservation equation (also called specie convection-diffusion equation) is:

$$\frac{\partial}{\partial t}(\overline{\rho}\widetilde{Y}_m) + \frac{\partial}{\partial x_i}(\overline{\rho}\widetilde{u}_j\widetilde{Y}_m) = \frac{\partial}{\partial x_i}\left(\left(\rho D_m + \frac{\mu_t}{Sc_t}\right)\frac{\partial \widetilde{Y}_m}{\partial x_i}\right) + R_m \tag{3.4}$$

where R_m is the net production/consumption rate by chemical reaction of specie m by addition due to e.g. chemical reaction. The majority of the subgrid-scale models, resulting from the filtering operation, in ANSYS Fluent, modelled from either the re-normalisation group based subgrid-scale model or the Smagorinsky-Lilly non-dynamic formulation model. The latter was employed in this study and is expressed as follows:

$$\mu_t = \rho L_s^2 |\overline{S}|, \tag{3.5}$$

where L_s is the mixing length subgrid scales and the rate of strain tensor is expressed as $|\overline{S}| \equiv \sqrt{2\overline{S}_{ij}\overline{S}_{ij}}$, $\overline{S}_{ij}$. In ANSYS Fluent, L_s is computed using

$$L_s = min(\kappa d, C_s V^{1/3}), \tag{3.6}$$

where κ is the von Kármán constant, d is the distance to the closest wall, and V is the volume of the computational cell. C_s is the homogeneous isotropic turbulence in the inertial subrange. In Fluent, $C_s = 0.1$ has been found to yield the best results for a wide range of flows and is the recommended value (*ANSYS FLUENT 12.0 User's Guide*, 2009).

Solving the governing equations

Historically, an explicit solver is known for its accurate resolution of shock propagation. An explicit density-based approach extracts the density field from the continuity equation and pressure from the equation of state. In the range of this study, poor results were gained and yielded underpredicted solutions for pressure and inadequate conservation of mass. The density-based solver, when solved explicitly, is very sensitive to the accuracy of the mesh containing cells with higher than average skewness, and easily causes error accumulation over a long-time solution. A second option is to use the pressure-based solver. Different from the density-based solver, the pressure field is extracted by solving a pressure correction

equation which is obtained by manipulating continuity and moment equations separately as a segregated algorithm approach (*ANSYS FLUENT 12.0 User's Guide*, 2009). Until recently, the pressure-based solver was secluded only for use of incompressible and medium-ranged compressible flows and a density-based solver more applicable for high-speed compressible flow with combustion. These guidelines were recently updated by ANSYS Fluent in newer versions, asserting that the pressure-based solver was now capable of simulations involving high-speed compressible flows with little differentiating the two solvers; the approach used to linearise and solve the discretized equations. Using the pressure-based approach (segregated) with the pressure-implicit with splitting of operators (PISO), extended and reformulated to solve and operate for a wide range of flow including high-speed compressible flow, good solution convergence was achieved, accurate for fully compressible, transonic, and supersonic flow. Recommended for transient flow calculations, PISO was used due to its ability to remain stable under substantial compressible flows.

There is a scholarly dispute on the use of spatial upwind schemes. In-house, a second-order upwind scheme is applied for the spatial discretisation of convective terms in the governing equations, seen to improve the simulation accuracy for compressible flow. This is contrary to what is considered best practice guidelines for use in numerical simulations for hydrogen applications, which recommends bounded central differencing (BCD) scheme when LES is used (Tolias et al., 2018). However, the renowned inadequacy of the central differencing schemes in a strongly convective flow lies in its inability to identify the flow direction (Tu et al., 2018). The way this works, in theory, is that when convective flux starts to dominate diffusive flux (i.e. cell Peclet number starts to grow), BCD starts to be non-physical, and leads to oscillations and divergence in simulations (Patankar, 1980). The Peclet number (Pe) is the ratio between the convection and conduction. When $Pe \gg 2$, the central-difference scheme is not applicable. To tackle these oscillations and divergence they invented *"bounded"* central difference. The numerical code checks convective fluxes and adapts the schemed accordingly: for $Pe = 1$, it acts as *"pure"* central difference, and for large Peclet number – as 1^{st} order upwind. Explored by Molkov et al. (2020), three similar cases were simulated using various upwind schemes: 2^{nd} order upwind scheme for all convective terms; BCD and 2^{nd} order upwind scheme (BCD for momentum equation only); BCD scheme for all convective schemes. The study showed that the 2^{nd} order upwind scheme was the better option, BCD overestimating the amount of burned hydrogen by 6% only after 50 ms. Indeed, once BCD reduces to 1^{st} order upwind scheme, which is more diffusive than 2^{nd} order upwind scheme, it provides a more intensive hydrogen-air mixing (partly due to numerical diffusion) and hence larger hydrogen combustion rate. For interpolation methods (gradients), the least-square cell-based was used, the default and recommended option for most simulations to achieve better accuracy in calculations (*ANSYS FLUENT 12.0 User's Guide*, 2009). The first order accurate time-step discretisation was employed for time advancement. Change to the second-order scheme for time advancement for the case with constant time step did not cause any difference in the pressure dynamics.

3.1.2 Combustion model

To simulate the combustion and turbulence-chemistry interaction, the eddy-dissipation-concept (EDC) was employed. Based on an extension of the eddy-dissipation model, EDC includes a detailed chemical mechanism in turbulent flows (Magnussen and Hjertager, 1977). It assumes that fine-scale reaction occurs in small scale turbulent structures when the chemical kinetics are faster than overall fine-structure mixing. In other words, the model expects that the chemical reaction occurs with a simple single-step reaction where the reactants and hot products are mixed molecularly. Combustion in the fine-scale is governed by the Arrhenius rates of equations, directly integrating the chemical source term in the calculation. The fine-scale volume calculation is one of the advantages, compared to the use of finite rate chemistry (FRC) model, which uses the Arrhenius kinetic expressions for the whole domain without fine-scale consideration (Echekki and Mastorakos, 2011). The use of EDC and FRC were compared by Molkov et al. (2020), the differences found not affecting the pressure transients by the combustion model. However, the fireball dynamics did prove to be influenced – a more physically accurate fireball shape was formed using EDC than FRC. The reaction rate is proportional to the mixing time defined by the turbulent kinetic energy and dissipation. The volume fraction of the fine-scale is modelled as (*ANSYS FLUENT 12.0 User's Guide*, 2009):

$$\xi^* = C_\xi \left(\frac{\nu\epsilon}{k^2}\right)^{3/4}, \tag{3.7}$$

where * denotes fine-scale quantities, k is the turbulence kinetic energy, ϵ is the turbulent dissipation rate, C_ξ is a volume fraction constant equal to 2.1377 and ν is the kinematic viscosity. Modelling the turbulence kinetic energy is obtained by taking the trace of the Reynolds stress tensor:

$$k = \frac{1}{2}\overline{u_i' u_i'}, \tag{3.8}$$

and accordingly modelling the dissipation rate as:

$$\epsilon_{ij} = \frac{2}{3}\delta ij(\rho\epsilon + Y_M), \tag{3.9}$$

where $Y_M = 2\rho\epsilon M_t^2$, and M_t^2 being the turbulent Mach number. Over a time scale, the species are assumed to react in fine structures:

$$\tau^* = C_\tau \left(\frac{\nu}{\epsilon}\right)^{1/2}, \tag{3.10}$$

where C_τ is a time scale constant equal to 0.4082 (*ANSYS FLUENT 12.0 User's Guide*, 2009). The species state after reacting for a time τ^* is denoted by Y_m^*. The rate of reaction

of the species i is evaluated as:

$$R_m = \frac{\rho(\xi^*)^2}{\tau^*[1-(\xi^*)^3]}(Y_i^* - Y_i), \tag{3.11}$$

where Y_i is the species mass fraction for species i in the surrounding fine-scales state. For fine scale length smaller than set filter width using LES, this is modelled as a function of the flow properties and cell size as:

$$\xi^* = C_\xi \left(\frac{u_\eta}{u_{SGS}}\right), \tag{3.12}$$

where the upper limit $\xi^* = 1$ is applied when the fine-scale velocity is larger than residual sub-grid scale velocity, u_{SGS} is the residual velocity at the sub-grid scale (SGS) level, u_η is the Kolmogorov's velocity calculated as:

$$u_\eta = \left(\frac{\mu \cdot u_{SGS}^3}{\rho \cdot L_{SGS}}\right)^{1/4}, \tag{3.13}$$

where μ is the laminar viscosity, and L_{SGD} the length scale. The characteristic sub-grid eddy time-scale is given as:

$$\tau_{SGS} = \frac{L_{SGS}}{u_{SGS}}, \tag{3.14}$$

and the characteristic Kolmogorov's time scale as:

$$\tau_\eta = \left(\frac{\mu \cdot L_{SGS}}{\rho \cdot u_{SGS}^3}\right)^{1/2}. \tag{3.15}$$

Assumed functional dependence between fine structures time scale and resident time is:

$$\tau^* = C_\tau \tau_\eta, \tag{3.16}$$

where it is assumed that within the residence time τ^*, all fine scales in the cell are perfectly stirred reactors (Bragin et al., 2013).

3.1.3 Radiation modelling

Simulation of combustion processes with a significant amount of combustion products requires modelling of radiative heat transfer, together with convection and conduction dynamics. This affects simulations, where radiative heat transfer is called for, when simulating flames

to determine loss of heat from the radiative transfer of combustion dynamics. This is true for asymmetrical molecules found in combustion products such as CO_2 and H_2O, absorbing and emitting thermal radiation at particular wavelengths, pressure and composition of the mixture – all required to describe the radiation transfer. The discrete ordinates (DO) radiation model is applicable across a whole range of optical thicknesses and a typical choice for modelling combustion processes (Murthy and Mathur, 1998). The DO radiation model is utilized, accounting for both scattered and radiative fluxes. Its added computational costs and memory requirements are considered moderate for most cases (*ANSYS FLUENT 12.0 User's Guide*, 2009). For an absorbing, emitting, and scattering medium at a position $\vec{r}$ in the direction $\vec{s}$ the radiative transfer equation is (Chui and Raithby, 1993):

$$\nabla \cdot (I(\vec{r}, \vec{s})\vec{s}) + (a + \sigma_s)I(\vec{r}, \vec{s}) = \alpha_p \cdot n^2 \frac{\sigma T 4}{\pi} \int_0^{4\pi} (\vec{r}, \vec{s}')\Phi(\vec{s} \cdot \vec{s}')d\Omega', \tag{3.17}$$

where $\vec{s}'$ is the scattering direction vector, s is the path length, $\vec{r}$ is the position vector in $\vec{s}$ direction, α_p is the absorption coefficient, n is the refractive index, σ_s is the scattering coefficient, I is the radiation intensity depending on the position and direction, T is the local temperature, Φ is the phase function and Ω' the solid angle. σ is the Stefan-Boltzmann constant equal to 5.672×10^{-8} W/(m^2 K^4). They define the number of control angles used to discretize each octant of the angular space, 4π. The angles themselves, θ, ϕ, are the polar and azimuthal angles measured with respect to the global Cartesian system (x, y, z). The angular discretization and pixelation within the DO model is defined by the theta and phi divisions, denoted as N_θ and N_ϕ respectively. The values for N_θ and N_ϕ are discussed in Chapter 4. In three-dimensional (3D) models applied only in this study, 8 octants are solved resulting in a total of $8N_\theta N_\phi$ directions $\vec{s}$.

3.1.4 Gas equation of state

The density for incompressible ideal gas is calculated as:

$$\rho = \frac{P_{op} M_m}{RT}, \tag{3.18}$$

where P_{op} is the operating pressure, R is the universal gas constant, M_m is the molecular weight and T is the temperature of the gas. When the flow is compressible, the gas law is included the local gauge pressure as:

$$\rho = \frac{(P_{op} + P) M_m}{RT}, \tag{3.19}$$

where P is the local gauge pressure.

3.1.5 Under relaxation factors

Under relaxation factors (URFs) were employed to ensure convergence in simulations, and simultaneously avoid any non-physical values at any stage of the simulation. By utilizing URFs, it takes part of the value from the previous iteration, a proportion between 0 and 1. This helps dampen the next step solution and remove steep oscillations, helping the solver stabilize the convergence behaviour. Especially for pressure and momentum, recommended default values of 0.3 and 0.7 respectively. Keeping the sum of factors of momentum and pressure to 1 when coupling between neighbour and skewness corrections for meshes that are distorted (*ANSYS FLUENT 12.0 User's Guide*, 2009). In this study with a particularly vigorous initial condition of instantaneous disappearance of the tank wall, a value of 0.3 was determined for the pressure. Furthermore, superimposed by setting limitations on certain parameters such as minimum and maximum pressure and static temperature are listed in Table 3.1. The minimum pressure and temperature of 30 K and 1000 kPa were set respectively to avoid any formation of hydrogen liquid phase during the expansion of hydrogen (Makridis, 2016). Temperature limits are necessary to prevent non-physical solutions and aid stability in the initial stages of simulations (phenomena such as condensation is not simulated), as the temperature could reach much lower temperature when the thermal energy is converted to kinetic energy as the gas is being accelerated. All maximum values were kept as recommended default values (*ANSYS FLUENT 12.0 User's Guide*, 2009). The convergence was reached when residuals were smaller than 10^{-6} for all variables including energy, with 20 iterations per time step inferred. An increase in the number of iterations did not improve convergence any further.

Table 3.1: Solution limits used in simulations in ANSYS Fluent.

Limitations	Values
Minimum absolute pressure, Pa	1000
Maximum absolute pressure, Pa	5×10^{10}
Minimum static temperature, K	30
Maximum static temperature, K	5000
Maximum turbulence viscosity ratio	100000

3.2 Setting up the computational domain

The test data in the experiment conducted by Weyandt (2005) will be used here for setting up the computational domain. In the experiment, the tank length was 0.84 m, a diameter of 0.41 m with an internal volume of 72.4 L. The tank was placed approximately 0.2 m above the ground over a propane burner. Initial storage pressure was 34.3 MPa and temperature 300 K (1.64 kg hydrogen). At the time of rupture in a fire (fire heat release rate was 350 kW), the pressure and temperature raised to 35.7 MPa and 312.15 K respectively, accepted as initial conditions for CFD simulations. The geometry and mesh were created using ANSYS ICEM. The computational domain was created as a hemisphere to resemble the overall shape

of the blast wave and fireball development. The outlining hemispherical domain of a 100 m in diameter was divided into three sub-zone hemispheres, catering to the various dynamics of the blast wave and fireball. Following the hydrogen boundary wall, a fireball zone of 20 m in diameter of hemisphere followed. Centred in the domain, the tank was placed 0.2 m above the ground. All three zones presented in Figure 3.1.

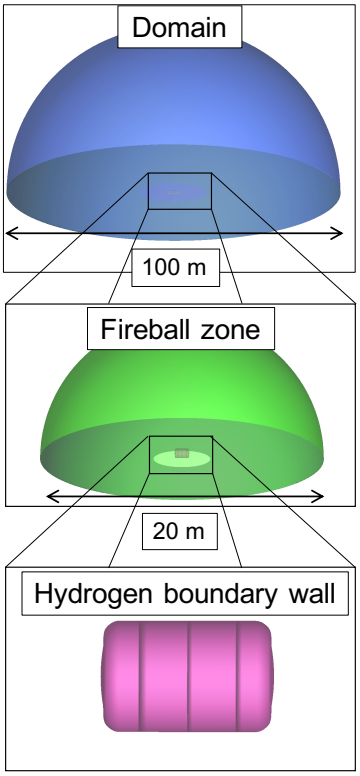

Figure 3.1: The created computational domain including fireball zone and the hydrogen tank.

The calculation domain was discretised using block-structured hexahedral[6] mesh. Near the tank, the mesh size ranged from 0.01–0.03 m composing hydrogen tank. This includes the near tank surface vicinity to better resolve the high gradients of velocity and pressure closest to the tank. Using a bi-geometric mesh law, the size monotonically increased from 0.03 m to 0.1 m up the first hemisphere, with a *"blast wave zone"* of 2 m in diameter, see Figure 3.2. In conducting simulations, there is a minimum numerical requirement of computational cells needed to accurately resolve a flame of between 3–5 CVs (Molkov, 2012). In other terms, the thickness of the front is distributed across up to 5 CVs, independent of cell size. Therefore, the finer the mesh, the smaller element of cellular structure will be simulated causing faster flame and shock wave propagation. In the *"fireball zone"* where a fine mesh is no longer

[6]A cell in a finite volume method, and for three-dimensional cases are either shaped tetrahedrally, polyhedrally or hexahedrally, which surround a computation point called a node that is to be approximated (Biswas and Strawn, 1998).

required, the mesh was gradually increased to 1 m in size at its maximum. Containing the remaining domain, the mesh reached a maximum cell size of 10 m.

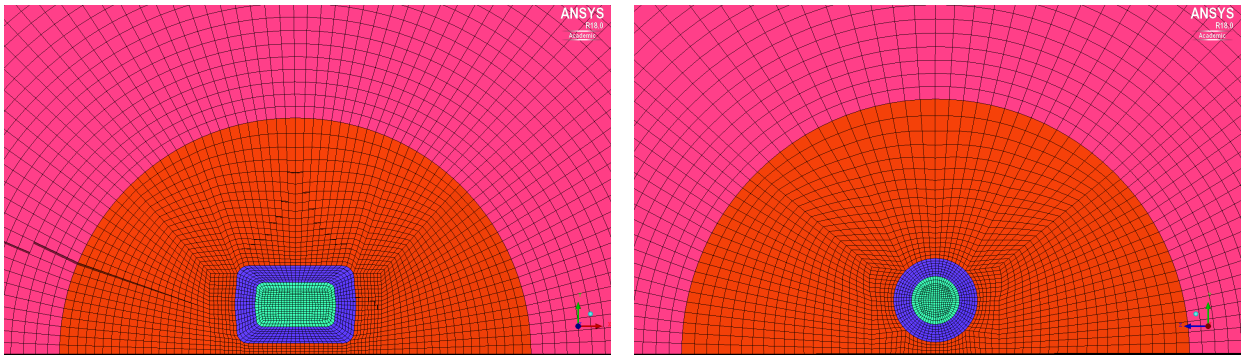

Figure 3.2: Hexahedrally meshed area in near vicinity of tank (2.5 m) in axial (left) and perpendicular (right) to the tank directions.

The quality of the mesh was an important parameter to control, as a poor quality may result in an inaccurate solution and slow convergence. This was measured in ANSYS Fluent before simulations by the maximum orthogonal quality, aspect ratio and the minimum orthogonal skewness of each cell. The quality ranges from 0 to 1, where values close to 0 correspond to the lowest quality in the case of the minimum orthogonal quality and reversed for the case of the maximum orthogonal skewness also raging from 0 to 1. The definition of skewness describes how close to the ideal, i.e. equilateral or equiangular, the cell is. It is recommended that both values for maximum orthogonal quality and orthogonal skewness should not fall under 10% (*ANSYS FLUENT 12.0 User's Guide*, 2009). The recommended value for the aspect ratio, describing the ratio of maximum to minimum values of any distances of the cell centroid to face centroid or node (stretching), is to not exceed 40 – subject to flow characteristics and the location of particular cells concerning the flow with relatively high velocity. In Table 3.2 the quality obtained after mesh generation are listed, a good generated mesh quality obtained.

Table 3.2: Mesh quality determined as used in simulations.

	Mesh quality	Range	Target value
Maximum orthogonal quality	0.37	0–1	> 0.1
Maximum orthogonal skewness	0.63	0–1	< 0.9
Maximum aspect ratio	13	∞	< 40

The total size of control volumes (CVs) was 311 114. This mesh was part of a rigorous mesh independence study performed by Molkov et al. (2020) for the current domain set-up. In refining (or redefining) the mesh, all regions were resolved to remove any bias from the quality of the mesh in any and all positions. For a direct comparison in mesh sensitivity, a total of five meshes were compared whereby the number of CVs ranged from 147k to

9M. To summarize the resuls, in terms of pressure dynamics the mesh sensitivity study between all five grids showed a good convergence, both in terms of arrival and maximum blast wave pressure. The effect of mesh refinement was seen most prominently in the amount of hydrogen burned in the same amount of time. This was associated with the reduced combustion for the finer grid; a finer grid leads to a decrease of burned hydrogen due to the length of cells reduced at the contact surface. The dissimilar combustion energy was seen to instead influence the pressure impulse. The simulated impulse is indeed more sensitive to mesh size compared to the maximum pressure because of thickening of the numerical shock with cell size – the impulse being the integral of pressure transient in time (widened on a coarser grid). Nevertheless, the performed mesh sensitivity analysis of peak pressure dynamics led to the conclusion that variation is limited to an acceptable engineering accuracy in the near field, negligible with the increase of distance.

3.2.1 Initial conditions

Atmospheric pressure i.e. 101 325 Pa (1 bar), and air i.e. $Y_{O_2} = 0.23$ and $Y_{N_2} = 0.77$ with quiescent conditions, $u_i = u_j = u_k = 0$, were set for the domain as initial conditions. For simplification, the selected gasses in air with low concentration, H_2, CH_4 and CO_2, were discounted. At the domain boundary representing ground, non-slip impermeable conditions were employed; boundary conditions for energy equation assumed infinitely thick solid behind the boundary with conjugate heat transfer between fluid and the solid. ANSYS Fluent provides parameters for soil boundary as density of 1600 kg/m^3, specific heat transfer of 800 J/(kg·K) and thermal conductivity of 1 W/(m·K). The time available for heat transfer within the location of the sensors was too short, as simulations ran with and without adiabatic boundary did not affect the pressure dynamics. The hydrogen temperature and pressure in the tank were set to be 312 K and 35.7 MPa respectively, as observed in the experiment before its failure (Weyandt, 2005). The volume and surface area of the tank was however altered due to the use of ideal gas as described below.

3.2.2 Ideal and real gas consideration

The use of real gas in high-pressure hydrogen release simulations is often recommended (Chen et al., 2010). However, its usage in simulations often promotes an added layer of impediments and divergence. This is due to the much more complicated equations of state in real gasses, the numerical solution procedure is prawn to sometimes produce untenable results averting convergence, and furthermore increases the calculation times drastically (Steinar and Gretler, 1994). Using ANSYS Fluent, it would introduce similar issues of non-ignition, and very poor convergence tested using a variety of real gas equations available including those from Redlich-Kwong and Peng-Robinson found adapted in its library database. Following communication with ANSYS Fluent, it was stated that available real gas tables were not yet developed accurately enough in the low-pressure low-temperature regions with high-speed jet and release flow of hydrogen. Besides switching to ideal gas equation state, the other suggestion was to apply a very small time step, between nano- and picoseconds, to help avoid simulation divergence. The latter implemented, early trials did not yield any improvement

and moreover, this would be computationally prohibitive. The usage of ideal gas when sufficiently compressed (10–20 MPa) is seen to overestimate the parameters such as mass flow rate and velocity (Cheng et al., 2005; Khaksarfard et al., 2010). These cases involved hydrogen released into air in geometry confinements, downstream of tubes or chambers, where a limited expansion in confinement is inferred. Contrarily, the expansion of hydrogen when released into an open ambient atmosphere is quite different, prompting the effort to investigate methods to overcome the over-prediction of ideal gas effects. The shock wave overpressure assumed at its maximum at the contact surface between the cylinder gas and the surrounding air was calculated. Based on the dimensionless starting shock pressure of a vessel burst, P_{st}, it can be calculated by using the one-dimensional (1D) gas dynamic equations cited in (Bragin and Molkov, 2011) as:

$$\frac{P_i}{P_s} = \frac{1 + \frac{2\gamma_s}{\gamma_s+1}(M_{sh}^2 - 1)}{\left(1 - \frac{\gamma-1}{\gamma_s+1} \cdot \frac{a_s}{a_g} \cdot \frac{M_{sh}^2-1}{M_{sh}}\right)^{\frac{2\gamma_g}{\gamma_g-1}}}, \tag{3.20}$$

with P_i and P_s is the tank initial pressure and surrounding (atmospheric) pressure respectively, γ the ratio of specific heats, $\gamma_s = 1.4$ for surrounding air and $\gamma_g = 1.39$ for hydrogen. The speed of sound ratio a_s/a_g was calculated using the ideal gas for the surrounding air, while for the compressed gas using the Abel-Noble gas modified method to account for the non-ideal behaviour of pressurized hydrogen. Calculating the former is as for any other gas:

$$a_s = \sqrt{\gamma \frac{P_s}{\rho_s}}, \tag{3.21}$$

on the other hand, the Abel-Noble equation of state adds a compressibility factor $Z = 1/(1 - b\rho)$, modifying Equation (3.21) into:

$$a_g = \sqrt{\frac{\gamma P_g}{\rho_g \cdot (1 - b\rho_g)}}, \tag{3.22}$$

in which b is the co-volume constant for Abel-Noble equation ($b = 7.69 \cdot 10^{-3}$ m^3/kg for hydrogen) (Molkov, 2012). Solving for the starting shock Mach number, M_{sh}, the pressure directly behind the leading shock wave propagating in air is defined as:

$$P_{st} = \frac{2\gamma_s M_{sh}^2}{\gamma_s + 1} - \frac{\gamma_s - 1}{\gamma_s + 1}. \tag{3.23}$$

For a stored hydrogen tank of pressure 35.7 MPa, $P_{st} = 5.8$ MPa was calculated as the starting shock pressure of a vessel burst, below the non-ideal threshold of hydrogen gas behaviour.

The ratio for the speed of sound can be used in another method of determining the starting shock pressure using Baker's method (Baker et al., 1983). Presented in Figure 3.3, the dimensionless starting shock overpressure is indicated by each curve ranging from 0.5 to 150 denoted as $\overline{P}_{SO}$. The squared ratio of speeds of sounds, $(a_s/a_g)^2$, is calculated to be 22. The ratio of initial pressures, (P_g/P_s), is calculated to be 338.5. These values lead to a starting shock value of 60, dimensionalized to become 6.1 MPa once multiplied by the atmospheric pressure.

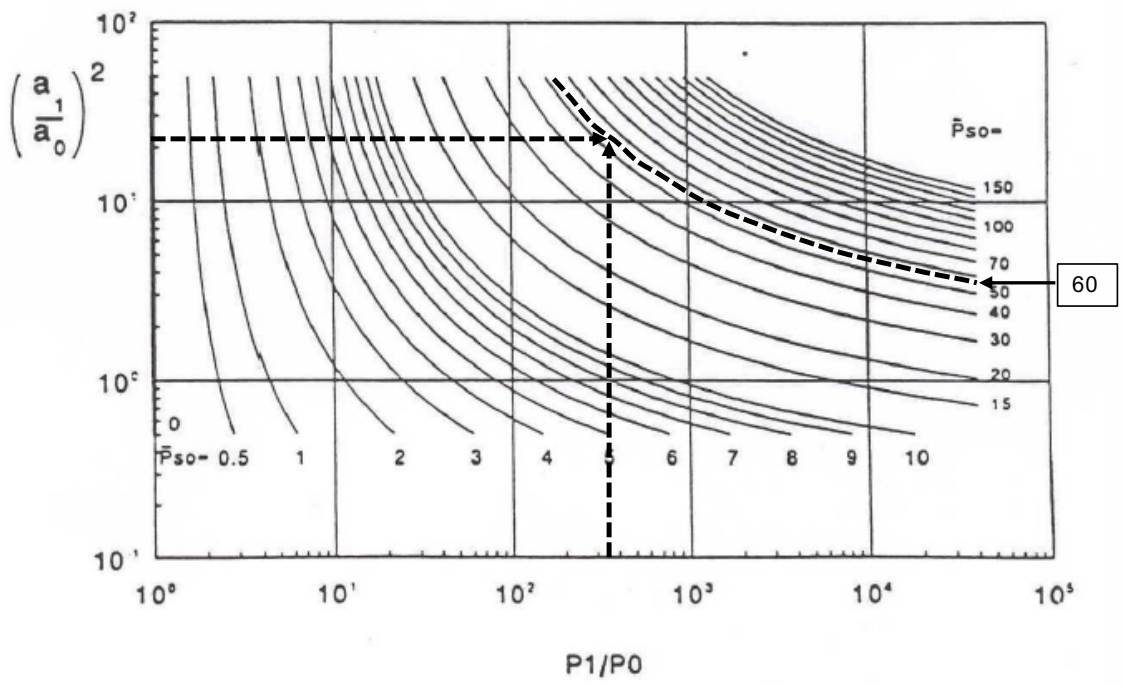

Figure 3.3: Starting shock of a tank, the dashed lines showing the determined starting shock pressure for the present stored hydrogen tank (Baker et al., 1983).

Because of two-dimensional (2D) and 3D character of the blast wave decay respectively at the side of the tank and the dome part of the tank in experiments, as well as the numerical requirement to have 3–5 CVs to resolve any physical discontinuity in simulations (here it is a shock or a contact surface), it is questionable to get a good agreement between simulated 3D starting shock and the 1D theoretical value calculated. Therefore, trial simulations were conducted to investigate the starting shock reproducibility using a 1D problem formulation. A test tube resembling a shock tube was developed with initial conditions of pressure hydrogen to observe the effect. A 3 cm×3 cm×10 m tube was created to resemble a simple 1D shock tube problem. The tube was divided into two separate areas, one end with high-pressure hydrogen (35.7 MPa), and the remaining area set as atmospheric conditions. Figure 3.4 shows a comparison of pressure distribution simulated in 1D and 3D (axial and perpendicular directions) up to 0.3 ms after tank rupture. The simulated value shock wave for 1D simulation is 5 MPa, up to 1 MPa below the calculated values. For 3D simulation,

the starting shock is 4 MPa in axial direction and close to 3 MPa in perpendicular direction. Indeed, the lower pressure effect of 3D phenomena is not to be neglected when estimating the starting shock pressure. Nevertheless, the simulations in this study are performed with the ideal gas equation of state, as the ideal gas behaviour of hydrogen could be accepted for pressures below 10 MPa with practically no error. However, some concerns must be properly addressed in the simulations, e.g. conservation of mechanical energy of real gas when simulating ideal gas.

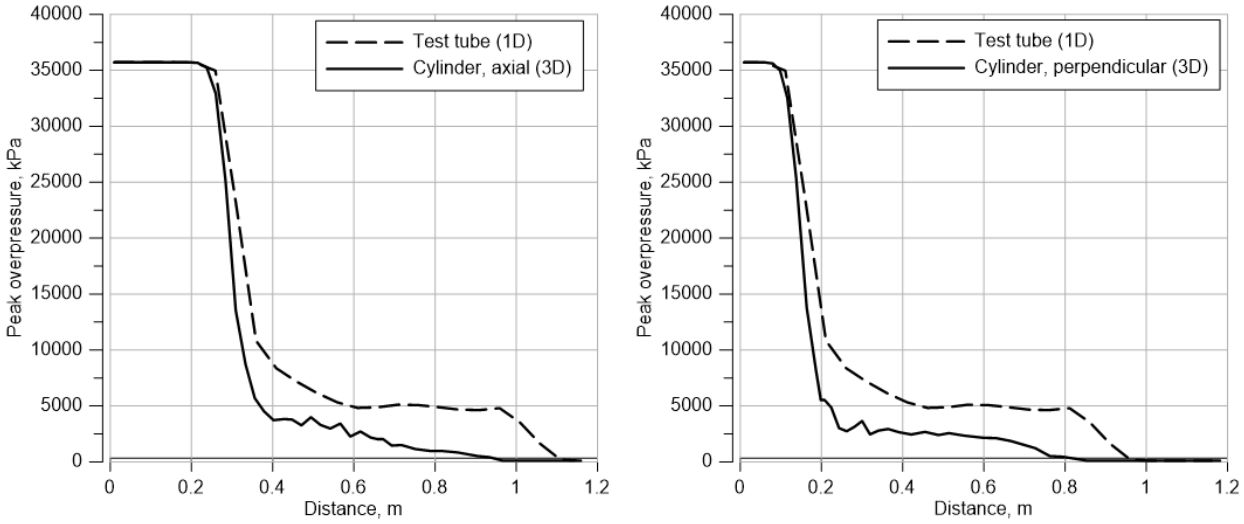

Figure 3.4: The pressure discontinuity shown by the peak pressure for 1D and 3D, release of the same pressurized hydrogen (35.7 MPa) in a test tube and of a cylinder in open atmosphere respectively.

In using ideal gas, the mechanical energy of compressed hydrogen during transition is overestimated in mass if the tank is kept as the same size, as calculated with real gas. To avoid this error in simulations, the tank volume was decreased compared to experimental value to maintain the same mass and mechanical energy of compressed gas in the experiment. Based on the Abel-Noble equation of state, the volume relationship between ideal and real gas used for geometrical scaling is:

$$V_{ideal} = V_{real} - mb, \tag{3.24}$$

where m is the mass of hydrogen, and b the co-volume constant can be used for geometrical scaling. This relationship comes from the definition of mechanical energy stored in compressed gas when ideal:

$$E_m^{ideal} = \frac{(P_g - P_s)V}{\gamma - 1}, \tag{3.25}$$

and for compressed conditions when real gas is assumed:

$$E_m^{real} = \frac{(P_g - P_s)(V - mb)}{\gamma - 1}. \tag{3.26}$$

With a calculated 1.64 kg of initial mass of hydrogen, the tank was scaled down from a volume of 72.4 L to 59.6 L, a reduction of 17%. In terms of the tank surface area effect, a reduction of 11.8% was seen, from 0.94 m^2 with real gas to 0.829 m^2 with ideal gas.

3.2.3 CFL number convergence

Solving conservation equations for mass, momentum and energy, it is important to ensure that during the simulation, the solutions are a result of these quantities being conserved to accurately represent a physical system. Implicit schemes are less sensitive to numerical instabilities (compared to explicit schemes), but for unsteady flows, an adequate time step is still an important parameter to adjust accordingly if numerical accuracy in the solution is to be ensured. To enforce numerical stability and accurate description of the resolved scales of motion, the time step is a meticulous choice to make. Stability was made certain by preemptively determining the Courant-Friedrichs-Lewy (CFL) number after a sensitivity study was carried out. By using a constant CFL number, provides an indication of the complexity of a problem, type of flow and model chosen to carry out simulations, and reflects it on the time step that would best optimize the solution on a particular grid. The CFL number is defined as $\text{CFL} = U\Delta t/\Delta x$, where Δt is the time step, Δx is the cell size and U is the flow velocity. In compressible flows, the characteristic velocity during shock waves is higher than the speed of sound. Therefore, the flow velocity is often replaced with the highest velocity of acoustic waves, $|U| + a$ in each cell to make it more applicable. This is useful in terms of limiting the time step as the isolated convective flow velocity might not be sufficient to capture all the prevailing acoustic wave-speeds in each cell. A user-defined function (UDF) is used to set the CFL number during transient simulations. The dynamic time step scheme based on the super-imposed CFL number is presented in Figure 3.5. As a function of calculation time, a lower time step for each chosen CFL number is initially calculated to capture the high velocity of acoustic waves. As the velocity magnitude decays with time, the time step values increase by up to three times. Thus, a significant saving of computational time compared to the constant time step simulations is achieved.

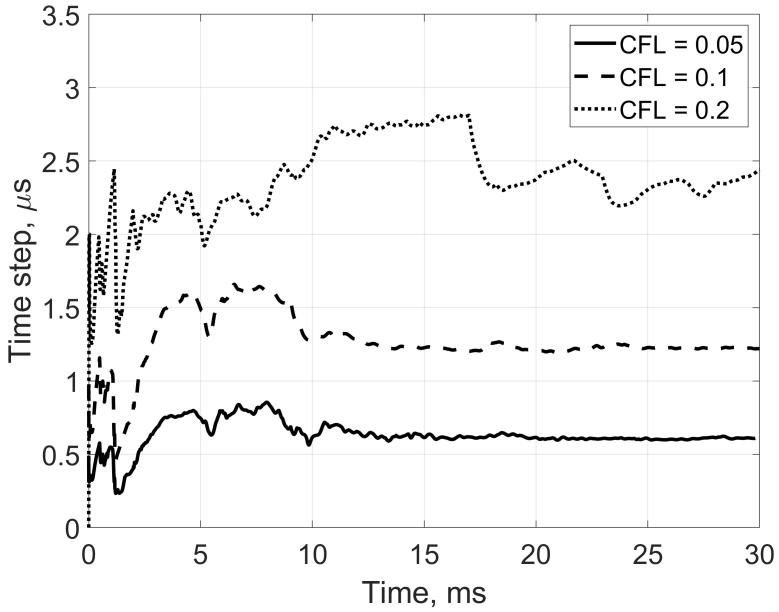

Figure 3.5: The time step calculated in simulation as a function of simulation time determined by the super-imposed CFL values.

In most cases, there is no definite way of predicting the upper bound CFL number, and is determined by trial and error until the convergence is obtained between different CFL numbers. A way of authenticating the applied CFL number is done by conducting a sensitivity test, reducing the CFL number until convergence in the results is found. CFL number convergence is given in Figure 3.6, comparing the dynamics of burned hydrogen (left) and pressure dynamics (right) for different CFL numbers. Minor difference is observed in the pressure dynamics using different CFL number, a larger difference seen in the burned hydrogen. When the physical equations, of which most important is the mass conservation, is converted into a numerical equation, there might be errors associated with the equation discretisation processes and attained numerical inaccuracy. Therefore, there might be a slight difference when using any numerical schemes whereby the accuracy of the solution is achieved when the mass balance was reduced to a very low level ($\pm$ 0.5% or less). Hence in the following analysis, the use of hydrogen mass conservation will be used as the primary indicator of numerical accuracy and CFL number convergence. Although the hydrogen imbalance might be small, -2% for CFL = 0.2, for CFL = 0.1 the imbalance is close to zero, and nearly coincides with the results obtained using CFL = 0.05, for both hydrogen imbalance and burned hydrogen mass. Determining the CFL convergence by the burned hydrogen and its imbalance, a CFL = 0.1 was chosen to use in simulations. In simulating the fireball development until it finishes, the methodology of determining the CFL number was altered to encourage less computational costs. A lower CFL is indeed to accommodate for the initial shock wave propagation. Once the primary blast wave has left the domain and is out of relevancy, the CFL number is increased gradually to 20 while making sure the hydrogen mass imbalance was kept within $\pm$ 1%.

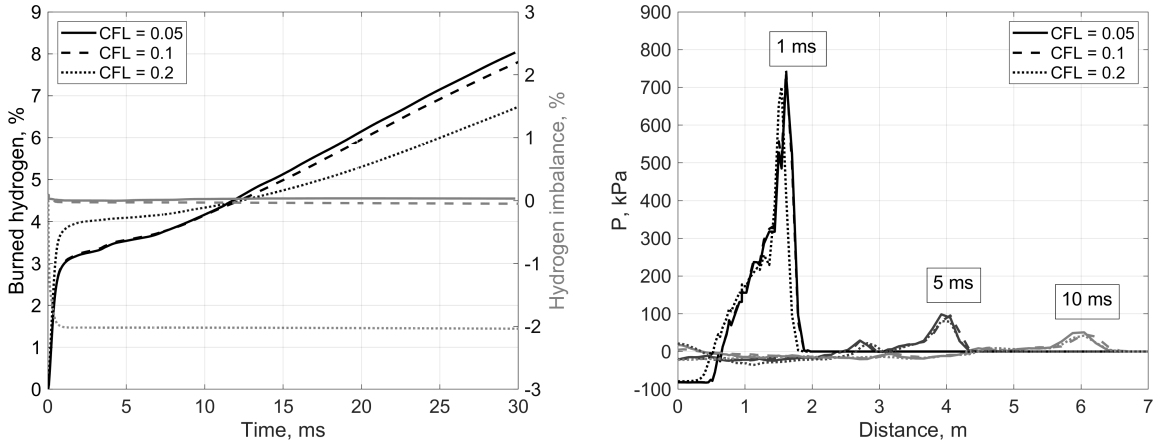

Figure 3.6: The hydrogen burned quantity and mass imbalance for different CFL numbers according to the simulated flow time (right), and the transient overpressure in perpendicular direction of the tank (right).

In practical terms, Table 3.3 gives a comparison of the CPU time (clock time) used for simulations with different CFL values. Indeed, an increased CFL number reduces the calculation time proportionally. As simulations were performed in parallel mode the number of central processing units (CPUs) are also listed for further clarity. It should be mentioned that the maximum available CPUs per computational machine was 64, but for various simulations, a lower amount of CPUs were utilised for each simulation due to availability, further increasing the computational time accordingly.

Table 3.3: Overview over calculation time depending on CFL number and utilised parallel CPUs.

CFL value	Simulation time, ms	Calculation time, hours	Parallel CPUs
0.05	30	216 (9 days)	64
0.1		134 (5.6 days)	
0.2		70 (2.9 days)	

3.3 Combustion dynamics

In simulations involving species transport and chemical reactions, there are usually three categories used: detailed, reduced and global reactions. The detailed chemical reaction model describes the use of a comprehensive reaction set involving all elementary reactions including truncated and skeletal mechanisms. The reduced model is simpler in a less detailed mechanism scheme, whereas a global model utilizes a one-step global reaction whereby $Fuel- > Products$ (Warnatz et al., 2006). Here, a few of the principal reactants and products in one or more functions steps still apply. Generally, a detailed chemical mechanism will have been developed for a wide range of operating conditions (pressure, temperature,

equivalence ratio) and is the most accurate. However, it is computationally costly because a detailed mechanism usually has at least tens or hundreds, and even thousands of species, and hundreds or thousands or more reactions. For hydrogen combustion in air, the requirements of nearly 40 elementary reactions for a near-complete chemical mechanism is needed (Bragin et al., 2013). For practical purposes, a detailed chemical mechanism is often reduced with some loss of accuracy and/or range of applicability. The 1-step or 2-step global reaction schemes are usually obtained by optimising (curve fitting) the kinetic data, in order to reproduce the properties (typically laminar flame speed) of the detailed or reduced mechanism for some targeted applications with a much narrower range of applicability and decreased accuracy. It is imperative that the conditions of the reaction scheme used must be investigated in order to determine the expected level of accuracy.

Due to the advantages gained in computational time, the use of a global chemistry model was targeted. The use of a detailed and global chemistry model was compared for the current application and gave little difference in blast wave overpressure in the near field, a maximum of 7% found (Molkov et al., 2020). More significantly, the reduction in simulation time was a little over 4 times, compared with the same mesh and model using a detailed reaction rate. In the current use of a single-step reaction, $2\,H_2 + O_2 \longrightarrow 2\,H_2O$, the global reaction rate constant can be expressed as:

$$R = A_t \cdot \exp(-\frac{E_a}{RT}), \tag{3.27}$$

where A_t is the temperature-dependent pre-exponential factor and E_a the activation energy corresponding to an energy barrier to be overcome during reaction. This reaction constant is proportional to the molar concentration of unreacted [H2] and [O2], and their global reaction orders expressed by the exponents as:

$$R_n = R \cdot [H_2]^a [O_2]^b, \tag{3.28}$$

where R_n is the net rate of production of species by a chemical reaction in system, a and b the reaction orders. The molar concentrations are themselves proportional to the partial pressure of that species in the gas phase. Following the Dalton's law of partial pressure, it can be used to express the dependence as $[H_2] = \frac{p_{H_2}}{RT}$ and $[O_2] = \frac{p_{O_2}}{RT}$. The partial pressure may also be expressed as the product of absolute pressure in the system and molar concentration of the respective specie. The values for the constants of the Arrhenius reaction, a, b, A and E, are derived differently by various authors. For instance, in the work of Marinov et al. (1995), the reaction rate parameters determined were validated against laminar flame speed experimental results. However, its thermodynamic range of applicability is bound in terms of pressure (≈ 1 bar) and equivalence ratio ($\Phi = 0.6 - 1.1$). Outside this range, a poor prediction was found attributed to various applications (Gerlinger et al., 2010). Other reaction rate constants are found derived targeting towards lean-fuel premixed hydrogen-air conditions (Jones and Lindstedt, 1988). Also, trial simulations with the corresponding constants gave excessively low values of hydrogen reaction at normal conditions and deemed non-applicable in this

study. Ultimately, the global one-step reaction scheme derived by Varma et al. (1986) was utilised. The scheme coefficients are $A_t = 9.87 \times 10^8$ and $E_a = 3.1 \times 10^7$ J/kmol, exponents a and b both equal to 1. Tested elsewhere, these values were deemed applicable for a wide range of hydrogen-air combustion (Hsu and Jemcov, 2000).

The ignition source in simulations was initiated dependent on diffusion mechanism of spontaneous ignition, caused by the mass and heat diffusion between the expanding hydrogen and the shock-heated oxygen in air once a combustible mixture is present, explained in more detail elsewhere (Wolanski and Wojcicki, 1973). Nevertheless, the physics of tank rupture and turbulence induced combustion can be to some extent mimicked numerically with diffusion ignition. The standard auto-ignition temperature found under normal conditions is around 858 K, subject to change depending on pressure and temperature (Verfondern, 2008). Seen in Figure 3.7, the temperature profiles with and without combustion of hydrogen-air activated are presented. In the zoomed-in portion, the temperature profiles show a deviation at already at 0.025 ms. Here, the temperature is right above 600 K, indicating when auto-ignition occurs for hydrogen released under conditions set in this study. The first peak in temperature is due to the initial reflection off the ground for both cases. The temperature for simulation with no combustion monotonically decreases until 500 K, still elevated from atmospheric temperature due to the compression of air as the blast wave propagates. The simulation with combustion present goes through more temperature variations. After the maximum temperature first peak, a second one occurs (around to 2.8 ms) as the reflected blast wave within the combustion zone promotes a higher temperature. Later due to enhanced turbulence, the temperature nears the adiabatic flame temperature of hydrogen-air combustion (i.e. 2500 K), as radiation heat loss from the flame to the surrounding is not considered.

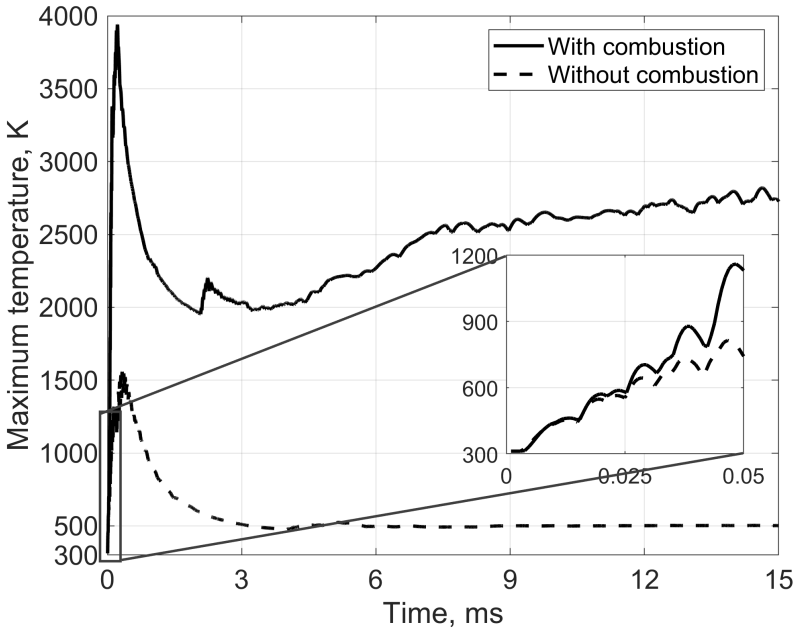

Figure 3.7: The maximum temperature profile in domain as a function of simulation time, recorded with and without combustion present.

Figure 3.8 illustrates the initial stage of combustion. As the starting shock initially expands at 0.1 ms, the temperature and reaction rate profiles surround the cylinder where the contact surface between hydrogen and air occurs. The dilution effect of combustion products is not yet pronounced (0.5 ms) as compared to later stages (1 ms), seen by the amount of water vapour present. As the blast wave propagates away from the combustion zone already after 3 ms, defined by the temperature profile, the reaction rate reduces in intensity although a high temperature still maintains. The general structure of the fireball at early stages already possesses a more mushroom-like shape externally, the effect of enhanced mixing due to turbulence and entrainment of air taking place inwards from the sides.

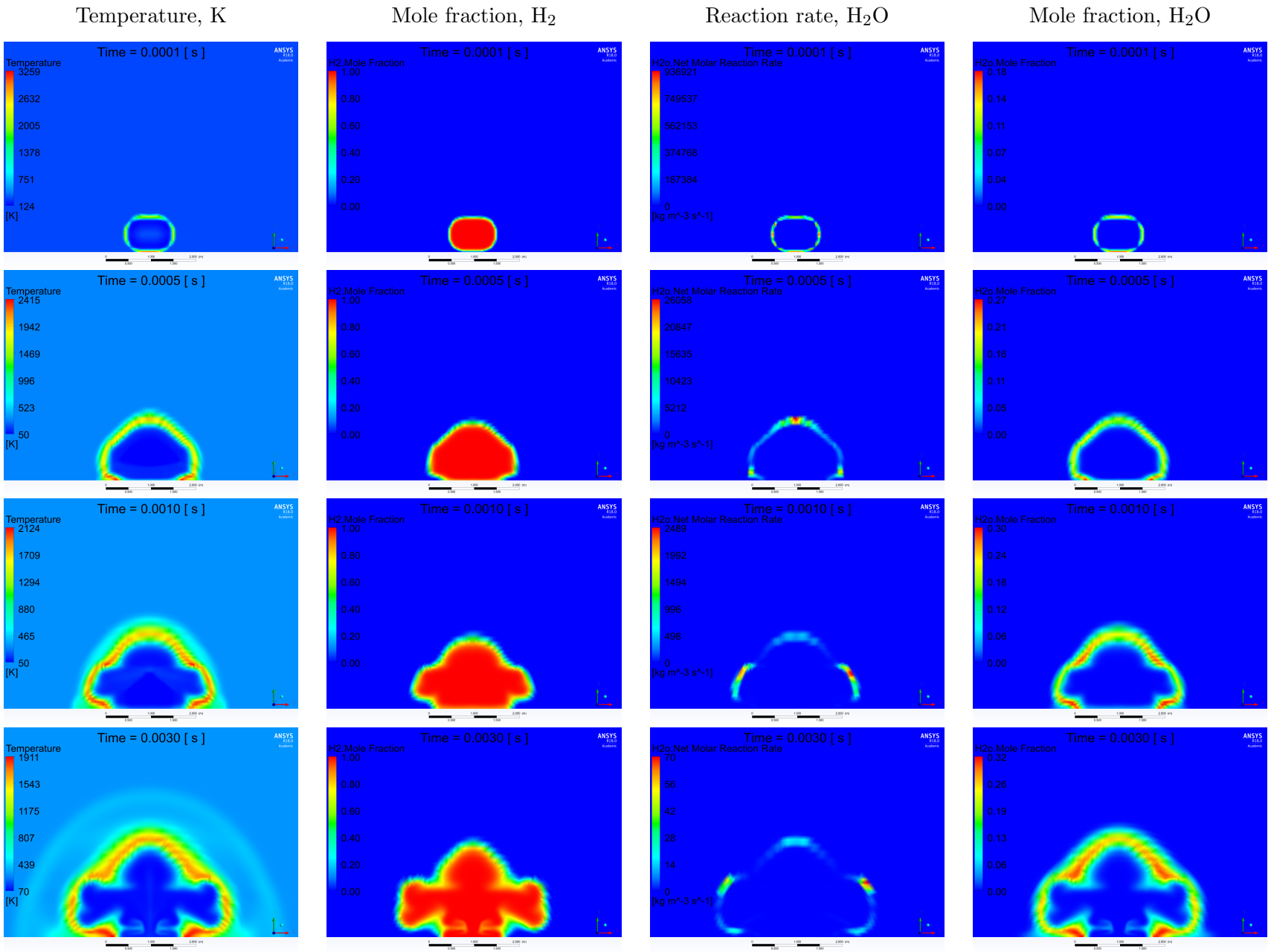

Figure 3.8: Dynamics of temperature, hydrogen mole fraction, water vapour production reaction rate and mole fraction for time 0.1-3 ms (perpendicular to the tank axis cross-section). Length of bottom ruler is 5 m.

Another look into the decay of discontinuity of pressure during high-pressure hydrogen *"instantaneous release"* into air is shown in Figure 3.9. The early propagation of pressure wave and rarefaction wave (0–70 μs) shows starting shock of about 4 MPa, which decays with distance faster along the tank axis as expected. As the starting shock propagates outwards, so does the rarefaction wave propagate inwards. Figure 3.10 shows the simulation for the same case with combustion. Here, the peak of the leading shock is increased to a little above 5 MPa, attained by the energy contribution of combustion.

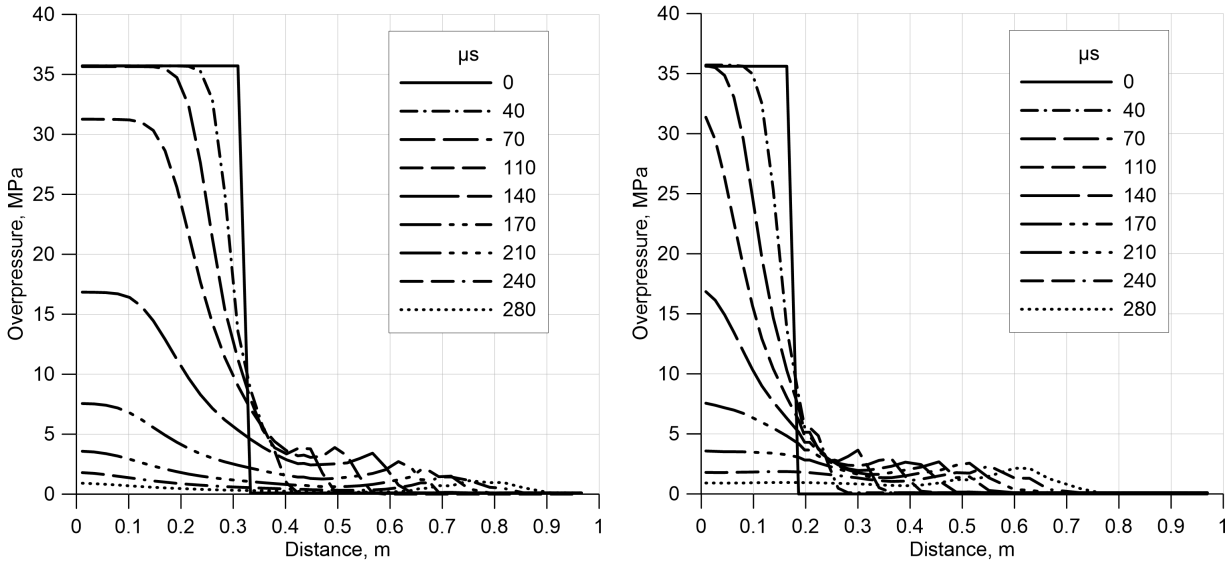

Figure 3.9: Pressure discontinuity decay at tank border in direction along the tank axis (left) and perpendicular to the tank axis (right), with no combustion initiated.

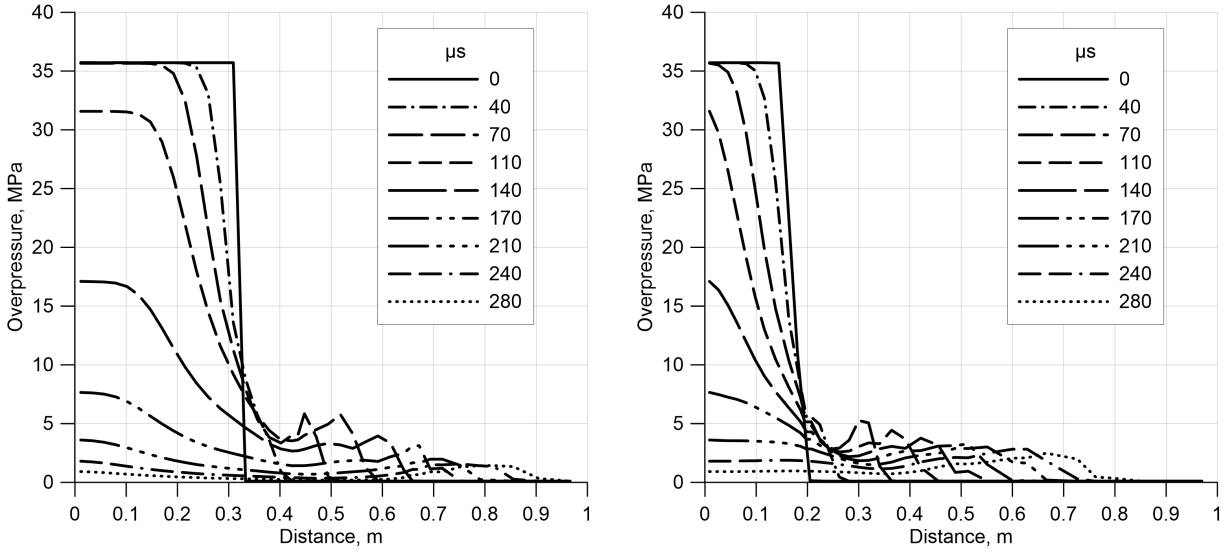

Figure 3.10: Pressure discontinuity decay at tank border in direction along the tank axis (left) and perpendicular to the tank axis (right), with combustion initiated.

3.4 Formation of the blast wave

The forming blast wave from tank rupture including the formation of positive and negative phase is visualized in Figure 3.11. As the primary shock is formed from the pressurized gas propagating outwardly at 0.2 ms, the reflection of the ground leads to two consequences. The first is a Mach stem reinforcing the primary wave. Secondly, two symmetrical shock waves move backwards (or upwards) towards the epicentre at 0.8 ms. Once the reflected waves have bounced off each other at 1.1 ms, and again off the ground at 1.8 ms, the secondary wave is formed moving behind the primary established wave at 2.5 ms. Meanwhile, the negative phase slowly establishes behind the first and second blast wave, as the shocked air over-expands causing the negative phase (pressure below atmospheric) at time 3.4 ms. At later stages (not shown in Figure 3.11), the reflected wave catches up with the primary wave and they combine in a singular blast wavefront.

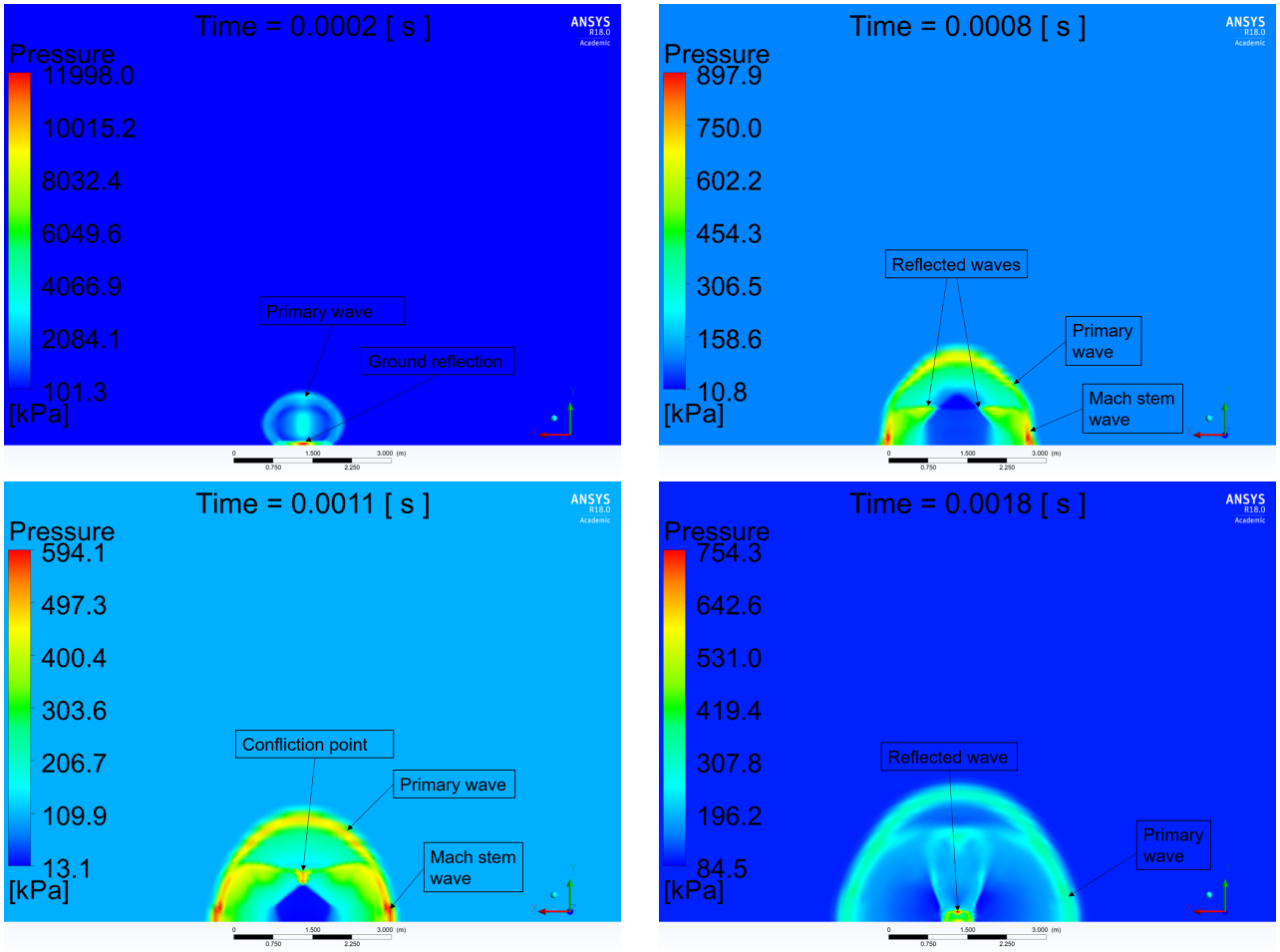

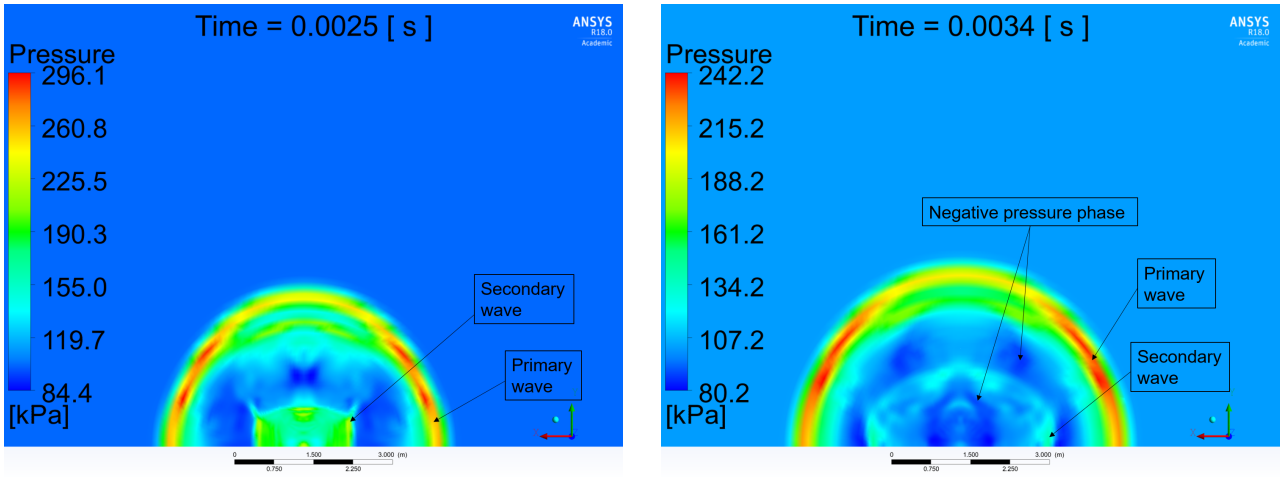

Figure 3.11: The pressure dynamics of primary and secondary wave at early stages of propagation. Length of bottom ruler is 3 m.

3.5 Development of a fireball

As the blast wave propagates and propagates away within milliseconds, the fireball lifetime is relatively much slower. Figure 3.12 shows that it takes up to 3 seconds to burn all hydrogen in the calculation domain. 50% is burned already after 0.5 s, 85% burned after 1.5 s. The remaining 15% of hydrogen takes 1.5 s to burn. This is found due to the dilution of mixtures by the combustion products (H_2O), in addition to a gradual mass and heat diffusion.

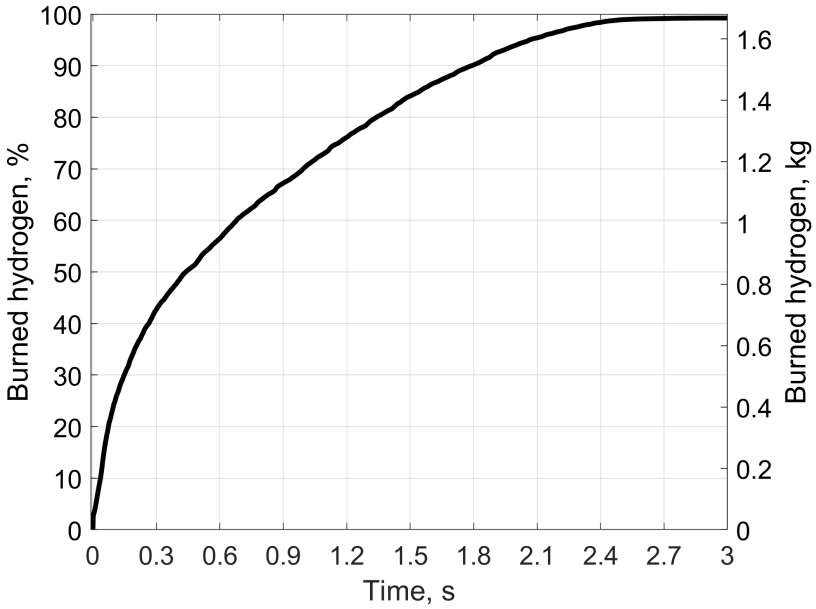

Figure 3.12: Hydrogen mass burned shown in percentage and mass until complete depletion.

Figure 3.13 presents the progression of fireball combustion zones represented by the temperature (left half) and by combustion products i.e. water vapour (right half). Likewise, the depletion of hydrogen mass and the oxygen present in the surrounding atmosphere are shown in Figure 3.14 respectively. At 0.05–0.5 s, combustion manifests itself mainly at the near-hemispherical contact surface where the cooled by expansion hydrogen reacts with heated by shock oxygen of air. Therefore, the hydrogen is mostly burned in its outer surface, fuel-rich concentrations found in the fireball core (oxygen mass fraction is close to zero). The fireball size increases with time, and at 0.8 s the fireball is dominated by buoyancy forces leading to its lift-off from the ground with a typical mushroom shape (see snapshots at 1.1 s and 1.5 s). The hydrogen is seen almost depleted after 2 s, and simulations ceased after 3 s when no further hydrogen remained to burn. It is however noticeable that although maximum hydrogen fraction in the domain was below the LFL for hydrogen ($Y_{H_2} < 0.005$), and considered complete, high-temperature combustion products are still present and rising.

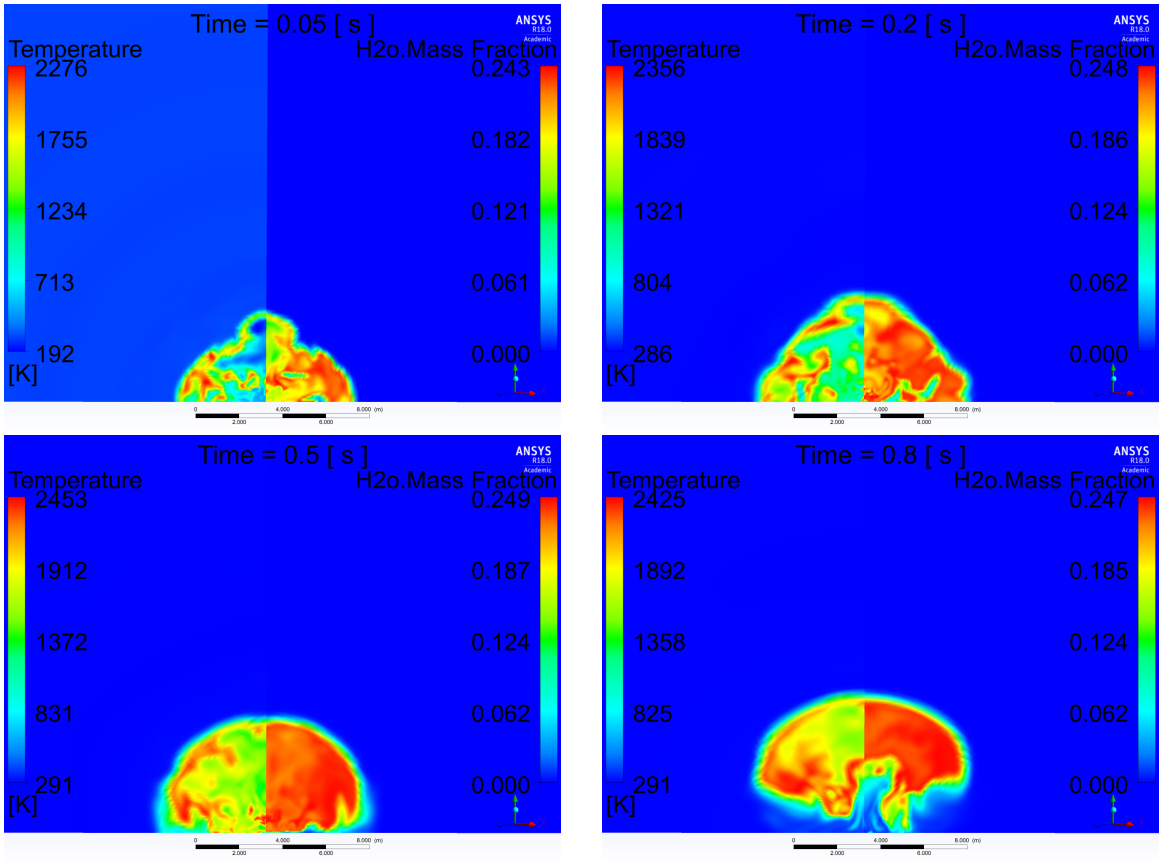

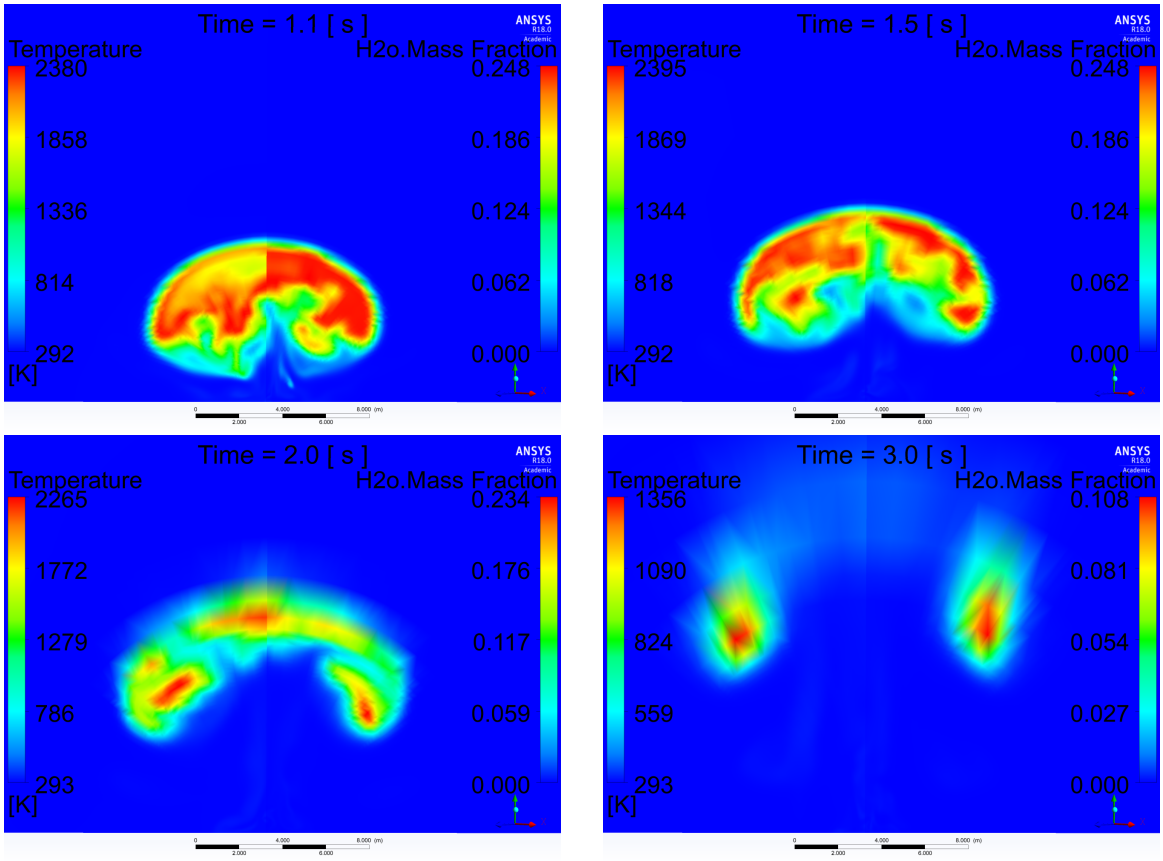

Figure 3.13: Various stages of fireball formation and dynamics at times 0.05–3 s, showing the temperature and water vapour mass fraction profile. Length of bottom ruler is 8 m.

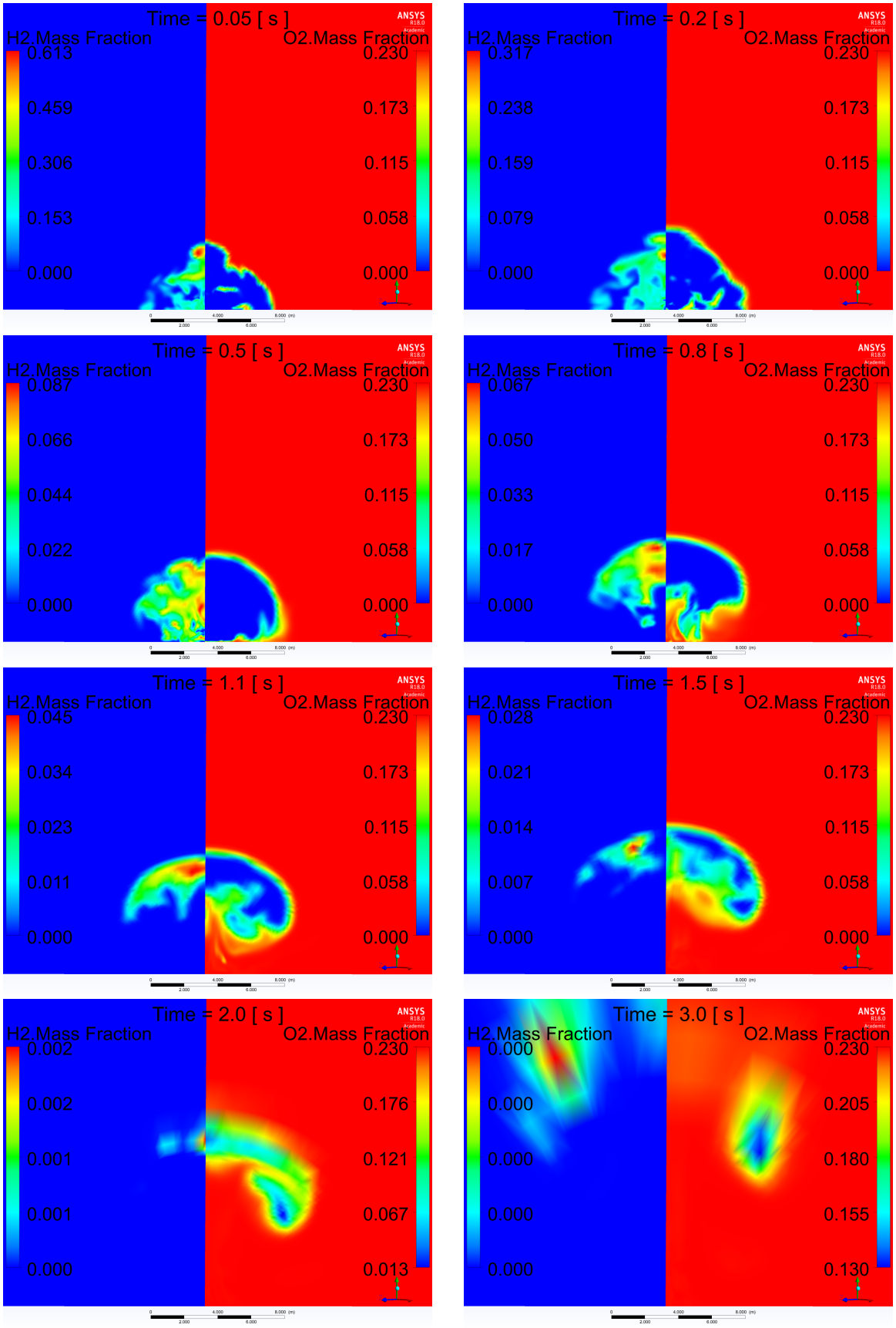

Figure 3.14: Various stages of fireball formation and dynamics at times 0.05–3 s, showing the hydrogen and oxygen mass fraction profiles. Length of bottom ruler is 8 m.

3.6 Concluding remarks

Described in this chapter is the methodology employed in developing a CFD model able to simulate complex phenomena following a high-pressure hydrogen tank rupture. The effect of different sub-models including turbulence and combustion methods has been determined, LES and EDC receptively, contended to ensure accurate results based on underlying physics. The created computational domain was meshed using hexahedral cells, which was ensured a good quality based on orthogonal, skewness and aspect ratio parameters. The created mesh was part of a rigorous independence study performed in which he peak pressure dynamics, excluding impulse as it depends on the cell size, gave good convergence (Molkov et al., 2020).

Convergence in the simulation was confirmed by conducting simulations with different CFL numbers – a CFL value of 0.1 was found to provide sufficiently accurate simulations results, both in terms of burned hydrogen and pressure dynamics. The use of ideal gas instead of real gas was substantiated; once hydrogen gas is instantaneously released, the pressure immediately falls below the threshold of real gas effects. Nevertheless, the conservation of mechanical energy of compressed real gas required downscaling of the tank volume in order to maintain the same energy as calculated by real gas equation of state.A global one-step reaction scheme was chosen, able to provide realistic hydrogen-air combustion simulation in the considered problem. Decrease of the computational cost associated with the use of global reaction scheme was almost four times compared to detailed reaction chemistry, an additional benefit of the chosen reaction scheme.

The formation of the blast wave was illustrated through snapshots, showing the primary and secondary shock including the formation of Mach stem. The following fireball displayed a typical development, a growth stage with rapid mixing and combustion occurring before rising due to buoyancy effects. However, to prove that the developed model demonstrates the ability to provide insight into the process of blast wave propagation and fireball dynamics with accuracy, it has to be validated against experimental data. This is the subject of the next chapter.

Chapter 4

Simulation of blast wave and fireball compared against experiments

In this chapter, the credibility of the developed CFD model in Chapter 3 is tested by its relationship to reality by comparison between attained numerical results and available experimental measurements. Here, an experiment of a hydrogen tank rupture in a fire is used to validate the model and understand underlying physical phenomena. This chapter was conducted in conjunction with a collective effort at the HySAFER centre with synthesized contributions from a total of six researchers (Molkov et al., 2018, 2020). Outlined in this chapter, it details the work conducted by the author unless stated otherwise by referring to the above papers.

4.1 Stand-alone tank rupture blast wave dynamics

The experimental data from a Type IV hydrogen stored tank rupture is performed and published elsewhere (Weyandt, 2005; Zalosh and Weyandt, 2005; Zalosh, 2007). The test data is summarized as follows: the tank length was 0.84 m, a diameter of 0.41 m with an internal volume of 72.4 L. Initial storage pressure was 34.3 MPa and temperature 300 K (1.64 kg hydrogen). At time of rupture in a fire (fire heat release rate was 350 kW), the pressure and temperature raised to 35.7 MPa and 312.15 K respectively, and accepted as initial conditions for CFD simulations. The tank was placed approximately 0.2 m above the ground over a propane burner. The measured maximum pressure was 300 kPa, 83 kPa and 41 kPa at 1.9 m, 4.2 m and 6.5 m respectively (perpendicular to the tank axis), and 64.8 kPa for the sensor at 4.2 m along the tank axis. The blast wave decayed faster along the tank axis, 28% reduction of overpressure from 83 kPa to 64.8 kPa was observed. The reported diameter of the fireball was about 7.7 m at time 45 ms after the tank rupture. The released mechanical energy of compressed hydrogen was estimated as 12.4 MJ and chemical energy (hydrogen reaction with air) as 197 MJ.

For comparison of blast wave and fireball between simulation and experiment (as described

above), the created geometry and mesh were as developed in Chapter 3. Figure 4.1 shows the experimental and simulated pressure transients at four sensor locations: the left graph shows the pressure transients in direction perpendicular to the tank axis for three sensors, and the right graph shows one sensor in the direction along the tank axis. At the closest sensor, 1.9 m, the peak overpressure obtained from the simulation is close to 550 kPa, overestimated by 80% compared to the experimental result. However, at the sensors further away, 4.2 m and 6.5 m, the overpressure is reproduced with a 4% overprediction. The sharp front not replicated at these locations is due to a coarser grid applied as a function of distance in the simulations to save computational time, with cells size ranging from 3–5 cm near the tank to 40 cm at 6.5 m distance from the tank. Numerical resolution of the shock wave requires 3–5 CVs, which also contributes to a gradual pressure increase in simulated shock wave. Nevertheless, the fact that the blast wave pressure dynamics are reproduced reasonably in the far-field (to be later defined) demonstrates that the sum of mechanical energy of compressed gas and chemical energy released during combustion and contributed to the blast wave are simulated quite well by the model.

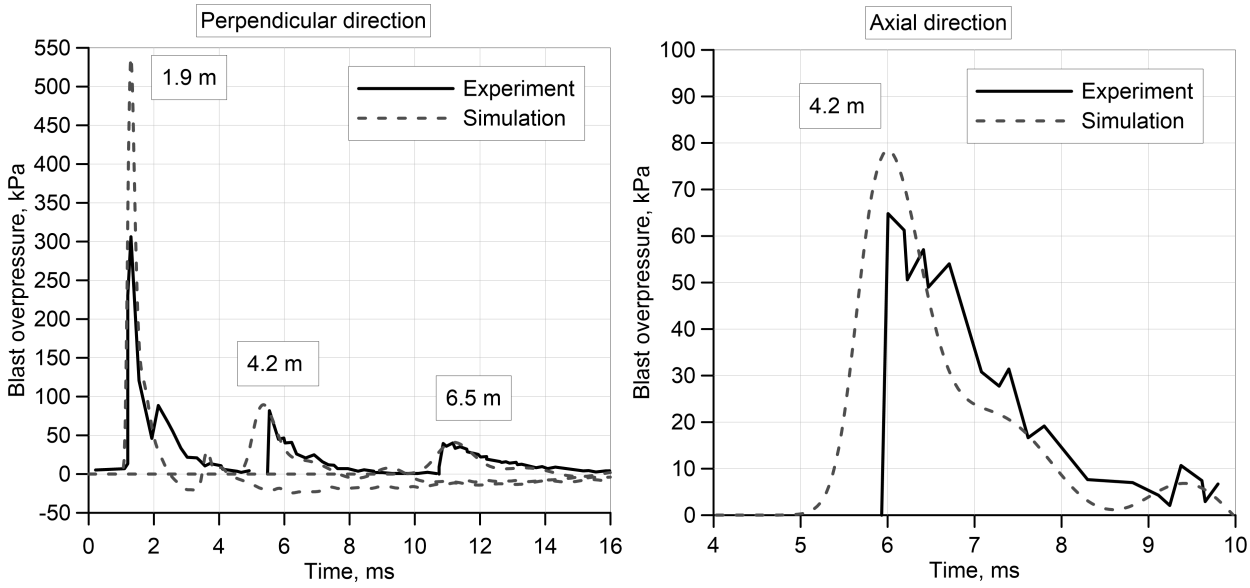

Figure 4.1: Simulations versus the experimental pressure transients: in direction perpendicular to the tank axis (left); in direction parallel to the tank axis (right).

Figure 4.2 presents the maximum simulated blast wave as a function of distance in comparison with experimental data. Again, these results give good comparisons for sensors at distances 4.2 m and 6.5 m. Close to the tank, the observed pressures at distance 1 m from the tank are 1420 kPa and 980 kPa, for perpendicular and axial directions respectively. Interestingly, the simulated overpressure at 1.9 m in the direction along the tank axis was practically equal to the experimental pressure recorded in the direction perpendicular to the tank. This invokes the uncertainty concerning the position of the tank at the instance of burst not documented in the conducted experiment explicitly. The difference in directional pressure decreases quickly, and from 5 m onwards the blast wave overpressure is equal in both directions.

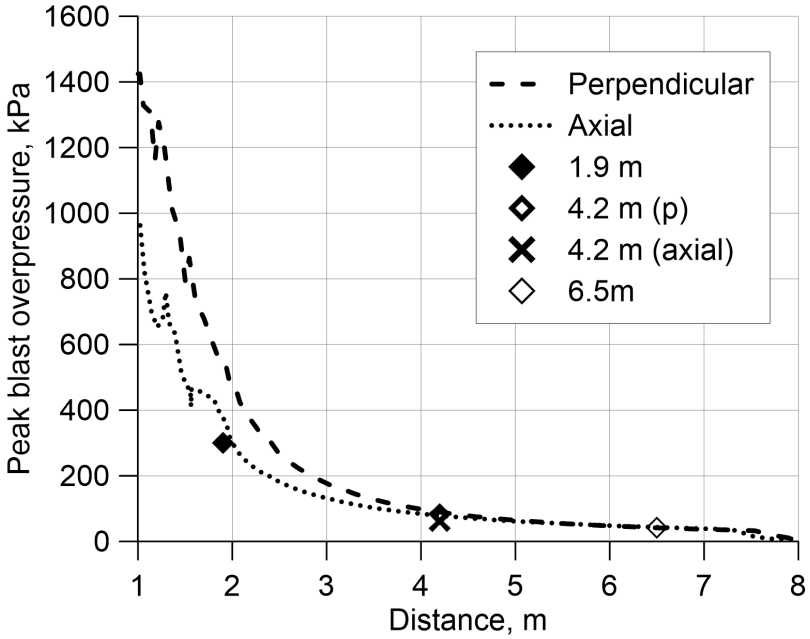

Figure 4.2: Peak overpressure for blast wave decay simulated in both perpendicular and axial direction of the tank, and corresponding experimental data (points), after simulated 13 ms.

The general overestimation of the peak overpressure obtained by the simulated data in the near vicinity of the tank can be explained by several reasons. Simulations are performed in the assumption of instantaneous removal of non-inertial tank walls, the compressed hydrogen expanding equally through the entire bounding surface of the vessel. Non-ideal depressurization of the vessel in experiment was a phenomena process neither repeatable nor accounted for in the simulations conducted. This includes mechanical energy losses in connection with the initial fracture of the tank, cratering of the ground and propulsion of fragments and materials. Quantifying these energy losses in connection with non-ideal behaviour and providing fragment kinetic energy was found in the literature to be predicted diversely, in the range 20–60%, based on the various modes of tank failure (High, 1989). Secondly, although the tank was scaled down to counteract the effects of non-ideal behaviour, not using real gas is a parameter not entirely negligible especially during the very early stages of depressurization. This could affect the pressure dynamics, causing an overestimated acceleration of shock wave leading to a correspondingly overestimated blast wave pressure. Thirdly albeit a bit more speculative, the recording pressure sensor in the near field could have been exposed to a variety of stimuli such as heat and mechanical stresses, leading to a less accurate representation of the peak pressure and pressure history.

4.1.1 Directional effects of cylinder on blast overpressure

When a pressure vessel bursts, the vast differences in blast overpressure in the near field area depending on its orientation are observed as directional effects. This is due to the more

pronounced three-dimensional (3D) effects at the tank ends, the shock wave decay on the tank sides are rather two-dimensional (2D) in the near field. There is an ambiguity in the literature specifying the near-field zone for explosive charges and vessel bursts alike, as an accurate assessment of the main blast parameters and patterns are found quite complex (Post et al., 2015). All the same, a near-field zone can be determined as using the Sachs-scaling parameter $\overline{Z} = r(P_s/E)^{1/3}$, where r is the distance from rupture point, P_s is the surrounding pressure and E is the stored tank energy. The near field was defined as $\overline{Z} < 1$, beyond which the overpressure can be calculated accurately independently of its original geometric vessel form (Geng et al., 2011). A comparison of the overpressures in axial and perpendicular direction is presented in Figure 4.3. After a distance of $\overline{Z} > 1$, the difference in dimensionless pressure is negligible, as they coincide onwards.

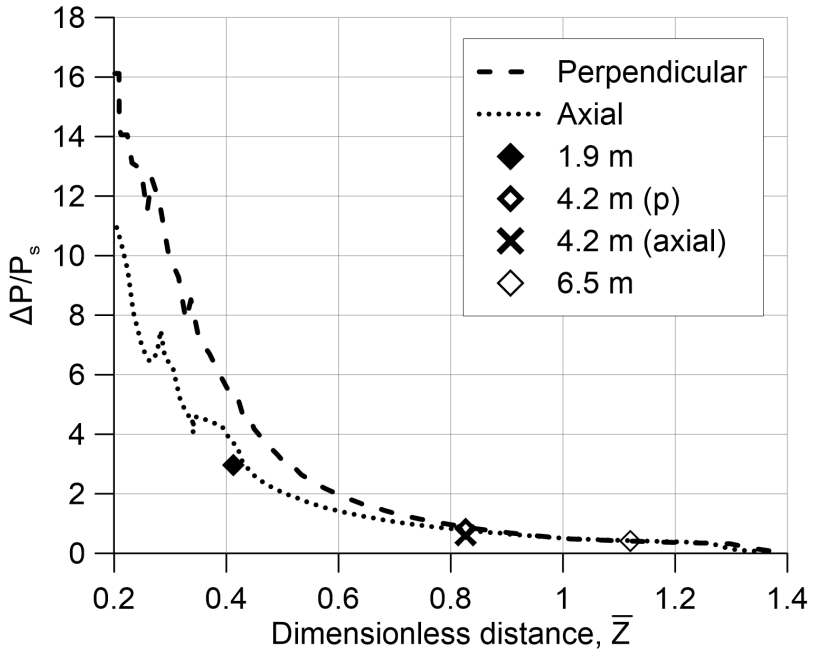

Figure 4.3: Dimensionless peak overpressure for blast wave decay in both perpendicular and axial directions of the tank (lines), and corresponding experimental data (points) as a function of the dimensionless distance, $\overline{Z}$.

4.1.2 Contribution of combustion energy to the blast wave strength

An effort was carried out to investigate the specific contribution of combustion to the overpredicted pressure peak seen in the first sensor (1.9 m) during combustion. To assist in the analysis of combustion contribution to the blast wave overpressure, the spatial distribution of pressure, temperature, molar fractions of hydrogen, oxygen contained in air and generated water vapour, as well as the water vapour reaction rate, are presented in Figure 4.4 at the moments 0.5–5 ms. Hydrogen, oxygen and water vapour are expressed by their molar concentration, a product of the molar fraction and the mixture density. Veritably, what the figures clearly indicate is that the relationship between the pressure and

reaction rate is proportional. Initially as the high-pressure hydrogen is released (see at 0.5 ms and 1 ms), the corresponding reaction rate is around 2000 kg/(m^3 s). Once the leading shock propagates ahead of the combustion (between 2 ms and 3 ms) the pressure within the combustion zone decreases from over 1000 kPa to around 300 kPa. The reaction rate subsequently reduces by about three orders of magnitude. Afterwards (at 4 ms and 5 ms), the water vapour production drops by about 2 orders of magnitude to 2 mol/m^3, though combustion remains at the surface between hydrogen and air.

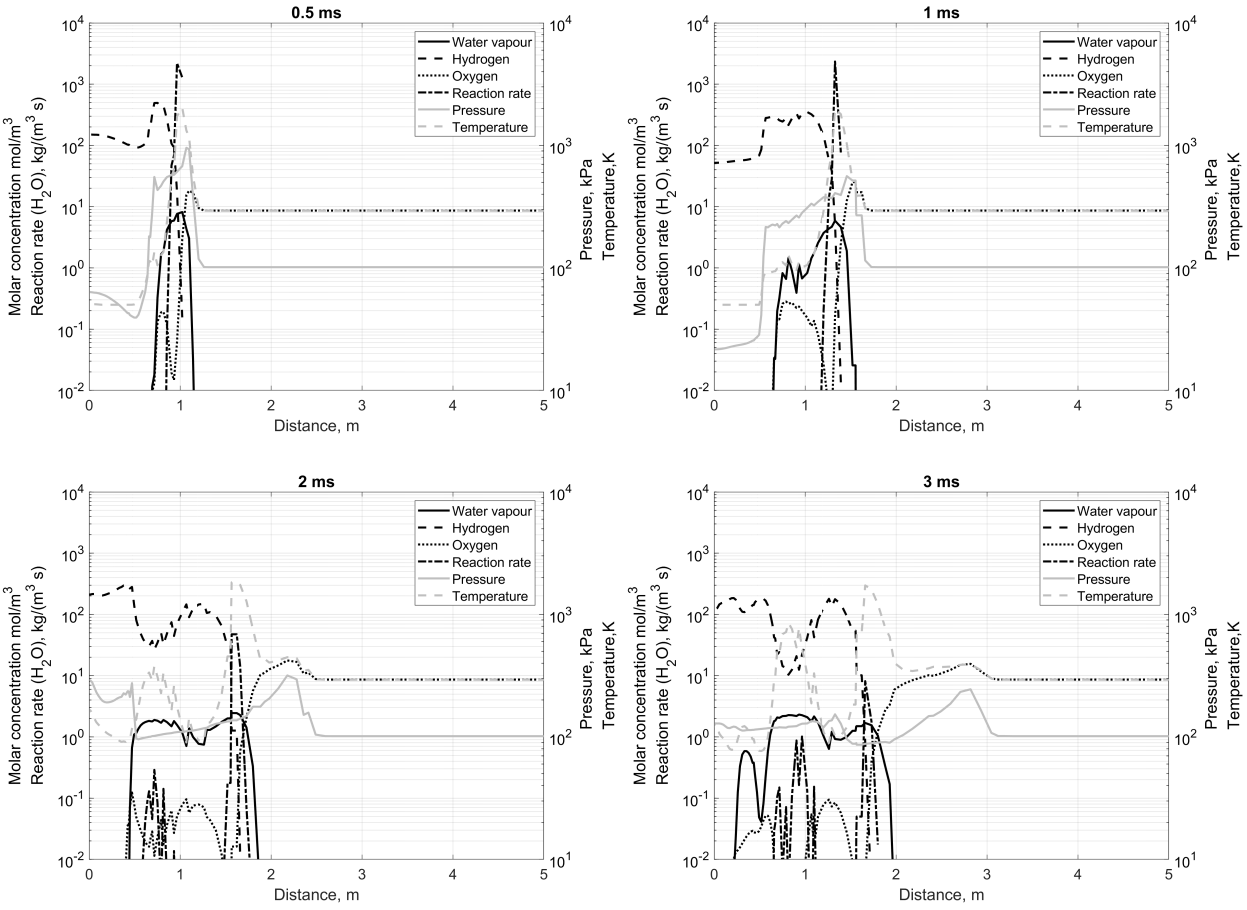

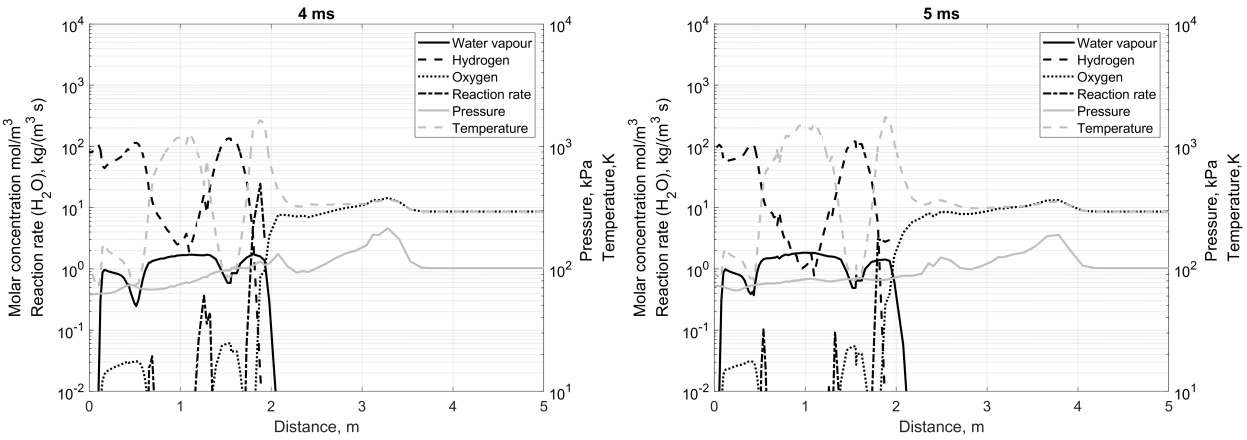

Figure 4.4: Spatial distribution of molar concentrations of hydrogen, oxygen, water vapour, water vapour reaction rate, pressure, and temperature at different instances in time for tank in axial direction.

The now qualitatively confirmed contribution of chemical reaction energy to blast wave strength needs to be quantified. The amount of energy contribution is hereon determined based on the primary pressure profile leaving the combustion zone characterised by the sharp front. It is followed by a tail-end decay to the negative phase, followed by a secondary blast wave. This distinction between the primary and secondary blast wave is the attributed last moment of contribution of energy from combustion feeding to the primary and maximum blast wave after 4 ms, opposed to earlier times up to that point (see Figure 4.4). Contribution of energy from combustion stops due to the secondary blast wave inhibiting the acoustic waves overcoming the positive temperature gradient generated spatially ahead towards the leading front. Due to the directional effects of a cylinder, the spatial distribution of pressure, temperature, molar fractions of hydrogen, oxygen contained in air and generated water vapour, as well as water vapour reaction rate, is presented in Figure 4.5 in perpendicular (left) and axial (right) direction after 4 ms for transparency.

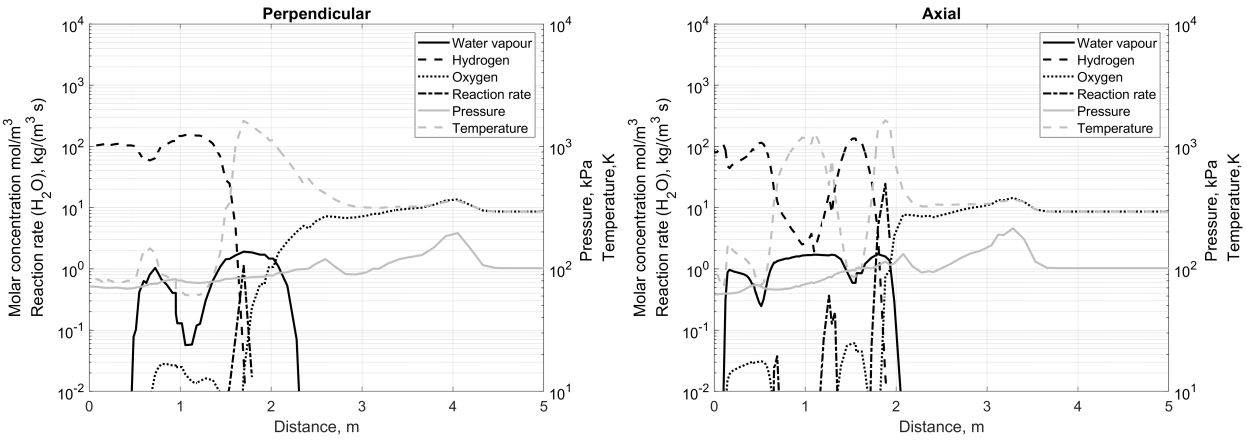

Figure 4.5: Molar concentrations, pressure, temperature and reaction rate of water vapour generation as a function of distance at 4 ms shown for tank perpendicular and axial direction.

Having determined the time at which the contribution occurs (i.e 4 ms), looking at Figure 4.6 easily gives us a value of 3% (i.e. 5.91 MJ) having contributed to the blast wave including its peak and impulse.

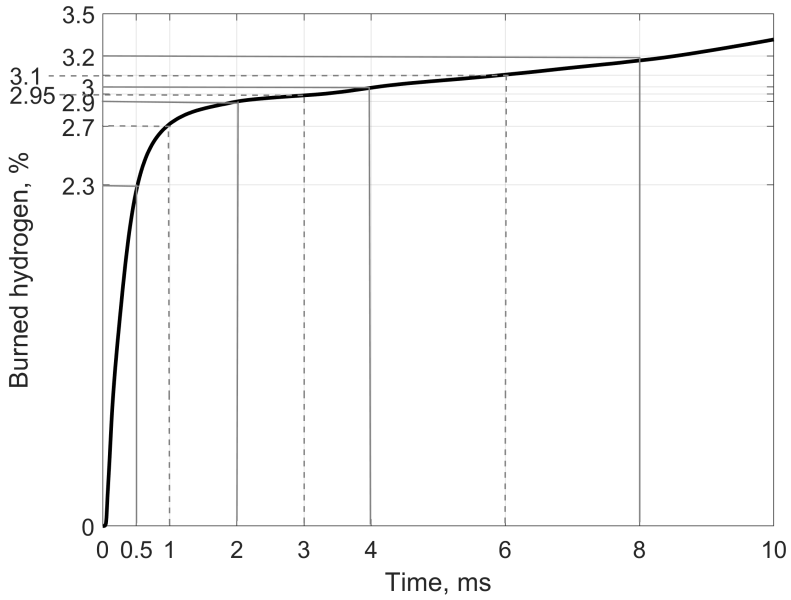

Figure 4.6: Percentage of total hydrogen inventory burned in the initial stages of rupture up to 10 ms.

4.1.3 Modelling hydrogen combustion enhancement due to fire

This section presents analysis of initial conditions of tank rupture in experiment, and the impact on the blast wave and combustion simulation results. A hot environment, to which

the tank is exposed to in a bonfire was attempted to be recreated. This was done in simulation by defining a region around the tank, and utilizing the option to *"patch"* different variables into particular cells within the flow field. Analysis focused mainly on the pressure dynamics in the near-field sensor at 1.9 m, where the effect would be most pronounced. Though experimental data is available only in the perpendicular direction to the tank axis, for analysis purposes both directions in simulation were compared. Denoted as *"hot air patch"*, a hexahedral volume of dimensions L×H×W = 1.5×0.7×0.9 m (0.95 m^3 in volume) was set with a temperature of 900 K, an averaged temperature surrounding the tank prior to rupture, see Figure 4.7. In order to infer an exaggerated effect of the presence of a heated air environment around the tank, a second simulation with a patch five times larger in volume was also conducted. The dimensions of the second patch were L×H×W = 2.6×1.2×1.5 m, with a corresponding volume of 4.75 m^3.

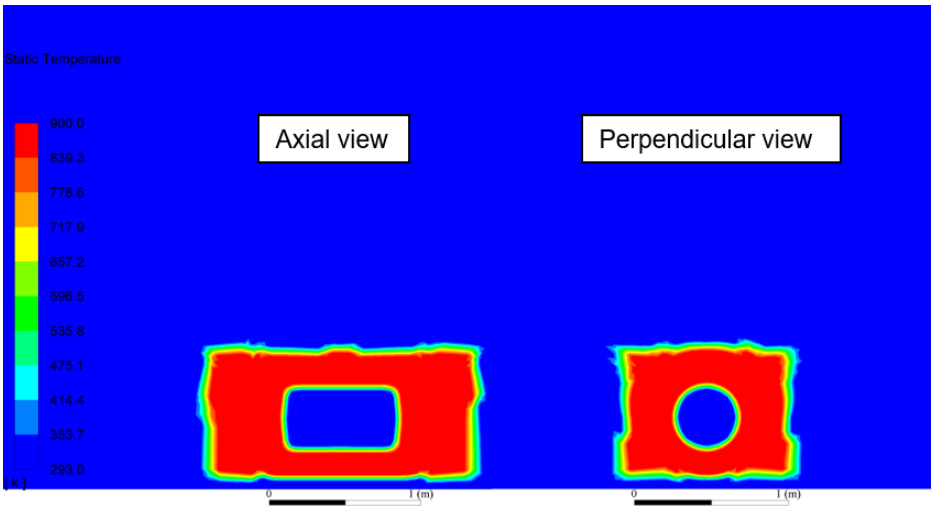

Figure 4.7: The patch L×H×W = 1.5×0.7×0.9 m where hot air initial conditions were imposed prior to rupture, shown in axial and perpendicular direction. Length of bottom ruler seen is 1 m.

Figure 4.8 presents the obtained blast overpressure at 1.9 m sensor, using various volumes of *"hot air patch"*. A patch volume of 4.75 m^3 results in a peak blast overpressure that is increased by 65 kPa, compared to 0.95 m^3 *"hot air patch"*. In either case, the peak blast overpressure is overpredicted by around twice as much, compared to the obtained experimental peak. The overstated peak is thought due to a larger fraction of contribution from combustion to take place. In all simulations, the blast wave reaches the negative phase as the air expands below ambient pressure. A corresponding second peak is seen in the descending part of the simulated pressure transient at around 3 ms for both patches, not obtained in experiment.

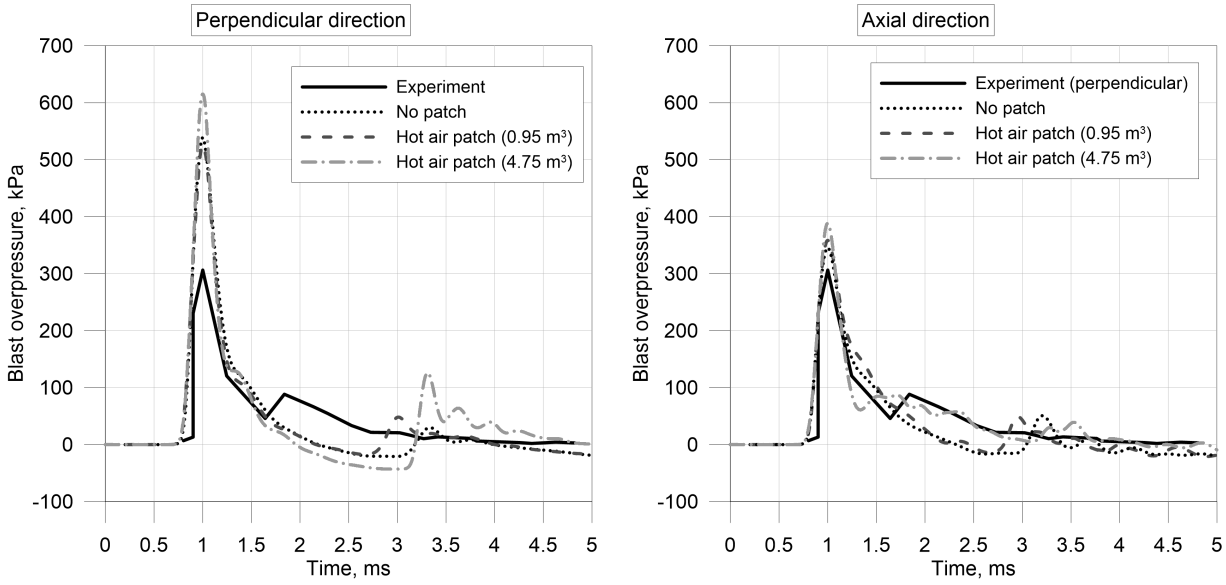

Figure 4.8: The effect of heated air around the tank prior to simulation of rupture, compared with experimental blast overpressure at 1.9 m sensor.

The effect of heated area promoting hydrogen-air combustion is confirmed in Figure 4.9, extended to 16 ms of simulation time. The amount of hydrogen burned show a higher percentage burned as a function of patch size. As the *"hot air patch"* size increases, so does the enhancement of combustion contribution not only to the incident shock wave, but also the secondary peaks correspondingly.

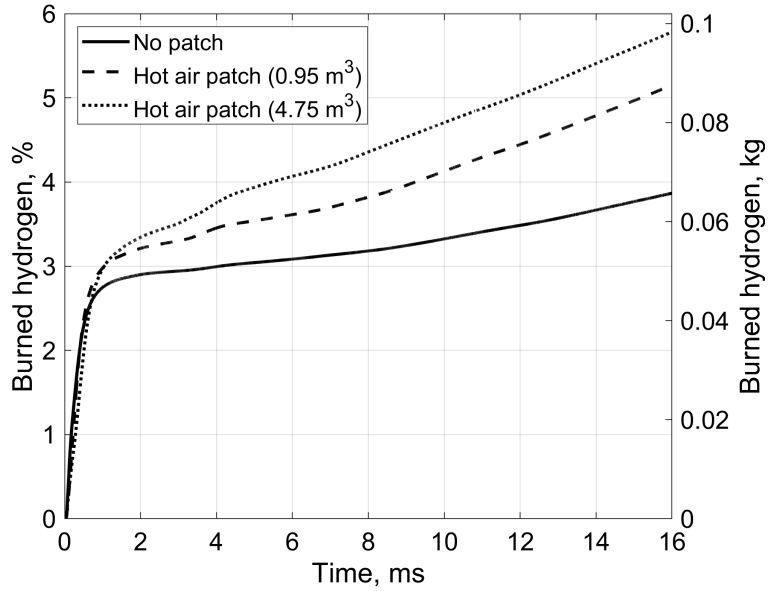

Figure 4.9: Amount of hydrogen burned depending on the patch set as initial condition prior to rupture.

4.1.4 Modelling combustion delay due to tank rupture

In all simulations conducted so far, hydrogen-air combustion starts instantly due to the compression heating of air by blast wave above the auto-ignition threshold, see Figure 3.7. In reality, the tank wall does not fail instantaneously, and air heating occurs over some finite time, with both effects delaying the initiation of combustion at some areas at the beginning of the process. This scenario is simulated by delaying the initiation of combustion in simulations by way of various methods outlined in the following sub-chapters.

Combustion delayed

Due to lack of visual or otherwise insight of how the tank wall disappears, several values of time delay before combustion was activated were studied numerically. Simulations for combustion initiation delays by 1 ms and 3 ms, i.e. before and after the shock wave had surpassed the first pressure sensor located at 1.9 m, are demonstrated in Figure 4.10. For the delay of combustion by 1 ms, the initiated combustion was observed to increase the peak pressure at the first sensor by two times in perpendicular direction, similar to the simulation with *"hot air patch"* seen in Figure 4.8. This increase is due to larger contact surface when the reaction is finally switched on with the initial blast overpressure still within the combustion zone. Until 3 ms when combustion was not activated, the combustion was turned off and the blast wave consists only of the mechanical energy released. Interesting to note, the peak overpressure for perpendicular direction was still overpredicted compared to experiment by 29%. Contrarily, in axial direction without combustion activated, the peak overpressure was underpredicted, 50 kPa below the experimental value. The noticeable effect once combustion was turned on after 3 ms was seen at the secondary peak in both directions (at distances 3–4 m), in which the energy contribution from combustion to the blast wave was allocated.

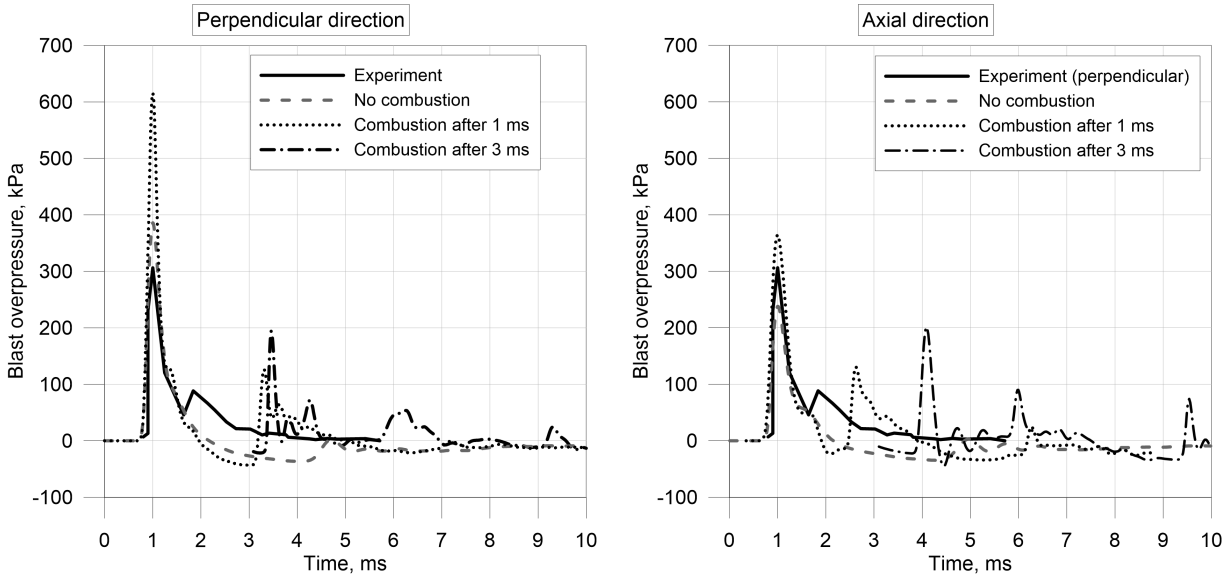

Figure 4.10: Simulations of tank rupture without combustion activated, delayed by 1 ms and 3 ms, compared with experimental blast wave overpressure at 1.9 m.

Burned gas patch

Previous simulations were carried out with initiation of combustion at the contact surface due to numerical realisation of diffusion mechanism of spontaneous ignition. However, the presence of the propane burner, fire and hot temperature plume present in experiment were absent in performed simulations. This would affect hydrogen combustion at the start of the shock wave propagation process, when hydrogen combustion is most reactive. Therefore, the properties of the patch were determined following the reaction of complete combustion of propane in air: $C_3H_8 + 5.0\,O_2 + 5.0 \cdot 3.762\,N_2 \longrightarrow 3\,CO_2 + 4\,H_2O + 5.0 \cdot 3.76\,N_2$. The amount of mass for each mole of CO_2, H_2O, and N_2 is 44 g, 18 g and 28 g, respectively. Taking into account the number of moles generated after one mole of propane is consumed, the mass fraction of H_2O of the products becomes 0.1, with the mass fraction of remaining species attained as nitrogen with mass fraction 0.9, replacing CO_2 with N_2. This was because the computation domain was limited by a few species (i.e. H_2, O_2, N_2 and H_2O), N_2 being the only inert gas.

Two patch areas surrounding the tank were used in separate simulations: one the size of the propane line burner used in experiment with dimensions L×W = 0.8×0.3 m, denoted as *"burner size patch"*. The patched temperature was 1300 K, the flame temperature measured in experiment (Weyandt, 2005). The second patch with dimensions L×W = 2.3×0.8 m, described as a pan encasing the line burner in experiment to protect it from wind, denoted as *"pan size patch"*. Both burner and pan patches had a plume height of 1.3 m, estimated based on experimental images. The temperature of the entire pan area was averaged, and set as 900 K. Presented in Figure 4.11, the change from burner to pan combustion products patch in obtained overpressure depends on the direction of the tank. Perpendicular to the tank axis, not much difference was observed in the magnitude of the first pressure profile and

peak for both sizes of patches. Both overpressure peaks were about 70% higher compared to the experiment. Contrarily, axially to the tank the peak pressure was substantially decreased due to the presence of patch. Presence of *"burner size patch"* still overpredicts the blast overpressure significantly, by 56%. However, the presence of *"burner size patch"* reduces the overprediction to 30%. The reason for the decrease of the first pressure peak for the pan size patch is due to the size of the big patch in axial direction being closer to the pressure sensor at 1.9 m. Therefore it *"artificially"*1 excludes combustion long enough, less energy contribution to the blast wave measured as a result.

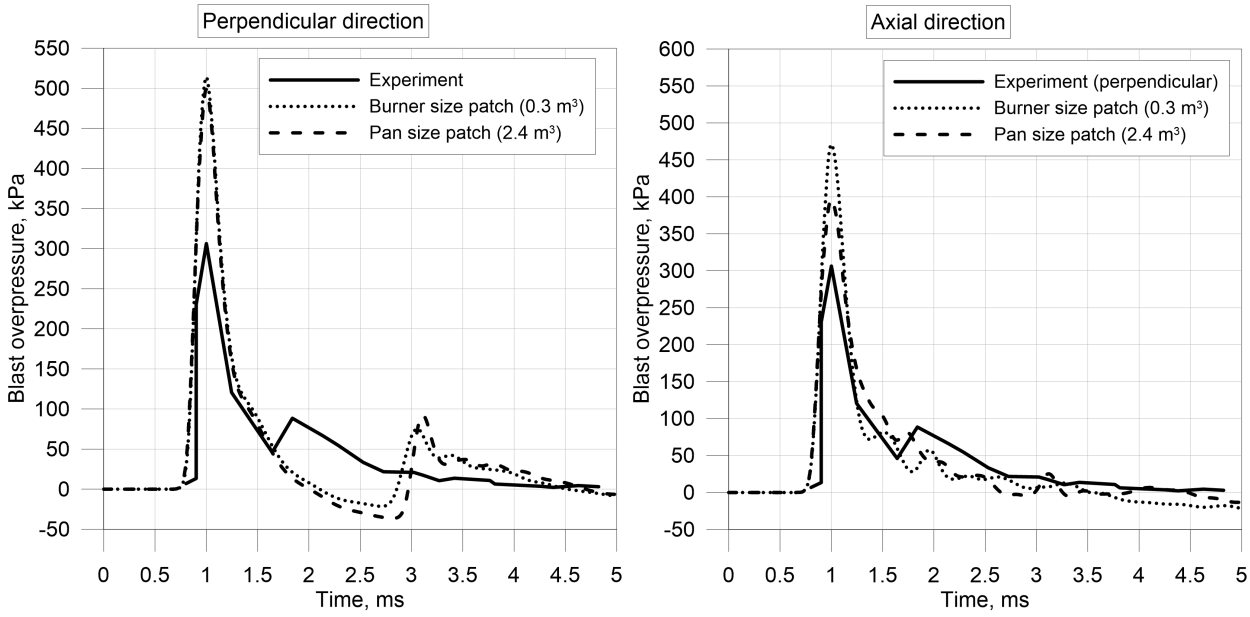

Figure 4.11: Combustion (burned) products consisting of species N_2 and H_2O patched in a region around the tank prior to rupture simulation, of sizes 0.3 m^3 (burner size) and 2.4 m^3 (pan size).

The effect of artificially excluding combustion, for sensors in both directions was investigated. It was conducted by extending the area of burned products to cover the area whereby the 1.9 m sensor is located with a 2 m radius (25.1 m^3) *"hemisphere patch"* containing combustion products as determined earlier. Contours of pressure, temperature and the reaction rate of water vapour are presented in Figure 4.12. No combustion is observed (see at 1 ms) until the moment 1.5 ms when hydrogen expands beyond the area of *"hemisphere patch"*. Subsequently, the combustion products and reaction rate between hydrogen and air manifests itself at 3 ms.

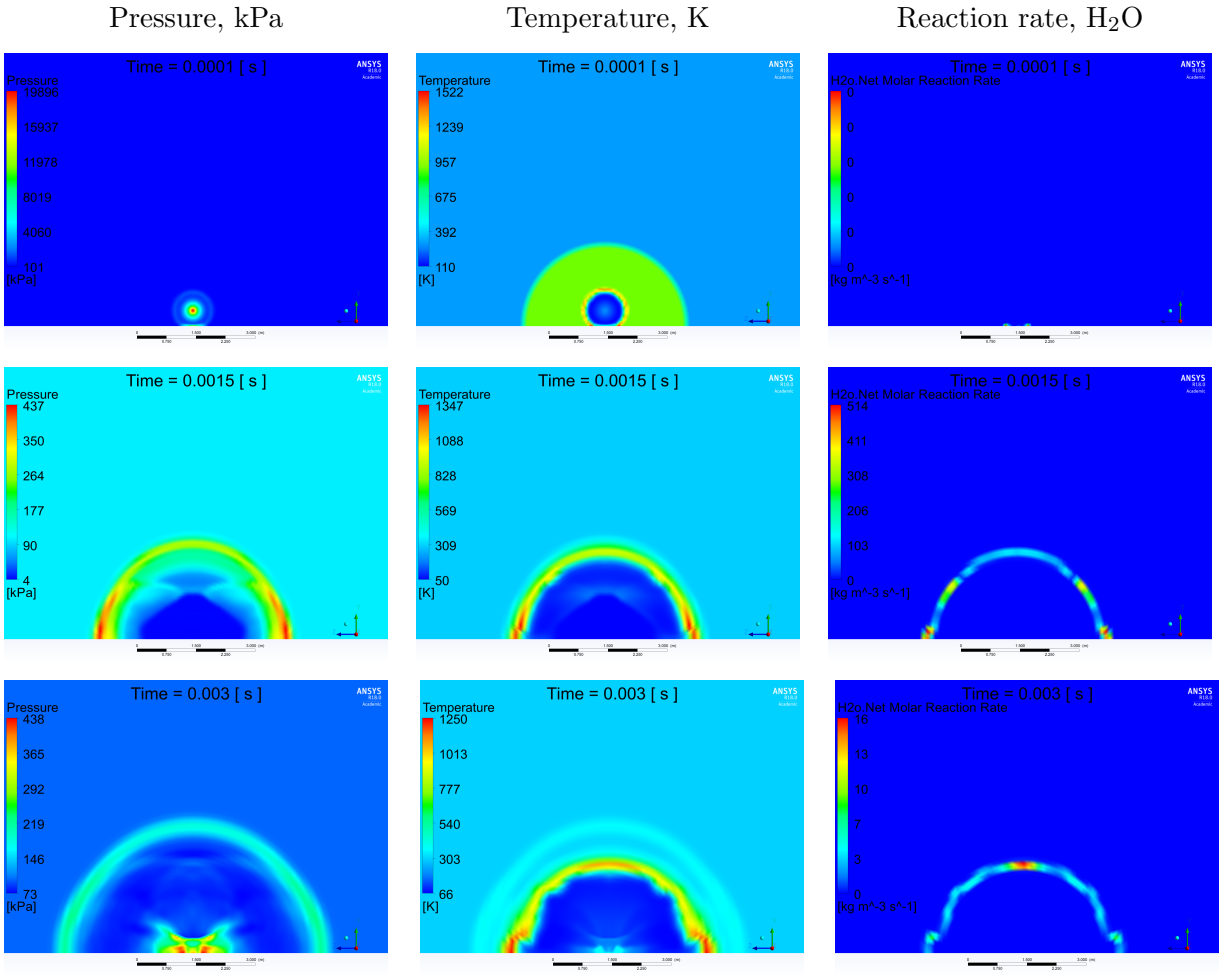

Figure 4.12: Pressure, temperature and H_2O reaction rate dynamics shown at 0.1 ms (top row), 1.5 ms (middle row) and 3 ms (bottom row), after a hemisphere of 2 m in radius of combustion products set as condition prior to rupture. Length of bottom ruler is 3 m.

Comparison of overpressure in present simulations with experimental pressure records and simulations without combustion is presented in Figure 4.13. In perpendicular direction, the peak overpressure was not only reduced compared to all previous attempts, but the presence of a sub-peak was observed (see at 2 ms) similar to that in experiment. This is again due to the initiation of combustion, feeding energy to the blast wave in that exact moment. However, it falls to the negative phase faster than observed in experiment. The artificial exclusion of combustion until the first sensor location in the axial direction naturally reduces the first overpressure peak below the experimental value, in agreement with simulation conducted with combustion turned off.

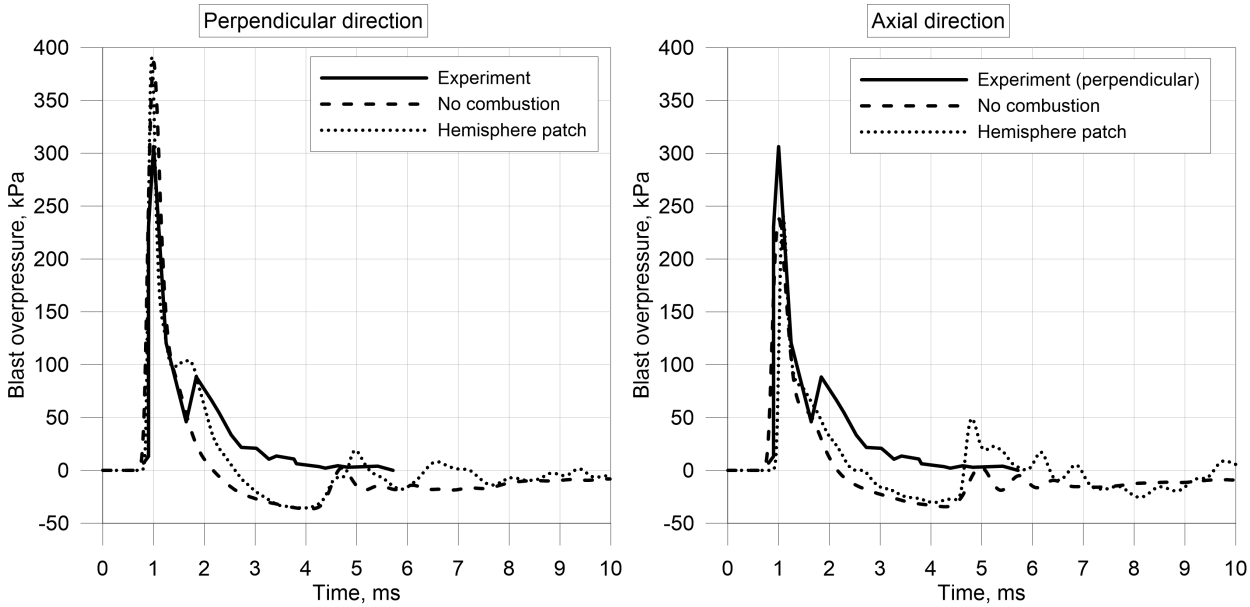

Figure 4.13: Comparison between experiment and simulations whereby combustion (burned) products of N_2 and H_2O patched in a region around the tank prior to rupture simulation and without combustion activated.

For all three aforementioned patches described (i.e. *"burner size patch"*, *"pan size patch"* and *"hemisphere patch"*), the amount of hydrogen burned depending on the patch inferred is shown in Figure 4.14. Without patch, *"burner size patch"* and *"pan size patch"* all show a similar trend, a rapid period of hydrogen burned until the blast wave propagates ahead of the combustion zone at 1–2 ms. Clearly, for the simulation whereby a large hemispherical patch is set prior to rupture, combustion is completely absent the first millisecond. Then, a slow combustion rate is seen within the first 11 ms, the blast wave overpressure already propagated away from the combustion zone.

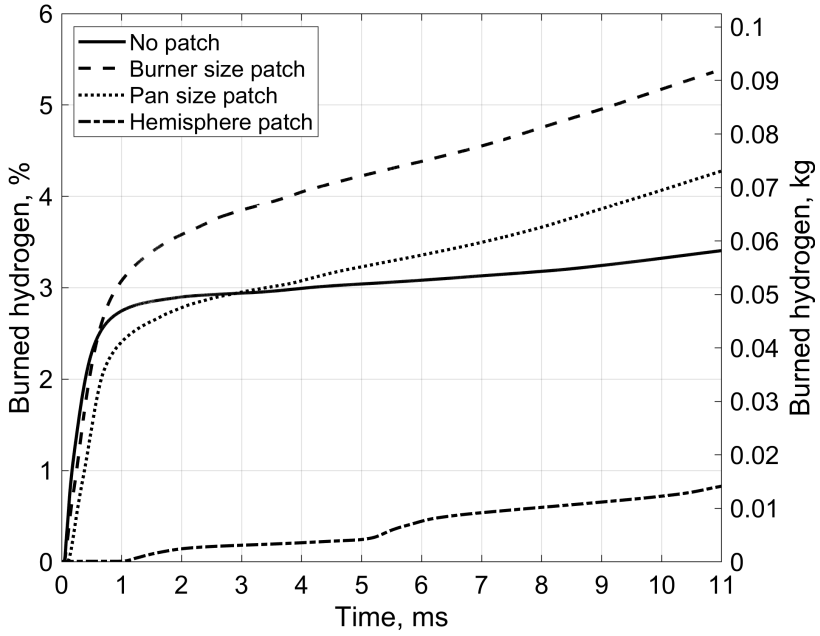

Figure 4.14: Amount of hydrogen burned depending on the specific patch set as initial condition prior to tank rupture.

Bonfire patch

Another attempt at setting an initial condition closer to that of the experiment was inspired by work conducted by Kashkarov (2016), in which a non-premixed propane burner underneath the tank was simulated, resembling the setup in experiment. The simulation provided information about the temperature and species distribution in propane-fuelled fire test. Thereby, access to these results (such as in Figure 4.15) allowed the composition of the established bonfire and hot plume to be reproduced in simulations. This was done by setting horizontal slices at different heights with similar temperatures and composition of species such as oxygen and other non-combustible products. This would also result in a much higher patch vertically, something previously not accounted for.

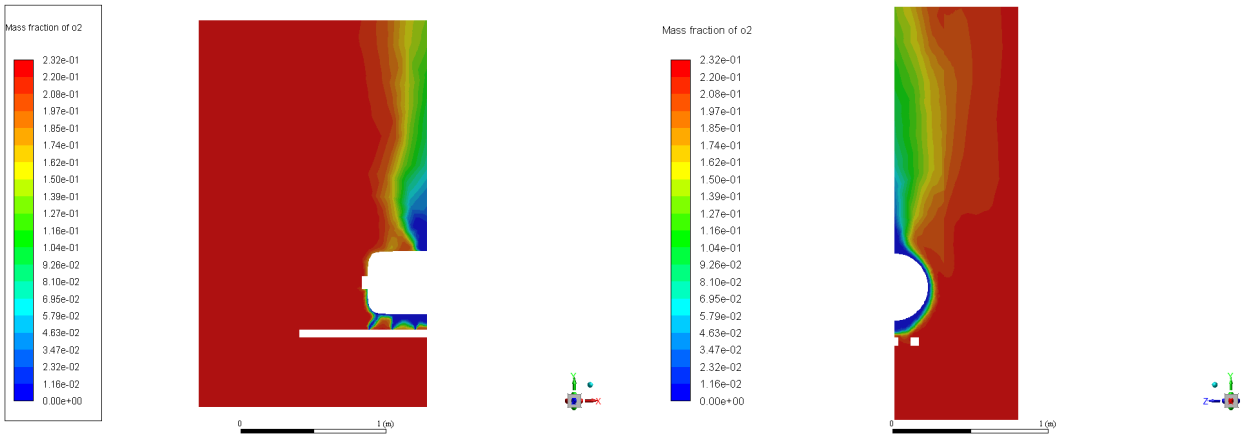

Figure 4.15: Snapshots of oxygen mass fraction distribution obtained in simulations of tank fire test (Kashkarov, 2016).

A volumetric cylinder around the tank of L×D = 1×0.5 m was first set, with combustion products composition approximated as $Y_{H_2O} = 0.1$, and $Y_{N_2} = 0.9$. The temperature was set as 2090 K (Kashkarov, 2016). Above the patched cylinder was a hexahedral patch of size L×W×H = 0.4×0.5×0.2 m, representing the fire area above the cylinder. The species mass fractions were kept the same, and the temperature was reduced to 1700 K. Finally, a third hexahedral volume representing the fire plume was patched including a mass fraction of $Y_{O_2} = 0.25$, reducing the amount of mass fraction N_2 from 0.9 to 0.65. Here, the temperature was set to be 1333 K. Initial conditions of temperature and species inferred are illustrated in Figure 4.16.

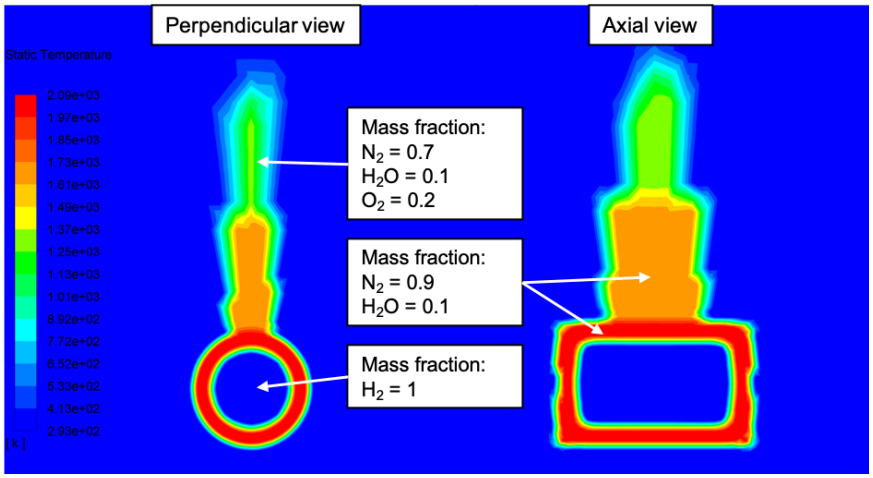

Figure 4.16: Distributions of approximated temperature and species following simulations by Kashkarov (2016). View in vertical perpendicular to the tank axis cross sections and vertical axial to the tank cross-section.

Although the most accurate attempt in terms of recreating experimental conditions prior to rupture, it did not add any effect in terms of blast overpressure dynamics (see Figure 4.17). The size of the *"bonfire patch"* was not large enough to influence the blast wave propagation at 1.9 m sensor, as seen with previous patches.

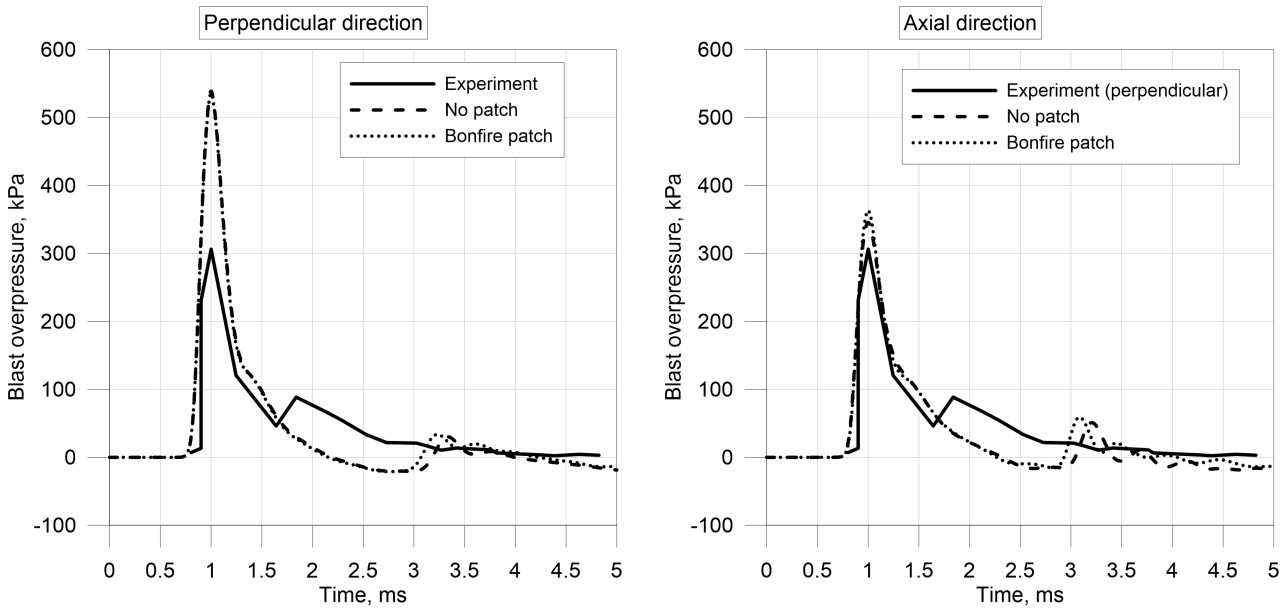

Figure 4.17: Comparison of simulated pressure dynamics accounting test fire temperature and species distribution with experimental pressure record and simulations without special conditions to account test fire.

4.1.5 Inclusion of pan geometry

To improve on the near field pressure dynamics, the pan wall geometry surrounding the tank as implemented in the experiment. This was realized by separating five cell zones defined as walls, four representing the side of the pan wall. The last separated cell zone acted as the pan floor. The pan bottom was 3 cm above the ground. The pan being 20 cm deep, the tank laid right above this height, see Figure 4.18.

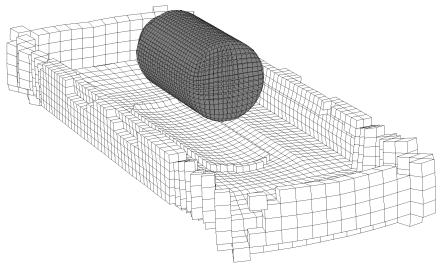

Figure 4.18: View of hydrogen cylinder located above pan in simulation.

The introduction of the burner pan into the geometry gave a better agreement between simulations and experiment for all four sensors, see Figure 4.19. Illustrated, the blast wave peak pressure in direction perpendicular to the tank axis drops significantly from about 540 kPa (see Figure 4.1) to about 350 kPa. The simulated pressure dynamics, i.e. the size and timing of the sub-peak, better reproduces the experimental obtained data too. This is due to the blast reflecting off the pan walls, deflecting more of the blast upwards rather than symmetrically. The use of *"bonfire patch"* did not give any difference in attained blast wave overpressure (as observed in Figure 4.17).

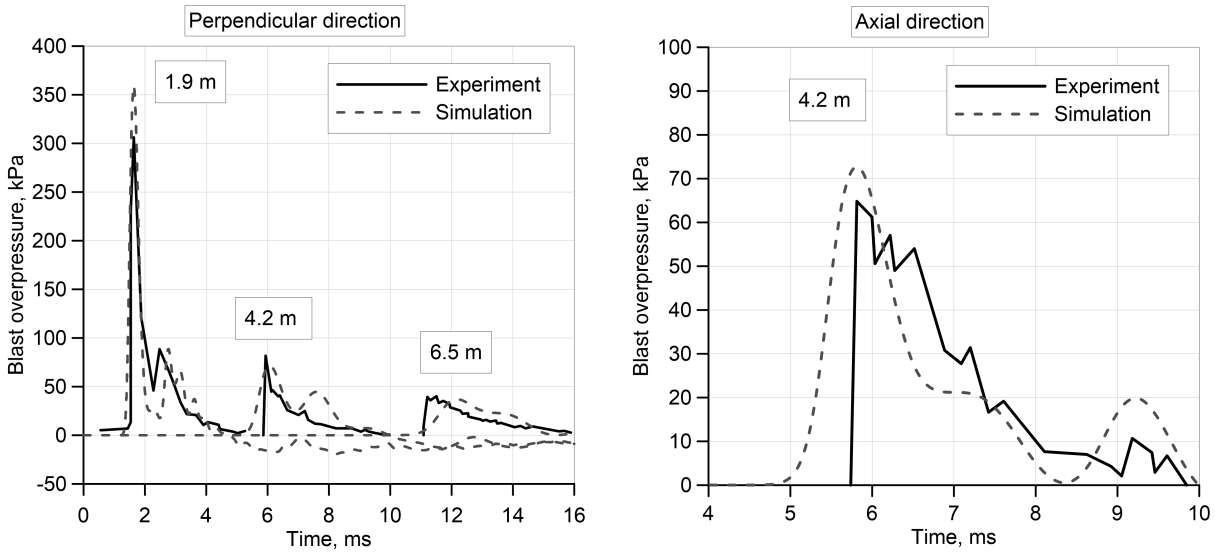

Figure 4.19: Simulations versus the experimental pressure transients for geometry including pan: in direction perpendicular to the tank axis (left) and along the tank axis (right).

4.2 Stand-alone tank rupture fireball dynamics

4.2.1 Effect of various patches

Firstly, the effect of various set patches of initial conditions was explored in terms of fireball development. In the early stages (at 20 ms), the fireball diameter was in no significant way influenced by the inclusion of various patches. However, the overall shape of the fireball development did see some variations, as presented in Figure 4.20. This would differ depending on the viewing angle. Certainly, the various parameters set as initial condition including the high temperatures enables enhanced combustion as per Arrhenius reactions. This would lead to the contact surface area not being exactly hemispherical and affected (increased or decreased) by the flow instabilities. Quantitatively, the fireball development for all three simulations is observed quite similar.

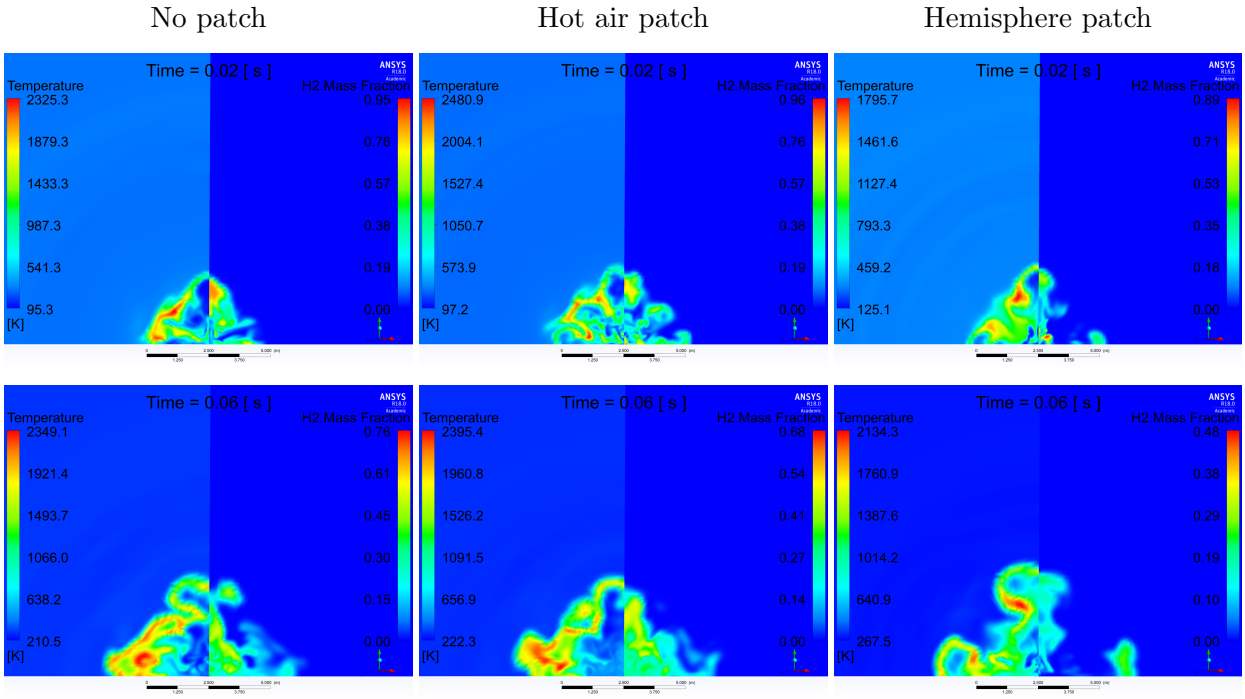

Figure 4.20: Fireball development and shape at 20 ms (top) and 60 ms (bottom) for simulations without any patch (left column), with hot air patch (central column) and hemispherical combustion products patch (right column). Length of the ruler at the bottom is 5 m.

4.2.2 Comparison of experimental and simulated fireball

To ascertain that the fireball size generated in simulations is accurate, a similar size would have to be obtained in experiment. The only experimental measurement of the diameter was taken after 45 ms, determined to be 7.7 m from a 45-degree angle. The model iteration used to compare included the pan geometry and bonfire patch. For the same angle and time,

the results were compared using the *"viewgraph norm"*, visually comparing the diameter and general size of the fireball. Although not comprehensively quantitative, it does provide a form of comparison. Figure 4.21 shows that at 45 ms the simulated fireball size and shape are in a good agreement with experimental observation.

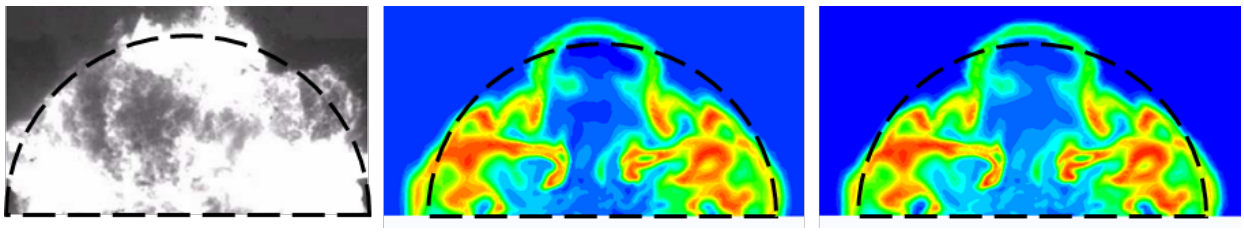

Figure 4.21: Direct comparison between experimental (left) and simulated fireball size at 45 ms with dashed hemisphere with 7.7 m diameter. Temperature raging from 149–2250 K (middle) and mass fraction H_2O (right) ranging from 0–0.32.

The fireball size went above 7.7 m as the time progressed beyond 45 ms. To assess its dynamics at the initial stage, Figure 4.22 shows changing in time height and width of the fireball taken from different directions (perpendicular, axial and diagonal to the tank). The maximum fireball size was measured at 16 m. Apparent, the fireball size depends to some extent on the view factor, varying at most by 2 m in diameter at 1 s.

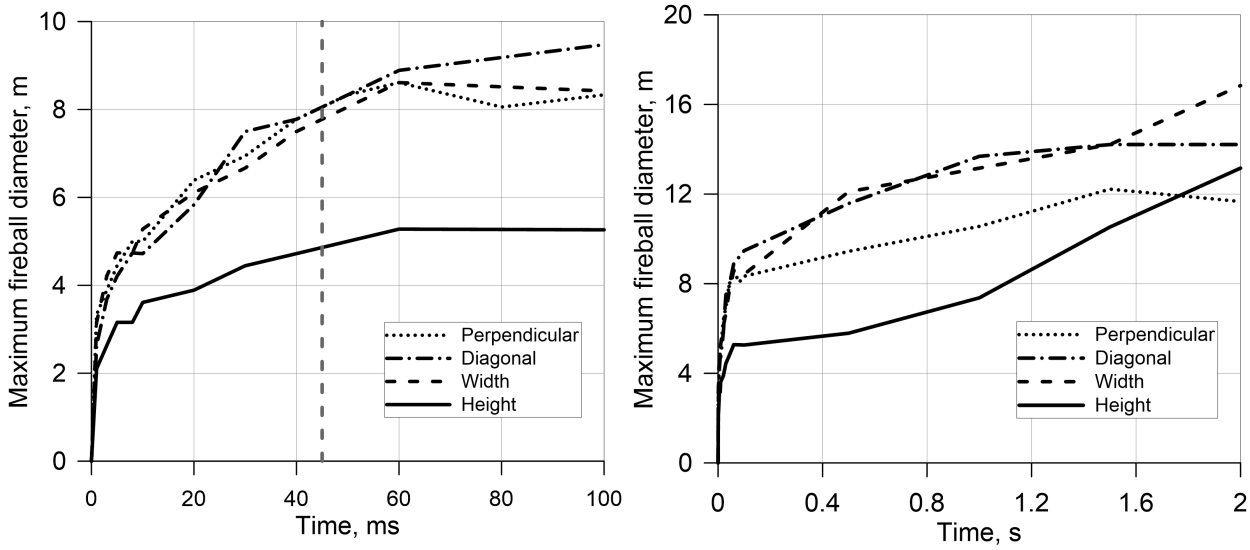

Figure 4.22: Simulated fireball height and horizontal size (in perpendicular, axial and diagonal to the tank axis) as a function of time. Vertical line shows fireball size at 45 ms.

Figure 4.23 presents the fireball development from 0.25 s onwards seen from a 45-degree angle. At the last snapshot (at 2 s), hydrogen-air combustion is complete. During the growth stage with rapid mixing and combustion (up to 1 s), an atypical lift-off effect due to buoyancy

occurs. With the presence of pan geometry throughout the simulation, the entrainment of air is not prominent from underneath. Therefore, there is a disentanglement of the fireball, whereby the upper part first lifts off detaching itself from the main fireball *"body"* after 1.5 s. The notion of a traditional fireball eventually dominated by buoyancy effects in its entirety is not always the case, and rather also depends on the pathway availability of air entrainment.

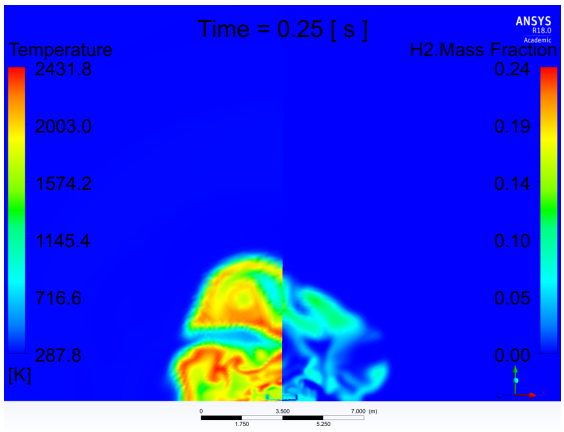

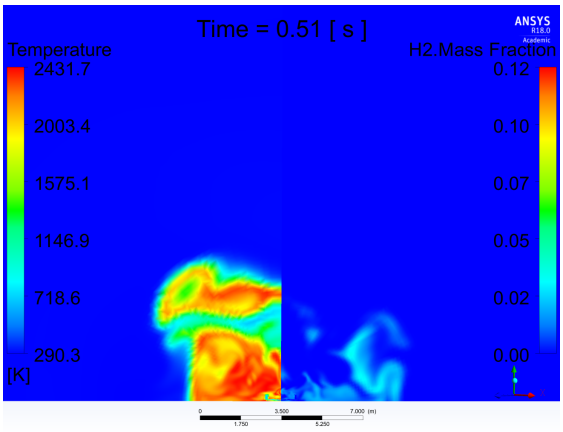

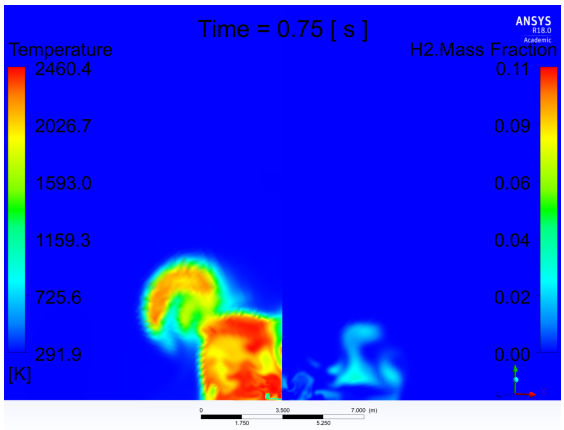

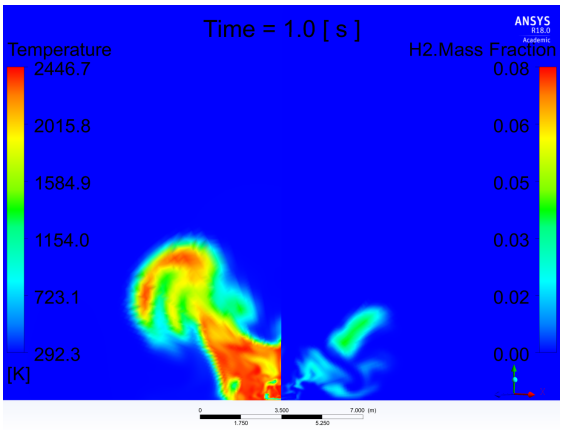

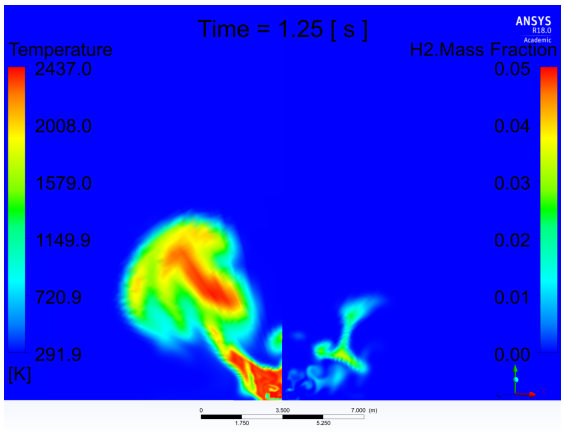

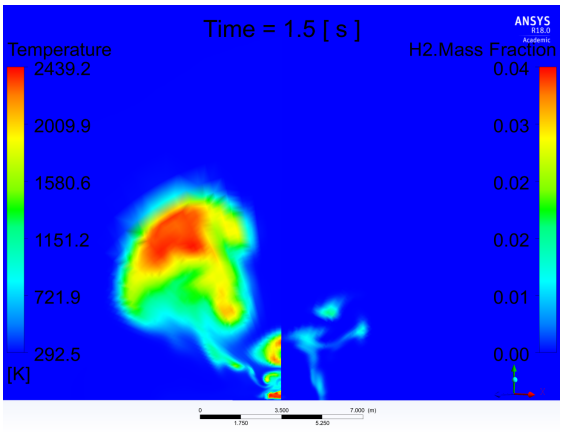

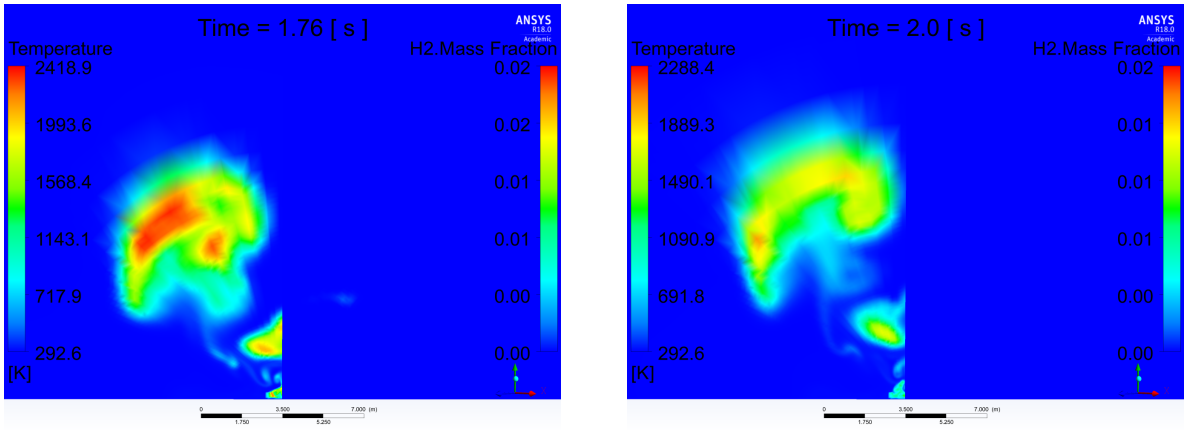

Figure 4.23: Fireball size and shape dynamics during the period 0.25–2 s, showing the temperature (left half) and hydrogen mass (right half). Length of bottom ruler is 7 m.

4.2.3 Effect of radiation

Thermal hazards such as radiative heat flux and thermal dose from a fireball require the activation of the radiation model in simulations. CFD simulations were validated against experimental data to see if radiation exchange has any effect on fireball size and shape. To properly account for the absorption coefficient, the DO model employed discretised the radiative transfer equation resolving the theta and phi pixels divisions by 5 control angles each. The control angle overhang is accomplished by pixilation and each solid angle is resolved by 3×3 divisions. These values are suggested values for simulations including a strong variation of temperature (*ANSYS FLUENT 12.0 User's Guide*, 2009). The absorption coefficient is calculated utilizing the Plank mean absorption for water vapour to properly compute the chemical reaction mechanism of hydrogen (Yan et al., 2015). Using a user-defined function in ANSYS Fluent, water the absorption coefficient is calculated for any particular cell based on the temperature and partial pressure of water vapour. For clarity, the effect of radiation was not seen on the generated blast wave and amount of hydrogen burned. Regarding the fireball size and shape, the inclusion of radiation model is shown in Figure 4.24. Maximum temperatures at the flame outer boundary were reduced with radiation present, due to the radiative heat losses. Observed at 20 ms, the fraction of water vapour in simulations with radiation exchange is larger than in simulations without radiation sub-model. The reduction of computational time without radiation was up to twice, and therefore the baseline simulations demonstrated above did not apply radiation sub-model. However, in cases whereby the thermal hazards in terms of radiative heat flux and thermal dose from the fireball effects were to be analysed, it was included (as in Chapter 5 and Chapter 7).

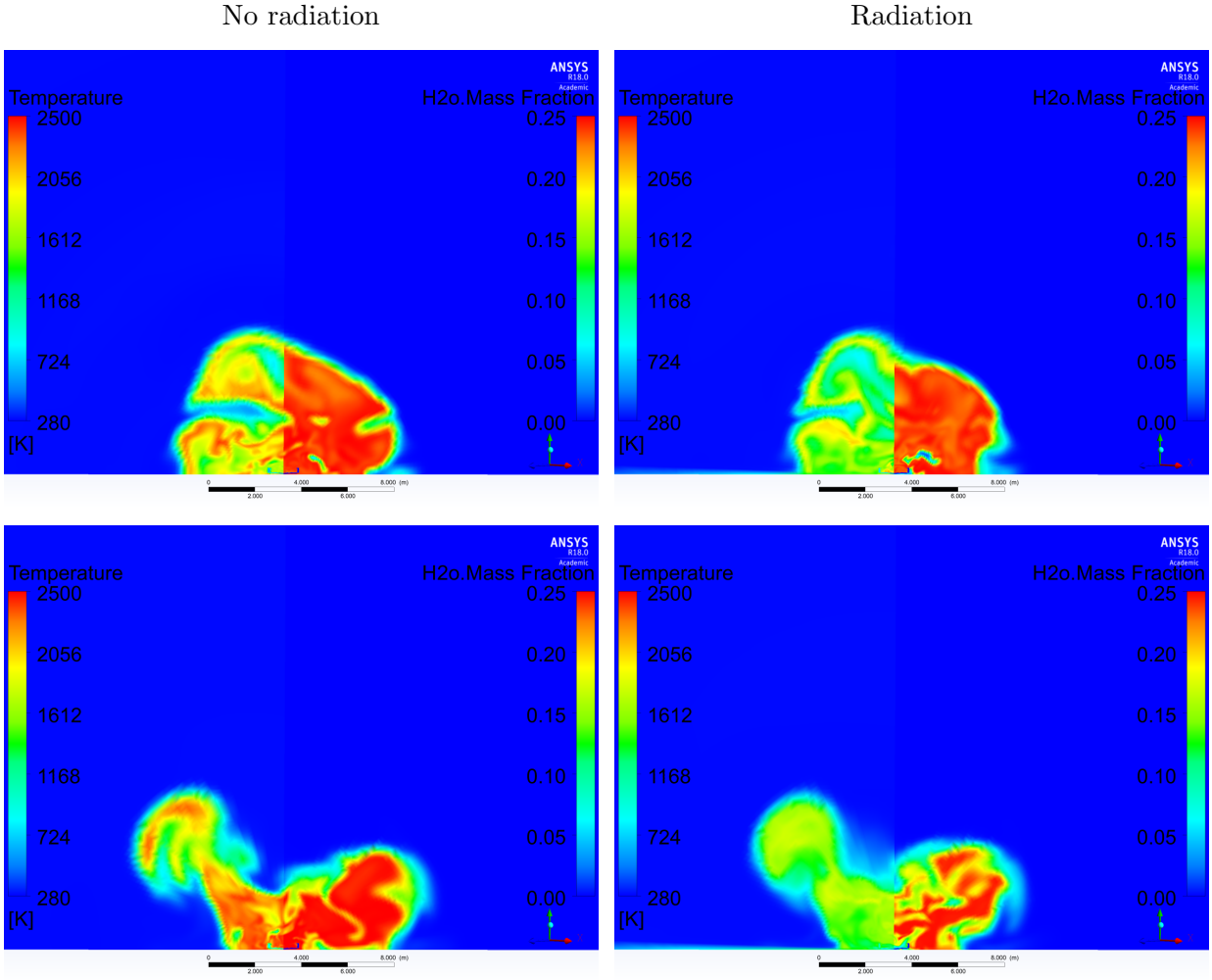

Figure 4.24: Fireball development shown for two times, 0.25 s (top) and 1 s (bottom), for simulation with and without radiation displaying temperature (left half) and water vapour mass fraction (right half). Length of the bottom ruler is 8 m.

4.3 Under-vehicle tank rupture dynamics

In (Molkov et al., 2020), the developed model was used in validating high-pressure hydrogen tank rupture for stand-alone tank using experiments conducted elsewhere (Weyandt, 2005; Tamura et al., 2006). In this section, the same model is applied for the analysis of a high-pressure hydrogen under-vehicle tank rupture, as conducted in experiment by Weyandt (2006). The experiment was carried out with the tank placed under a typical SUV vehicle. The cylinder had dimensions of 41 cm in diameter and 84 cm in length, initially filled to a pressure of 31.8 MPa. In experiment, it was expected that the tank rupture under a vehicle has significant energy losses on the creation and propelling projectiles, e.g. the vehicle body frame was moved 22.3 m from its original position. The positioning of the pressure sensors in experiment (rear, side and diagonal) are illustrated in Figure 4.25.

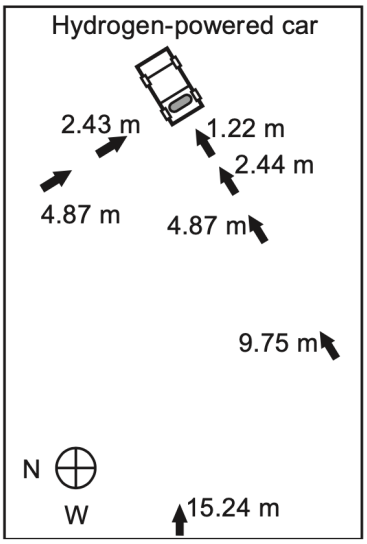

Figure 4.25: Under-vehicle tank rupture setup including vehicle and pressure sensor locations (Weyandt, 2006).

4.3.1 Computational domain

The calculation domain was a hemisphere of a 100 m radius, the car model placed in the centre. The vehicle was 5.2 m long, 1.82 m wide with a total height of 1.43 m (including a ground clearance of 0.25 m). The tank was located close to the back seat, shaped as a truncated cylinder. The tank was placed 1 m from the rear, 4.2 m from the front. The thermal boundary condition of the vehicle was set to that of steel, with a thickness of 0.02 m to account for the one-dimensional heat transfer. The volume of the tank was scaled from 88 L to 73.4 L due to the use of ideal gas, with a tank pressure of 31.8 MPa and temperature of 306.15 K before rupture as in experiment. Tetrahedral cells (later converted to polyhedral mesh in ANSYS Fluent) were used for the current simulations, found favourable for a complex geometry of a under-vehicle tank. The geometry of the vehicle body was meshed with a maximum length 0.1 m, including the ground underneath the vehicle and wheels (see Figure 4.26). At the location of the tank and in its near vicinity, the mesh size was set between 0.03–0.05 m, to cater to the initial blast wave propagation. From the vehicle, the mesh is bi-geometrically increased up to the rectangular prism of volume 336 m^3 (L×W×H = 12×6×4 m) up to 1 m. Up to the hemisphere domain, the mesh was further increased to a maximum CV size of 7.5 m.

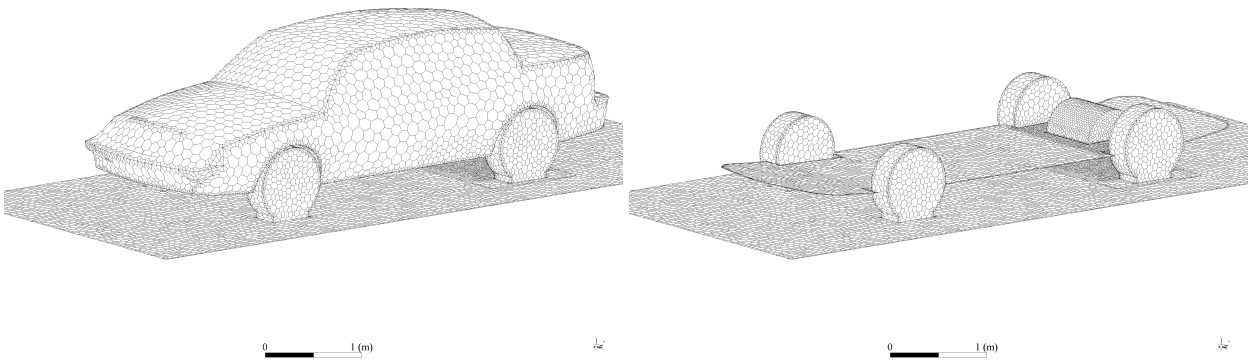

Figure 4.26: Vehicle and tank meshed with polyhedral control volumes.

4.3.2 Sensitivity analysis

To ensure the accuracy of the new constructed tetrahedral mesh, an independence test was conducted for two meshes for the whole domain, one coarse and the other fine, 140k CVs and 382k CVs respectively. The CFL number to ensure numerical stability was 0.1, based on previous tank rupture simulation and sensitivity analysis. Shown in Figure 4.27, a good convergence was obtained in the blast overpressure. What this demonstrates is that despite the complex tank and car geometry, the created mesh retains a good quality and its resolution is sufficient to model key physical processes, even for the coarser of the two grids used in simulations hereinafter. With regards to the amount of hydrogen burned, it is again displayed the inevitable discrepancies appearing due to the reduction in cell size leading to a decrease of burned hydrogen. The detailed explanation of cell size and effect of burned hydrogen is investigated in (Molkov et al., 2020).

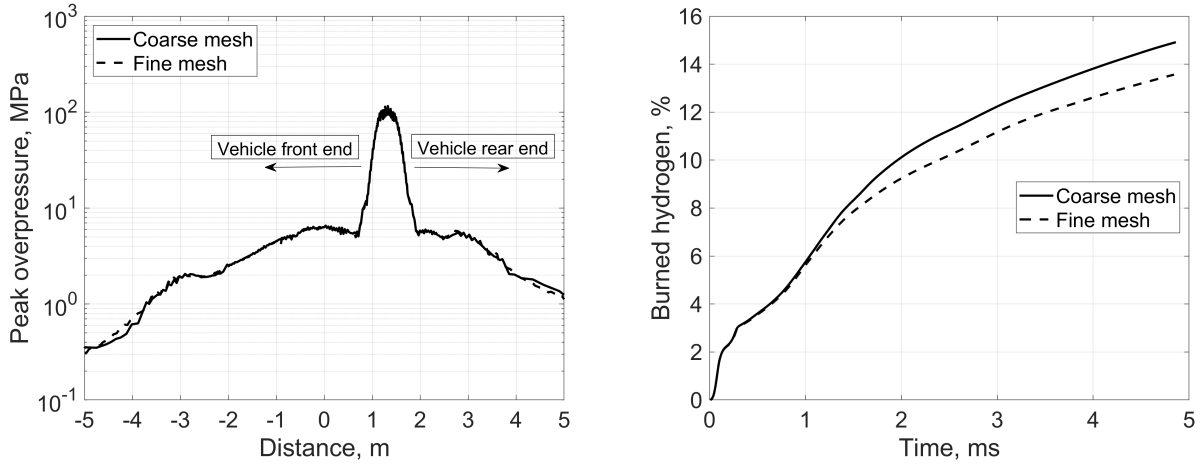

Figure 4.27: Mesh sensitivity test between coarse and fine mesh, shown for peak overpressure (left) and amount of hydrogen burned (right).

4.3.3 Blast wave propagation under vehicle

The blast wave generated from under-vehicle (see Figure 4.28) is dominated by reflections retaining a high blast pressure as the blast wave initially reflects both off the ground and the vehicle bottom surface (see at 0.2 ms and 1 ms). After 2.5 ms, the blast wave has propagated out the rear of the vehicle (and sides of the vehicle), and the maximum blast wave pressure is reduced to 1350 kPa. Once the primary blast wave has propagated beyond the bottom surface of the vehicle after 4 ms, the pressure decreases significantly to 450 kPa.

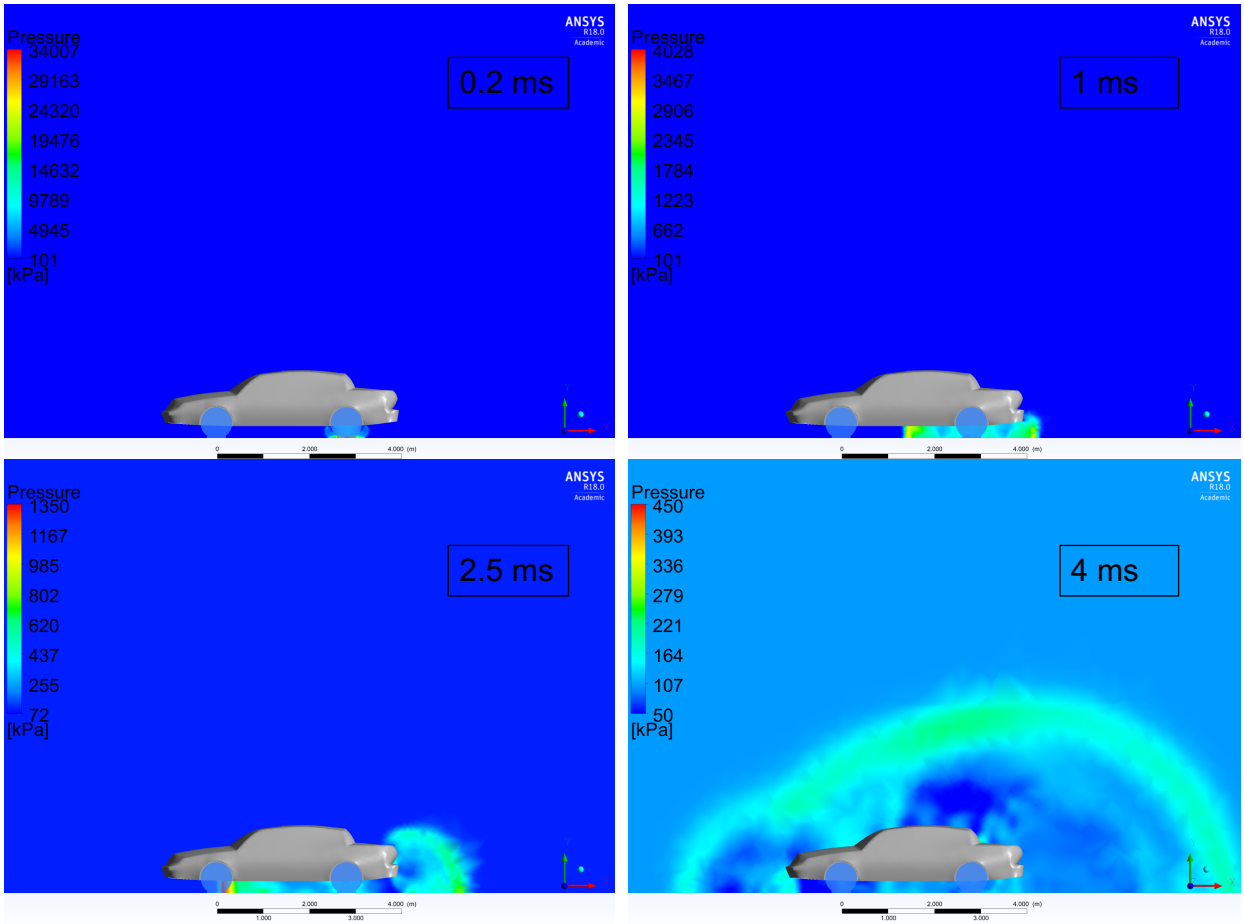

Figure 4.28: The blast wave propagation of an under-vehicle tank rupture seen in various times 0.2–4 ms.

As the vehicle was kept stationary during simulation, its inevitable displacement was analysed analytically. Displacement of the vehicle was calculated based on the pressure forces from high-pressure tank rupture exerted on the bottom part of vehicle. The dimensions of the vehicle being L×W = 5.20×1.82 m, with a corresponding total bottom surface area of 9.46 m^2. The weight of vehicle was estimated 1850 kg based on standards for a typical SUV vehicle, excluding passengers. The force was extracted as the integral of pressure by area under the vehicle, expressed as $F = \int pdA$. This is conducted for various time moments

up until 10 ms, a conservative value for when the blast wave front has well passed the under-vehicle surface area. Once obtained, it is numerically integrated to get the impulse expressed as:

$$I = \int F \, dt. \tag{4.1}$$

From Newtonian mechanics considerations the impulse can be expressed as:

$$I = m \left(\frac{u_2 - u_1}{t} \right). \tag{4.2}$$

Therefore, since the initial velocity is $u_1 = 0$ m/s, the car velocity at every time moment can be calculated as:

$$u_2 = \frac{I \cdot t}{m}. \tag{4.3}$$

Knowing the velocity at every time moment, the displacement distance, s, is calculated as a numerical integral as:

$$s = \int u_2 \, dt. \tag{4.4}$$

Following these steps, the displacement of the vehicle after 10 ms is calculated to be 1.5 cm only. The effect of air resistance working on the vehicle is not included. Nevertheless, this rudimentary estimation indicates that having a stationary vehicle in the early stages of under-vehicle blast wave simulation would not defer greatly to reality.

4.3.4 Simulation of blast wave compared with experiments

Depending on the position of the pressure sensors recorded in experiment, the simulated values are correspondingly given in Table 4.1. In the experiment, the heights of the pressure sensors were not explicitly given, and therefore, three heights are tested i.e. 0.25 m, 0.8 m and 1.3 m. In any case, simulations grossly overpredict experimental blast wave overpressure in the near field, found between 600–8000 kPa compared to the experimentally obtained value of 140 kPa at distance 1.22 m. This trend of overprediction is seen across all sensors, except one (4.2 m sensors on the side of the car), where the overpressure is underpredicted by 13% for recorded heights 0.8 m and 1.3 m. In fact, for the pressure sensor places furthermost away at 15.24 m, the simulated overpressure including peak shown in Figure 4.29 is well overpredicted by 70% compared to experiment. It is believed that the reason for such a drastic difference between experimentally observed and simulated overpressure is neglected energy losses. Clearly, mechanical energy allocated to vehicle destruction and dislocation, ground cratering and tank wall projectiles were not taken into account. Also, since the vehicle was considered as fixed in space, accounting for the deformation of the structural elements that would affect turbulent combustion present, in reality, is neglected.

Table 4.1: Comparison between experimental and simulation overpressures at various distances, h = height.

Position of sensor	Distance, m	Peak blast overpressure, kPa			
		Experiment	Simulation		
			h = 0.25 m	h = 0.8 m	h = 1.3 m
Rear	1.22	140	8000	1190	600
	2.44	56	3500	1000	400
	4.87	30	251	200	155
	9.75	14	31	35	36
Side	2.43	80	350	250	190
	4.2	69	90	60	60

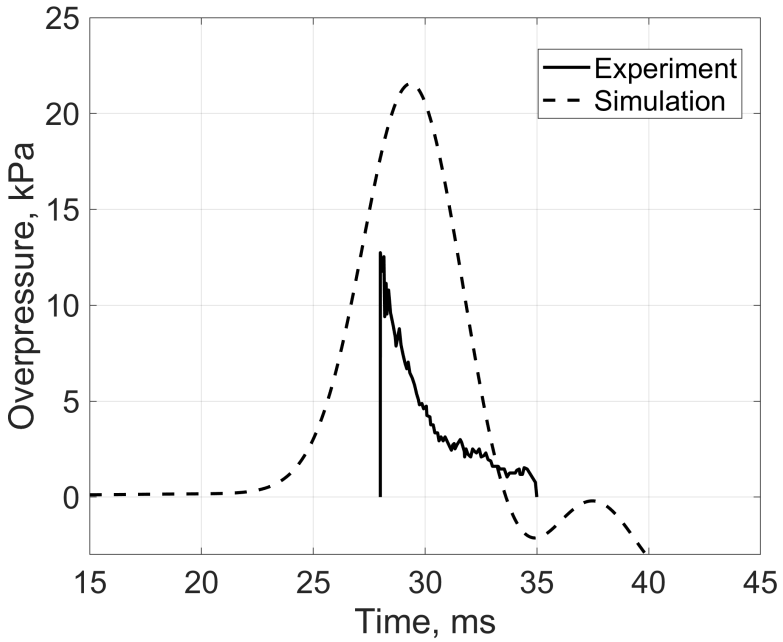

Figure 4.29: Comparison of experimental and simulated overpressure dynamics in sensor located at 15.24 m.

4.4 Concluding remarks

The developed CFD model for stand-alone hydrogen tank rupture in Chapter 3 was validated against experimental data available in open literature (Weyandt, 2005). Compared, the blast overpressure was well reproduced in the far-field, demonstrating that the sum of mechanical and chemical energy released in experiment is simulated well by the model. The ability to reproduce the generated blast wave in the near field was challenged, due to dissimilar tank rupture dynamics. Attaining to directional effects of the cylindrical vessel, the difference in

pressures in directions perpendicular and along the tank axis in the near zone was confirmed, a Sachs-scaled distance of $\overline{Z} < 1$ determined as near field. The amount of chemical energy contributed to the blast wave was established as 3% (5.91 MJ), based on the duration of pressure profile within the combustion zone. The reduction of pressure at the contact surface was the main reason for the significant decrease of reaction rate around 1–3 ms after the tank rupture.

The near field overpressure being overpredicted, was partly due to the idealised uniform release of pressure across its area, which certainly is not the case in the conducted experiment. Therefore, efforts to recreate conditions surrounding the tank prior to rupture included the usage of various patches and the inclusion of pan geometry. A *"hot air patch"* was seen to enhance the blast wave overpressure at the first sensor of 1.9 m. Contrarily, the use of combustion patches *"artificially"* delayed the combustion process and leading to less energy contribution to the blast wave. The inclusion of pan geometry yielded the better comparison of the blast wave overpressure in the near field. The simulated fireball was able to accurately reproduce the fireball size and shape as seen in experiment – a diameter of 7.7 m after 45 ms.

The validity of the developed model has been proven compared with another conducted set of experiments of high-pressure (70 MPa) hydrogen stand-alone tank ruptures in (Molkov et al., 2020). Therefore, it is deemed applicable as a contemporary tool for hydrogen safety engineering to assess the hazards from tank rupture in a fire for various storage volumes and pressures. The validity of the model is found not applicable for under-vehicle tank rupture, due to the lack of energy allocated to the displacement and deformation of vehicle.

Chapter 5

Effect of fire on stand-alone tank rupture dynamics

From the relatively vast experience of CNG vehicles and information on their stored tank failure sources, a large percentage leading to a tank rupture was in combination with a fire (in conjunction with a faulty TPRD) (Tschirschwitz et al., 2019). Furthermore, experiments conducted of induced rupture are performed using the presence of a bonfire, degrading the integrity of the tank until it fails catastrophically (Weyandt, 2005; Tamura et al., 2006; Shen et al., 2018). The direct effect of fire heat released rate and size engulfing a high-pressure hydrogen tank rupture prior to rupture is however not yet known. The presence of fire as it may enhance the process towards a conceivable tank rupture, may have an adverse effect on the consequences of tank rupture, such as the blast wave and fireball. The displaced area of flame around the tank may reduce the quantity of oxidiser such as oxygen in the air, causing less combustion and energy contribution to the blast wave pressure generated. By the use of the numerical simulations, this unexplored knowledge gap is investigated. This chapter is based on a conference paper published at the 14th International Postgraduate Research Conference (Marshall-Ponting et al., 2019).

5.1 Heat release rate and fire area

It is generally reported that rarely does a fire spread beyond the first vehicle, reported in data of vehicle car fires (Department for Communities and Local Government et al., 2010). Recent experiments disclosed otherwise, as fire from a gasoline vehicle spread to a nearby vehicle from the interior and exterior materials (Tamura et al., 2014). Another way for a fire from a gasoline vehicle to spread to nearby vehicles is by fuel spilling, demonstrated to cause a nearby car to be engulfed in flames in 15 min (Jiang et al., 2018). The heat release rate (HRR) of fuel during combustion is usually established by testing, as it is not a fundamental property of fuel and depends on the fire arrangement and thermal conditions. The HRR is often found by first measuring the burning rate and then relating it to the heat of combustion. The HHR in vehicle fire from a fuel spill varies depending on the vehicle,

ranging from 2 MW for a passenger car to well over 200 MW for heavy goods vehicles (Gottuk and White, 2016). For fuel spills of gasoline, the determined value found in the literature lists an HRR of 2.5 MW, per 1 m^2 spill surface area (NRC Staff: United States Nuclear Regulat, 2015). This maximum burning rate is derived from burning dynamics of fuels at steady state. Nevertheless, this is close to the value found in an experiment conducted with the objective to examine the HRR of a fire starting in an engine bay of a modern family car (Department for Communities and Local Government et al., 2010). Here, a sudden peak of 2.8 MW was observed, associated with a spillage of gasoline fuel. Using this peak, a correlation that relates the rate of heat release to the pool diameter for various fuels provided by Drysdale (2011). In this study, propane gas is used as surrogate fuel to simulate fire, as it during combustion produces the same combustion products as liquid hydrocarbon fuel, i.e. carbon dioxide and water vapour. For propane, an area of 2 MW/m^2 was calculated. However, for typical gaseous fuels, the specific heat release rate can be much smaller, up to 60% (Ingason and Li, 2017). Considered for the use of propane, the HRR is reduced by half to 1 MW/m^2 used in this study. Propane mass flow rate was calculated to satisfy design fire HRR based of $\dot{Q} = \dot{m}H_C$, where $\dot{Q}$ is the HRR, $\dot{m}$ is the mass flow rate and H_C is the heat of combustion (lower heat value), 46.35 MJ/kg for propane. The calculated area of propane burner was assumed continuously fed and quasi-steady. The HRR together with the two burner fire areas selected are listed in Table 5.1, *"small fire"* and *"big fire"* referring to fire of areas 2 m^2 and 21 m^2 respectively, both chosen to enclose the stand-alone tank and an envisioned vehicle (sedan) surface area.

Table 5.1: Calculated burner area sizes and heat release rates.

Size	Mass flow rate of propane, kg/s	Total HRR, MW	Propane burner area, m^2	Length × width, m
Small fire	0.042	2	2	2 × 1
Big fire	0.453	21	21	7 × 3

5.2 Numerical details of fire and rupture simulation

The CFD model used for simulating blast wave of a stand-alone tank rupture was developed in Chapter 3, including the governing equation for LES, Equations (3.1–3.3), solved using an implicit pressure-based solver. The computational domain and mesh developed for a high-pressure hydrogen tank rupture were also kept the same. For simulation of the propane fire burner, the combustion was applied using the eddy dissipation model (EDM), with a single-step infinitely fast irreversible global reaction of propane-air given in the ANSYS Fluent material database. Based on the extended Arrhenius equation, values of activation energy and pre-exponential factor for the reaction rate used in ANSYS Fluent are listed as 4.84×10^9 J/kmol and 1.26×10^8, respectively (Westbrook and Dryer, 1981). A fixed time step size was set at 5 ms, ensuring the local convective CFL number below 5 found to provide numerical stability. Convergence level of 1×10^{-6} was set for continuity and species, with 20 iterations per time step inferred. Initial conditions for species in the domain were

set as follows: $Y_{O_2} = 0.23$ and $Y_{N2} = 0.75$. When using EDM for fire simulation, it has a products limiter term that will prevent combustion occurring when the products fraction is zero (*ANSYS FLUENT 12.0 User's Guide*, 2009). Therefore, the mass fractions for CO_2 and H_2O were 0.01 each, based on the previous experience allowing an effective initiation of combustion in simulations.

The simulation of fire was initiated by the fuel supply from an assigned burner area normal to the floor boundary. The inlet boundary for fire burner was presumed a constant temperature and mass flow rate according to the determined mass burning rate and heat release rate. To ensure that the effect of heat transfer mechanism in fire was upheld, thermal radiation was applied by the discrete ordinate radiation model, solving the radiative transfer equations for radiation intensities propagation, see Equation (3.17). An important feature to consider for accurate fire simulations of propane, the absorption coefficient was evaluated as a constant of 5 above a temperature of 399 K. Accounting for absorption by CO_2, H_2O and soot, this value is based on simulations conducted with propane fire, which gave good reproduction of fire test flame temperatures (Kashkarov et al., 2017). Initial conditions of the tank are set to pressure 70 MPa and temperature of 300 K attaining an initial hydrogen mass of 4 kg (internal volume of 72.2 L).

Keeping the same computation domain for rupture simulation, conditions of the tank surface changed from impermeable to permeable allowing compressed hydrogen to expand. Correspondingly, the burner area dedicated as the mass inlet was reverted to wall boundary (asphalt). In switching the mixture properties from propane-air mixture to hydrogen-air mixture in ANSYS Fluent, species of propane and carbon dioxide were included to ensure the domain species properties were kept unchanged. The combustion and turbulence-chemistry interaction for tank rupture simulations were based on the EDC model, details given in Section 3.1.2. Using ideal gas, the chemical source term calculated using the Arrhenius reaction rate for a global one-step chemistry model. The inclusion of radiation was activated, the discrete ordinates model modified using data from Yan et al. (2015) for the calculation of the water vapour mean absorption coefficient, as done similarly in Section 4.2.3.

To enforce numerical stability and accurate description of the resolved scales of motion, the CFL number of 0.1 was super-imposed, ensuring an averaging time-step of around 1×10^{-6} s throughout simulations. In simulating the fireball, the methodology of determining the CFL number was altered to encourage less computational time, as a lower CFL number was first and foremost to accommodate for the initial shock wave propagation. Once the shock had left the domain and out of relevancy, the CFL number was increased gradually up to 20, while ensuring that the mass imbalance was $\pm$ 1%.

5.3 Simulated fire and released HRR

In simulating the development of fire up to 15 s, the simulations were initiated by the fuel released into the quiescent air. To ensure that a pseudo-steady-state fire was achieved before rupture during the, three sensors were placed 25 mm under the tank to measure the stability

of the fire by the temperature profile, as required by regulation and executed in experiments by Makarov et al. (2016). Figure 5.1 shows the transient fluctuations of temperature for all sensors, including the measurement of total heat release rate for both *"small fire"* and *"big fire"* simulations. The temperature profile for *"small fire"* is quite steady at 1100 K, and for a given mass flow rate of 0.0415 kg/s of propane, the calculated HRR of 2 MW is attained in the simulation. *"Big fire"* induces high-intensity natural convection flow leading to the development of large-scale turbulence and mixing. As a result, temperature oscillations for *"big fire"* (Figure 5.1, right) have wider amplitudes. The calculated HRR of 21 MW is attained for a given mass flow rate of 0.453 kg/s. With a maximum temperature well below the adiabatic flame temperature of propane ($\approx$ 2300 K), this was expected due to the high radiative heat loss from the flame to the surroundings during simulation and excess of not reacting fuel in the area where temperature records were obtained.

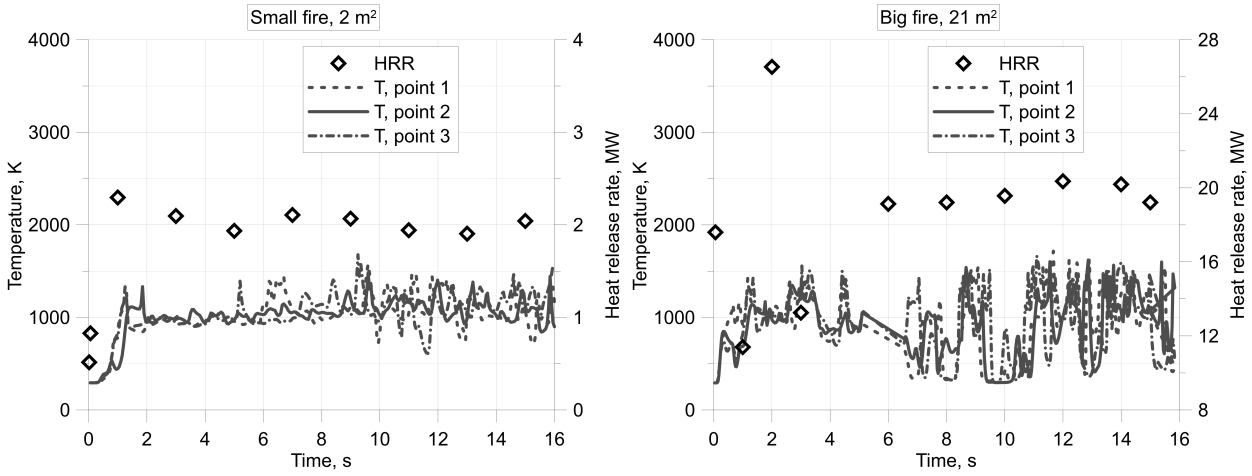

Figure 5.1: Temperature profiles for three temperature sensors and total heat released during propane burner fire simulation. Points 1, 2 and 3 represent locations of temperature measurements placed 25 mm under right edge, centre and left edge of tank along its axis.

Figure 5.2 shows oxygen mass fraction in axial and perpendicular direction to the tank axis direction for both *"small fire"* and *"big fire"* simulation. Due to the nature of flames intermittency and turbulence in the reactive flow surrounding the tank, the magnitude of fire surrounding each tank does not represent the entire propane burner fire area prescribed. In perpendicular direction especially, the momentum of entrainment is seen to minimize the extent of width of *"big fire"* being 3 m, showing minimal difference to *"small fire"* width of 1 m. The differences between *"small fire"* and *"big fire"* are more distinctive for lengths 3 m and 7 m respectively. As the fire area is not equilateral, its influence on the blast wave pressure will likely be different. In addition, within the fire, some concentrations of oxygen are seen in pocket areas around the tank, likely to induce some hydrogen-air combustion within the fire boundary during initial hydrogen release.

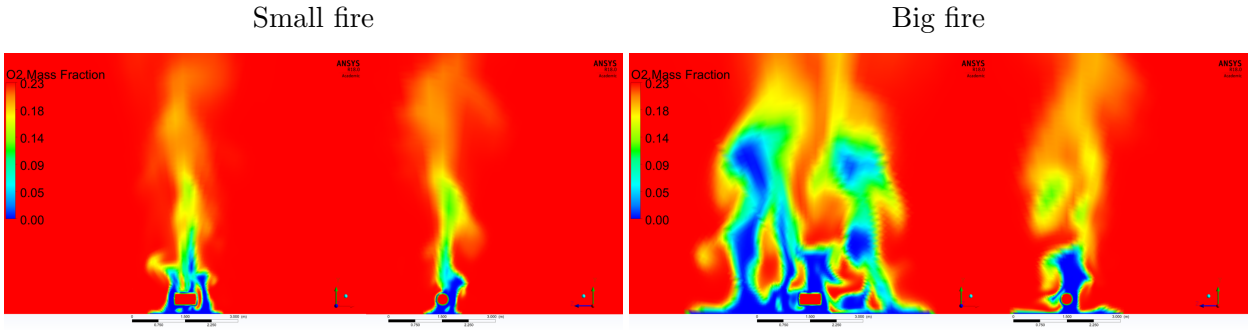

Figure 5.2: Contour of oxygen mass fraction shown for both fire simulations prior to rupture; directions shown are axial (left half) and perpendicular (right half) to the tank axis. Bottom ruler length is 3 m.

5.4 Tank rupture blast wave dynamics

The present section analyses hydrogen expansion after tank rupture simulated as instantaneous removal of the tank wall (as described in Section 5.2). Figure 5.3 shows the Mach number (i.e. ratio between gas speed and local speed of sound) of flow induced by expanding hydrogen for three simulated cases – *"big fire"* (21 MW), *"small fire"* (2 MW) and no fire at all – in vertical cross-section of the calculation domain. The Mach number echoes the development of the initial blast wave propagation after rupture. The local speed of sound (i.e. air speed of sound) varies with the various fire cases, it being inversely proportional to the density. In the simulated fire (see Figure 5.1), its temperature is around 1100 K, close to four times the ambient temperature. As temperature and density are inversely proportional, the density of gas in the flame is reduced accordingly (by up to 3/4). With the expected lower density of air within the fire, the effect shown by the Mach number is visible within the first transient 5 ms shown in Figure 5.3. Here, at 0.2 ms and 0.8 ms the Mach number profile is seen more pronounced when fire is present prior to rupture. As the primary shock wave is formed and propagates outwardly, the propagated distance is seen furthest and most disruptive for *"big fire"* rupture, followed by *"small fire"* rupture case. In the case of rupture without fire present, the propagation of blast wave is highly hemispherical even after 5 ms due to lack of density perturbations in ambient air. Also, the absence of fire may contribute to a more uniform distribution of energy of combustion to the blast wave.

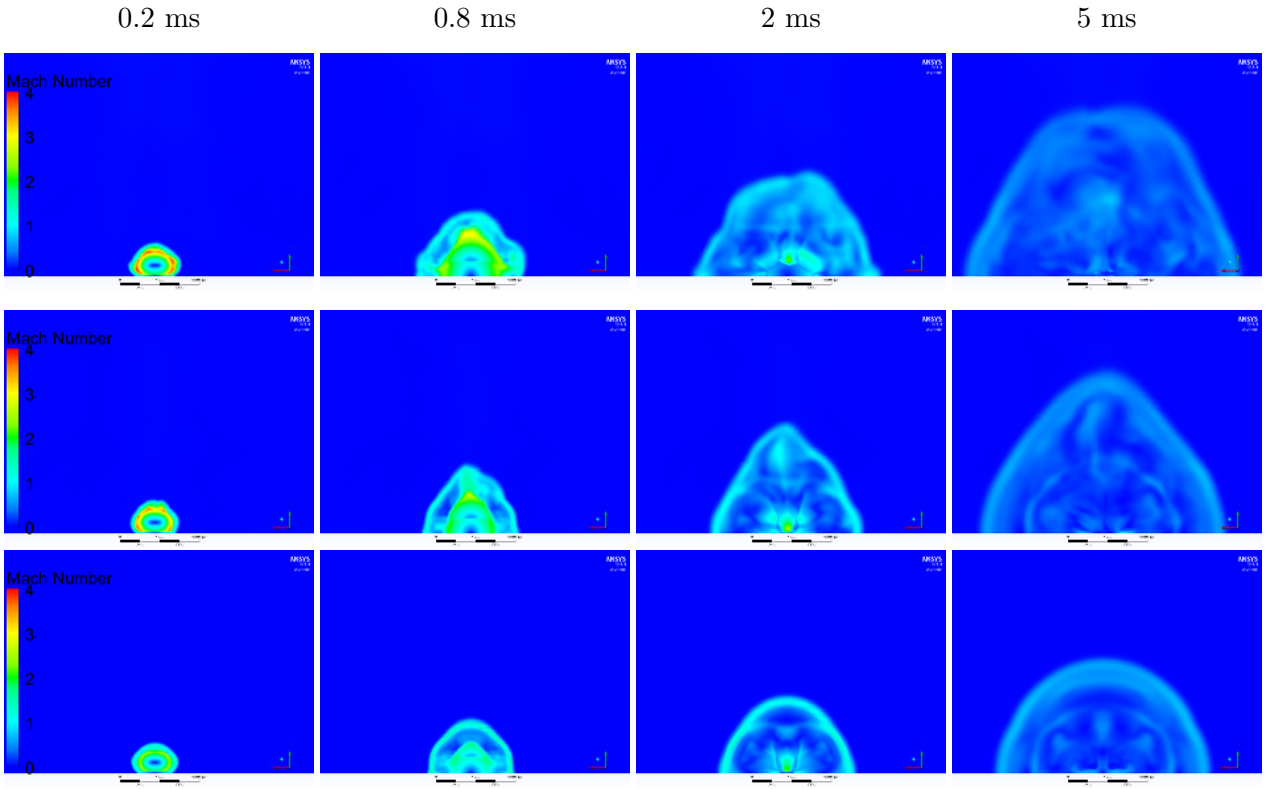

Figure 5.3: Dynamics of Mach number for *"big fire"* (top row), *"small fire"* (middle row) and *"no fire"* (bottom row) after tank rupture simulation at various times, in direction axial to the tank axis. Length of bottom ruler in contour is 4 m.

The thermal energy during a high-pressure hydrogen release is converted to kinetic energy as the gas is being accelerated and causes temperatures to decrease as low as 50 K for all simulations, shown in Figure 5.4. However, the effect of fire present prior to rupture reduces the area of low temperature region significantly during the first 5 ms depending on the fire size. The generated fireball of *"big fire"* rupture is more swirly and intertwined in all directions, compared to the two other simulations of rupture. At 5 ms, a cone-like display of the growing fireball is seen for *"small fire"* rupture, enhancing the fireball growth vertically due to the pre-existing fire plume. *"No fire"* rupture develops more like a mushroom form externally with slight mixing at the core, the higher temperature areas mostly around the edges pertaining to the contact surface. The temperature of the adiabatically compressed air is above that of the fire from 0.2 ms of around 2200 K across all simulations. This indicates that auto-ignition of hydrogen-air has been initiated, irrespective of the presence of fire.

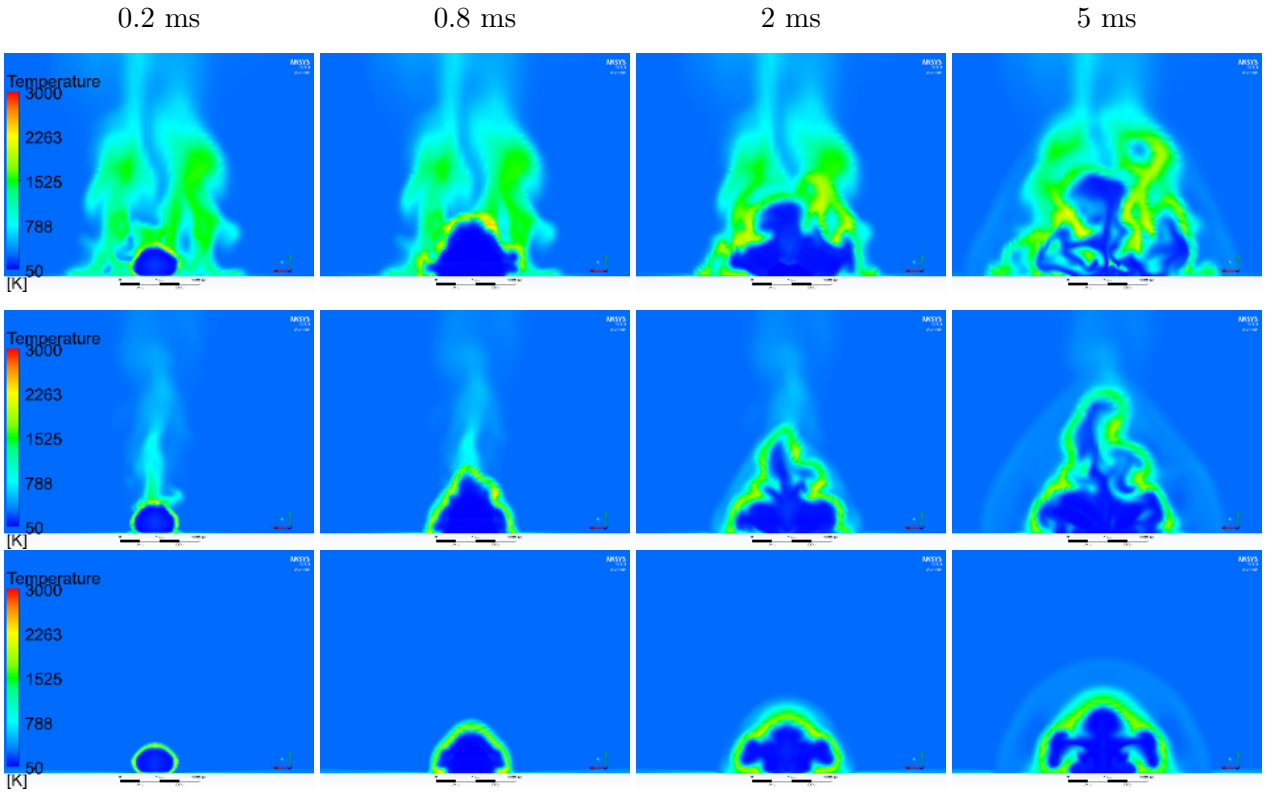

Figure 5.4: Dynamics of temperature for *"big fire"* (top row), *"small fire"* (middle row) and *"no fire"* (bottom row) after tank rupture simulation at various times, in direction axial to the tank axis. Length of bottom ruler is 4 m.

The dynamics of released hydrogen is shown by the mass fraction in Figure 5.5. Up to 2 ms as hydrogen expands, the contact surface is intact and connected for all three simulations with minimal swirls and twists. At 5 ms, similar to the temperature profile, hydrogen distribution is highly affected by initial conditions of fire presence prior to rupture. Its presence enhances the turbulence diffusion of the contact surface between hydrogen and its surroundings. For *"big fire"* rupture especially, the hydrogen is intensely diffused and spread out more which assumes a larger percentage of hydrogen burned. *"No fire"* experiences the least amount of dispersion, the mass of hydrogen still aplenty concentrated at around its rupture point.

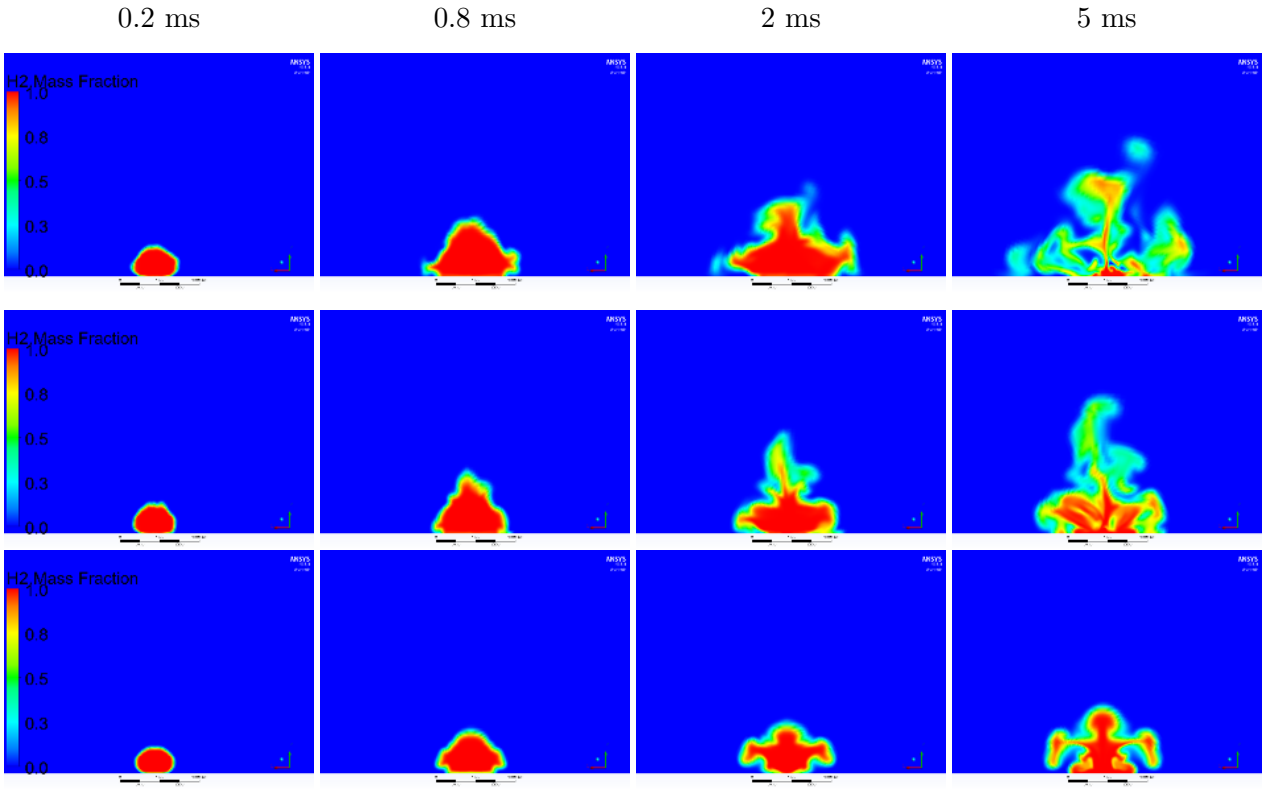

Figure 5.5: Dynamics of mass fraction of hydrogen for *"big fire"* (top row), *"small fire"* (middle row) and *"no fire"* (bottom row) after tank rupture simulation at various times, in direction axial to the tank axis. Length of bottom ruler in contour is 4 m.

Figure 5.6 shows the amount of hydrogen mass burned for all three simulations of tank rupture for the first 10 ms. Within the first millisecond, already over 3% (0.15 kg) of hydrogen is burned during *"big fire"* simulation, compared to *"no fire"* close to 2% (0.8 kg). Afterwards, there is a decrease in hydrogen combustion for all three simulations established at 2 ms, more pronounced for *"no fire"* and *"small fire"* ruptures. Furthermore, they interchange whereby *"big fire"* rupture gains a faster rate of hydrogen combustion compared with *"no fire"* rupture. In the following section, the sudden decrease of the rate of hydrogen burned found in all three simulations will be explored.

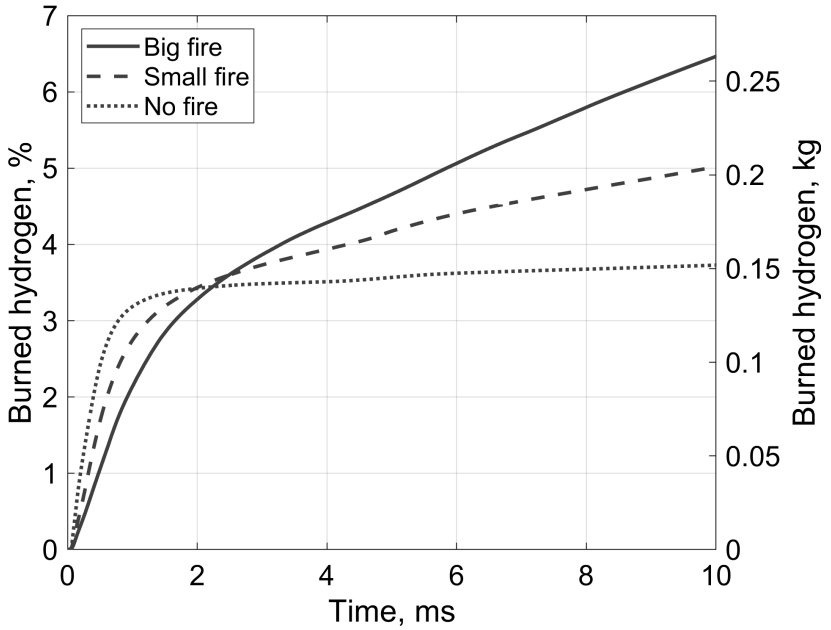

Figure 5.6: Amount of hydrogen burned as a function of time for all three initial conditions prior to rupture.

5.4.1 Effect of fire on blast wave strength in the near field

The connection between blast wave pressure, concentrations of hydrogen and oxygen and the chemical reaction rate for production of water vapour spatially distributed at various times during the initial stages rupture are analysed hereafter. For *"no fire"* rupture presented in Figure 5.7, while the expansion of hydrogen occurs, the reaction rate at the contact surface is seen very pronounced at 0.2 ms and 0.8 ms. At 3 ms as the pressure propagates ahead of the reaction zone, the reaction rate subsequently is reduced substantially, from around 8×10^3 kg/(m^3 s) to 50 kg/(m^3 s). Also, the reflected secondary blast wave that occurs at 1 m distance from tank rupture results in a higher reaction rate. The reaction rate constant expressed by the Arrhenius equation is proportional to the molar concentrations of reactants, which is again proportional to the partial pressure of a species in the gas phase according to the equation of state. During the initial expansion phase where the blast wave and contact surface are linked, two things occur accordingly. The high pressure causes a reaction rate of water vapour production of several magnitudes higher compared to later stages when the blast wave is well ahead of the reaction zone. Second, the species concentrations, also pressure-dependent, increases equally providing concentrations high enough to initiate ignition and sustain combustion even within a fire. For *"small fire"* rupture illustrated in Figure 5.8 at 0.2 ms, the expanded hydrogen has reached beyond the 2 m^2 fire area, and the molar concentrations of oxygen in compressed air ahead is above that found in ambient air (i.e. 9 mol/m^3). Thereafter, the following development of pressure, species concentrations and reaction rate are quite similar to *"no fire"* rupture. For *"big fire"* rupture, the reaction rate is seen significantly lower (see Figure 5.9), compared to the two other simulations

at 0.2 ms and 0.8 ms. Only at 3 ms does the reaction rate increase. Indeed, the contact surface of hydrogen has expanded beyond the fire zone and the sudden availability of oxygen concentration intensifies the reaction rate with values up to 1000 kg/(m^3 s), despite the blast wave being ahead of the contact surface. A higher *"plateau"* in blast wave pressure observed in between distances 1 m and 4 m from rupture point is a direct result of the sustained high reaction rate, the chemical energy contributing to a higher pressure.

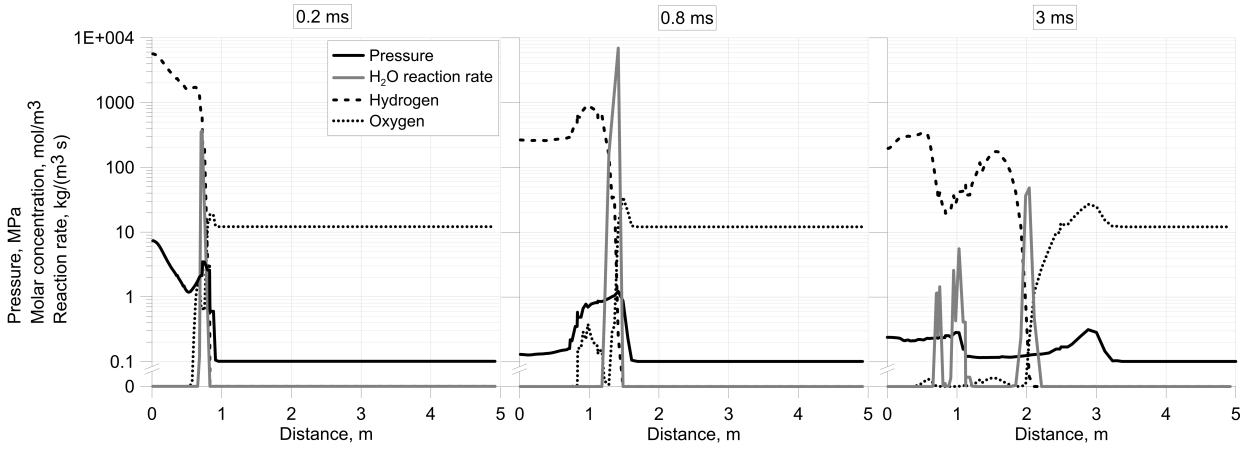

Figure 5.7: Pressure, molar concentrations of H_2 and O_2 and reaction rate of H_2O of *"no fire"* rupture, measured axial to the tank axis at various times.

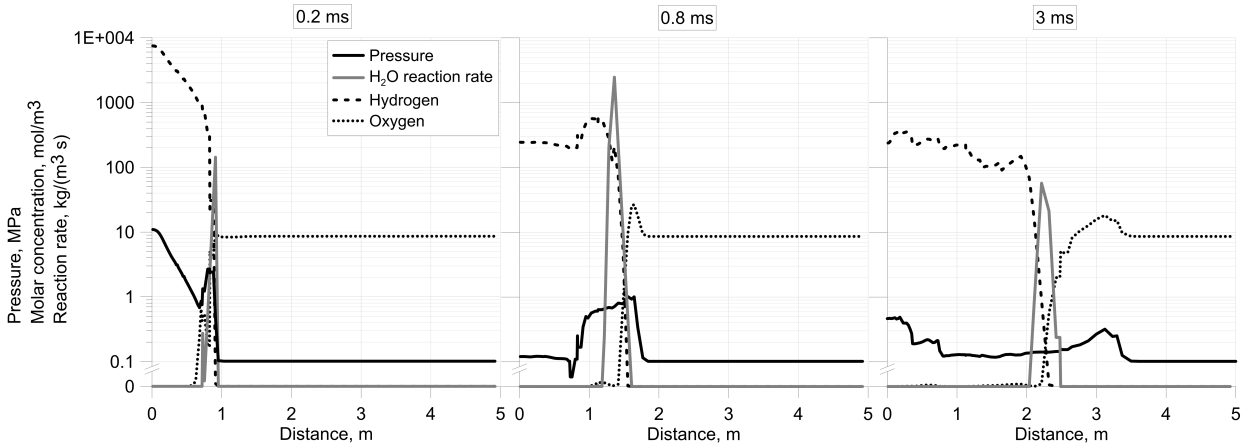

Figure 5.8: Pressure, molar concentrations of H_2 and O_2 and reaction rate of H_2O of *"small fire"* rupture, measured axial to the tank axis at various times.

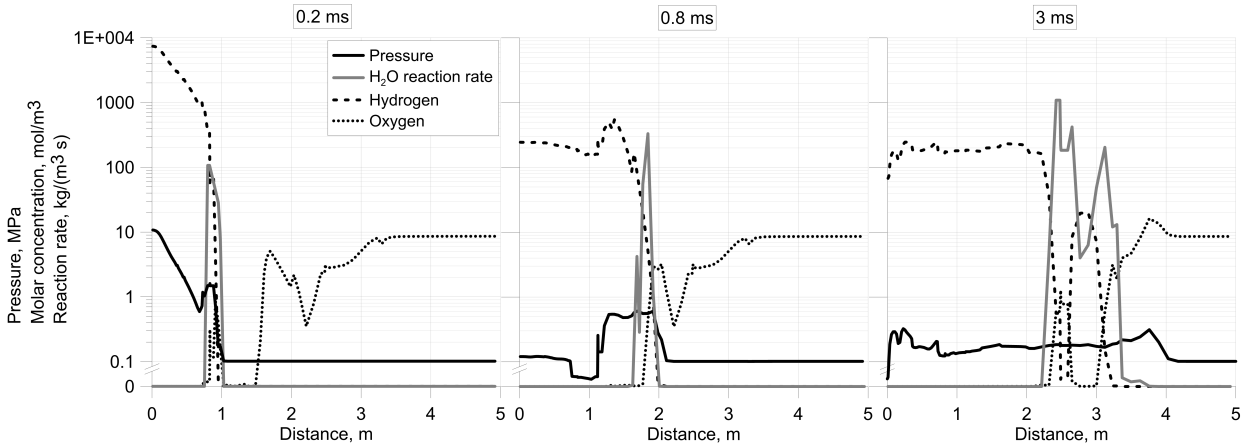

Figure 5.9: Pressure, molar concentrations of H_2 and O_2 and reaction rate of H_2O of *"big fire"* rupture, measured axial to the tank axis at various times.

The peak blast wave pressure is shown in Figure 5.10 (upper graph) for both directions (axial and perpendicular to the tank axis), the lower graph illustrates the difference in blast wave pressure of *"big fire"* and *"small fire"* ruptures from *"no fire"* rupture. For *"small fire"* and *"big fire"* ruptures after 0.5 m, the blast wave overpressure is reduced by 1 MPa and 3 MPa respectively, compared to *"no fire"* seen in Figure 5.10 (lower graph). For *"big fire"* especially, this represents a reduction of over 80% in both directions. At the respective borders of *"small fire"* areas in length and width, the blast wave overpressure quickly aligns with that of *"no fire"* and *"small fire"*. For *"big fire"* rupture, the effect of fire apparently diminishes before the blast reaches beyond the fire plume area. As previously observed in Figure 5.2, the varying size of fire prior to ignition influences the blast wave overpressure differently outside the fire core, more noticeable for *"big fire"* rupture. With regards to harmful pressure effects on humans, the blast wave overpressure seen up to 4 m for all simulated cases is well above the 1% fatality probability threshold of 0.1 MPa (Molkov and Kashkarov, 2015). In the far-field, i.e. where the differences between the three simulations are minimal, the hazard distances are easily approximated using available models (Kashkarov et al., 2020). The obtained differences in blast pressure in the near field are significant, perhaps most impactful with regards to projected fragments, either by primary fragments from the vessel itself or secondary fragments from an object located close by, both beyond the scope of this study.

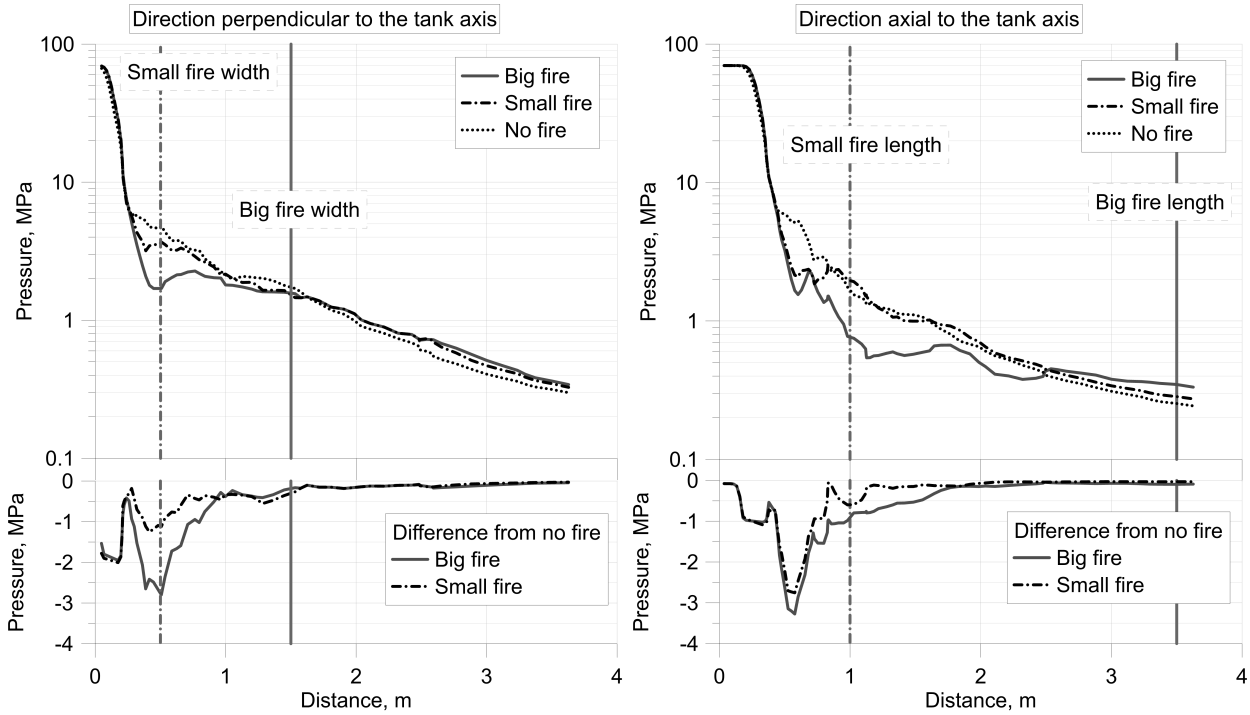

Figure 5.10: Peak blast wave pressure of tank rupture engulfed in fires of various areas (upper graph). Differences in peak pressure are shown in the lower graph.

5.5 Fireball development

The fireball development and the effect of different initial conditions are presented in Figure 5.11, by the temperature (left half) and hydrogen mass fraction (right half). The fireball development from 0.1 s to 0.5 s for *"no fire"* expands due to mixing of hydrogen and air, combustion mostly dominated by momentum forces. After 1 s, the influence of buoyancy forces increases and causing an eventual lift off at 1.5 s. The fireball growth process is observed similar for *"small fire"* simulation, but with an enhanced mixing process and deformities at the contact surface. With the presence of *"big fire"*, a vertically elongated fireball shape is early observed (see at 0.5 m), and a shorter duration required for hydrogen mass to be consumed and buoyancy effects to manifest and ensure fireball lift-off.

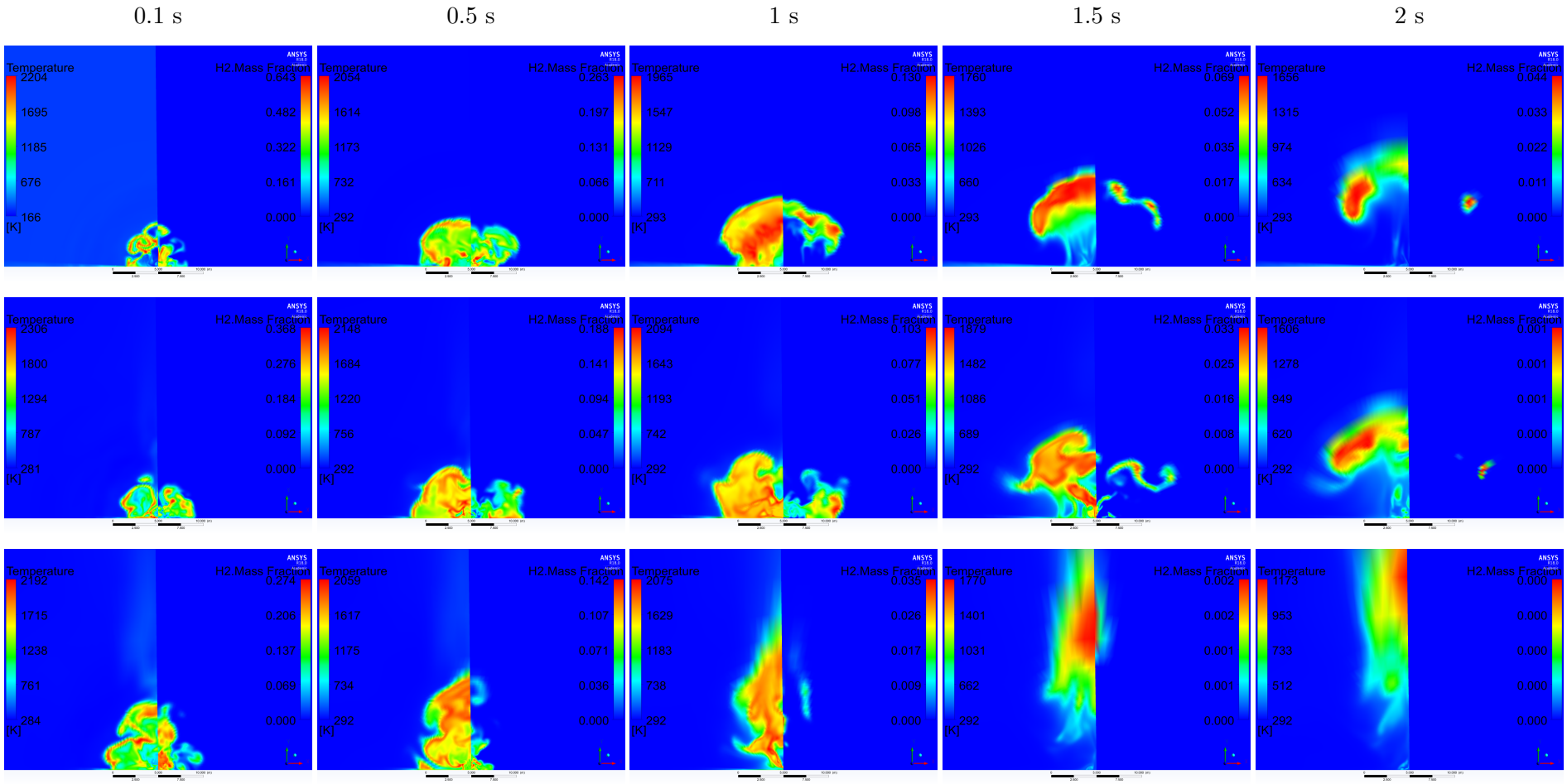

Figure 5.11: The development of fireball temperature (left half) and mass fraction H_2 (right half) for *"no fire"* (top row), *"small fire"* (middle row) and *"big fire"* (bottom row).

The time it takes for the released hydrogen (4.08 kg) to burn is shown in Figure 5.12, 3 s for *"no fire"* simulation and 2.4 s for *"small fire"* simulation. Using 1.8 s for all hydrogen to be consumed in *"big fire"* simulation, it is almost twice faster than without fire present. This is quite significant with regards to thermal hazard distances discussed hereafter. It is be noted, that the thermal radiation from the fire itself as it may equally cause harm and injury to humans (especially for 21 MW fire) are not investigated in this study, only focusing on its effect on fireball of tank rupture.

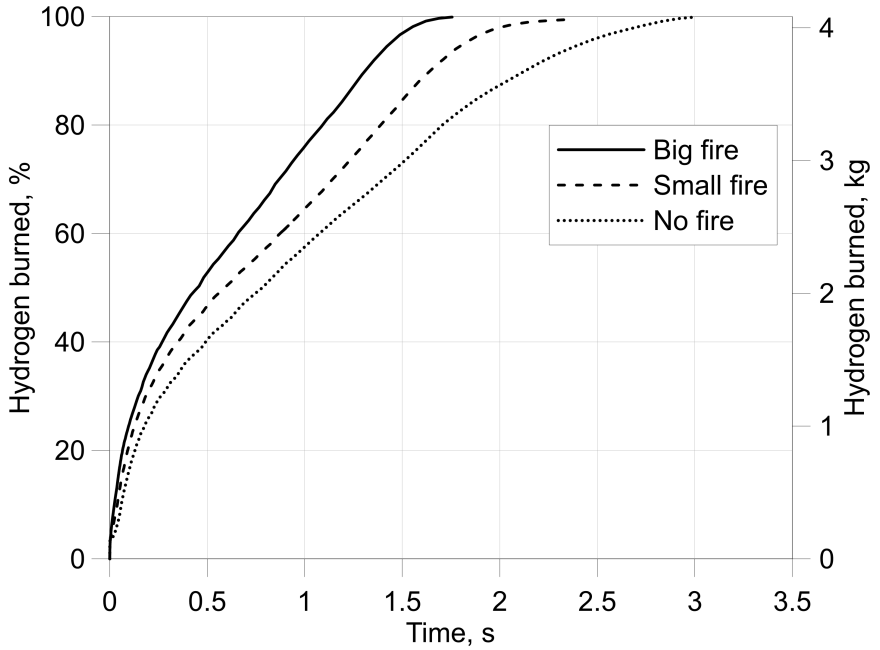

Figure 5.12: Amount of hydrogen burned as a function of time for all three conditions prior to rupture until all hydrogen is consumed.

5.5.1 Thermal hazards of fireball

The incident radiation (heat flux) received at 5 m, 10 m and 15 m away from the rupture point during the lifetime of the fireball (up to 2 s) are depicted in Figure 5.13. Effects of thermal radiation on personnel for the given radiation intensity are shown by the horizontal lines, a value of 1.6 kW/m^2 causing no discomfort for long exposure, and 37 kW/m^2 causing a 1% lethality in 10 s (Wang et al., 2017). The heat received at these points reduces drastically due to a rapid cooling process and lifting of the fireball above the ground, depending on the initial condition including fire. However, for simulation with *"no fire"* due to its long life cycle even at 15 m may still cause injury to humans albeit below the fatality threshold. Contrarily for simulations with *"big fire"* and *"small fire"*, 15 m is considered a safe distance. For the case of *"small fire"*, the distance of 10 m emit an incident radiation of 8 kW/m^2, subject to first-degree burns depending on the exposure time.

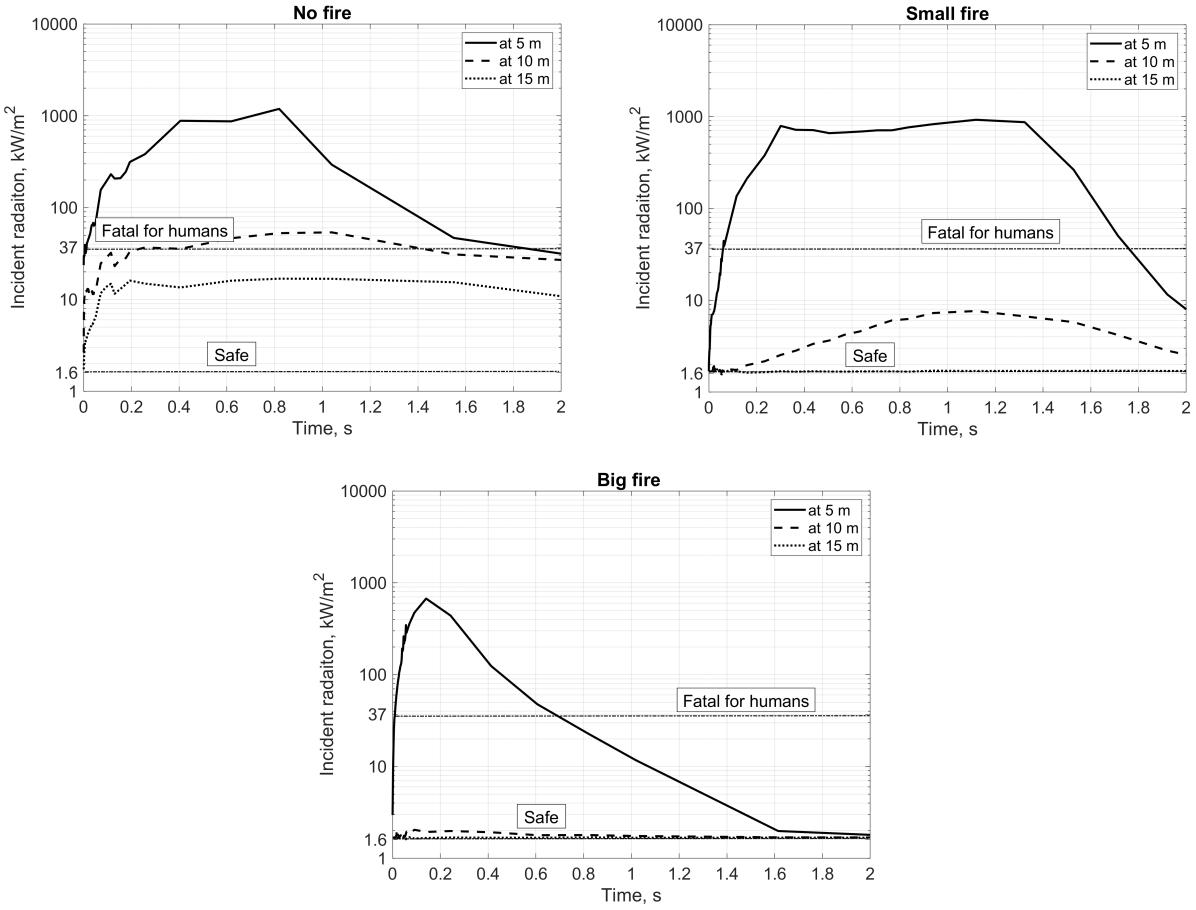

Figure 5.13: Radiation emitted for *"no fire"*, *"small fire"* and *"big fire"* rupture simulation, including harm effects of fatality and safe values found in (Wang et al., 2017).

The hazards from a high-intensity fireball are best ascertained using the thermal dose, as it also depends on the exposure time. Once a fireball has emerged, it is the thermal radiation energy that may cause the most injury. The most convenient way of analysing potential harm is by a function of both the thermal radiation and exposure duration as (LaChance et al., 2009):

$$T_d = I^{4/3} \cdot t, \tag{5.1}$$

where T_d is the thermal dose, I is the radiative heat flux, and t is the exposure time. Different levels of burns occur from the resulting thermal dose: first-degree, 100 $(\mathrm{kW/m^2})^{4/3}$ s, second-degree, 290 $(\mathrm{kW/m^2})^{4/3}$ s, and third-degree, 1000 $(\mathrm{kW/m^2})^{4/3}$ s, burn. Seen in Figure 5.14, the thermal doses compared show similar trends for *"big fire"* and *"small fire"*. In perpendicular direction, the thermal dose falls below the first-degree threshold after around 8 m. For the case of *"no fire"* however, this distance is extended to 16 m, doubling the distance. In axial direction, *"no fire"* falls below the first-degree threshold after 14 m. A

bigger difference is seen for simulation with *"big fire"* and *"small fire"*, the former reaching below first degree threshold after 6 m, followed by *"small fire"* case close to 10 m.

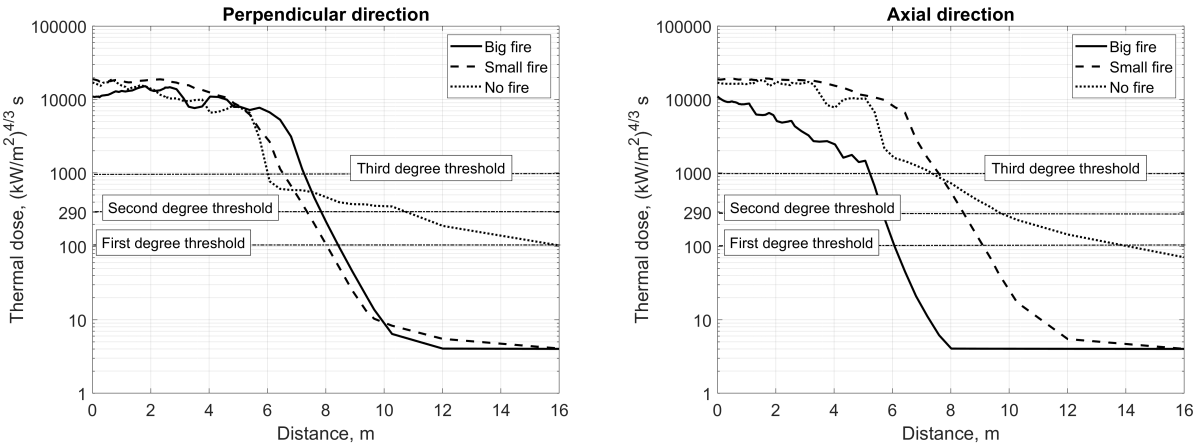

Figure 5.14: Thermal dose for *"big fire"*, *"small fire"* and *"no fire"* rupture simulation, in perpendicular (left) and axial direction (right), including the average threshold for burns.

5.6 Concluding remarks

In this study, CFD simulations were used to analyse the isolated effect of fire size and HRR on a stand-alone tank rupture. The details of propane fire surrounding tank prior to rupture contained two areas, 2 m^2 and 21 m^2, of a HRR of 2 MW and 21 MW respectively. Both fires encapsulated the tank prior to rupture, pockets of oxygen concentrations present within the disparate flames. During the initial stages after rupture, between 0.2–5 ms, the effect of presence fire caused higher velocity, a more pronounced fireball development and enhanced hydrogen mass diffusion. In the near field (up to 2 m), the presence of fire depending on its area led to a reduced blast wave overpressure, up to 80% – a direct result of the limited oxygen available reducing the chemical energy contributing the generated pressure. In the far field outside of the respective fire zone areas, the differences in pressure were quickly reduced. The presence of fire also influenced the fireball duration as the released hydrogen was consumed twice as fast with fire present prior to rupture. In turn, this led to a decreased hazardous thermal dose effects. These gathered results shed light on the effect of fire surrounding the tank prior to rupture not previously accounted for, to be considered when creating consequence analysis and harmful criteria within hydrogen applications.

Chapter 6

Blast wave of tank rupture in an experimental tunnel

One of the first attempts to identify and investigate hazards associated with hydrogen vehicles in road tunnels was undertaken in the project HyTunnel, as part of the European Network of Excellence on Hydrogen Safety (Kumar et al., 2009). Included in the project, a programme of experiments and complementary CFD modelling activities were to be performed for selected scenarios, to examine current practise and previously conducted research. Among experiments to be conducted includes a Type IV tank (70 MPa, 36 L) rupture in a tubular steel *"explosive"* tunnel. The steel experimental tunnel construction is of a total length of 70 m and an internal diameter of 3.7 m. Inside the tunnel, a solid concrete surface acts as the tunnel floor set as a chord 0.5 m above the bottom of the tube. A photo of the experimental tunnel, and a sketch including its internal dimensions are presented in Figure 6.1. The tunnel is designed to withstand around 3 MPa of pressure resulting from a blast wave within the tunnel (D4.1 HyTunnel-CS, 2019). With an induced rupture of a 70 MPa pressurised tank, it raises the question concerning the maximum exerted pressure on the structure of the tunnel. The starting shock pressure of a tank rupture can be found using a one-dimensional gas dynamic equations, see Equation (3.20–3.23). This is calculated to be 9.8 MPa, based on the initial stored parameters of the tank determined. This reveals little about the exerted pressure on the internal tunnel structure because of the fast decrease of the starting shock pressure due to its three-dimensional expansion. Furthermore, the blast wave pressure generated from a cylinder tank may be different depending on its orientation within the tunnel prior to rupture. A more pronounced decay will occur perpendicular to the tank ends, compared to a more two-dimensional decay along the tank axis. Therefore, numerical simulations are performed in this pre-test study to investigate the blast wave of a high-pressure tank rupture exerted on a tunnel structure, with regards to its orientation prior to rupture.

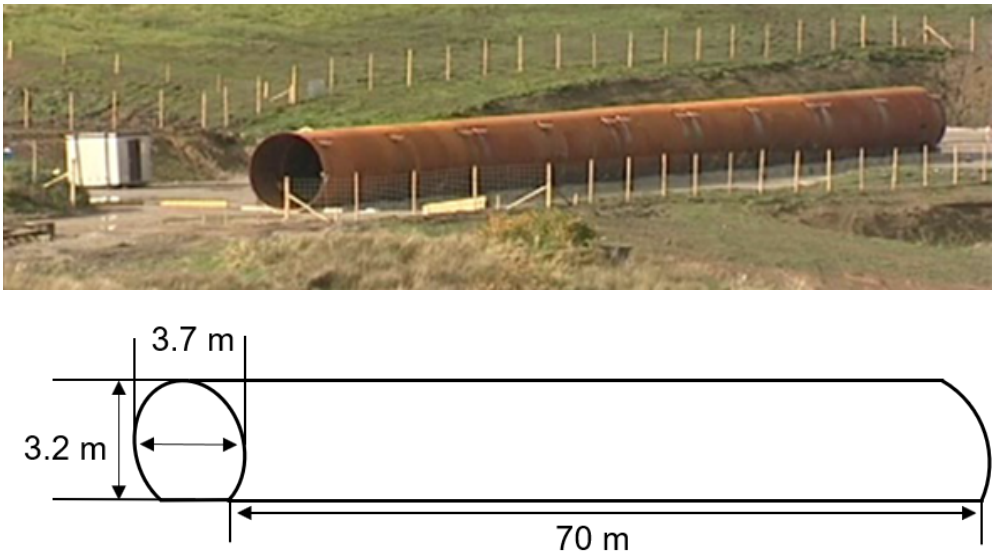

Figure 6.1: Photo of experimental tunnel (top), and a simple sketch of the tunnel internal dimensions (bottom).

6.1 Numerical details of tank rupture in experimental tunnel

The CFD model used for simulating blast wave of a stand-alone tank rupture is developed and described in Chapter 3, including the governing equation for LES, Equations (3.1–3.3), solved using an implicit pressure-based solver. Solving the combustion and turbulence-chemistry interactions was based on the EDC model, details given in Section 3.1.2. Using ideal gas, the chemical source term was calculated using the Arrhenius reaction rate for the global one-step chemistry reactions. The use of a radiation model was omitted due to its little influence observed on the generated blast wave overpressure (see Section 4.2.3), which in turn promotes a faster computational time. This developed model was validated against experimental values of the blast wave and fireball in Chapter 4 in an open atmosphere. The computational domain created consisted of a tunnel with a diameter of 3.7 m and a length of 70 m. Within the tunnel, the tank was placed 20 m from the nearest exit, 50 m from the farthest exit. This was to ensure a symmetric initial propagation of blast wave on both sides before first reaching the nearest 20 m tunnel exit. The tank was placed 0.15 m from the ground as a stand-alone vessel. The structural boundary of the tunnel was treated as rigid, as the experimental tunnel structure was not expected to deform during experiments. The domain boundary dimensions at both exits were designed to allow a sufficient space outside the tunnel to limit any boundaries effects and approach realistic conditions. The calculation domain extended 35 m beyond tunnel ends in both directions to include free space and had the same cross-section as the tunnel, though 3 times larger (i.e. 11 m). The computational domain developed is illustrated in Figure 6.2.

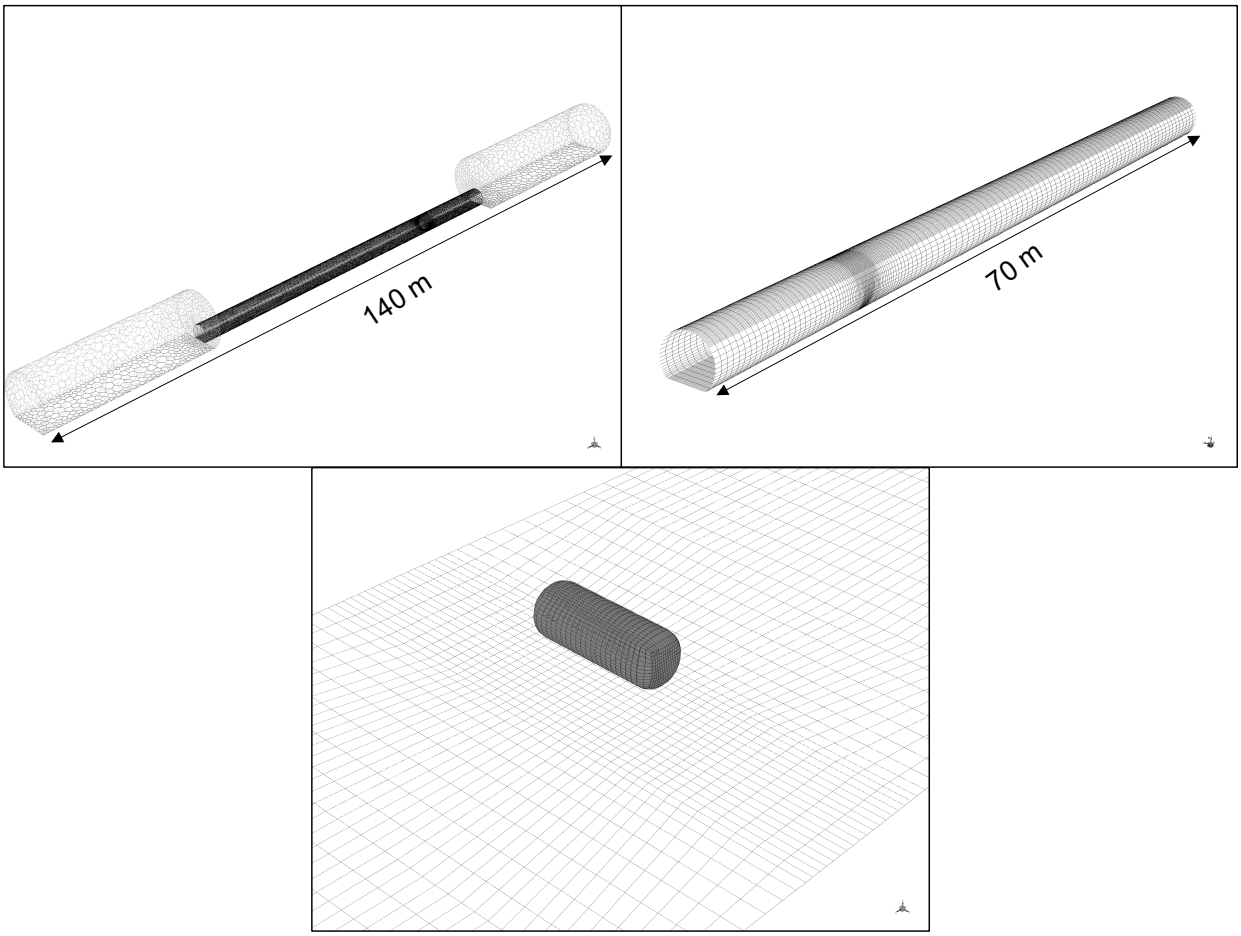

Figure 6.2: General view of calculation domain (upper left), tunnel section of the domain (upper right) and enlargement of hydrogen tank (bottom), all shown with surface mesh.

The tunnel domain was set with different degrees of hexahedral mesh resolutions to cater to various stages of blast wave propagation. CVs near the tank (up to 2 m) contained the most refined mesh, ranging between 0.03–0.05 m. The wall boundary immediately adjacent to the tank was meshed with CV lengths of 0.06 m to cater to the initial blast wave reflections. From the rupture point towards the far end of the tunnel, the mesh length was bi-geometrically increased from rupture point up until a maximum of 0.8 m in length at the farthest exit of 50 m. The boundary zone outside the tunnel was initially meshed using tetrahedral shaped CVs and varied in size from 0.2 m close the tunnel exit and up to 1 m at the boundary wall. One of the advantages using ANSYS Fluent is the ability to convert mesh, with one option being combining tetrahedral cells into polyhedral ones and executed for the boundary zone across all three tunnels. In this case, the size of CVs was reduced by up to 30 percent. Both exits of the tunnel were interfaced with the outside domain, matching the hexahedral mesh from inside the tunnel with the polyhedral mesh from the outside. The total mesh size produced was 326k, including the free areas outside of tunnel geometry.

With the introduction of confinement effects within a tunnel, a mesh sensitivity test was performed to remain thorough. The original (coarse) mesh of inside the tunnel was increased by a factor of 1.5×1.5×1.5 for all (three-dimensional) cell directions, and the total number of CVs increased to a size of 770k, denoted as fine mesh. Accordingly, the mesh in the near vicinity of the tank was reduced to around 0.01–0.02 m. The initial blast wave overpressure in the tunnel for both meshes are presented in Figure 6.3. Compared at 1 ms, a similar blast wave profile is observed, albeit with a 10% increased peak blast overpressure for the coarse mesh. The knowledge of the minimum requirement of computational cells required to accurately resolve a flame front is 4–5 CVs. Therefore, an increased cell size consequently increases the contact surface leading to an increased amount of energy from combustion contributing to the blast wave during initial stages. This overprediction in peak overpressure diminishes with time, and at 5 ms and 15 ms, both meshes converge in both peak overpressure and general blast wave profile. As the difference in meshes is not sustained, the coarse mesh is maintained for the calculations.

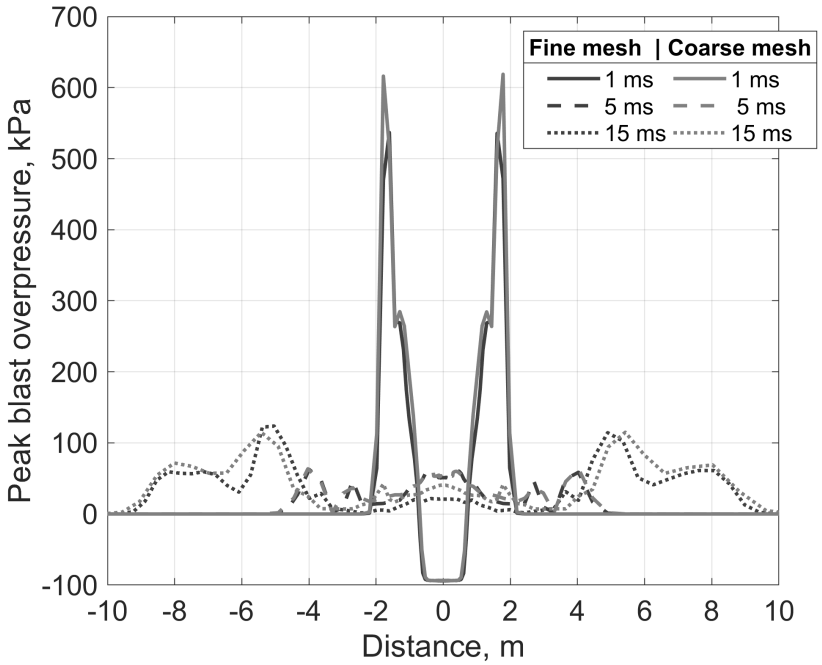

Figure 6.3: Mesh sensitivity test conducted for initial blast wave propagation in tunnel for denoted fine and coarse mesh with ruptured tank located at 0 m.

Initial conditions of the tank pressure and temperature prior to rupture were extracted from a failure criterion of an identical cylinder tank in a fire (Kashkarov et al., 2017). In the study, the rupture pressure and temperature were found to be 74.4 MPa and 327.5 K respectively, from initial conditions of 70 MPa and 300 K. The tank volume was 36 L, with internal dimensions of 26.2 cm and a length of 66.8 cm. Scaled to equate the same mass of 1.4 kg of hydrogen using ideal gas in simulations, the volume of the tank was reduced by 29% to 25.3 L. This corresponded in the diameter being reduced to 23 cm in diameter and a

length of 49 cm. Initial conditions of the remaining domain inside the tunnel were set for atmospheric conditions: 101325 Pa and 300 K. To initiate the tank rupturing, the *"walls"* of the tank were instantaneously removed. The tunnel walls were set to be impermeable with non-slip condition, the thermal boundary condition modelled as a thermally thick steel wall with a density of 8030 kg/m^3, and a specific heat of 502 J/(kg K). The floor boundary was set to model a thermally thick concrete wall concrete with a density of 1600 kg/m^3, and a specific heat of 800 J/(kg K). A CFL number of 0.1 was set, found as the converging value in the model validation study for cylinder tank rupture simulations, concluded in Chapter 3.

6.2 Confinements effects on blast wave propagation

Presented in Figure 6.4 are two cases of blast wave simulations, one in an open atmosphere and the other in the experimental tunnel for the same tank parameters (36 L, 74 MPa). Both simulations are shown with the same adaptive blast wave pressure range. The computational domain in the open atmosphere corresponds to that developed in Chapter 3. Once the blast wave is released and reflects off the floor (at 2 ms), the blast wave characteristics are observed comparable for both cases of rupture. For instance, a hemispherical expansion of the blast wave is observed for both simulation, confinement effects seemingly absent. Also, they both display a similar blast wave overpressure values, with a maximum of 708 kPa. At 5 ms, the blast wave within the tunnel reaches its internal walls (seen only vertically) and reflects, the blast wave strength amplifying rather than attenuating three-dimensionally as in the open atmosphere. The maximum pressure is located at the tunnel wall, due to the formation of a Mach stem. This is a consequence of the inability of the reflected shock to redirect (or detach) completely back to its original direction. Following at 10 ms and 20 ms, the flow field behind the primary blast wave in the tunnel mainly consists of complex interactions resulting from the secondary and tertiary reflected waves. Due to the high intensity of the reflected blast wave within the tunnel, the same interactions present in the open atmosphere (e.g. Mach stem formation and reflected blast waves) are seen much less prominent in comparison.

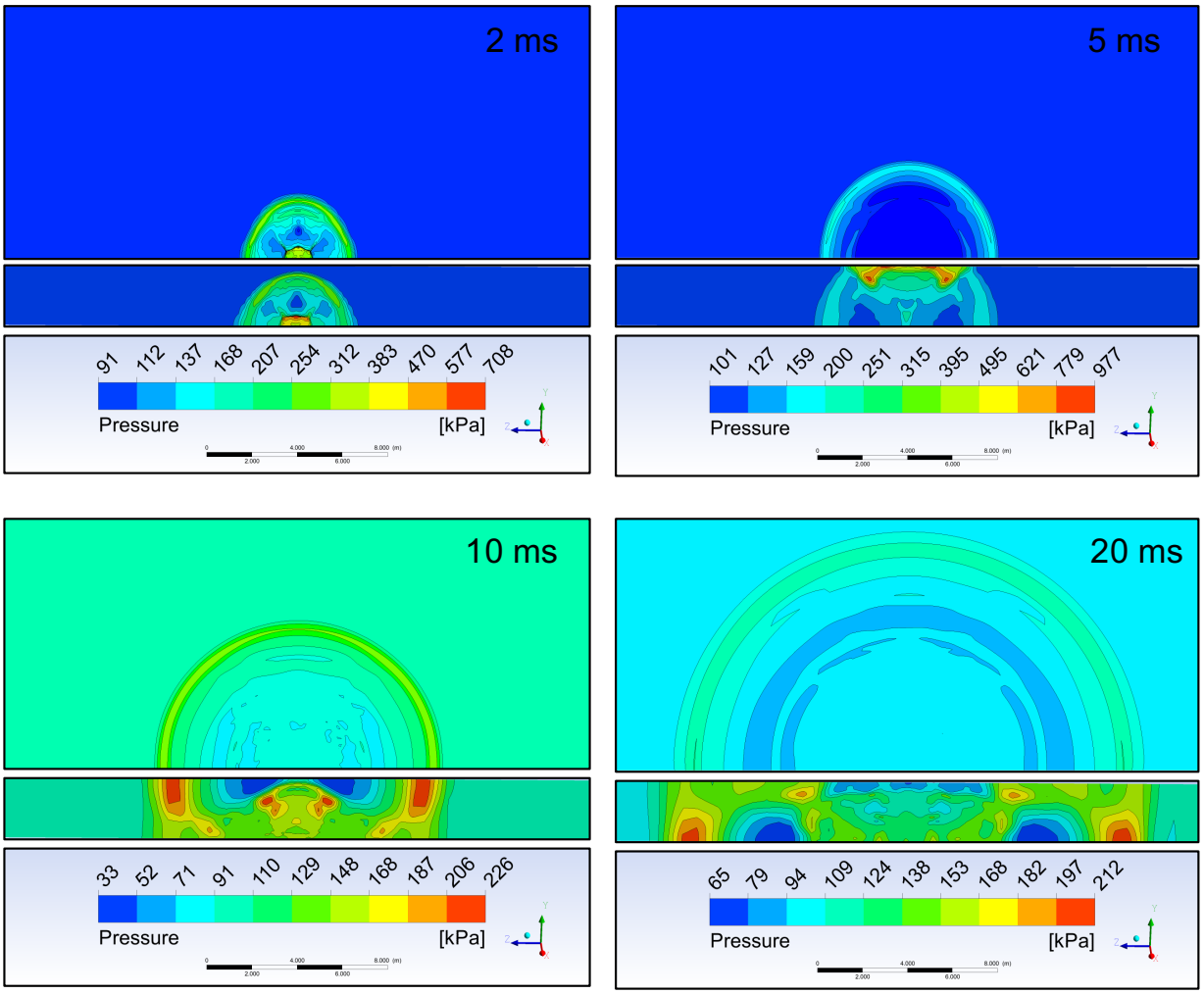

Figure 6.4: Comparison of blast wave propagation in open space and in experimental tunnel for various times. Length of the bottom ruler is 8 m.

Shown in Figure 6.5 is the measured decay of blast wave overpressure in the open atmosphere and the effect of tunnel confinement. Before the blast wave reaches the tunnel walls (see the zoomed-in portion of Figure 6.5), it displays a starting shock overpressure of around 5 MPa and subsequently decays to 100 kPa within a distance of 4 m. This closely resembles the behaviour of the blast wave propagation in open atmosphere. However, the tunnel confinement effects of the cross-section area (diameter of 3.7 m) constrict the blast wave to a significantly lower one-dimensional decay rate as a function of tunnel distance. From 5 m to 40 m, the peak overpressure decays by only 50 kPa. In open atmosphere, the blast wave continuously decays rapidly as the released energy expands three-dimensionally. The difference between blast wave overpressure decay patterns increases as a function of distance in orders of magnitude: in open atmosphere 0.4 kPa compared to 50 kPa within the tunnel after 40 m.

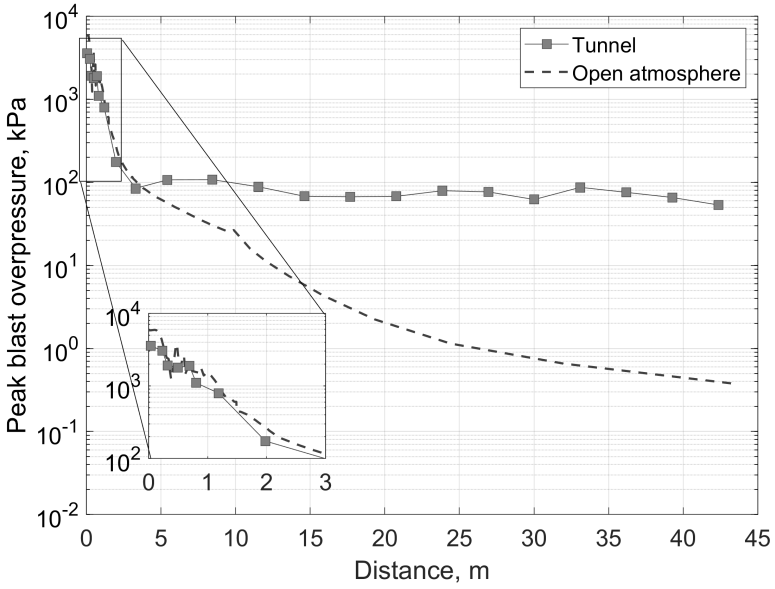

Figure 6.5: Peak blast wave propagation after a hydrogen tank (25 L, 74 MPa) rupture in open atmosphere versus within the experimental tunnel.

6.3 Effect of tank rupture orientation in tunnel

In Figure 6.6, the cross-section view of the blast wave propagation at the tank epicentre is displayed for two tank orientations: perpendicular and axial along the tunnel axis direction. Initially for both cases, as the rupture simulations are initiated (< 0.1 ms), the released pressure develops according to the cylindrical shape of the tank. As both tanks are equally placed 30 cm above the ground, the blast wave seemly reaches the floor simultaneously after 0.1 ms. The maximum recorded pressure of 21270 kPa bounces off the concrete set floor for both cases. At 1 ms for the tank in perpendicular orientation prior to rupture, the blast wave has reached the tunnel wall with a maximum pressure of around 1400 kPa. This is 18% lower than the 1700 kPa maximum pressure on tunnel wall for tank in axial orientation. As the blast waves start to spread along the tunnel axis at 20 ms in both cases (not shown), the second waves reflected off the walls are observed with an overpressure of close to 1000 kPa. Captured at 30 ms, a slightly higher maximum pressure is again observed for the axially positioned tank in the tunnel, the effect of tank orientation seemly not yet entirely diminished.

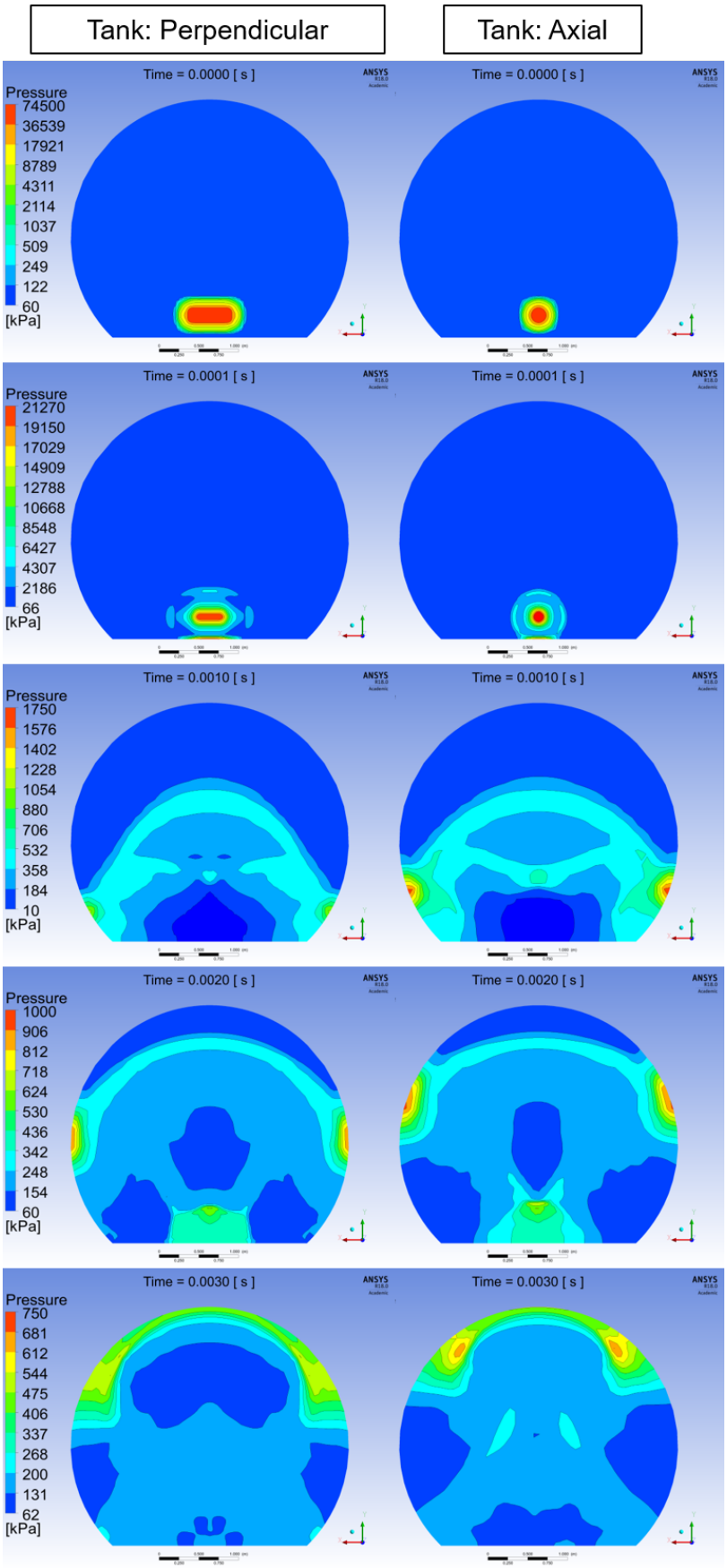

Figure 6.6: Pressure distribution in tunnel cross-section at rupture location during tank rupture set perpendicularly (left column) and axially (right column) to the tunnel axis. The length of the bottom ruler is 1 m.

The maximum overpressure exerted on the tunnel walls and floors during the initial release of the blast wave as a function of distance is presented in Figure 6.7. The overpressure recorded are irrespective of the blast wave contact point location of the wall or floor, and encapsulates both initial starting shock wave and reflected blast wave overpressures. For tank set in axial orientation, the maximum overpressure exerted on the tunnel wall of 4 MPa is measured, twice the value compared to the 2 MPa observed when the tank is oriented in perpendicular direction. This ascertains the significant directional effects of a cylindrically shaped tank, resulting in different exerted blast wave strengths on nearby structures. The blast wave overpressure below the tunnel structural strength threshold of 3 MPa is only attained for the case of tank oriented perpendicular to the tunnel axis tank orientation. Due to the same location of the tank above the ground (0.3 m), a similar exerted pressure to the floor is 20 MPa for both tank orientations. The tunnel floor surface overpressure quickly decreases with distance, falling under 0.2 MPa after 5 m. From 10 m onwards, the peak blast wave overpressure exerted on the tunnel floor and walls are nearly conformed for both tank orientations, blast wave reflections seen to have diminished accordingly.

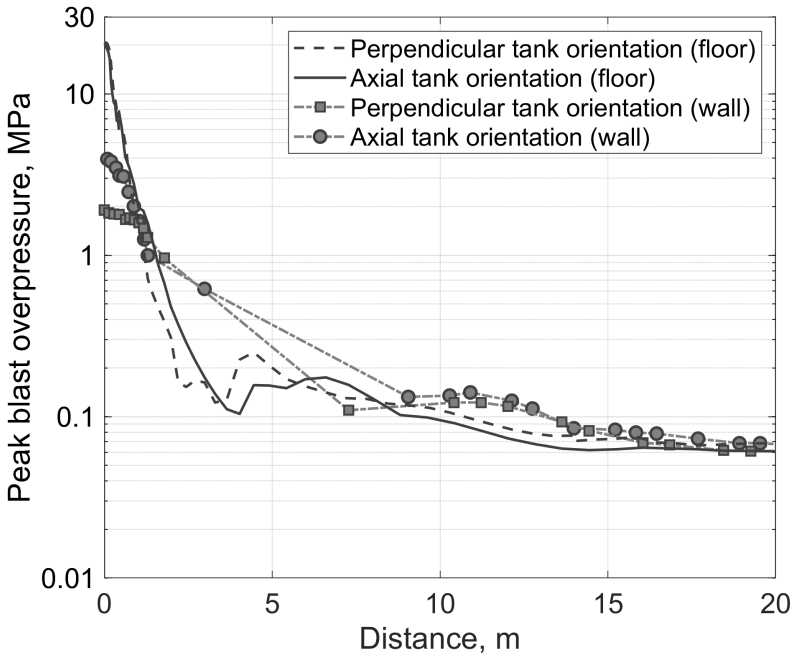

Figure 6.7: Peak blast wave overpressure exerted on tunnel floor and walls for tanks (74 MPa, 36 L) orientation set in axial and perpendicular direction to the tunnel axis.

Shown in Figure 6.8 is the blast wave propagation featured on the tunnel wall for tanks in perpendicular (left column) and axial (right column) orientation. The effect of tank orientation is most pronounced near the rupture epicentre. For the tank in axial orientation at 5 ms, the maximum of 1028 kPa is observed, over twice the value compared to 413 kPa for the tank in perpendicular orientation. After 20 ms, the maximum pressure exerted onto the wall are quite similar, with an only 3% difference i.e. 228 kPa versus 221 kPa. This

trend continues at 50 ms and 100 ms, a maximum of 2% difference in the maximum pressure measured irrespective of tank initial orientation. Although the flow field behind the leading shock is complex, the leading shocks themselves arrive at the tunnel exit at the similar time soon after 0.1 s. Seemly, the effect of tank orientation prior to rupture diminishes after approximately two tunnel diameters away from the tunnel rupture. With the energy of both tanks mostly conserved within the tunnel, the propagation of blast wave and its attenuation of irrespective of orientation is considered identical between the two cases. Not accounting for any deformation of the tunnel structure, it uncovers minor long term effects towards the generated blast wave based on the tank orientation prior to rupture.

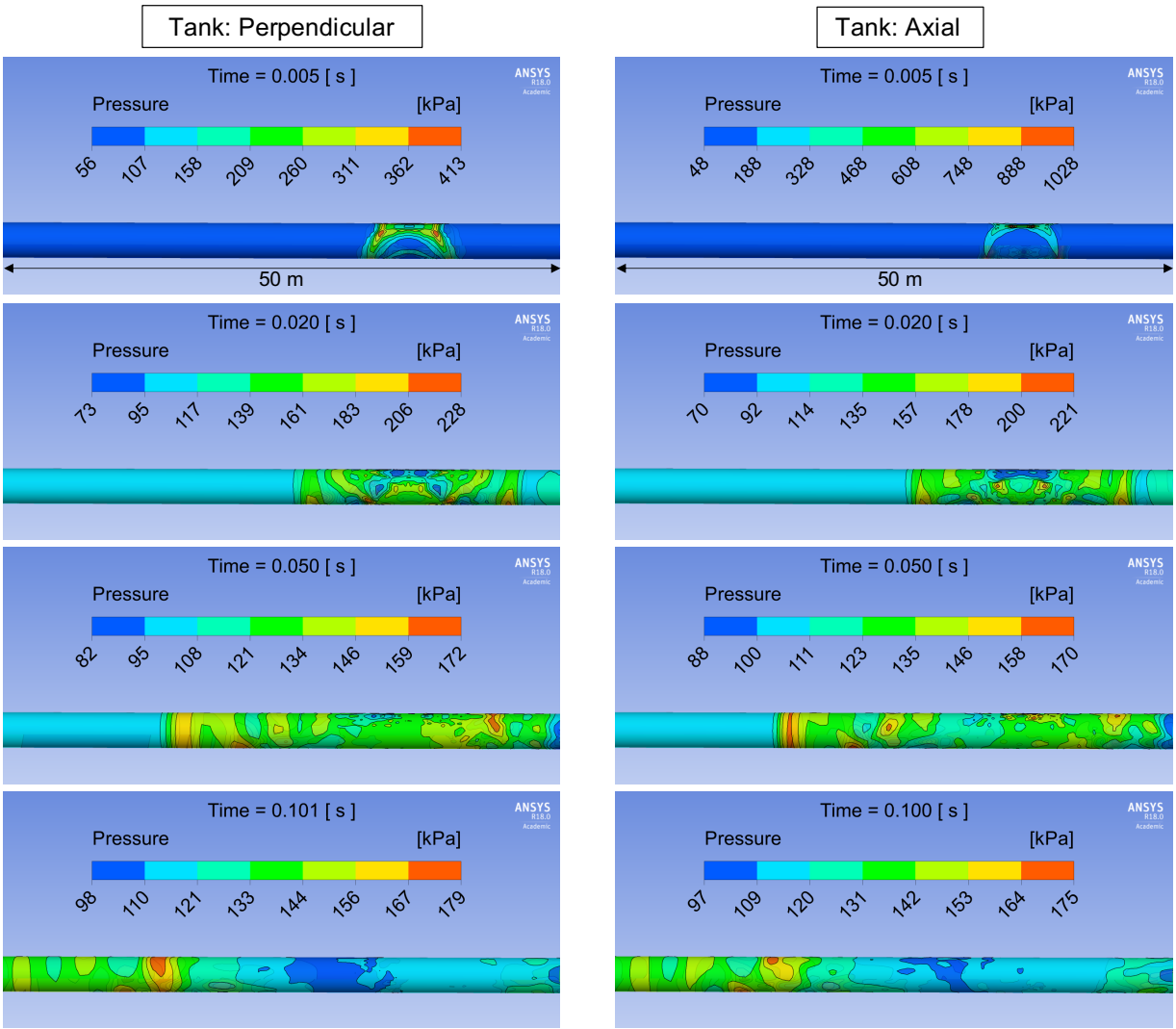

Figure 6.8: Blast wave overpressure exerted on tunnel walls for tanks (74 MPa, 36 L) orientation set in axial and perpendicular direction to the tunnel axis.

6.4 Concluding remarks

The originality of this work is in the direct comparison of a blast wave of a tank rupture (36 L, 74 MPa) between in an open atmosphere and a tunnel, with regards to its confinement effects. The maximum blast wave overpressure differs significantly between the two cases, e.g. peak overpressure compared at 40 m distance from the ruptured tank location was found to be 0.4 and 50 kPa in an open atmosphere and a tunnel respectively. It ascertains the vastly different patterns of blast wave decay depending on the presence of tunnel confinement: a more three-dimensional decay in an open atmosphere compared to a more one-dimensional decay pattern found within the tunnel. The rigour of this research is in the numerical simulations performed using a developed CFD model, which has been validated against experimental data. The created computational domain, including tank and tunnel, was carefully reconstructed to that of the planned experiment, with accurate boundary conditions and a reasonable time-step scheme. Furthermore, a mesh sensitivity test was conducted to ensure accuracy in capturing the starting shock and blast wave dynamics. The significance of this study has been to explore the exerted blast loading on an experimental tunnel, based on the orientation of the cylindrical tank vessel. The orientation of the tank set in axial direction along the tunnel axis direction resulted in a pressure of 4 MPa exerted on the tunnel wall structure, 1 MPa above the designed tunnel strength limit of 3 MPa. Contrarily, when the tank was set in perpendicular orientation, the maximum exerted on the tunnel wall in the near field was measured to be 2 MPa. Despite differences seen in the near-field pressure wave propagation, its propagation and decay further away were very similar irrespective of the tank orientation.

Chapter 7

Simulated tank ruptures in tunnels and prediction of blast wave decay

Limited experimental and numerical studies have been performed to understand the phenomena and develop engineering tools for blast wave propagation in tunnels. Using explosive charges of various types, the quantity is often equated by the mass of TNT. Fitted laws for free-field decays where the blast propagates freely in all directions are proposed by several authors in the open literature such as in (Brode, 1959; Henrych, 1979; Uystepruyst and Monnoyer, 2015), using the Hopkinson-scaled distance $Z = r/W^{1/3}$, where r is the distance from the point source and W is the quantity of the explosive. Free-field decay laws are used in prediction of blast wave decay in tunnel, including confinements effects in the modified scaled distance. In this study, instead of using an explosive mass such as TNT, determining the equivalence from a stored hydrogen mass is not straightforward. Generally, the equivalent TNT mass would be calculated based on the energy of explosion generated from the gas in question as (Crowl, 2010):

$$W = \frac{\eta \cdot m \cdot E_C}{E_{TNT}}, \tag{7.1}$$

where η is an empirical explosion efficiency, m the mass of flammable material, E_C the heat of combustion of flammable material, and E_{TNT} the heat of combustion of TNT. E_{TNT} is arbitrarily standardized as 4200 kJ/kg, is often subject to other revised values. In one case for hydrogen, E_{TNT} was found equal to 4686 kJ/kg, and E_C equal to 14584.8 kJ/kg (Lopes, 2011). The lower heat of combustion of 1 g of hydrogen is equal to 119.89 kJ (Molkov, 2012). Thus, the TNT equivalent of hydrogen is as high as 28.65, i.e. 28.65 g of TNT is an energetic equivalent to 1 g of hydrogen. Factors adjusting the explosion efficiency, η, such as adequate mixing of the combustible material with air and thermal to mechanical energy conversion efficiency varies across various sources. For instance, it was determined as 4% by Mannan (2005), whereby other reported estimations range between 1–10% (Crowl, 2010). This range outputs vast differences in obtained TNT mass equivalence for hydrogen gas quantities. The

energy of rupture expressed in terms of equivalent TNT mass is a methodology not optimal and often considered obsolete (AMEC, 2014).

Another approach available for blast wave decay calculation is built on energy, E, in a tank. It veers away from TNT-equivalence and considers atmospheric pressure to present a dimensionless distance parameter. It is based on high explosives blast curves utilizing the common Sachs-scaling approach defining an energy-scaled distance cited in (Baker et al., 1983):

$$\overline{Z} = r\left(\frac{P_s}{E}\right)^{1/3}. \tag{7.2}$$

Baker et al. (1975) proposed both a near field and far-field pressure versus distance relationship based on results of numeric calculations of bursts of tanks containing perfect gasses. The effects of the containing vessel and its fragments were disregarded, with all of the energy within the gas vessel put into the flow field. This methodology is seen successfully used in predicting blast wave overpressure of hydrogen in open atmosphere (Center for Chemical Process Safety, 2010). The modified Sachs-scaling approach accounting not only for mechanical energy of compressed gas, but a fraction of released chemical energy was later developed and validated (Molkov and Kashkarov, 2015; Kashkarov et al., 2020). The model for prediction of blast wave decay after hydrogen tank rupture in a fire in the open atmosphere included both a stand-alone and under-vehicle tank rupture scenarios.

The Hopkinson and Sachs-scaled distance were utilised by Silvestrini et al. (2009) in predicting blast wave decay of explosives in a tunnel, after introducing a so-called energy concentration factor (ECF). The ECF was introduced as the ratio between the volume of the confined region and the volume of the explosion hemisphere. In other words, adapting a free-field decay law into one that considers geometry. The reduction of volume available for the gas to expand in a confined space is taken into account with this geometrical factor, as the spatial density is subsequently increased. For instance, in a configuration whereby a charge is placed at the centre of a tunnel, the ECF can be written as follows (Silvestrini et al., 2009):

$$ECF = \frac{V_{Hemisphere}}{V_T} = \frac{\frac{2}{3}\pi r^3}{2 \cdot rA_T} = \frac{1}{3}\frac{\pi r^2}{A_T}, \tag{7.3}$$

where A_T is the cross-section area of the tunnel. As a result, the Sachs-scaled distance can be altered with regards to the geometry to become:

$$\overline{Z}_{ECF} = r\left(\frac{P_s}{ECF \cdot E}\right)^{1/3}. \tag{7.4}$$

For peak overpressure arising from tank rupture or cloud explosions, the ECF model was seen to poorly reproduce the peak overpressure (Li, 2018). Tested for not only stored hydrogen, but also stored methane and CNG tank rupture in tunnel, the calculated overpressure

using the ECF method were mostly underpredicted. Details specifying if the Hopkinson or Sachs-scaling used was not disclosed, but nonetheless found inapplicable. Compared to high explosives, bursting vessel has lower initial overpressure with slower decay in terms of distance, with longer positive phase durations and larger negative phases and strong secondary shocks (Stoffen, 2005). Therefore, this methodology is deemed ill-fated for determination of blast wave decay in a tunnel generated by a high-pressure hydrogen tank rupture, imploring novel methods to be developed and validated. For a hydrogen tank rupture, it is clear that a blast wave strength depends not only on the amount of released energy but on the rate of the energy released. Validation experiments of full-scale tunnels are seen expensive and laborious and are not yet available. The use of CFD model eliminates these restrictions and allows the ability to simulate scenarios in a wide range of conditions. This chapter is based on a paper published in the International Journal of Hydrogen Energy (Molkov and Dery, 2020).

7.1 Numerical experiments

The CFD model used for simulating blast wave of a stand-alone tank rupture is developed and described in Chapter 3, including the governing equation for LES, Equations (3.1–3.3), solved using an implicit pressure-based solver. Solving the combustion and turbulence-chemistry interactions was based on the EDC model, details given in Section 3.1.2. Using ideal gas, the chemical source term was calculated using the Arrhenius reaction rate for the global one-step chemistry reactions. The use of a radiation model was omitted due to its little influence observed on the generated blast wave overpressure (see Section 4.2.3), which in turn promotes a faster computational time. This developed model was validated against experimental values of the blast wave and fireball in Chapter 4. The simulated scenarios account for the experimentally measured pressure and temperature in stored hydrogen tanks before rupture, of industry standard tank Type IV (Tamura et al., 2006).

7.1.1 Tunnel geometry

Tunnels are constructed in a wide range of physical and operational circumstances that will determine the type of tunnel used, specified for the appropriate traffic. The cross-section of a tunnel is determined mainly by three factors. First is the required clearance gauge of the lanes where the vehicles will circulate, depending on the planned traffic flow. Secondly, equipment such as ventilation, various safety technology and lighting must be considered (Anagnostou and Ehrbar, 2013). The standard minimum solution for cross-section areas in road tunnel following the guidelines for the equipment and operation was found. For box profile tunnels without requirements accommodating passage for an eventual broken-down vehicle, the minimum width and height of the road necessary is found least conservative (with regards to excess space) in Germany. According to its tunnel construction manual, the width and height are 3.5 m and 4.5 m respectively (Maidl et al., 2014). To compare, the UK tunnel standard the minimum the width and height are 3.65 m and 5.3 m respectively (The Highway Agency et al., 1999).

In this study, a lane of a minimum width of 3.5 m was considered to treat the worst-case scenario; the blast wave would expand and dissipate less following the close-in effects of the tunnel walls. Following the lane width, a standard 1 m is extended on each side referring to the area outside the marked driving lane, totalling a single lane width of 5.5 m. For the second tunnel geometry, as road traffic is mostly constructed using two lanes and in some countries (e.g. Germany) constitute up until 90% of all rural roads, two lanes was chosen (Brilon and Weiser, 2006). This was actualized by extending the single-lane tunnel by another lane of width 3.5 m, totalling the width to 9 m. The height was kept the same at 4.5 m. A third and final tunnel geometry was chosen as part of the parametric study, to accommodate the road tunnel with the largest cross-section area currently constructed. This was found as the Yerba Buena tunnel, part of the San Francisco–Oakland Bay Bridge. This tunnel features a double-decked design, each with five lanes, the larger upper deck with the bigger cross-section area of 140 m^2 (Vickers, 2017). In extending the number of lanes to five (i.e. 19.5 m), the height was also correspondingly increased to meet the required cross-section area. The calculated height was 7.2 m. The tunnels geometry is similar to that used in (Shentsov et al., 2019). All chosen tunnel cross-sections are included in Table 7.1.

Table 7.1: Tunnel dimensions.

Tunnel	Height, m	Width, m	Length from tank to tunnel exit, m	Hydraulic diameter, m	Cross-section area, m^2	Aspect ratio
Single-lane, 1L	4.5	5.5	150	4.95	24.1	1.3
Double-lane, 2L		9	150, 1500	6	39.5	2
Five-lane, 5L	7.2	15.5	150	10.5	139.1	2.7

7.1.2 Computational domain

A rectangular prism with sizes L×H×W = 300×100×75 m being 2250000 m^3 acted as the computational domain to place a 200 m long tunnel into, limiting the boundary conditions altering any pressure dynamics in and around the tunnel. Initially thought of as box profiles, chamfered edges were eventually inferred at the tunnel top corners reducing the generation of pressure spikes at the corner edges. Each tunnel employed was placed on the midpoint of the outer boundary domain. For the tunnels extended to a length of 1550 m, the outer domain was removed, and the tunnel exits set as non-reflective boundaries. The rupture location was set 50 m from the nearest exit. This was done to ensure a stabilized and undisturbed pressure propagation and stabilisation throughout the long end of the tunnel (i.e. 150 m and 1500 m) without influence from the nearest exit. The stored hydrogen vessel in the tunnel was geometrically rendered as a hemisphere, placed on the ground. This was to reduce the number of control volumes (CVs) otherwise required to properly resolve the tank rupture dynamics and reflection from tunnel ground. Observed in Chapter 6, the tank geometrical influence on the generated blast wave only occurs in the near vicinity of the rupture point. The tunnel dimensions were set according to the determined in Table 7.1, including the distance from tank to the farthest tunnel exit.

Following the geometrical domain set-up, it was then meshed accordingly. A hexahedral

type mesh was used to ensure an accurate approximation of the initial high gradient pressure and velocity values. The mesh size was set between 0.02–0.03 m in the near vicinity of the hydrogen surface. This refined area around each respective tank was kept unchanged across all three tunnels for consistency and stability. Using a bi-geometric meshing law, the mesh size would grow longitudinally ranging from 0.05 to 0.75 m uniformly along the tunnel length. Outside the tunnel zone was meshed with tetrahedral (later converted to polyhedral) shaped CVs and varied in size relative to its position away from the tunnel. This was carried out with a scale factor of 2 to a max CV size of 10 m. However, this would be dependent on the need of accuracy required in its position. For instance, CVs close to the tunnel entrance and exit would be smaller in size and was set to be 0.1 m, matching the internal tunnel mesh at the exits.

Figure 7.1 illustrates the entire domain surface mesh (left), the mesh containing sub-zones of the tunnel (middle) and tank grid (right). The quality of the mesh was measured and assured in ANSYS Fluent by the maximum orthogonal quality, aspect ratio and the minimum orthogonal skewness. The quality ranges from 0 to 1, where values close to 0 correspond to low quality in the case of the minimum orthogonal quality and reversed (i.e. 1 to 0) for the case of the maximum orthogonal skewness. A value of 0.4 and 0.7 was obtained respectively for each ran case, with a corresponding maximum aspect of 28.4. The recommended value for the aspect ratio, describing the ratio of maximum to minimum values of any distances of the cell centroid to face centroid or node (stretching) is not to exceed 40 – subject to flow characteristics and the location of particular cells with respect to the flow with relatively high velocity. The bottleneck for improved mesh arose from the coarseness of the large CVs at the boundary outside the tunnel, whereby the ambient conditions does not require a sophisticated mesh. Nonetheless, these quality values were all above the recommended quality threshold of values 0.1 and 0.9 for maximum orthogonal quality and maximum orthogonal skewness respectively (*ANSYS FLUENT 12.0 User's Guide*, 2009).

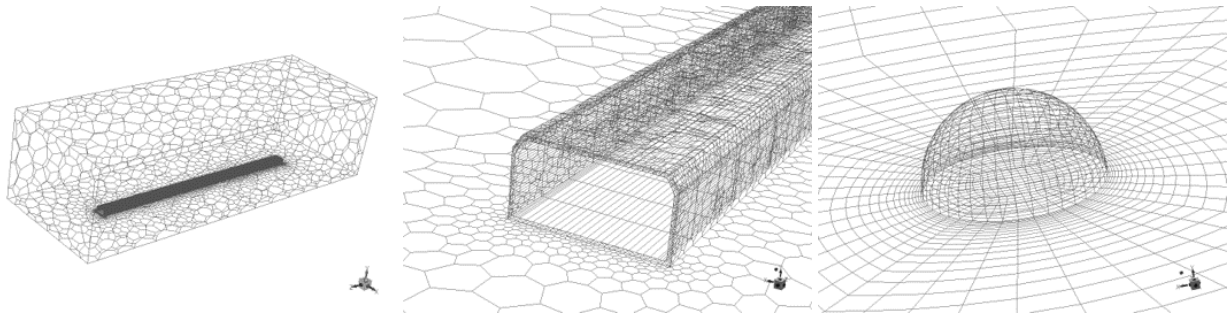

Figure 7.1: Surface mesh for the entire domain (left), tunnel (centre) and hydrogen hemispherical tank (right).

7.1.3 Initial conditions

Initial conditions of the domain were set with a pressure of 101325 Pa and temperature of 280 K as ambient conditions. The hydrogen tank was then set to contain H_2 only, with

a pressure of 94.5 MPa, and a temperature of 395 K, values extracted from conducted experiment (Tamura et al., 2006). The tank in experiment was engulfed in fire, leading to the increased rupture pressure and temperature. Therefore, to remain assertive, the near vicinity of the tank was patched to envisage an increased temperature and combustion products. The circumference of the patch around the tank had a width double the radius of each tank, and a diameter of the tank as the added height. The patch was set with a temperature of 900 K, and contained $Y_{H_2O} = 0.1$, and $Y_{N_2} = 0.9$. Replicating the tank rupturing in the simulations was modelled directly as an instantaneous release of the stored hydrogen. The properties of the different size of tanks simulated are listed in Table 7.2. They cover the tank sizes currently available for hydrogen-powered vehicles.

Table 7.2: Parameters of hydrogen tanks used in rupture simulation in all three different tunnels, for initial tank temperature of 395 K for all tanks).

Tank diameter, m	Simulated volume (ideal gas), L	Volume (real gas), L	H_2 mass, kg	Rupture pressure, MPa
0.25	10	15	0.6	95
0.45	30	43	1.7	
0.61	60	86	3.5	
0.77	120	176	6.9	
		160	5.2	70
		140	2.6	35

Outside the tunnel, the walls were set to being stationary, impermeable and with no-slip conditions. Thermal heat flux properties of the wall were set as concrete with a density of 2300 kg/m^3 and wall temperature equal to that of ambient conditions. Outside the tunnel, non-reflective properties were applied to ensure any parameter such as energy, mass, momentum did not influence the properties inside the tunnel in any way. The effect of omitting the effect of heat transfer from the tunnel walls was briefly investigated, found to cause insignificant effects on the propagated blast wave. Nonetheless, all simulations were performed with heat transfer activated as it could affect the fireball dynamics at later stages. A parameter that would affect the decay of pressure is the boundary between the hydrogen and the wall. There are several reasons why the pressure may decay in a tunnel in addition to wall friction: the gas properties such as density and viscosity at the contact surface, and the rarefaction wave degrading the front (Forsen, 2008). However, for LES simulations in ANSYS Fluent, there is an alternative near-wall approach for the wall shear stress. This method analytically integrates the power-law for near wall velocity distribution denoted as the Werner-Wengle wall functions (Wengle and Werner, 1993). In trial simulations, no difference was observed. Generally, to explore physics at wall boundary with LES, it would require significantly finer mesh values next to wall areas as it does not have dedicated wall or near-wall functions.

7.1.4 Simulation sensitivity studies

The potential of a CFD model in reproducing experiments depends, among other factors, on a physical soundness of sub-grid scale models of turbulence and combustion related to the mesh resolution applied. The balance between a fine enough mesh to capture calculations of minor turbulent and diffusive mechanism, but still coarse enough to ensure a practical computational time is always tricky to get just right. The former more crucial, this would ensure that simulations are not mesh dependent, removing that accuracy-bias from results obtained. A sensitivity test was carried out using two meshes in a double-lane tunnel using a 95 MPa, 15 L (0.6 kg) tank; one coarse with a total control volume number of 176k, and the other with 486k denoted as fine mesh. It is to be noted that the mesh outside the tunnel was kept the same during the mesh sensitivity test. Modelling both meshes gave close convergence in the peak pressure during early stages of simulation where the pressure is most abrupt, with slight under prediction for the coarse grid as can be seen in Figure 7.2 (left). The measurements were obtained from 25 cm above the ground where the pressure is maximum due to the blast wave reflections and Mach stem generation and propagation. The study itself is already conservative and things like energy loss on car deformation and its translation in space, road cratering, presence of obstacles are not taken into account. Therefore, the coarse grid is utilized in all simulations to generated data and at the same time retain an affordable computational time. A CFL value of 0.1 for cylinder tank rupture has been established in Chapter 3. However, with the introduction of a hemispherical tank as initial condition required a new CFL sensitivity study. The converged CFL number was found increased to 0.2 (see Figure 7.2, right). Intentionally, with the introduction of a hemispherical tank, the initial stages of reflections and thus higher pressures and associated velocities are reduced compared to the tank located slightly above the road level. This causes a lower requirement to time step, allowing the computational time to be decreased by twice as much.

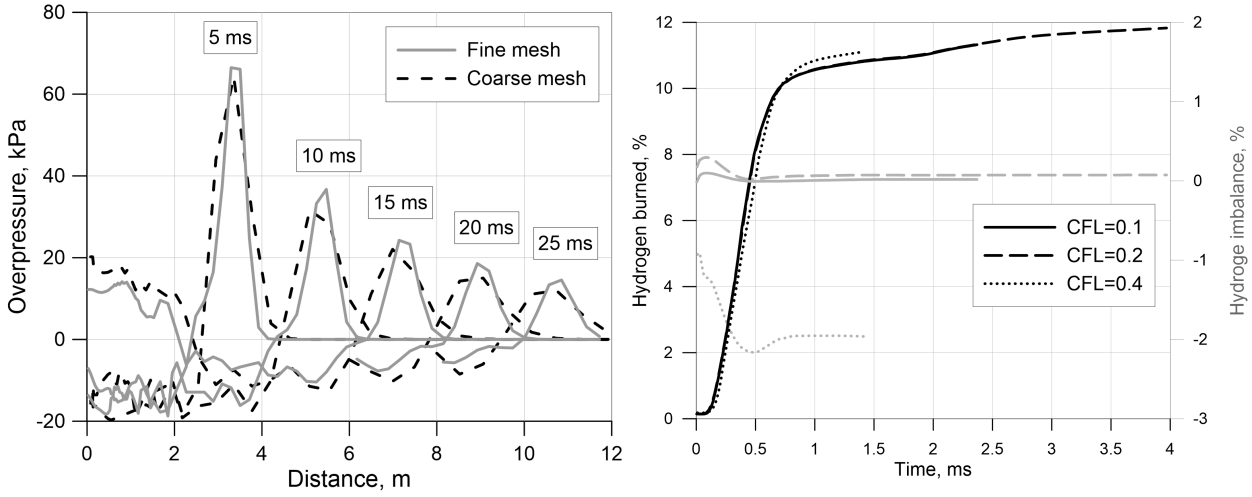

Figure 7.2: Sensitivity study conducted for the mesh (left) and CFL number (right).

7.2 Blast wave propagation and fireball dynamics in tunnels

7.2.1 Blast wave propagation

Figure 7.3 demonstrates snapshots of blast wave propagation for a tank volume of 176 L (6.9 kg) (pressure at the moment of rupture is 95 MPa) within a part of a double-lane tunnel. Shown at 0.8 ms is the hemispherical shape of the released blast wave of the tank, as it initially expands similar to in open atmosphere without confinement effects. The blast wave first reflects from the tunnel ceiling at height 4.5 m (see snapshot 5 ms). Not shown is the blast wave reflection from the tunnel walls (width 9 m). The vertical and horizontal reflections both contributing to the complex flow field overpressure distribution. Once the blast wave initially reflects off the top of the tunnel, the formation of the Mach stem is seen (snapshots 5 ms and 10 ms). The Mach stem propagates along the tunnel and due to reflections from both ceiling and floor can be observed on both these surfaces (see e.g. snapshots 30 ms and 40 ms). Behind the planar blast wave established at about 50–70 ms, the repeatedly reflected waves also form Mach stems. The secondary shocks eventually catch up with the primary blast wave (due to hotter gases and thus higher speed of sound transforming energy to the *"slower"* moving primary shock front), seen in the time between 10–60 ms. As the secondary and tertiary waves coalesce with the primary shock after a distance of around 30 m (at 70 ms), the primary blast wave with multiple strong reflections transforms and propagates as a one-dimensional planar structure. This is clearly seen at snapshots 80 ms, 90 ms and 100 ms, by the uniform primary blast wave overpressure independent of the height within the tunnel. Non-uniformities in the pressure distribution behind the leading front still can be observed.

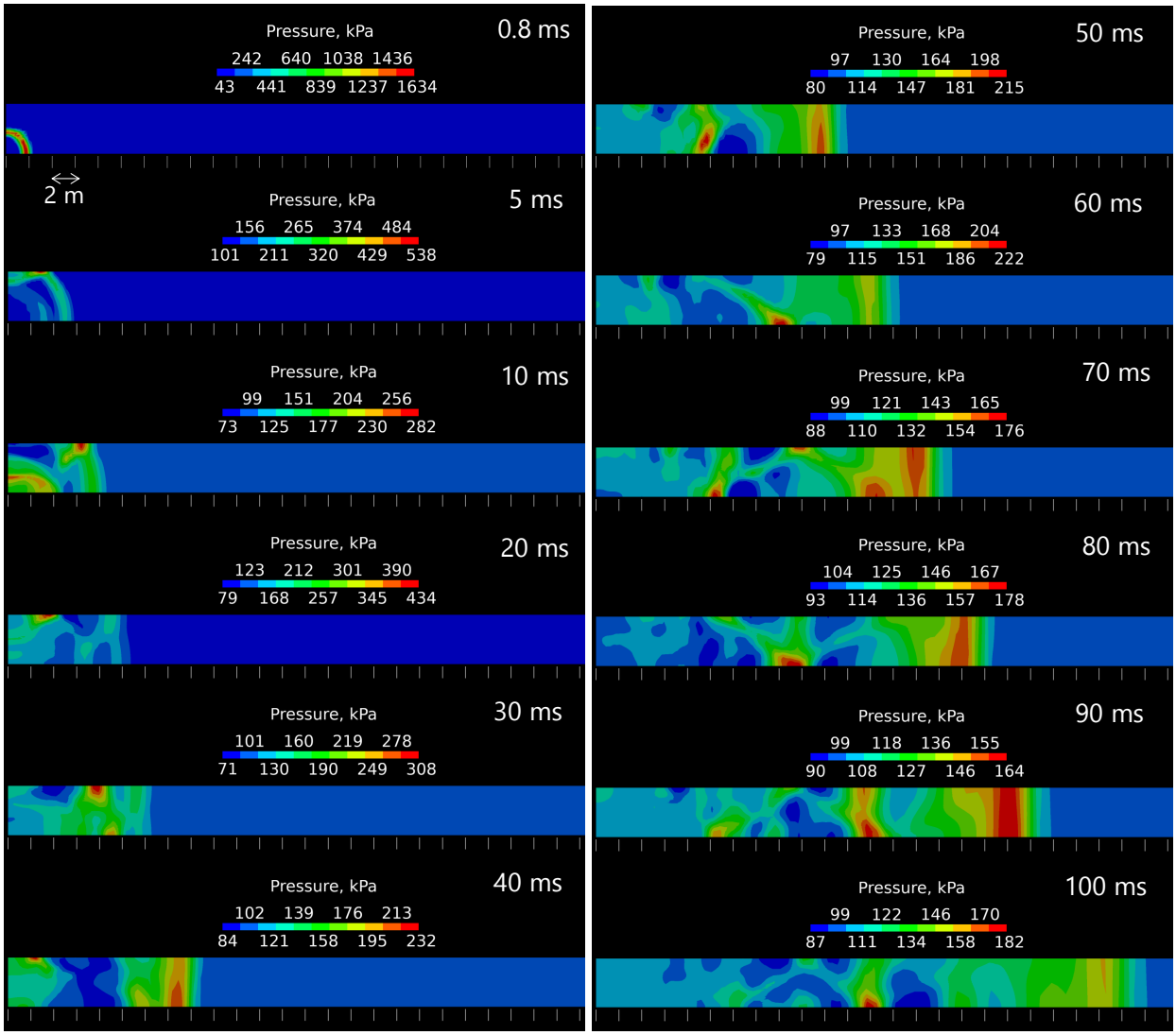

Figure 7.3: Initial blast wave propagation in a double-lane tunnel, of a 95 MPa 176 L (6.9 kg) tank rupture.

Figure 7.4 shows the maximum overpressure that is recorded in a cross-section area throughout the process for a selection of conducted tunnel simulations. Shown for various tunnel heights, the maximum pressure is dominated by reflections caused by interactions with the tunnel structure causing at corresponding distances overpressure higher than its preceding overpressure. The distance of reflection dominance on the maximum blast wave pressure varies according to the various tunnel structures, albeit with the same tank size. Once the reflections subside the wave front is gradually transformed into a one-dimensional flow. After this, the overpressure of the wave front is mostly independent of the height within the tunnel. A simple quantitative criterion is set as the ratio between the maximum and minimum overpressure of the blast wave front to be equal within 1%, $\Delta P_{max}/\Delta P_{min} = 1 \pm 0.01$ across the tunnel cross-section. The distance whereby the pressure is seen independent of the

height occurs for single-lane and double-lane tunnel is after 30 m and 31 m respectively. For both tunnels with comparatively small aspect ratios of 1.2 and 2 respectively, the blast wave reflections from ceilings and walls occur almost simultaneously. Therefore, not only would they interact and even compensate each other out, but the total duration of the reflection period is shorter and results in a decreased distance of transition from Zone 1 (dominated by reflections) to Zone 2 (one-dimensional planar shock propagation). With a width almost three times more than the height (aspect ratio 2.7), the five-lane tunnel exhibits reflection dominance up until 95 m before dying down to establish a planar blast wave front.

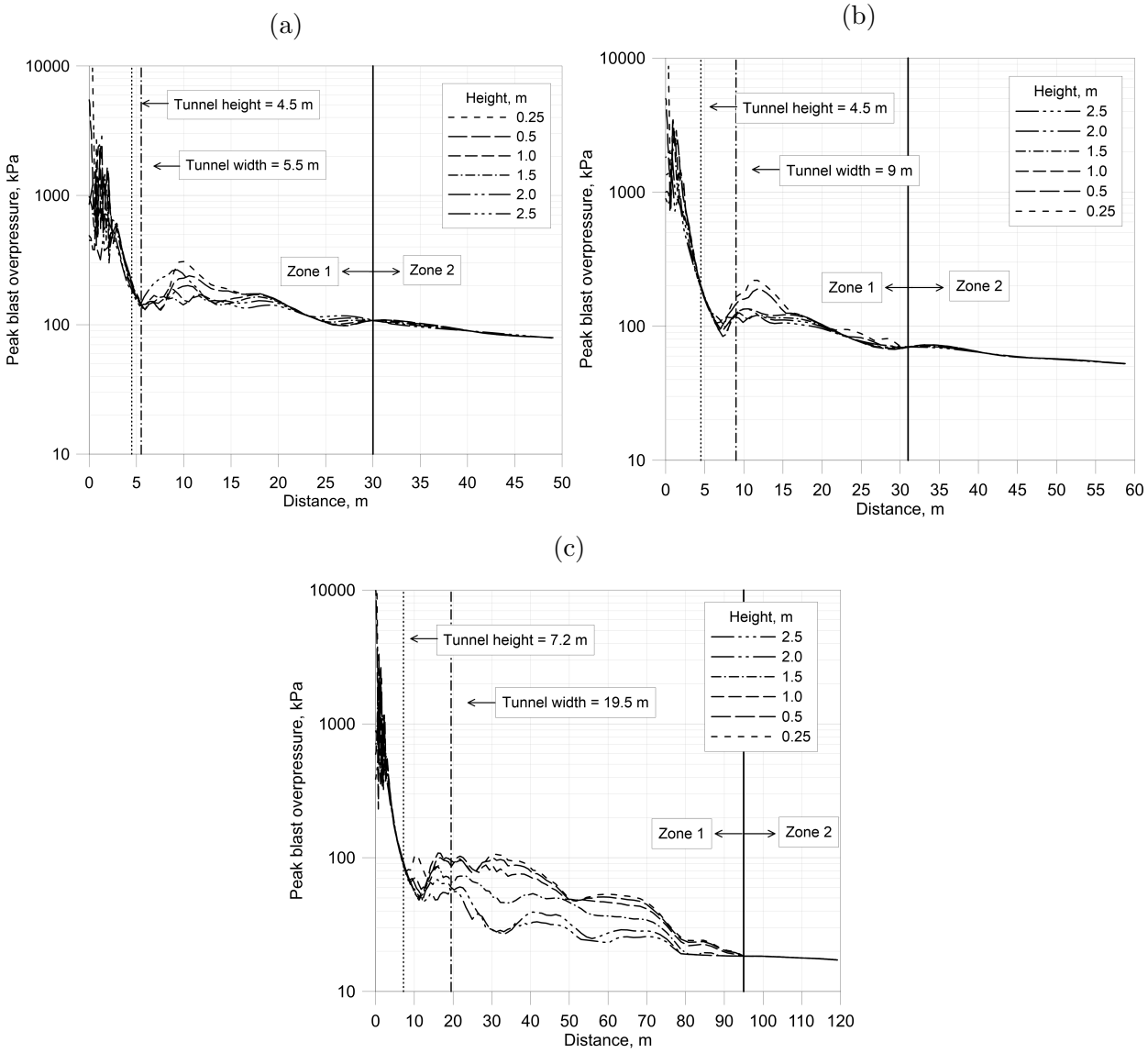

Figure 7.4: Peak overpressure dynamics of a 95 MPa 176 L (6.9 kg) tank and various tunnel cross-sections and aspect ratio: (a) single-lane (24 m^2, 1.2); (b) double-lane (40 m^2, 2); (c) five-lane (139 m^2, 2.7).

The locus whereby the blast wave front is equal is henceforth denoted as Zone 2, and prior to that dominated with reflections as Zone 1. When the wave front is still turbulent, the loss in kinetic energy due to the internal energy dissipation between fluid layers, the major source of blast wave decay. In Zone 2 however, the distance plays the major factor dictating the blast wave overpressure and its decay based on the area of the cross-section, obstacles, roughness of the wall and eventual branching of the tunnel. It was considered that the transition zone between Zone 1 and Zone 2 is between 5–10 times the hydraulic diameter of the tunnel (Thibault et al., 1987). The hydraulic diameter is calculated as:

$$D_T = \frac{4A_T}{wp}, \tag{7.5}$$

where wp represents the wetted perimeter of the cross-section area. The hydraulic diameter represents an equivalent diameter of non-circular ducts or pipes, defining the confinement parameter of the tunnel and taking into consideration both the height and width of the tunnel. Another more recent study determined the transition zone 6 times the hydraulic diameter of the tunnel (Yan and Du, 2015). Albeit a more precise estimate, the accuracy seen compared to determined transitions zones based on simulations in this study were not able to encapsulate all scenarios (see Figure 7.5). As it only takes into account the tunnel volume, the complexity of blast wave interactions behind the primary shock depends on several other parameters besides the tunnel dimensions, such as the tank parameters, and is addressed at a later stage.

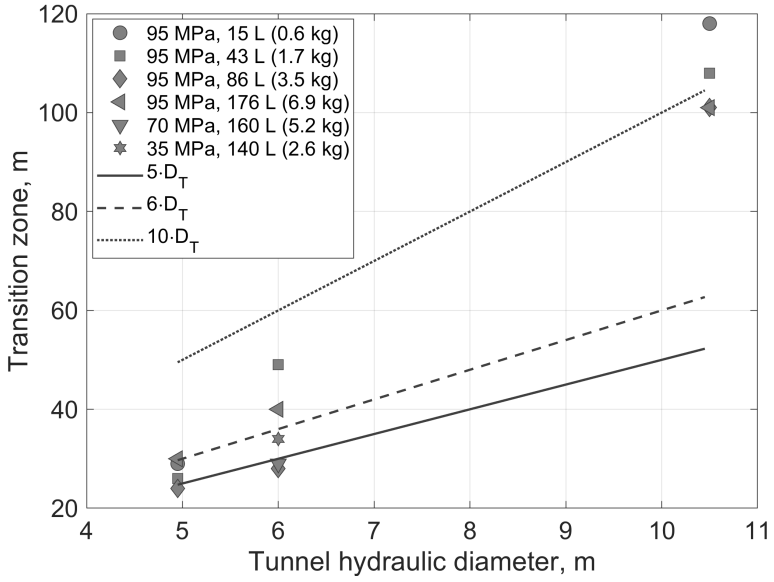

Figure 7.5: The transition zone determined in simulation, and its estimation based on number of hydraulic diameters.

Figure 7.6 presents the maximum blast wave measured across the cross-section as a function of

distance over the entire duration course of blast wave propagation. Capturing the maximum blast wave including those from reflections is a conservative approach that somewhat acts irrespective of any zone. The general trend for all curves is similar. In the beginning, the pressure peak is observed to decay quite significantly with some oscillations due to initial reflections of the tunnel structure. Once the planar blast wave front is established, the pressure attenuation rate is significantly reduced until the tunnel exit.

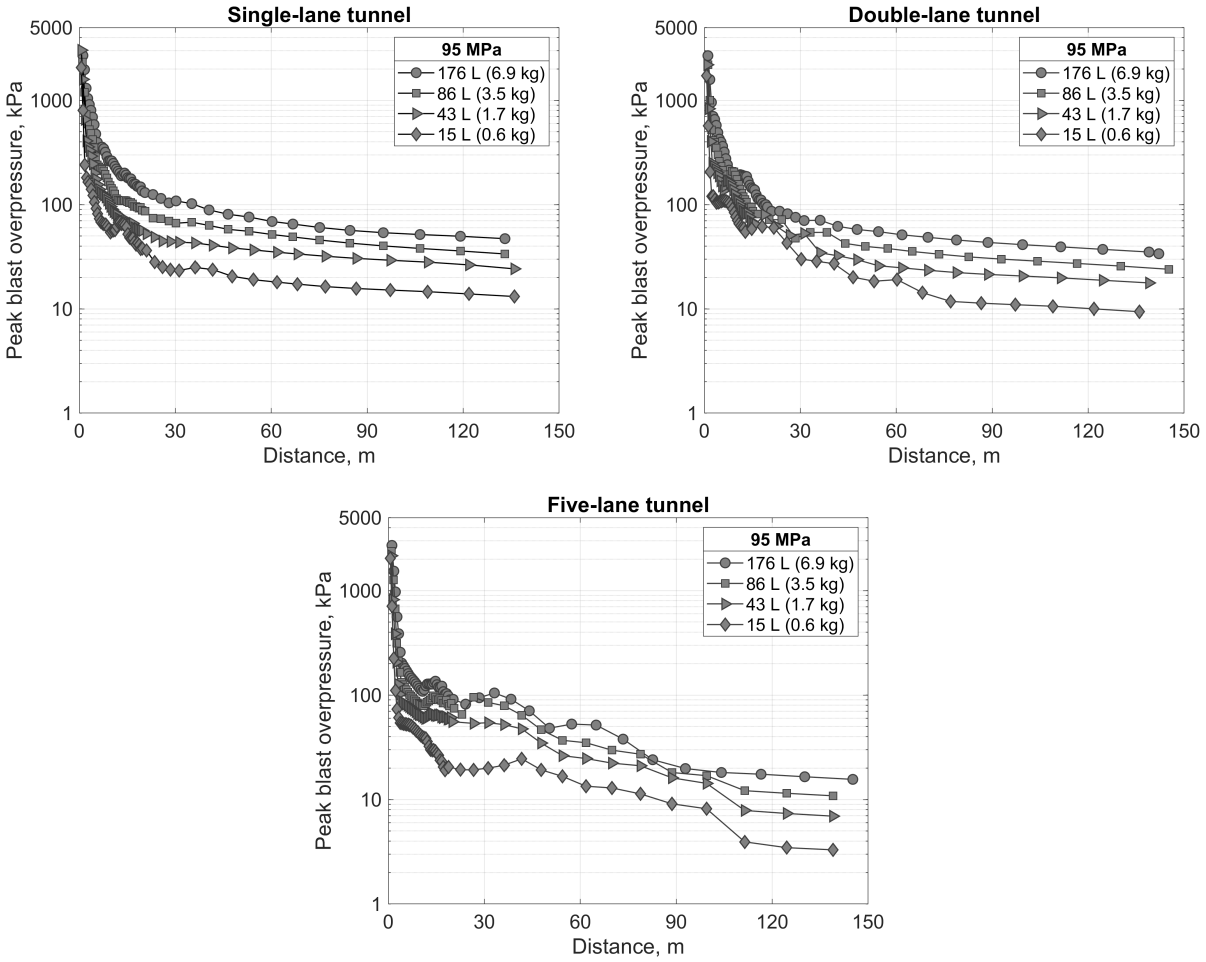

Figure 7.6: Peak blast wave overpressure as a function of distance and stored amount of hydrogen in ruptured tank at initial pressure of 95 MPa.

Depending on the stored hydrogen pressure, the decay in a 1500 m tunnel length is shown in Figure 7.7 for the same amount of hydrogen volume simulated of 120 L. Extended in length from 150 m to 1500 m, a similar trend is seen with a pecking order depending on the rupture pressure, 95 MPa giving the highest overpressure during the whole duration within the tunnel. A 26% decrease in rupture pressure, i.e. to 70 MPa, results in an overpressure decrease by 5 kPa close to the 1500 m exit. Correspondingly, a 63% decrease in rupture pressure, i.e. to 35 MPa, results in an overpressure decrease by 15 kPa.

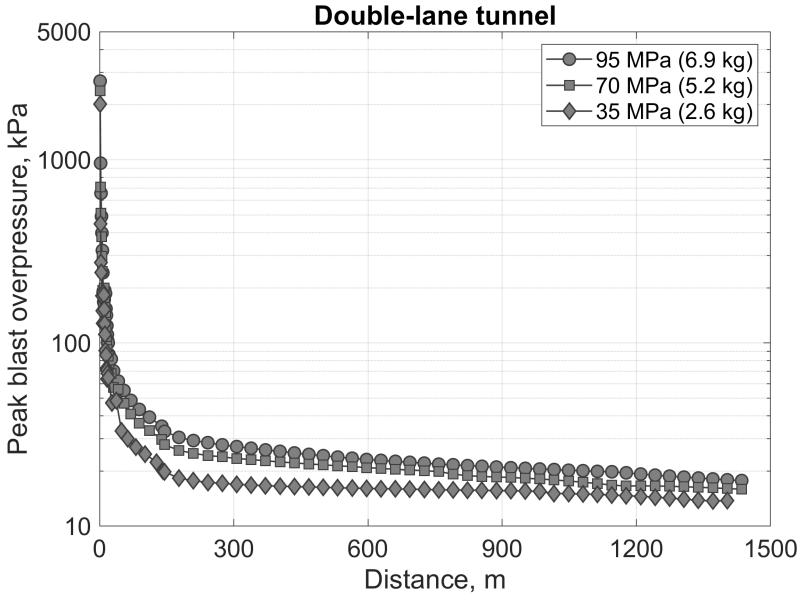

Figure 7.7: Peak blast wave overpressure as a function of tunnel distance extended up to 1500 m, shown for different stored hydrogen pressure at the moment of tank rupture (Simulated tank volume is 120 L).

7.2.2 Fireball dynamics in tunnel

The dynamics of the fireball following a blast wave in a tunnel was investigated in a single-lane tunnel, 95 MPa, 176 L (6.9 kg) tank rupture. The inclusion of radiation was activated, the discrete ordinates model (see Section 3.1.3) modified using data from Yan et al. (2015) for the calculation of the water vapour mean absorption coefficient. For the entire mass of hydrogen mass to attain complete combustion, the total time was 28 s, see Figure 7.8. With confinement effect restricting the amount of air entrainment, a significantly long duration is needed for the entire amount of hydrogen to deplete due to combustion. Although not explicitly compared, the oxygen required for combustion is not readily available as compared to in open atmosphere. At around 5 s, 60% (4 kg) of hydrogen is burned, and a decrease in the rate of burned hydrogen is observed. This is due to the dilution of mixtures by the combustion products (H_2O), in addition to a gradual mass and heat diffusion.

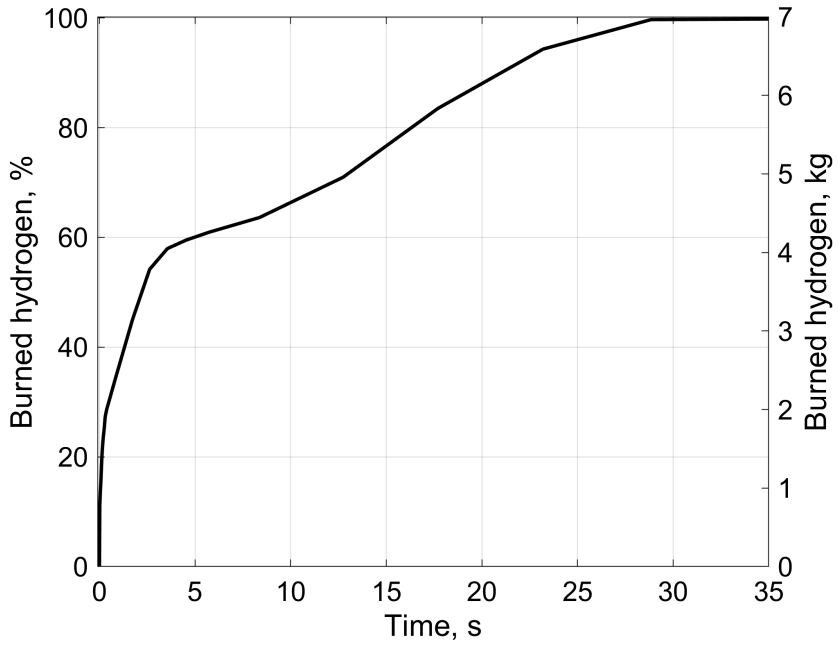

Figure 7.8: Amount of hydrogen burned of a 95 MPa 176 (6.9 kg) tank rupture in a single-lane tunnel.

Figure 7.9 shows the temperature distribution in a tunnel, the rupture point 50 m from the nearest exit, 150 m from the farthest exit. The tunnel is without ventilation systems, traffic movements or wind – its dispersion based only on internal inertia and natural convection. Seen during the preliminary period of fireball as the blast wave propagates out of the nearest tunnel exit (0.01–0.1 s), a symmetrical development of the high-temperature fireball (i.e 2000–2500 K). At 0.1 s, the fireball shifts 20 m towards the nearest exit. This occurs due to the difference in the driving forces caused by the exited blast wave. It creates a back-draft caused by vacuum pulling the fireball in its direction. This effect continues up to 1 s, when the effect of the blast wave exited on the farthest end causes an equilibrium in the back-draft forces. At 5 s and 10 s, the fireball maximum temperature decreases to below 1500 K. Seen at 20 s, buoyancy forces created by the energy release of the rupture drives the fireball towards the tunnel ceiling, impinging on the tunnel ceiling and spreading in both directions. At 40 s, the fireball longitudinally occupies the entire 200 m tunnel and propagates out of both tunnel exits. Here, thermal stratification is observed, due to the cold air from outside during natural convection process ensues (see snapshots at 60–200 s). Once the fireball exits from the tunnel, the maximum temperature is seen to drop dramatically towards atmospheric conditions. Extracted from simulations data, it is only after 197 s that the maximum temperature in the tunnel domain is below 363 K (70°C), the *"no-harm"* temperature limit for humans (minimum temperature causing skin burn upon exposure) (Molkov, 2012).

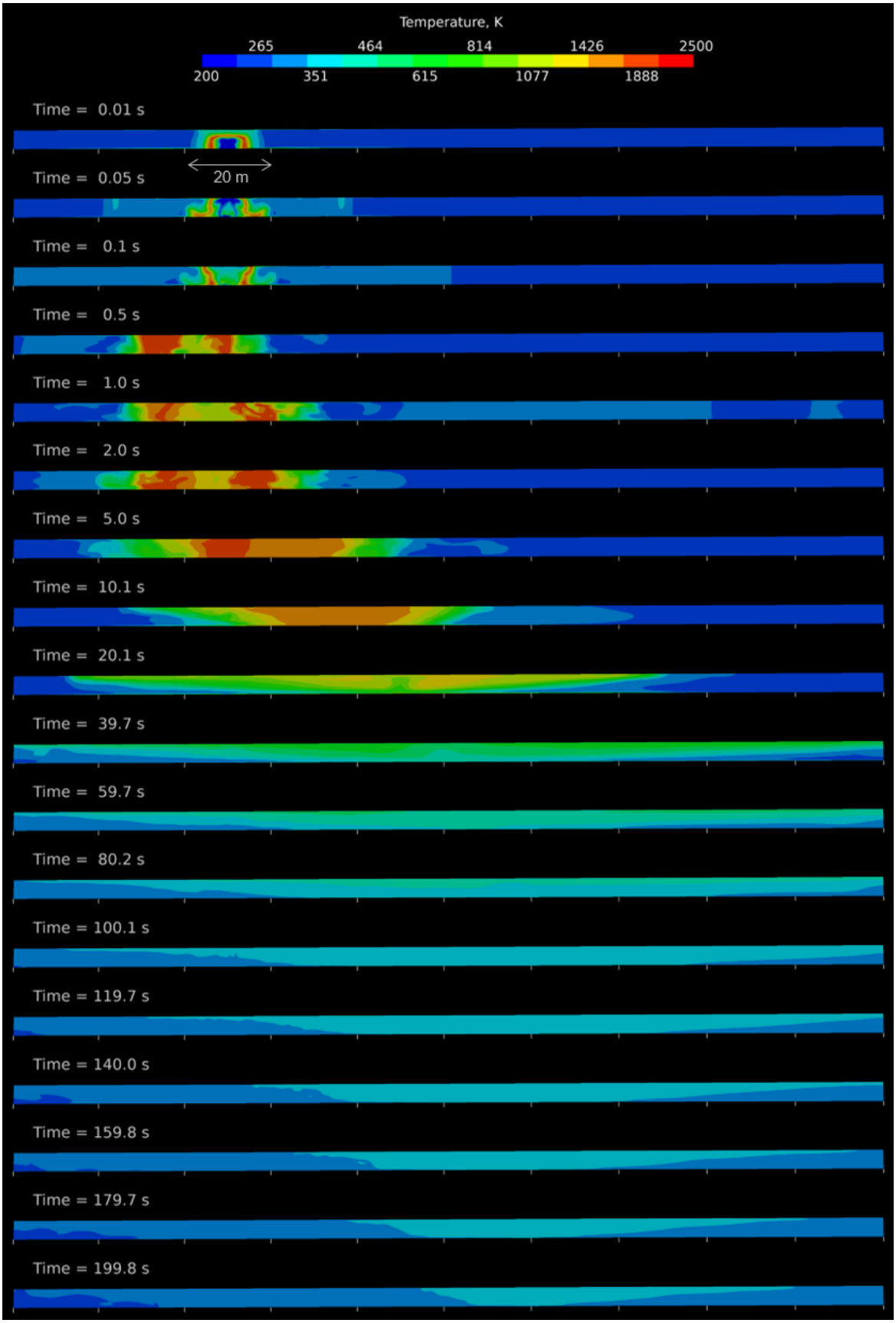

Figure 7.9: Snapshots of temperature distribution in a tunnel central cross-section, after a 176 L (6.9 kg) 95 MPa tank rupture between 0.1–200 s.

The determination of the fireball size from simulations is conducted measuring high-temperature region above the *"no-harm"* temperature threshold of 363 K, (e.g. Figure 7.10). This was done until the fireball reached the exits, which occurred after 35 seconds.

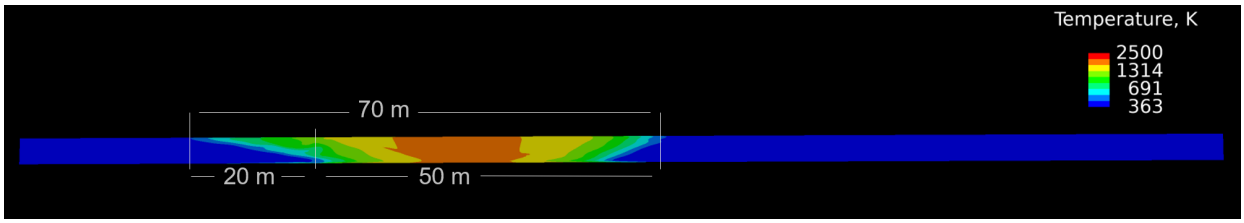

Figure 7.10: An example of how the fireball length in tunnel was measured, defined by the minimum temperature of 363 K (figure for the time instance 10 s).

Presented in Figure 7.11, the maximum fireball length is measured as a function of time. It eventually encapsulates the entire length of the tunnel. A simple correlation proposed based on theoretical considerations for general hydrocarbon fuels, $L_{max} = 102(m/A_T)$, by Li (2019) gives a calculated fireball length of 29 m, reached in simulation under 1 s. The determination of fireball length is indeed a dynamic process, not considered in the model and limits its accuracy and applicability.

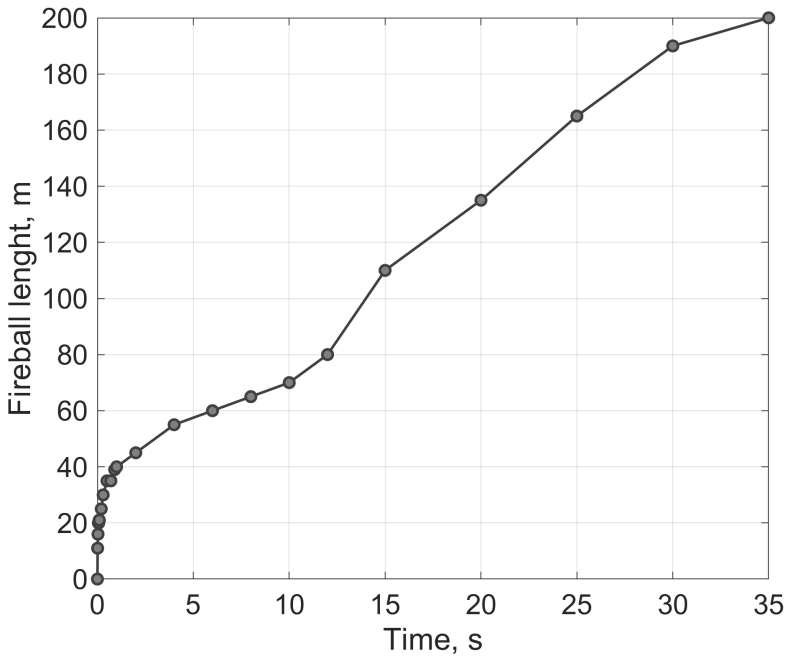

Figure 7.11: Fireball length in a single-lane tunnel as function of time, after a 95 MPa, 176 L (6.9 kg) tank rupture.

A method of determining the thermal energy from fireball in a tunnel is proposed as (Chen

et al., 2017):

$$L_T = D_F \sqrt{\frac{0.5\pi(bG)m^{1/3}T_F^{2/3}D_F^2 - SQ_T}{SQ_T F}}, \tag{7.6}$$

where Q is the heat dose, T_F is the temperature of the fireball, D_F is the fireball diameter, m is the mass of fuel, S the cross-section area of the tunnel and Q_T the tunnel equivalent heat dose. F and bG are constant coefficients having values 161.7 and 2.04×10^4 respectively, based on liquid propellant explosions test results (High, 1968). The fireball length is taken from Figure 7.11, and the fireball temperature is taken conservatively as the highest measured temperature at each measured fireball length. For certain damage thresholds listed in Table 7.3, the simulated and calculated damage range are presented. The model is seen to mostly overpredict the damage threshold, in some cases up to 30%.

Table 7.3: Simulated and calculated thermal doses after an fireball exposure time of 5 s and 15 s, the values for damage threshold found elsewhere (Mannan, 2005).

	Damage threshold, kJ/m^2	Damage range, m			
		5 s exposure		15 s exposure	
		CFD	Model	CFD	Model
Third-degree burn	375	50	55	95	103
Second-degree burn	250	56	66	100	125
First-degree burn	125	58	95	125	178

Another health hazard present due to confinement effects is the oxygen concentration levels. Presented in Figure 7.12 is the mass fraction of oxygen in the tunnel following the development of fireball. Initially seen from 0.01 s to 0.1 s, the absence of oxygen is sustained close to the rupture point. Following the same trend as seen in Figure 7.9, entrainment and buoyancy effects increase the oxygen concentration longitudinally along the tunnel (0.1–20 s). At 30 s and onwards, oxygen gradually becomes omnipresent within the tunnel. An oxygen mass fraction of less than 0.06 is considered lethal after exposure of more than 40 s with alarm levels generally set at an oxygen mass fraction of 0.21 and lower (Verfondern, 2008). The longest duration of exposure with oxygen concentrations below 0.06 is around 20 s, when positioned at a height close to the ceiling (i.e. 4.5 m).

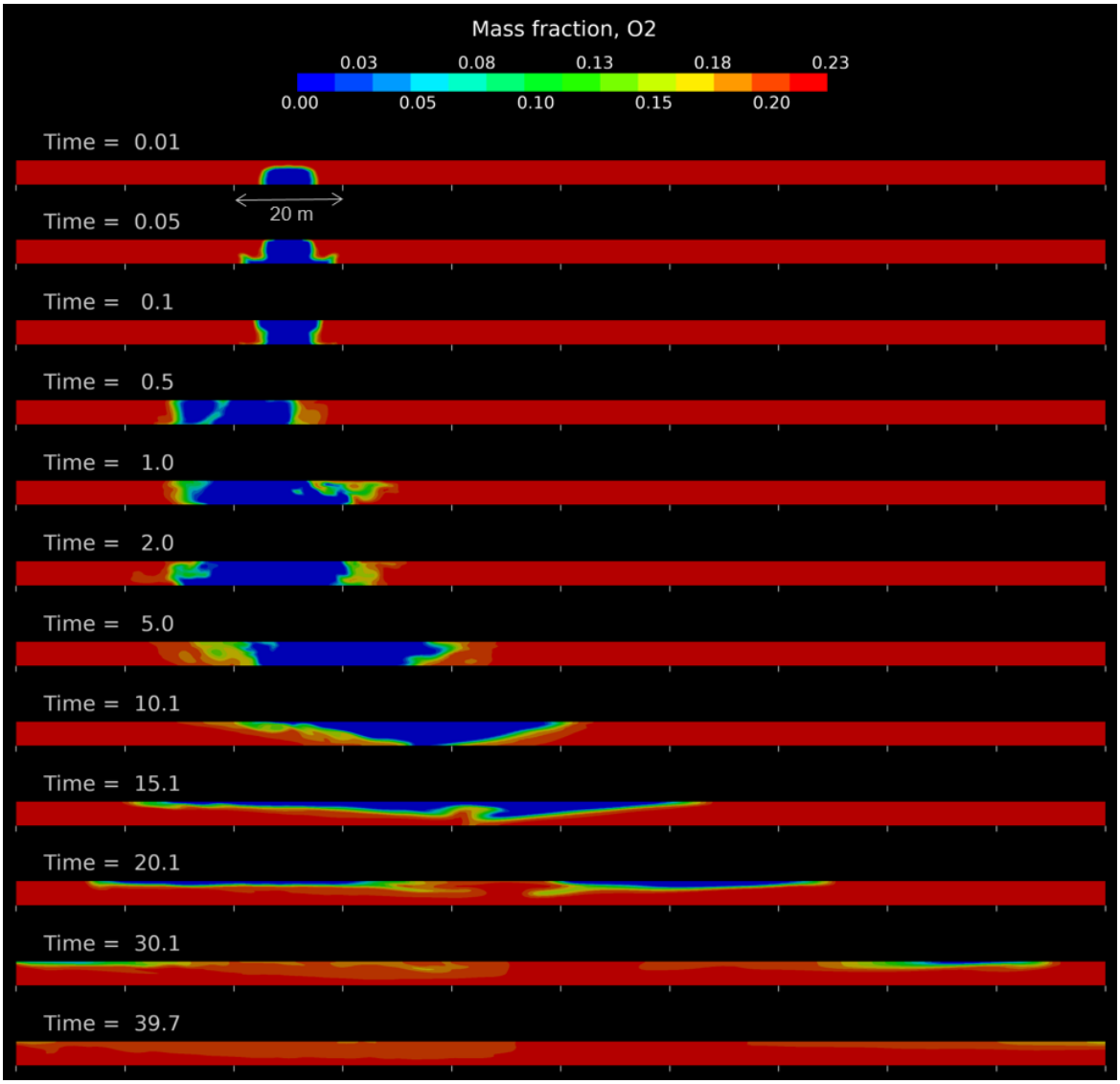

Figure 7.12: Oxygen mass fraction concentration in a single-lane tunnel, following a 176 L (6.9 kg) 95 MPa tank rupture from 0.01 s to 40 s.

7.3 Prediction of blast wave decay in a tunnel

7.3.1 Power law empirical model

A conceptual model, often referred to as an analytical model, compromises all relevant information including mathematical equations and modelling assumptions that describe the physical system or process of interest. The model is qualified when results equal that of reality. However, when data from reality is not available, an analytical model may be verified through numerical results from CFD. The initial form of blast wave decay law in a tunnel established is to be derived indicating the dependence of the peak overpressure, P,

on the ratio of charge weight, m, to volume of tunnel, V_T, to form a correlation as:

$$P \propto A \left(\frac{m}{V_T} \right)^b, \tag{7.7}$$

where A and b are all derived empirically based of best curve fits. Their values are found by various authors, e.g. Curran et al. (1966); C. Smith and J. Sapko (2005); Fang et al. (2019), and vary depending on the tunnel and point source used. The latter coefficient b represents the attenuation of maximum blast wave overpressure by many factors such as the change of cross-section area and the presence of obstacles. Although the coefficients are seen fitted based on a one-tunnel-case applicability, the effort to employ the same methodology is done in this study. Steering away from the ratio of charge weight used previously, the use of stored hydrogen volume is inferred, amending Equation (7.7) to become:

$$\frac{\Delta P}{P_s} = A \left(\frac{V_T}{A_T \cdot L} \right)^b, \tag{7.8}$$

where L the distance from rupture point in a tunnel. The relationship between the two constants is one whereby the former constant varies as the power of the later, a functional power law is determined using least-squares fitting given the function of the form $y = Ax^B$, the coefficients being (Goldstein et al., 2004):

$$b = \frac{n \sum_{i=1}^{n} (\ln x_i \ln y_i) - \sum_{i=1}^{n} (\ln x_i) \sum_{i=1}^{n} (\ln y_i)}{n \sum_{i=1}^{n} (\ln y_i)^2 - (\sum_{i=1}^{n} \ln x_i)^2}, \tag{7.9}$$

$$a = \frac{\sum_{i=1}^{n} (\ln y_i) - b \sum_{i=1}^{n} (\ln x_i)}{n}, \tag{7.10}$$

where $B \equiv b$ and $A \equiv e^a$. Listed in Table 7.4 are all 14 simulations data fitted with listed values for A and b. The goodness-of-fit is represented by the R^2 coefficient, the correlation between the observed and estimated data and ranges between 0 to 1 where 1 represents a perfect fit. The validity of the model is considered from distances in the tunnel whereby confinements effects are introduced. Not assured within a tunnel which of the height or width the blast wave reaches first, the hydraulic diameter was used as the starting point.

Table 7.4: For various tunnel cross-sections and tank volumes, best-fitted values for coefficients A and b including the goodness-of-fit R^2, including calculated mean averages.

Tunnel	Tank volume, m^3	A	b	R^2	Mean of A	Mean of b
Single-lane	0.015	27.6697	0.4404	0.7716	27.0	0.42
	0.043	22.8936	0.4026	0.7365		
	0.086	20.1289	0.3773	0.5782		
	0.176	38.0784	0.4795	0.5674		
Double-lane	0.15	41.8157	0.4722	0.6513	39.9	0.47
	0.043	51.1545	0.4902	0.7354		
	0.086	37.2518	0.4524	0.6804		
	0.176	41.6277	0.4595	0.6679		
	0.159	33.7284	0.4503	0.6718		
	0.139	33.6602	0.4849	0.712		
Five-lane	0.015	67.0796	0.4995	0.5158	105.6	0.54
	0.043	128.0979	0.5491	0.5867		
	0.086	125.5372	0.5619	0.6705		
	0.176	101.7864	0.552	0.5889		

The values of A and b are noticed to vary the least within the same tunnel cross-section, and the most when the cross-section area is altered. Until now, the value of A has not been associated with any measurable parameter of the tunnel. Yet, by evaluating the mean values for A, a close similarity to the squared hydraulic diameter, D_T^2, of each tunnel is found, see Table 7.5. Calculating the overarching mean for $b_{avg} = 0.48$, Equation (7.8) can be changed to its final form:

$$\frac{\Delta P}{P_s} = D_T^2 \left(\frac{V}{A_T \cdot r} \right)^{0.48} . \tag{7.11}$$

Table 7.5: Comparison between the calculated tunnel diameter and the best curve fitted value for A.

Tunnel	D_T^2, m	Fitted A	Difference, %
Single-lane	24.5	22.9	6.5
Double-lane	36	33.7	6.3
Five-lane	110.3	101.8	7.7

The determined correlation compared with a selection of simulated data is presented in Figure 7.13. It can be early established that this methodology of creating a universal power-law fit of blast wave propagation in a tunnel has its limitations (as hypothesized). The slope constant for b is highly empirical and unable to represent more than one tunnel. Change in the parameter A to D_T^2 only is seen to fall below the simulated data for single-lane

and double-lane tunnel with almost negligible difference seen in the five-lane tunnel. The use of the calculated mean value for b, dented as b_{avg}, is however seen more dramatic. Except for the case of the double-lane tunnel where the mean value is almost the same as the fitted value, it either underpredicts (single-lane tunnel) or overpredicts (five-lane tunnel) the simulated data.

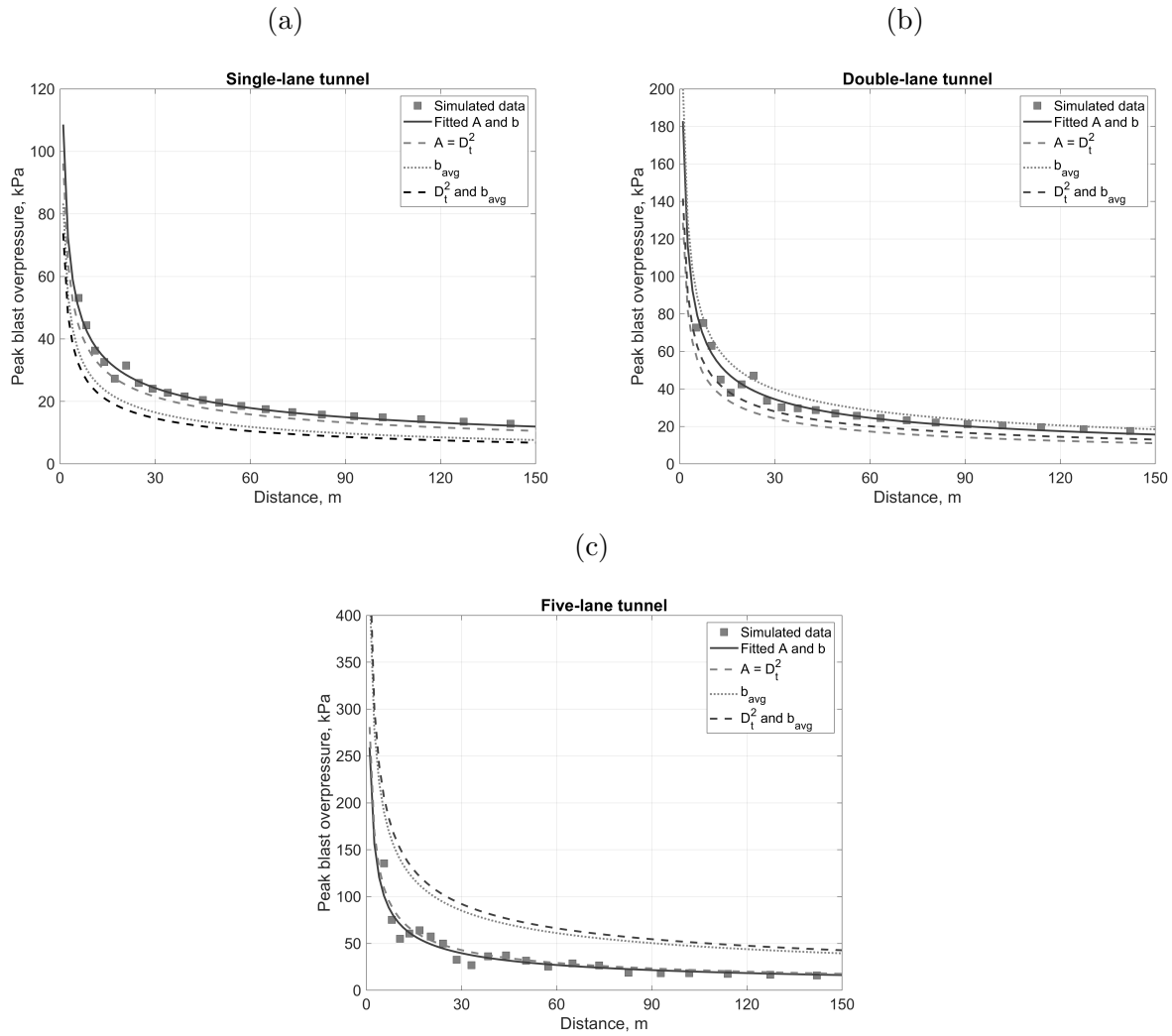

Figure 7.13: Simulated and fitted peak overpressure of different tank volumes (and masses): (a) 15 L (0.6 kg); (b) 43 L (1.7 kg); (c) 176 L (6.9 kg).

Using Equation (7.11), the model becomes less accurate, when attempted to be attuned for a wider application scheme. Aiming to develop a universally applicable model across various tunnel sizes, this is a major challenge to overcome. In practice, this would require individual experiments for each tunnel, the data then used to fit a one tunnel case model.

7.3.2 Development of a universal correlation

Dimensionless parameters

To determine a decay law for blast wave overpressure in a tunnel, the main parameters of influence is ascertained. There are various interpretations of these parameters, but most certain are: atmospheric pressure, P_s, the energy of the blast, E, the cross-section area of the tunnel, A_T, and the distance from the energy release point, L. To find the relationships between these four physical quantities is firstly done by identifying the three basic dimensions as $M = kg$, $L = m$, $T = s$. Table 7.6 shows the variables for the parameters mentioned together with their dimensions.

Table 7.6: Variables for the parameters and dimensions.

Variable	Symbol	Basic dimensions
Atmospheric pressure	P_s	$M^1L^{-1}T^{-2}$
Energy	E	$M^1L^2T^{-2}$
Tunnel cross-section area	A_T	$M^0L^2T^0$
Distance from release	L	$M^0L^1T^0$

Using the Buckingham Π theorem (Buckingham, 1916), with four physical quantities presented and three dimensions, there are one $(4 - 3 = 1)$ independent dimensionless Π parameter. Choosing three parameters (i.e P_s, L, E) as repeating variables, following the rules of the similitude analysis, one dimensionless quantity is derived as $\Pi_1 = (P_s L A_T)/E$. The defined dimensionless number is taken here as an energy-scaled dimensionless distance for tunnels of cross-section area A and distance L along the tunnel from the epicentre of tank rupture:

$$\overline{L} = \frac{P_s L A_T}{E}. \tag{7.12}$$

Looking closely, this equation is similar to the Sachs-scaling equation, in which the radius, r, is replaced by $(LA_T)^{1/3}$. The blast wave overpressure is made dimensionless by dividing it by the surrounding (atmospheric) pressure:

$$\overline{P} = \Delta P / P_s. \tag{7.13}$$

Mechanical and chemical energy contribution to the blast wave overpressure peak

The total energy released during high-pressure hydrogen tank rupture in a fire, which contributes to the maximum pressure in the blast wave, includes not only the instantaneously released mechanical energy of compressed gas (the physical explosion). It also contains a fraction of chemical energy released by hydrogen combustion at the contact surface with

heated by the starting shock air (Molkov et al., 2020). The energy contributing to the blast wave strength is defined as:

$$E = \alpha \cdot E_m + \beta \cdot E_{ch}, \tag{7.14}$$

with E_m and E_{ch} being the total mechanical and chemical energy of the released hydrogen respectively. The mechanical energy of compressed gas using the Abel-Noble equation of state of real gas is (Johnson, 2005):

$$E_m = \frac{(P_g - P_s)(V - mb)}{\gamma - 1}, \tag{7.15}$$

where P_g and P_s are the tank and atmospheric pressures respectively, V and m are the tank volume and mass respectively, b is the co-volume constant for hydrogen defined as 7.69×10^{-3} m^3/kg and γ the ratio of specific heats. The mass of tank, m, is calculated considering real gas given as:

$$m = \rho V = \frac{P_g}{P_g b + \frac{RT}{M_m}}, \tag{7.16}$$

where T is the tank temperature, M_m is the molar mass of hydrogen (0.002 kg/mol) and R the universal gas constant defined as 8.314 (J $\cdot$ K)/mol. The total chemical energy of the released hydrogen is calculated as:

$$E_{ch} = m \cdot H_C, \tag{7.17}$$

where H_C is the hydrogen heat of combustion in air (lower heating value) defined as 1.199×10^8 J/kg. α is an empirical mechanical energy coefficient to account for ground effects. First observed by Henrych (1979), the shock wave energy from a discharge close to the ground would be reflected in its entirety and therefore the energy associated with the generated blast wave calculations would be twice as large. Although a simple factor of 2 would be sufficient, this is assumed the ground is perfectly smooth and rigid with no irregularities. However, a factor of 1.8 is used, some energy assumed lost due to partial reflection (Baker et al., 1983). The calculated mechanical energies are given in Table 7.7.

Table 7.7: Based on tank mass and pressure, the calculated mechanical energy released from rupture.

Hydrogen volume, L	Tank pressure, MPa	Mechanical energy, MJ	
		E_m	$E_m \cdot \alpha$
15	95	3.5	6.3
43		10.5	18.9
86		21	37.8
176		42	75.6
160	70	28.6	51.5
140	35	12.5	22.5

A chemical energy coefficient, β, indicates the fraction of the total hydrogen chemical energy gradually released during complete combustion contributing to the blast wave. Based on experiments, a study conducted revealed that 5.2% of the chemical energy of a 35 MPa cylinder tank (72 L) contributes to the blast wave overpressure (Molkov and Kashkarov, 2015). Elsewhere, a numerical study revealed an approximate 10% contribution of chemical energy to the blast wave overpressure, from a cylinder tank (36 L) of initial pressure of 95 MPa (Cirrone, 2018). Needless to say, the method of defining the coefficient β of simulations is needed. Figure 7.14 demonstrates that the percentage of burned hydrogen in time for different masses simulated shows quite similar behaviour for all cases. This is due to the similar geometry of the ruptured hemisphere with a similar propagation of the starting shock and the contact surface behind the shock where hydrogen is burned with air. Some subtle differences are noticed, such as that the smaller the tank the higher the rate of hydrogen burned before the decrease in combustion rate is attained. This is physically sound, as the energy displaced from a vessel by volume is proportional to r^3, whereas the contact surface area expands by r^2. Therefore, the chemical energy displaced released during combustion at the contact surface is proportional to $1/r$. In other words, the smaller tank the larger the fraction of chemical energy released.

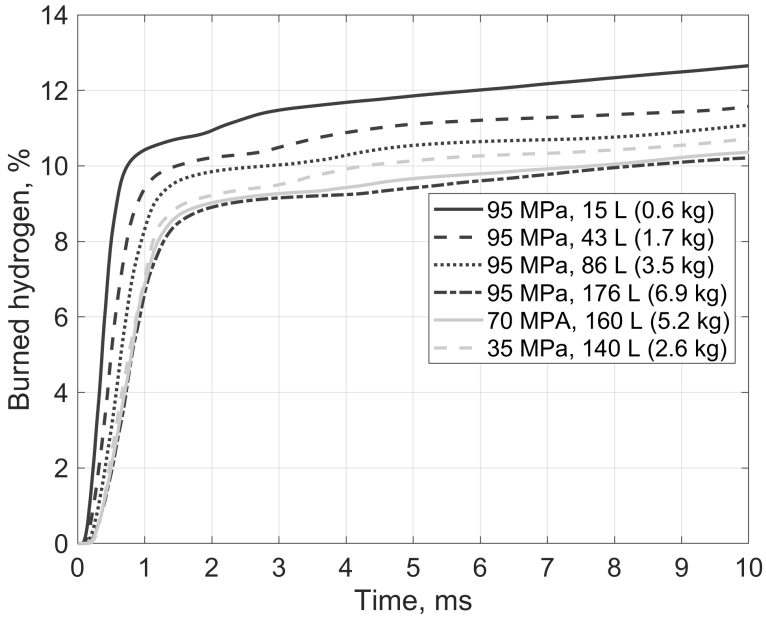

Figure 7.14: Percentage of hydrogen burned for various tank masses within the first 10 ms.

Based on a thorough analysis of CFD simulations presented in Section 4.1.3, the contribution of combustion energy, i.e. β, to the peak overpressure ceases when the drastic decrease in the combustion rate is observed at about 1–2 ms after tank rupture (see Figure 7.14). This indicates that the high-pressure zone of the blast wave has propagated away from the combustion zone located at the contact surface. However, the energy from combustion to the blast wave still occurs, through the increase of the pressure impulse instead of the peak pressure. The contribution of combustion to the peak pressure ceases when temperature gradient changes from negative to positive value thus preventing acoustic waves from the reaction zone to propagate and reach the leading front of the blast wave. An example of when exactly to ascertain that the contribution has ceased is shown in Figure 7.15, following a simulation with 95 MPa, 176 L (6.9 kg) tank rupture. As the leading shock is still being fed energy from combustion, after 4 ms, the temperature gradient is negative (below zero) and thus acoustic waves feed the peak of the blast wave. Distribution of parameters at 7 ms indicates that for the first instance whereby the temperature gradient becomes positive (above zero). This indicates the exact moment when contribution from combustion to the peak overpressure breaks off. The positive temperature trend continues (see the distribution of parameters at 12 ms), confirming the halt of energy being fed ahead as the positive temperature gradient grows even further.

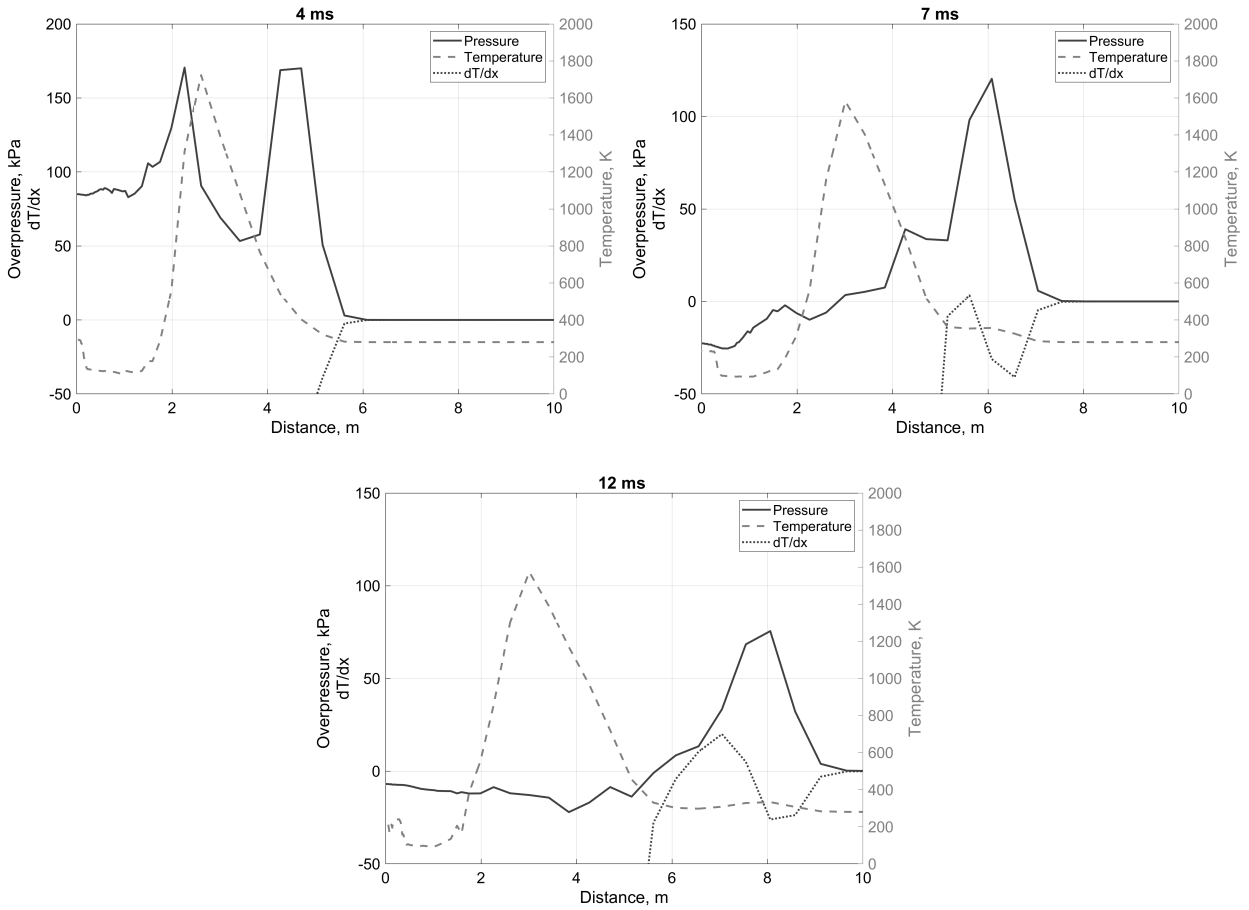

Figure 7.15: The transient pressure, temperature and temperature gradient after a 95 MPa, 176 L (6.9 kg) tank rupture, seen at 4 ms, 7 ms and 12 ms.

The methodology of determining β is applied for all simulations. The determined fractions of chemical energy contributed to the blast wave maximum overpressure are given in Table 7.8. Despite the little differences in percentages of combustion energy contributing to the leading shock, it is not entirely representative with regards to the amounts of energy found quite diverse, between 8–79 MJ. Compared with the mechanical energy released (Table 7.7,) they are quite comparable proving the importance of contributions from both energy sources. For the sake of conservatism, the use of $\beta = 0.12$ is recommended when applying the final derived correlation.

Table 7.8: The determined contributions of combustion energy fed to the leading shock, based on tank mass and pressure.

Tank volume, L	Tank pressure, MPa	Total chemical energy, MJ	Leading shock contribution	
			β	$\beta \cdot E_{ch}$, MJ
15	95	69	0.12	8.28
43		208	0.11	22.9
86		417	0.11	45.9
176		834	0.095	79.2
160	70	618	0.10	61.8
140	35	309	0.11	30.9

To quantify the isolated effect of contribution of hydrogen combustion at the contact surface to the blast wave strength, CFD simulation with the release of only mechanical energy is performed (the combustion model deactivated). Figure 7.16 demonstrates that hydrogen combustion after a 95 MPa, 176 L (6.9 kg) tank rupture in a fire contributes significantly to the blast wave strength. The effect is seen to sustain throughout the tunnel, and at the 150 m exit, the difference in peak overpressure is 45 kPa, 63% decreased when combustion is absent.

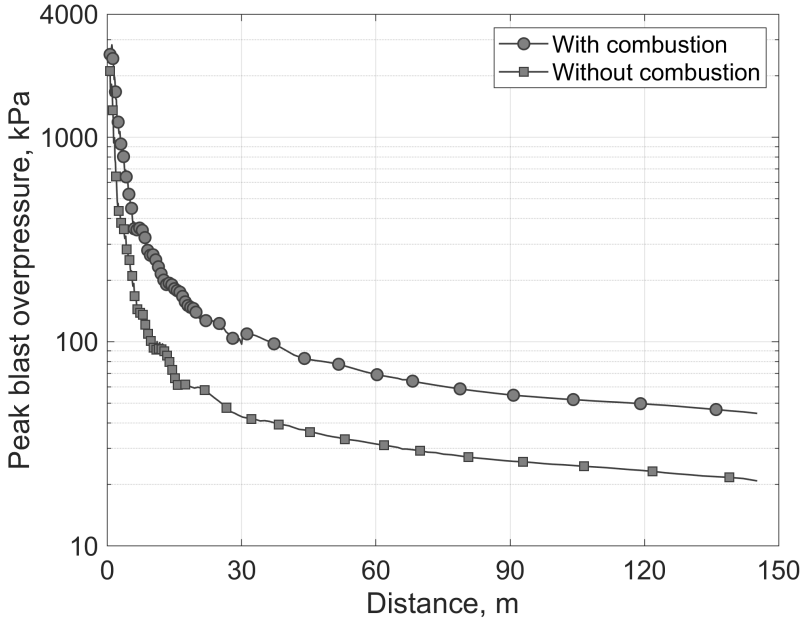

Figure 7.16: CFD simulation results for blast wave peak overpressure as a function of distance for a 95 MPa, 176 L (6.9 kg) tank, with and without combustion present in simulation.

Correlation in dimensionless $\overline{P} - \overline{L}$

Using the dimensionless value derived, $\overline{P}$ is plotted as a function of $\overline{L}$ for each tunnel based on CFD simulations described above of tank volumes in the range 15–176 L (0.6–6.9 kg) in Figure 7.17. Within each tunnel, a conformed blast wave decay pattern is seen across the tank masses ruptured. Furthermore, the decay is found independent of the maximum pressure obtained both from Zone 1 dominated by reflections and Zone 2 obtained from the planar wave.

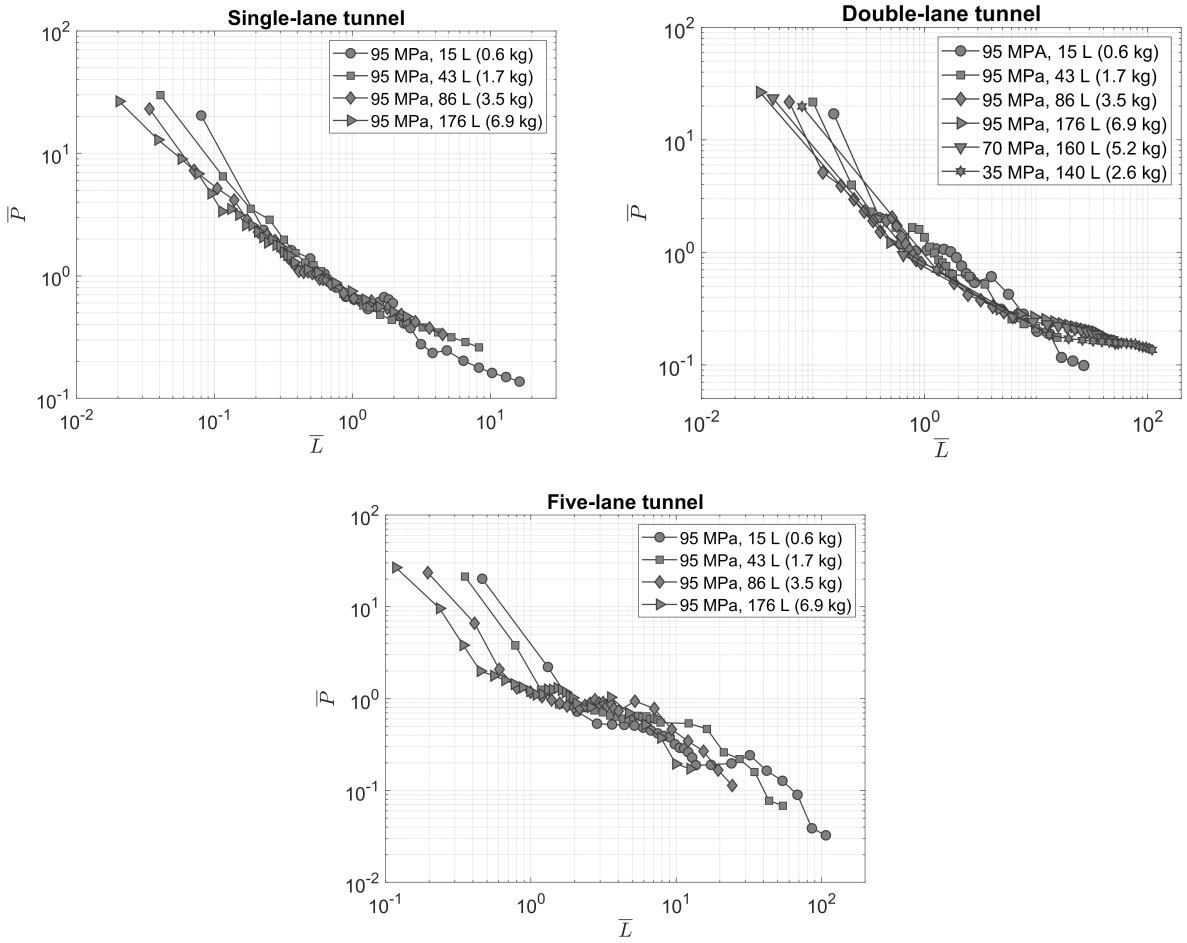

Figure 7.17: Dimensionless parameter, $\overline{P}$, as a function of dimensionless parameter, $\overline{L}$, in tunnels for various volumes 15–176 L (0.6–6.9 kg) and tunnels (single-lane, double-lane and five-lane).

To verify the universality the derived correlation, the results for different tunnels and hydrogen tank volumes are combined in Figure 7.18. A significant scatter is observed and thus the correlation in original parameters $\overline{L}$ and $\overline{P}$ cannot be accepted as universal.

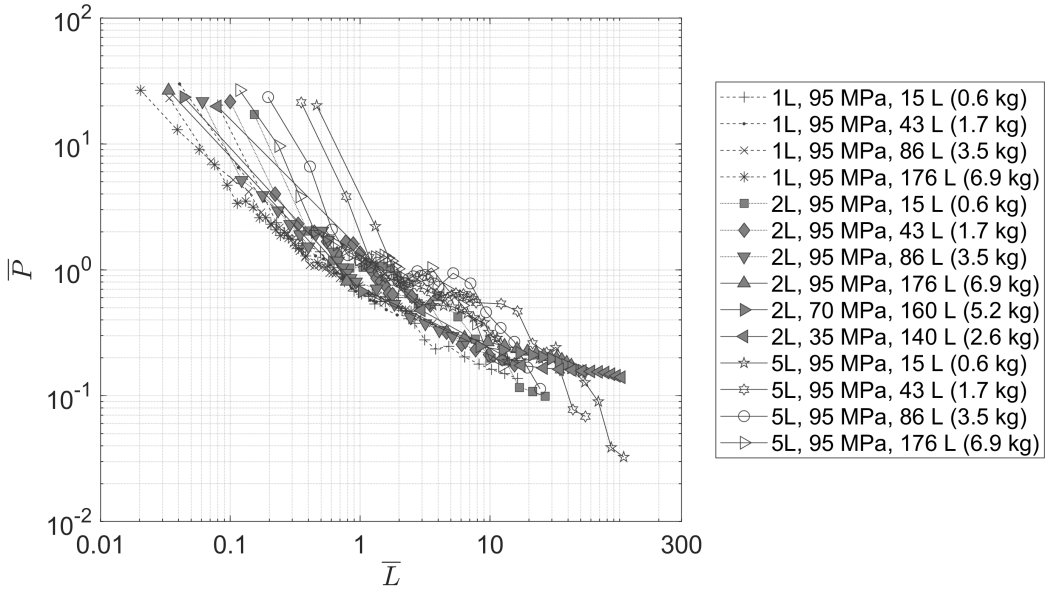

Figure 7.18: Dimensionless blast wave peak overpressure, $\overline{P}$, as a function of dimensionless distance, $\overline{L}$, in tunnels for various volumes 15–176 L (0.6–6.9 kg) and tunnels (1L 2L and 5L): combined results.

Modified correlation accounting for tunnel aspect ratio

Especially the data for five-lane tunnel deviates strongly from the remaining data obtained for single-lane and double-lane tunnels. It shows a much higher dimensionless blast wave pressure, attributed to the maximum pressure being dominated by reflections. It is shown that this effect is caused by the tunnel aspect ratio. Thus, it must be taken into consideration when building a universal correlation. To cater to the geometrical shape of each tunnel, a width-height aspect ratio parameter is included into the original dimensionless parameter $\overline{L}$, divided by another dimensionless parameter i.e. the aspect ratio (AR) of the tunnel. To remain vigilant, the AR^n parameter is tested in power $n = 1$, as well as in powers $n = 0.5$ and $n = 2$, other values not seen to further improve the convergence of plotted data. Presented in Figure 7.19, $n = 1$ shows the better convergence of all plotted data compared to the use of powers $n = 0.5$ and $n = 2$, determined by the coefficient of determination, R^2. Following, the amended $\overline{L}_1$ is thereby given as:

$$\overline{L}_1 = \frac{P_s L A_T}{E \cdot AR^n}, \tag{7.18}$$

where AR is the width-height aspect ratio of a tunnel. To improve the convergence of different curves observed in Figure 7.18 through the range of studied tanks and tunnels parameters, the original dimensionless pressure, $\overline{P}$, is altered to $\overline{P}_1 = \overline{P}/\overline{L}_1$.

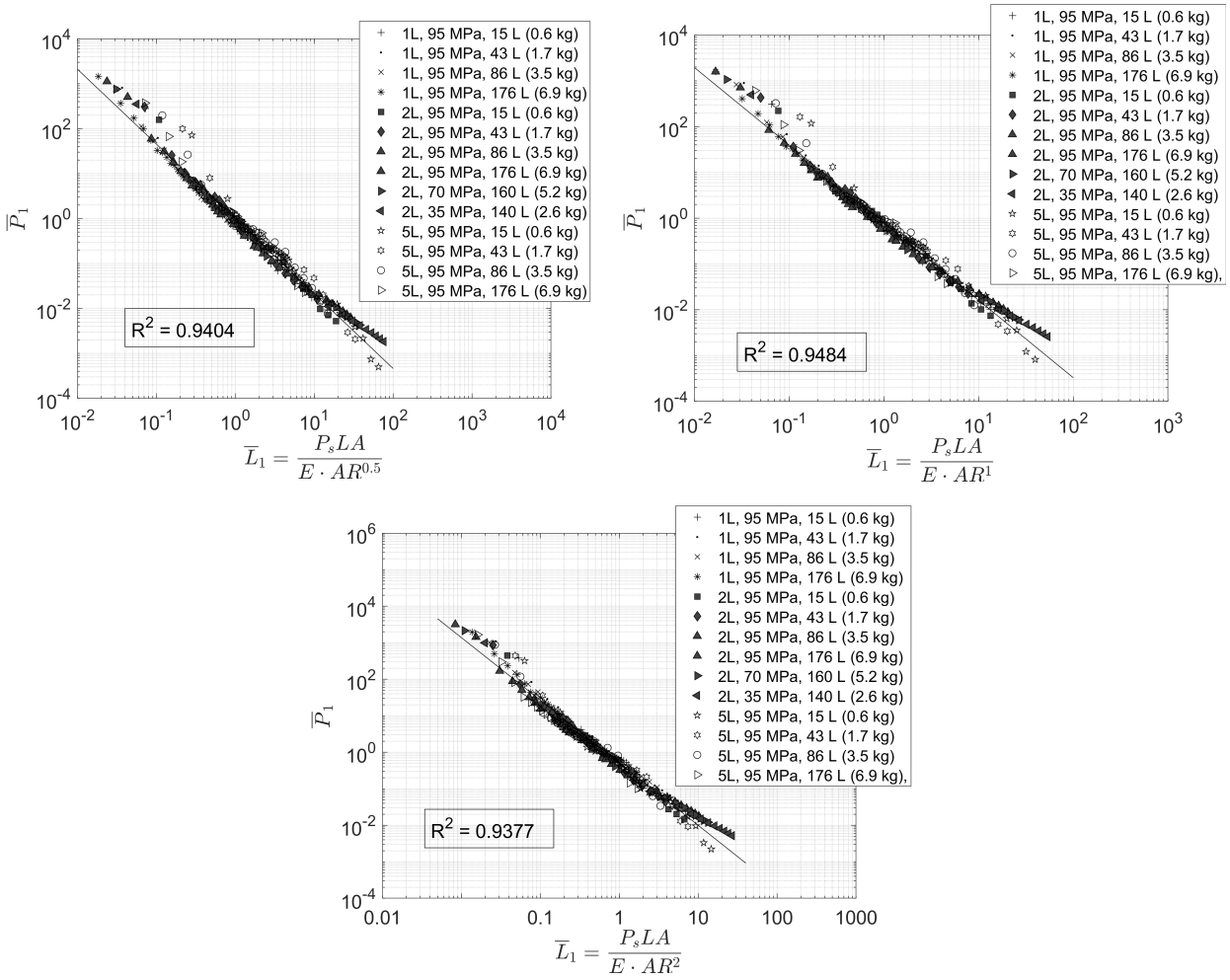

Figure 7.19: The correlation in dimensionless parameters $\overline{L}_1 - \overline{P}_1$ for different tunnels and hydrogen tanks, the aspect ratio (AR) tested in powers $n = 0.5$, $n = 1$ and $n = 2$.

Determination of transitional zone based on $\overline{L}_1$

Having determined the dimensionless parameter, $\overline{L}_1$, the determination of the transition between Zone 1 (being dominated by strong blast wave reflections) and Zone 2 (of quasi-one-dimensional planar blast wave propagation) is revisited (finally!). Based on the tunnel hydraulic diameter, Equation (7.18) is amended to:

$$\overline{L}_{D_T} = \frac{P_s D_T A_T}{E \cdot AR}, \tag{7.19}$$

where $\overline{L}_{D_T}$ being the dimensionless tunnel hydraulic diameter including tank parameters. The calculated values for D_T are 4.95 m, 6 m and 10.5 m for single-lane, double-lane and five-lane tunnels respectively. Plotted in Figure 7.20 includes the fraction L_{TR}/D_T characterising the transition zone distance as a function of the number of tunnel diameters. The transition

zone distance is seen within a hydraulic diameter factor between 4–13, depending on the parameters of the tank. Indeed, a smaller tank results in a longer distance, due to the decreased planar wave overpressure allowing reflections to *"dominate"* the maximum pressure further. The effect of increased cross-section area also adds to a longer transition zone, as a larger area decreases the density and temperature of the flow field behind the primary shock, which again slows down the process of reflected blast wave coalescing with the shock front.

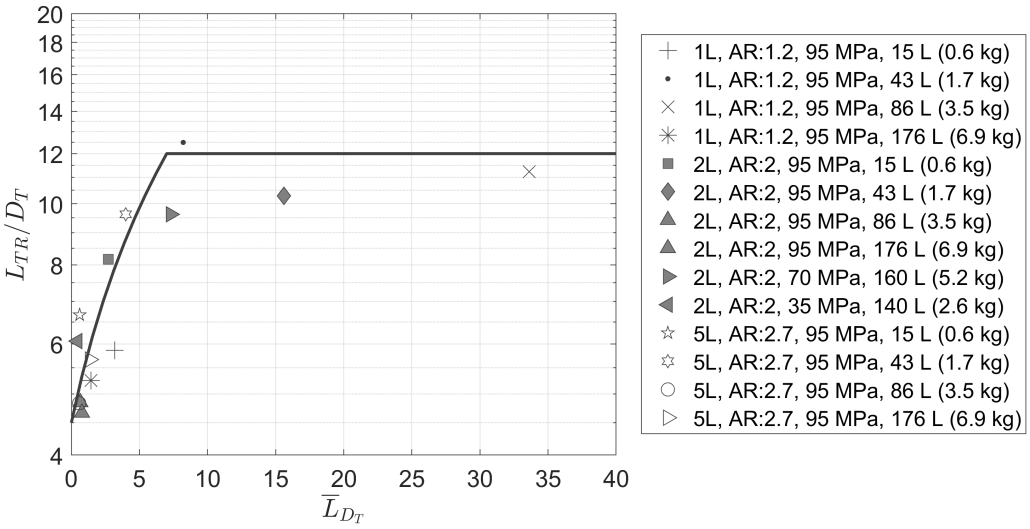

Figure 7.20: The transition zone as a function of tunnel hydraulic diameter shown as a function of dimensionless tunnel hydraulic diameter.

Something noticeable with the proposed decay correlation in dimensionless parameters $\overline{P}_1 - \overline{L}_1$ is the divided tail-end in Figure 7.20 seen between the 150 m and 1500 m long tunnels simulations. This was found due to the omission of influence of friction and minor losses from the wall on the blast wave overpressure along tunnel length. It is not trivial to introduce the roughness of the tunnel wall in simulations and it is considered as a smooth wall in this study. When ignored, the lack of energy absorption leads to a less decayed blast wave. The loss of pressure to the wall involves thermal energy transmission and viscous loss due to non-slip boundary condition, omitting the effect of elastic or inelastic deformation of the walls and wall roughness. The energy absorbed by the set concrete wall in simulations is seen negligible and the rigid boundary is set by restraining the normal motion of the particle on the wall (non-slip boundary condition). The influence of blast wave decay due to frictional losses on the walls of the tunnel first manifests as a function of distance 30 times the tunnel hydraulic diameter (Skjeltorp, 1968). Quantifying its effect on the attenuation of a shock wave and its energy considering roughness and their complex relationship in-between may provide a better basis for decay law. However, this is out of the scope of this study.

Modified correlation accounting for friction and minor losses

The friction and minor losses attributed to the tunnel are directly influencing the attenuation of a blast wave in a tunnel. The minor losses can be expressed through friction losses by the equivalent length method. Thus, only friction losses are considered further, especially because only straight tunnels without bends, expansions and branching are simulated. The basic quantity that measures the effect of friction is the friction parameter fL/D (McCabe et al., 2005). Generally denoted as f, the friction factor is based on the fraction between the wall shear stress and the dynamic pressure. In adiabatic friction flow, the temperature of the gas changes. The viscosity also varies, and the Reynolds number and friction factor are not constant. In gas flow however, the effect of temperature on viscosity is small, and the effect of Reynolds number on the friction factor f is still minimal. Also, unless the Mach number is nearly unity, the temperature change is small and therefore, it is satisfactory to use an average value for f as a constant in calculations. This friction factor has a general equation for friction in smooth-pipe flow given as (Nikuradse, 1950):

$$\frac{1}{\sqrt{f}} = 0.869 \cdot \ln(Re \cdot \sqrt{f} - 0.8). \tag{7.20}$$

The Reynolds number, Re, for the flow of gas in a tunnel behind the blast wave was calculated using the hydraulic diameter of a tunnel, the characteristic density of air in the blast wave, the velocity of air behind the shock wave and dynamic air viscosity for parameters of the air. This was conducted for various distances in from initiation of Zone 2 (where the blast wave is planar) until when the blast wave arrived close to the tunnel exit. The range of Re number for different scenarios was found from 2.095×10^7 to 1.842×10^8, encapsulating all tunnels and tanks. This corresponds to a friction factor with the range of 0.0065 ± 0.001, used to build the correlation. As a conservative approach in the use of the correlation performed later, the lowest value of friction factor $f = 0.0055$ is recommended. To include friction losses, the dimensionless length $\overline{L}_1$ defined by Equation (7.18) is modified to become the dimensionless tunnel length:

$$\overline{L}_2 = \frac{P_s L A_T}{E \cdot AR} \left(\frac{fL}{D_T} \right)^m. \tag{7.21}$$

The fraction parameter was tested in its original power $m = 1$, in addition to in power $m = 0.5$ and $m = 2$. Furthermore, with the introduction of the friction parameter, the determined power $n = 1$ determined in Equation (7.18) was re-tested. This resulted in a best fit curve matrix of $\left(\frac{fL}{D_T}\right)^{m=0.5,1,2}$ and $(AR)^{n=0.5,1,2}$. Based on the R^2 coefficient and the mean squared error, the combination seen to give the best fit curve based on the convergence of all plotted data resulted in a final dimensionless length parameter, $\overline{L}_T$, as:

$$\overline{L}_T = \frac{P_s L A_T}{E \cdot AR^{0.5}} \left(\frac{fL}{D_T} \right). \tag{7.22}$$

Indeed, $m = 1$ and the power in the AR parameter has changed from Equation (7.18), from $n = 1$ to $n = 0.5$. Ultimately, the dimensionless parameter $\overline{P}_1$ is modified to its final form $\overline{P}_T$ expressed as:

$$\overline{P}_T = \overline{P}/\overline{L}_T. \tag{7.23}$$

Plotted in dimensionless parameters $\overline{L}_T$ and $\overline{P}_T$, the correlation displays all the data of blast wave decay in various tunnels for different tanks collapsed onto the same curve trend ($R^2 = 0.9914$), presented in Figure 7.21.

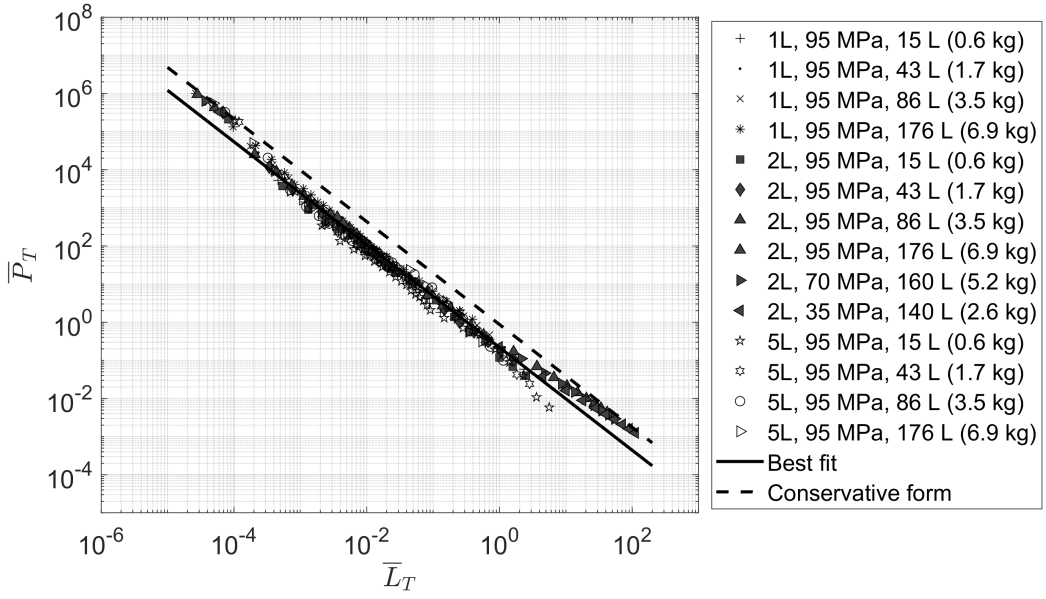

.png

Figure 7.21: The dimensionless universal correlation for blast wave decay for arbitrary hydrogen tank rupture in a fire in different tunnels.

The universal correlation: best fit and conservative form

The best fit for the universal correlation is:

$$\overline{P}_T = 0.22 \cdot \overline{L}_T^{-1.35}. \tag{7.24}$$

The conservative (upper limit) form of the correlation is found to be:

$$\overline{P}_T = 0.87 \cdot \overline{L}_T^{-1.35}. \tag{7.25}$$

The universal correlation: examples of use

To demonstrate the use of the universal correlation using a direct problem example, the correlation is applied to calculate blast wave overpressure for known parameters of tunnel and tank at selected distances. The three hazard distances thresholds and four corresponding hazard zones, i.e. *"no-harm"* (<1.35 kPa), *"slight injury"* (1.35–16.5 kPa), *"serious injury"* (16.5–100 kPa), *"fatality"* (>100 kPa), are listed elsewhere (Kashkarov et al., 2020).

1. A high-pressure stored hydrogen tank of 15 L is chosen. The rupture scenario includes the tank exposed in a fire in the middle of the tunnel, 13 km from either exit. The tank NWP may be initially assumed lower, but increased to 70 MPa after being exposed to a fire. The tunnel imagined is the Lærdal tunnel, 24.5 km long with a cross-section area of 56.4 m^2 (Norwegian Public Roads Administration, 2004). However, these dimension does not include friction and minor losses due to expansion and contraction of the cross-section area. Therefore, the attained calculated distances are deemed conservative.

2. The hydrogen mass in the tank assuming a temperature of 300 K is calculated by Equation (7.16) as 0.6 kg. The mechanical energy calculated by Equation (7.15) is $E_m = 2.53$ MJ. Equation (7.17) gives the total chemical energy as $E_{ch} = 70$ MJ. Recommended values of $\alpha = 1.8$ and $\beta = 0.12$ are used, calculated the total energy contributing to the blast wave maximum overpressure as 13.1 MJ.

3. The tunnel cross-section area used is 56.4 m^2, the hydraulic diameter determined using the general term of $D_T = 4A_T/wp$. However, the Lærdal tunnel is shaped like a semicircle, with a corresponding diameter of 9 m.

4. The transition zone distance is established to be between 4 and 13 times the size of the tunnel hydraulic diameter. Equation (7.19) gives $L_{D_T} = 3.3$, resulting in $L_{TR}/D_T = 7$ using Figure 7.20. 7 times the tunnel diameter gives a transition zone distance of 63 m, after which the blast wave is considered planer.

5. Characteristics concerning the tunnel internal wall roughness for calculation of the friction losses are not readily available. Nevertheless, to account for friction losses the friction factor used is 0.0055 for conservative purposes as determined in this paper.

6. What is the blast wave pressure after 100 m? Using Equation (7.22), the dimensionless parameter $\overline{L}_T$ is calculated to be 2.64. With this, the correlation derived (Equation (7.24)), the value for $\overline{P}_T$ is calculated to be 0.059.

7. To determine the dimensionless pressure using Equation (7.23), $\overline{P} = \overline{P}_T \cdot \overline{L}_T = 2.64 \cdot 0.059 = 0.155$. To find the dimensional blast wave overpressure, $\overline{P}$ is multiplied by the atmospheric pressure (see Equation (7.13)).

8. For a distance of 100 m away from rupture, the calculated blast wave overpressure is 15.7 kPa, found within the *"slight injury"* zone. For a distance of 1000 m (1 km), the calculated blast wave overpressure is 3.2 kPa, and for 12 km the blast wave overpressure is 0.6 kPa, well under the *"no-harm"* threshold. If calculated using the conservative

form, the blast wave overpressure for distances for 100 m, 1 km and 12 km are 65.62 kPa, 12.6 kPa, 2.2 kPa respectively.

In the inverse problem example, the three pressure thresholds are used as an input, along with tank and tunnel parameters, to define three hazard distances (four hazardous zones) in a tunnel.

1. For the inverse problem, the author would like to know where exactly the *"no harm"* distance, i.e. ΔP <1.35 kPa, is within the same tunnel.
2. The calculated $\overline{P}$ for 1.35 kPa is 0.0133.
3. Equation (7.24) is altered from its original form to get the dimensionless distance as $\overline{P} = \left(0.22 \cdot \overline{L}_T^{-1.35}\right) \overline{L}_T = 0.22 \left(\frac{P_s L A_T}{E \cdot AR^{0.5}} \cdot \frac{fL}{D_T}\right)^{-0.35}$.
4. To calculate distance, L, having all the other parameters is a trivial task using a mathematical tool e.g. Excel, MATLAB, Wolfram Alpha etc.
5. Thus, the *"no-harm"* zone ($\Delta P = 1.35$ kPa) is found beyond 3392 m within the tunnel by using the best fit correlation.

Using the procedure in the previous sections, the hazard distances for *"fatality"*, *"serious injury"*, *"slight injury"* and *"no-harm"* zones within the Lærdal tunnel can be calculated. They are given in Table 7.9 for the best fit and conservative form of the correlation.

Table 7.9: Calculated zones of hazard distances following a 70 MPa, 15 L (0.6 kg) tank rupture in Lærdal tunnel.

	Fatality	Serious injury	Slight injury	No-harm
Threshold pressures	>100 kPa	16.5–100 kPa	1.35–16.5 kPa	<1.35 kPa
Distances (best fit), m	<8	8–94	94–3392	>3392
Distances (conservative), m	<52	683–52	683–24798	>24798

The same methodology can be used for a stored hydrogen tank of 62 L, the volume of a single tank used for current Toyota Mirai hydrogen-powered vehicles (*Toyota Mirai Technical Specifications vs FCHV-Adv*, 2014). Within the same tunnel and rupture pressure of 70 MPa (300 K), the calculated hazard distances are given in Table 7.10.

Table 7.10: Hazard zones following 70 MPa, 62 L (2.4 kg) tank rupture in the Lærdal tunnel.

	Fatality	Serious injury	Slight injury	No-harm
Threshold pressures	>100 kPa	16.5–100 kPa	1.35–16.5 kPa	<1.35 kPa
Distances (best fit), m	<15	15–190	190–6895	>6895
Distances (conservative), m	<105	105–1388	1388–50415	>50415

7.4 Concluding remarks

To investigate the behaviour of blast wave decay in a tunnel after tank rupture in a fire and build the correlation, a total number of 14 simulations of high-pressure hydrogen tank rupture has been conducted. They include a wide array of stored hydrogen mass in the range 0.6–6.9 kg and rupture pressures in the range 35–95 MPa, tunnels with cross-section areas ranging from 24 m^2 to 139 m^2, aspect ratios between 1.2 and 2.7 and tunnel lengths from the location of tank rupture to furthest tunnel exit of 150 m and 1500 m.

The originality of this research is in the use of the complementarities and synergies of two research techniques, i.e. the similitude analysis and the thoroughly validated contemporary CFD model for simulation of complex physical phenomena inherent to hydrogen tank rupture in a fire in a tunnel. This methodology allowed all data on blast wave decay from different tank rupturing in various tunnels to finally collapse into one curve. The rigour of this work is in the universality of the correlation, which is built using the validated against experiments with tank rupture in a fire CFD model. Indeed, the derived dimensionless parameters, $\overline{P}$ and $\overline{L}$, encapsulate all important factors of influence. These include the mechanical energy and fraction of the chemical energy of released during tank rupture hydrogen depending on tank volume and pressure (defining hydrogen mass), and tunnel parameters such as its cross-section area, aspect ratio and length. The effect of friction and minor losses on pressure decay is also accounted for in the correlation.

The significance of this study is the developed universal correlation for calculation of blast wave decay after high-pressure hydrogen tank rupture in a fire in a tunnel. The correlation can be used for assessment of consequences of arbitrary tank rupture in a tunnel of any cross-section area, aspect ratio and length for people, vehicles and tunnel infrastructure. It is currently the only available reduced tool for calculation of hazard distances for humans and equipment in tunnels after hydrogen tank rupture in a fire. The consequences of tank rupture in a fire in a tunnel calculated using the correlation can be used to feed the quantitative risk assessment. Thus, the correlation is an essential contribution to the hydrogen safety engineering discipline to make the deployment and use of hydrogen vehicles in tunnels inherently safer.

This is a theoretical and numerical study of mainly academic interest rather than already validated by experiments source of guidelines for inherently safer use of hydrogen-powered vehicles in tunnels. However, in the absence of experimental studies on high-pressure hydrogen tank rupture in a fire in a tunnel, it recommends a methodology on how to develop the universal dimensionless correlation to be used for hazards and associated risk assessment, planning of experiments, and ultimately in safety guidelines when validation experiments are available. It is thought that the availability of validation experiments, including those planned in HyTunnel-CS project, could only affect the coefficients in the equations for the best fit and the conservative correlations but will not change its general form and parameters included.

Chapter 8

Conclusions

This doctoral study was targeted to close a number of knowledge gaps identified in hydrogen safety engineering associated with the employment of high-pressure hydrogen storage systems. Analytical and numerical methods, including computational fluid dynamics (CFD), were used as a contemporary tool to investigate the hazards from catastrophic failure. The aim to understand the hazards of a high-pressure hydrogen tank rupture in a tunnel and characterise the blast wave propagation and fireball dynamics has been fulfilled. Following a critical literature review on hazards associated with hydrogen storage and consequences from rupture of a tank in a fire, the scientific novelties and practical significance of the work are outlined below.

- The methodology employed in developing a CFD model able to simulate complex phenomena such as high-pressure tank rupture of storage hydrogen is defined. The numerical model included the use of LES for turbulence with the Smagorinsky-Lilly model for simulation of sub-grid scale turbulence. For combustion, the EDC model was used, contended to ensure accurate results based on underlying physics. To contain an effective computational time, the use of a global one-step reaction scheme was chosen, still able to provide realistic hydrogen-air combustion simulation. The use of ideal gas equation of state and essentially omitting real gas effects were substantiated; once hydrogen gas is released immediately falls below the non-ideal threshold. Nevertheless, the mechanical energy released as ideal gas led to a re-scaling of the stored hydrogen volume to maintain the same energy as in real gas conditions. The use of an adaptive time step by implementing a CFL number = 0.1 was determined through a sensitivity analysis, ensuring numerical stability and a hydrogen mass imbalance of below 0.1% during simulations. All decisions were catered to the pursuit of ensuring a CFD model able to provide insight into the process of blast wave propagation and fireball dynamics, subject to validation.
- The developed CFD model is validated against available experimental data, of a hydrogen tank (35 MPa) rupture in a fire. The ability to reproduce the generated blast wave in the near field was explored, subject to the non-instantaneous tank rupture

sequence and directional effects of the cylindrical vessel. Measures included recreating initial condition of temperature and species surrounding tank prior to rupture and the inclusion of bonfire pan geometry as in experiment. These efforts all aided in an overall better reproduced near field blast wave overpressure as measured in experiment. It was illustrated that the generated blast wave being fed energy from the combustion, occurring at the contact surface between heated by starting shock air and cooled by expansion hydrogen at the start of the process. The simulated fireball was able to accurately reproduce the fireball size and shape as measured in experiment. The same CFD approach was also validated against an experimental test of a 70 MPa hydrogen stored tank rupture in a fire (Molkov et al., 2020). Developed and validated, it is applied as a contemporary tool for hydrogen safety engineering to assess the hazards from tank rupture in a fire for scenarios including confined spaces. For an under-vehicle tank rupture, the model was found inapplicable due to the lack of energy allocated for displacement and deformation of the vehicle.

- A tank engulfed in fire, depending on the fire properties, i.e. size and HRR, leads to a reduced blast wave strength and fireball thermal hazards when the tank is catastrophically ruptured. The released hydrogen from tank rupture surrounded by fire experiences less chemical reaction due to the limited amount of oxidizer available. This reduces the initial combustion of hydrogen and less chemical energy contribution to the generated blast wave. This was shown by inferring a propane burner size of areas 2 m^2 and 21 m^2, simulated to engulf the tank prior to rupture. The subsequent blast wave and fireball were then compared to when rupture occurs without fire present. The starting shock wave pressure in the near field was found to be reduced by up to 80% when fire was present, the effect diminishing outside the fire zone area. The subsequent fireball was also influenced by the presence of fire, leading to a shorter lifetime duration and thereby causing less hazardous thermal dose effects. These results will aid in creating more accurate consequence analysis and harmful criteria, taking into regards the effect of fire prior to rupture.
- The validated model is used to assess the blast wave behaviour in a tubular experimental tunnel, in which a planned experiment is to be conducted as part of the HyTunnel project. Following a hydrogen tank rupture, the difference between blast wave in an open atmosphere and confinement effects of a tunnel was investigated. The blast wave overpressure decay pattern in a tunnel was found one-dimensional due to confinement effects, with a decay much less pronounced than the three-dimensional decay in an open atmosphere. For instance, at 40 m, the overpressure in open atmosphere was 0.4 kPa, compared to 50 kPa within a tunnel. The exerted blast wave loading on the experimental tunnel internal structure was explored, based on the orientation of tank in tunnel prior to rupture. When the tank was placed in orientation axial to the tunnel axis direction, an overpressure of 4 MPa was exerted on the tunnel wall, 1 MPa above the strength limit of the tunnel structure of 3 MPa. However, when the tank was placed perpendicular to the tunnel axis, a lower maximum pressure of 2 MPa was measured, well below the threshold strength of the tunnel structure. Clearly, the directional effects of a cylinder tank following a rupture results in a significantly

different exerted blast wave pressure on nearby structures.

- A numerical study was conducted investigating the blast wave propagation in tunnels of three different cross-section areas between 24–139 m^2, of different initial high-pressure hydrogen tank volumes 15–176 L (0.6–6.9 kg) and rupture pressures (35 MPa, 70 MPa and 95 MPa). Previous blast wave decay laws derived using condensed material from explosive charges were tested. Despite modifications made to better fit the properties of stored hydrogen, the established model was found to be non-universal. Therefore, a novel model for blast wave decay in tunnel was proposed based on developed dimensionless parameters for blast wave pressure and distance in a tunnel. The mechanical and chemical energy of released hydrogen contributing to the blast wave were determined, and the tunnel dimensions of cross-section area including effects of aspect ratio and minor and friction losses considered. This resulted in a near linear fit between the two dimensionless parameters, and thereby a novel correlation able to predict blast wave across various stored hydrogen and tunnel dimensions.

Among challenges and limitation that arose during this research study, the recommendations for further work are many. To generally mention a few, additional validation of the CFD model for high-pressure tank rupture based upon upcoming experiments, including the implementation of real gas to remove any ideal gas bias and exploring various rupture modes of tank, is needed. Another is to improve the developed universal correlation for blast wave decay in tunnel by including the presence of various tunnel parameters like vents, bends and obstacles such as vehicles. As it stands, the correlation is deemed highly conservative.

References

AMEC (2014). Intermediate report Annex 2: Consequence Assessment Methods for Human Health (Tast 2), *Technical report*, Encvironment & infrastructure UK Limited.

American Institute of Chemical Engineers (ed.) (1994). *Guidelines for Evaluating the Characteristics of Vapor Cloud Explosions, Flash Fires, and BLEVEs*, Center for Chemical Process Safety of the American Institute of Chemical Engineers, New York, NY.

Anagnostou, G. and Ehrbar, H. (2013). *Underground. The Way to the Future*, CRC Press.

Anderson, J. D. (1995). *Computational Fluid Dynamics: The Basics with Applications*, McGraw-Hill Series in Mechanical Engineering, McGraw-Hill, New York.

ANSYS FLUENT 12.0 User's Guide (2009). https://www.afs.enea.it/project/neptunius/docs/fluent/html/ug/main_pre.htm. (accessed 2018-04-25).

Baker, W. E., Cox, P., Westine, P. S., Kulesz, J. J. and Strehlow, R. (1983). *Explosion Hazards and Evaluation*, Elsevier Scientific Publishing Company.

Baker, W. E., Kulesz, J. J., Ricker, R. E., Westine, P. E., Parr, V. B., Vargas, L. M. and Moseley, P. K. (1975). Workbook for predicting pressure wave and fragment effects of exploding propellant tanks and gas storage vessels, *Technical report*, Southwest Research Inst., San Antonio, TX, United States.

Baker, W. E., Kulesz, J. J., Ricker, R. E., Westine, P. S., Parr, V. B., Vargas, L. M. and Moseley, P. K. (1978). Workbook for estimating effects of accidental explosions in propellant ground handling and transport systems, *Technical report*, Southwest Research Inst.; San Antonio, TX, United States.

Beard, A. and Carvel, R. (eds) (2012). *The Handbook of Tunnel Fire Safety*, 2nd ed edn, ICE, London.

Benselama, A. M., William-Louis, M. J. P., Monnoyer, F. and Proust, C. (2010). A numerical study of the evolution of the blast wave shape in tunnels, *Journal of Hazardous Materials* **181**(1): 609–616.

Berger, J. O. (2013). *Statistical Decision Theory and Bayesian Analysis*, Springer Science & Business Media.

Birk, A. M., Davison, C. and Cunningham, M. (2007). Blast overpressures from medium scale BLEVE tests, *Journal of Loss Prevention in the Process Industries* **20**(3): 194–206.

Biswas, R. and Strawn, R. C. (1998). Tetrahedral and hexahedral mesh adaptation for CFD problems, *Applied Numerical Mathematics* **26**(1): 135–151.

Bragin, M. V., Makarov, D. V. and Molkov, V. V. (2013). Pressure limit of hydrogen spontaneous ignition in a T-shaped channel, *International Journal of Hydrogen Energy* **38**(19): 8039–8052.

Bragin, M. V. and Molkov, V. V. (2011). Physics of spontaneous ignition of high-pressure hydrogen release and transition to jet fire, *International Journal of Hydrogen Energy* **36**(3): 2589–2596.

Brilon, W. and Weiser, F. (2006). Two-Lane Rural Highways: The German Experience, *Transportation Research Record: Journal of the Transportation Research Board* **1988**: 38–47.

Brode, H. L. (1959). Blast Wave from a Spherical Charge, *The Physics of Fluids* **2**(2): 217–229.

Buckingham, E. (1916). *Model Experiments and the Forms of Empirical Equations*, Vol. Volum 37 av TRANSACTIONS ASME, Verlag nicht ermittelbar.

C. Smith, A. and J. Sapko, M. (2005). Detonation wave propagation in underground mine entries, *Journal of the Mine Ventilation Society of South Africa* **58**: 20–25.

Center for Chemical Process Safety (1994). Appendix C: Effects of Explosions on Humans, *Guidelines for Evaluating the Characteristics of Vapor Cloud Explosions, Flash Fires, and BLEVEs*, John Wiley & Sons, Inc., pp. 351–357.

Center for Chemical Process Safety (1999). *Guidelines for Consequence Analysis of Chemical Releases*, American Institute of Chemical Engineers, New York.

Center for Chemical Process Safety (2010). *Guidelines for Vapor Cloud Explosion, Pressure Vessel Burst, BLEVE, and Flash Fire Hazards*, American Institute of Chemical Engineers, Chicester, USA.

Chen, F., Mao, J., Zhou, J., Hou, P., Liu, L. and Chen, S. (2017). Thermal Environment inside a Tunnel after Thermobaric Explosion, *Shock and Vibration* p. 11.

Chen, H., Zheng, J., Xu, P., Li, L., Liu, Y. and Bie, H. (2010). Study on real-gas equations of high pressure hydrogen, *International Journal of Hydrogen Energy* **35**(7): 3100–3104.

Cheng, Z., Agranat, V. and Tchouvelev, A. (2005). PRD hydrogen release and dispersion, a comparison of CFD results obtained from using ideal and real gas law properties, *International Conference on Hydrogen Safety*.

Chui, E. H. and Raithby, G. D. (1993). Computation of Radiant Heat Transfer on a Nonorthogonal Mesh Using the Finite-Volume Method, *Numerical Heat Transfer, Part B: Fundamentals* **23**(3): 269–288.

Cirrone, D. M. C. (2018). *Hazards from Catastrophic Failure of High-Pressure Hydrogen Storage*, PhD thesis, Ulster University.

Coleman, M., Cain, M., Harley, C. and Sharp, D. (1988). A review of energy release processes from failure of pneumatic pressure vessels, *Technical report*, General Physics Corporation, Cape Canaceral Air Force Station, Florida.

Cox, L. A. (2009). *Risk Analysis of Complex and Uncertain Systems*, Springer Science & Business Media.

Crowl, D. A. (2010). *Understanding Explosions*, John Wiley & Sons.

Cullis, I. G. (2001). Blast waves and how they interact with structures, *Journal of the Royal Army Medical Corps* **147**(1): 16–26.

Curran, D. R., Norway and Forsvarets forskningsinstitutt (1966). *Underground Storage of Ammunition: Experiments Concerning Accidental Detonation in an Underground Chamber*, Norwegian Defence Construction Service, Kjeller, Norway.

D4.1 HyTunnel-CS (2019). Detailed research programme on explosion in underground transportation systems. Fuel Cells and Hydrogen Joint Undertaking (FCH JU), Grant Agreement Number 826193, https://hytunnel.net/wordpress/wp-content/uploads/2019/12/HyTunnel-CS_D4.1_Detailed-research-programme-on-explosion-in-underground-transportation-systems.pdf. (accessed 2020-06-18).

Dadashzadeh, M., Kashkarov, S., Makarov, D. and Molkov, V. (2018). Risk assessment methodology for onboard hydrogen storage, *International Journal of Hydrogen Energy* **43**(12): 6462–6475.

Department for Communities and Local Government, Communities and Local Government, Sustainable Buildings Div and Sustainable Buildings Div (2010). *Fire Spread in Car Parks*, Building Research Establishment, Watford, England.

Drysdale, D. (2011). *An Introduction to Fire Dynamics*, 3rd ed edn, Wiley, Chichester, West Sussex.

Durbin, D. J. and Malardier-Jugroot, C. (2013). Review of hydrogen storage techniques for on board vehicle applications, *International Journal of Hydrogen Energy* **38**(34): 14595–14617.

Dusenberry, D. O. (ed.) (2010). *Handbook for Blast-Resistant Design of Buildings*, J. Wiley, Hoboken, N.J.

Echekki, T. and Mastorakos, E. (2011). Turbulent Combustion: Concepts, Governing Equations and Modeling Strategies, *in* T. Echekki and E. Mastorakos (eds), *Turbulent Combustion Modeling*, Vol. 95, Springer Netherlands, Dordrecht, pp. 19–39.

Fang, Y., Zou, Y.-L., Zhou, J., Yao, Z.-g., Lei, S. and Yang, W. (2019). Field Tests on the Attenuation Characteristics of the Blast Air Waves in a Long Road Tunnel: A Case Study, *Shock and Vibration* **2019**: 11.

Forsen, R. (2008). Tunnel explosion characteristics, *Proceedings from the Third International Symposium on Tunnel Safety and Security: Stockholm, Sweden, March 12 - 14, 2008* pp. 327–334.

Fowler, C. P., Orifici, A. C. and Wang, C. H. (2016). A review of toroidal composite pressure vessel optimisation and damage tolerant design for high pressure gaseous fuel storage, *International Journal of Hydrogen Energy* **41**(47): 22067–22089.

Galassi, M. C., Papanikolaou, E., Baraldi, D., Funnemark, E., Håland, E., Engebø, A., Haugom, G. P., Jordan, T. and Tchouvelev, A. V. (2012). HIAD – hydrogen incident and accident database, *International Journal of Hydrogen Energy* **37**(22): 17351–17357.

Gambone, L. R. and Wong, J. Y. (2007). Fire protection strategy for compressed hydrogen-powered vehicles, *Internati onal* .

Geng, J., Baker, Q. and Thomas, K. (2011). Pressure vessel burst directional effects, *Proceedings of the ASME 2011 Pressure VEssels & Piping Division Conference* **4**(PVP2011): 3–9.

Gerlinger, P., Nold, K. and Aigner, M. (2010). Influence of reaction mechanisms, grid spacing, and inflow conditions on the numerical simulation of lifted supersonic flames, *International Journal for Numerical Methods in Fluids* **62**(12): 1357–1380.

Goldstein, M. L., Morris, S. A. and Yen, G. G. (2004). Problems with fitting to the power-law distribution, *The European Physical Journal B - Condensed Matter and Complex Systems* **41**(2): 255–258.

Gottuk, D. T. and White, D. A. (2016). Liquid Fuel Fires, *in* M. J. Hurley, D. Gottuk, J. R. Hall, K. Harada, E. Kuligowski, M. Puchovsky, J. Torero, J. M. Watts and C. Wieczorek (eds), *SFPE Handbook of Fire Protection Engineering*, Springer New York, New York, NY, pp. 2552–2590.

Hadjisophocleous, G. V., Benichou, N. and Tamim, A. S. (1998). Literature Review of Performance-Based Fire Codes and Design Environment, *Journal of Fire Protection Engineering* **9**(1): 12–40.

Hansen, O. R., Hinze, P., Engel, D. and Davis, S. (2010). Using computational fluid dynamics (CFD) for blast wave predictions, *Journal of Loss Prevention in the Process Industries* **23**(6): 885–906.

Hansen, O. R. and Middha, P. (2008). CFD-based risk assessment for hydrogen applications, *Process Safety Progress* **27**(1): 29–34.

Harrison, D., Welchman, E., Chabal, Y. J. and Thonhauser, T. (2015). Materials for hydrogen storage, *Handbook of Clean Energy Systems* pp. 1–19.

Henrych, J. (1979). *The dynamics of explosion and its use*, number 1 in *Developments in civil engineering*, Elsevier Scientific Pub. Co. ; distribution for the U.S.A. and Canada, Elsevier/North-Holland, Amsterdam ; New York : New York.

High, R. W. (1968). The Saturn Fireball, *Annals of the New York Academy of Sciences* **152**(1): 441–451.

High, W. (1989). Design of small vessel rupture containment systems, *IChemE SYMPOSIUM SERIES No. 115* p. 141.

Hord, J. (1978). Is hydrogen a safe fuel?, *International Journal of Hydrogen Energy* **3**(2): 157–176.

Hordeski, M. F. (2009). *Hydrogen & Fuel Cells: Advances in Transportation and Power*, Fairmont Press ; CRC Press, Lilburn, GA : Boca Raton, FL.

HSE (2012). Failure Rate and Event Data for use within Risk Assessments (28/06/2012), http://www.hse.gov.uk/landuseplanning/failure-rates.pdf. (accessed 2018-01-18).

Hsu, K. and Jemcov, A. (2000). Numerical investigation of detonation in premixed hydrogen–air mixture–assessment of simplified chemical mechanisms, *Fluids 2000 Conference and Exhibit*, p. 2478.

Hwang, H. T. and Varma, A. (2014). Hydrogen storage for fuel cell vehicles, *Current Opinion in Chemical Engineering* **5**(Supplement C): 42–48.

HySAFE (2009). Deliverable D113. Initial Guidance for Using Hydrogen in Confined Spaces - Results from InsHyde, https://www.kennisplatformtunnelveiligheid.nl/wp-content/uploads/2014/04/HYSAFE_D113_version_1-1.pdf. (accessed 2017-12-05).

INERIS (2012). Formalization of knowledge and tools in the area of major risks (EAT-DRA-76). Vessel bursts, phenomenology and effect modelling - Omega 15, *Technical report*, The French National Institute for Industrial Environment and Risks.

Ingason, H. and Li, Y. Z. (2017). Spilled liquid fires in tunnels, *Fire Safety Journal* **91**: 399–406.

Jeffries, R. M., Hunt, S. J. and Gould, L. (1997). Derivation of fatality probability function for occupants buildings subject to blast loads, *Probabilistic Safety Assessment and Management '96*, Springer, London, pp. 669–675.

Jiang, X.-h., Zhu, G.-q., Zhu, H. and Li, D.-y. (2018). Full-scale Experimental Study of Fire Spread Behavior of Cars, *Procedia Engineering* **211**: 297–305.

Johnson, I. (2005). The Noble-Abel Equation of State: Thermodynamic Derivations for Ballistics Modelling, *Technical Report DSTO-TN-0670*, Weapons Systems Division, Defence Science and Technology Organisation.

Jones, W. and Lindstedt, R. (1988). Global reaction schemes for hydrocarbon combustion, *Combustion and Flame* **73**(3): 233–249.

Jorgensen, S. W. (2011). Hydrogen storage tanks for vehicles: Recent progress and current status, *Current Opinion in Solid State and Materials Science* **15**(2): 39–43.

Kashkarov, S. (2016). *Fire Resistance of On-Board High Pressure Storage Tanks for Hydrogen-Powered Vehicles*, PhD thesis, Ulster University.

Kashkarov, S., Li, Z. and Molkov, V. (2020). Blast wave from a hydrogen tank rupture in a fire in the open: Hazard distance nomograms, *International Journal of Hydrogen Energy* **45**(3): 2429–2446.

Kashkarov, S., Makarov, D. and Molkov, V. (2017). Model of 3D conjugate heat transfer and mechanism of compressed gas storage failure in a fire, *International Conference on Hydrogen Safety*, Hamburg, Germany.

Khaksarfard, R., Kameshki, M. R. and Paraschivoiu, M. (2010). Numerical simulation of high pressure release and dispersion of hydrogen into air with real gas model, *Shock Waves* **20**(3): 205–216.

Kim, W., Shentsov, V., Makarov, D. and Molkov, V. (2017). Simulations of Blast Wave and Fireball Occurring Due to Rupture of High-Pressure Hydrogen Tank, *Safety* **3**(2): 16.

Kinney, G. F. and Graham, K. J. (2013). *Explosive Shocks in Air*, Springer Berlin / Heidelberg, Berlin, Heidelberg.

Kivity, Y. (2012). Attenuation of blast waves in tunnels with corrugated walls, *20th International Shock Interaction Symposium*, Stockholm.

Knock, C. and Davies, N. (2012). Blast Waves from Cylindrical Charges, *in* K. Kontis (ed.), *28th International Symposium on Shock Waves*, Springer Berlin Heidelberg, Berlin, Heidelberg, pp. 87–92.

Kumar, S., Miles, S. D., Adams, P., Kotchourko, A., Hedley, D., Middha, P., Molkov, V., Teodorczyk, A. and Zenner, M. (2009). HyTunnel Project to Investigate the use of Hydrogen Vehicles in Road Tunnels, https://www.h2tools.org/sites/default/files/ICHS_import/paper_35.pdf. (accessed 2020-06-18).

LaChance, J. L., Houf, W. G., Fluer, L. and Middleton, B. (2009). Analyses to support development of risk-informed separation distances for hydrogen codes and standards., *Technical Report SAND2009-0874, 983689*, Sandia National Laboratories.

LaChance, J., Tchouvelev, A. and Engebo, A. (2011). Development of uniform harm criteria for use in quantitative risk analysis of the hydrogen infrastructure, *International Journal of Hydrogen Energy* **36**(3): 2381–2388.

Li, Y. Z. (2018). Fire and explosion hazards of alternative fuel vehicles in tunnels, *Technical report*, RISE Research Institutes of Sweden, Borås.

Li, Y. Z. (2019). Study of fire and explosion hazards of alternative fuel vehicles in tunnels, *Fire Safety Journal* **110**: 102871.

Liepmann, H. W. and Roshko, A. (2001). *Elements of Gasdynamics*, Dover Publications, Mineola, N.Y.

Lopes, K. B. (2011). Analysis of the effects of explosion of a hydrogen cylinder on the transfer of radioactive liquid wastes at nuclear power stations, *INAC 2011: International Nuclear Atlantic Conference*, Brasil, p. 15.

Magnussen, B. F. and Hjertager, B. H. (1977). On mathematical modeling of turbulent combustion with special emphasis on soot formation and combustion, *Symposium (International) on Combustion* **16**(1): 719–729.

Maidl, B., Thewes, M. and Maidl, U. (2014). *General Principles for the Design of the Cross-Section*, Wiley-VCH Verlag GmbH, D-69451 Weinheim, Germany, pp. 1–20.

Makarov, D., Kim, Y., Kashkarov, S. and Molkov, V. (2016). Thermal Protection and Fire Resistance of High-Pressure Hydrogen Storage, *8th International Seminar on Fire & Explosion Hazards*, ISFEH 8, Hefei, China.

Makridis, S. (2016). Hydrogen storage and compression, *Methane and Hydrogen for Energy Storage*, Institution of Engineering and Technology, pp. 1–28.

Malhotra, A., Carson, D. and McFadden, S. (2017). Blast pressure leakage into buildings and effects on humans, *Procedia Engineering* **210**: 386–392.

Mannan, S. (2005). *Lees' Loss Prevention in the Process Industries*, Vol. 1 of *Hazard Identification, Assessment and Control*, third edn, Elsevier Butterworth-Heinemann.

Marinov, N. M., Westbrook, C. K. and Pitz, W. J. (1995). Detailed and global chemical kinetics model for hydrogen, *8. international symposium on transport properties, San Francisco, CA (United States), Oct 1995* .

Marshall-Ponting, A., Ji, Y., Keraminiyage, K. P., Lee, A., Poppelreuter, T., Swan, W., Udeaja, C. E. and van Dijk, H. (2019). *Conference Proceedings of the 14th International Postgraduate Research Conference 2019 : Contemporary and Future Directions in the Built Environment*, University of Salford, Salford.

Martinsen, W. E. and Marx, J. D. (1999). An improved model for the prediction of radiant heat from fireballs, *International Conference and Workshop on Modelling the Consequences of Accidental Releases of Hazardous Materials, CCPS, San Francisco, California, September*, pp. 605–621.

Maus, S., Hapke, J., Ranong, C. N., Wüchner, E., Friedlmeier, G. and Wenger, D. (2008). Filling procedure for vehicles with compressed hydrogen tanks, *International Journal of Hydrogen Energy* **33**(17): 4612–4621.

McCabe, W. L., Smith, J. C. and Harriott, P. (2005). *Unit Operations of Chemical Engineering*, McGraw-Hill's Chemical Engineering Series, 7. ed edn, McGraw-Hill Higher Education, Boston, Mass.

Molkov, V. (2012). *Fundamentals of Hydrogen Safety Engineering I*, Free download from www.bookboon.com.

Molkov, V., Cirrone, D., Shentsov, V., Dery, W., Kim, W. and Makarov, D. (2018). Blast wave and fireball after hydrogen tank rupture in a fire, *11th International Colloquium on Pulsed and Continuous Detonations (ICPCD)*, St. Petersburg, Russia.

Molkov, V., Cirrone, D., Shentsov, V., Dery, W., Kim, W. and Makarov, D. (2020). Dynamics of blast wave and fireball after hydrogen tank rupture in a fire in the open atmosphere, *International Journal of Hydrogen Energy* .

Molkov, V. and Dery, W. (2020). The blast wave decay correlation for hydrogen tank rupture in a tunnel fire, *International Journal of Hydrogen Energy* .

Molkov, V. and Kashkarov, S. (2015). Blast wave from a high-pressure gas tank rupture in a fire: Stand-alone and under-vehicle hydrogen tanks, *International Journal of Hydrogen Energy* **40**(36): 12581–12603.

Murthy, J. Y. and Mathur, S. R. (1998). Finite Volume Method for Radiative Heat Transfer Using Unstructured Meshes, *Journal of Thermophysics and Heat Transfer* **12**(3): 313–321.

Neto, C., L, M., Doz, G. N., Neto, C., L, M. and Doz, G. N. (2017). Study of blast wave overpressures using the computational fluid dynamics, *Revista IBRACON de Estruturas e Materiais* **10**(3): 669–677.

Nikuradse, J. (1950). Laws of Flow in Rough Pipes, http://ntrs.nasa.gov/search.jsp?R=19930093938. (accessed 2020-04-29).

Ning, H. and Bin, Q. (2012). Influence Analysis of Roadway Friction on Shock Wave Attenuation, *Applied Mechanics and Materials* **179-181**: 1619–1622.

Norwegian Public Roads Administration (2004). Road Tunnels, *Technical Report 21*, Statens vegvesen.

NRC Staff: United States Nuclear Regulat (2015). *Fire Dynamics Tools (FDTs) Quantitative Fire Hazard Analysis Methods for the U.S. Nuclear Regulatory Commission Fire Protection Inspection Program: NUREG-1805 - Scholar's Choice Edition*, Scholar's Choice.

Nussey, C. (2006). Failure frequencies for major failures of high pressure storage vessels at COMAH sites: A comparison of data used by HSE and the Netherlands, http://www.hse.gov.uk/comah/highpressure.pdf. (accessed 2018-01-18).

Patankar, S. V. (1980). *Numerical Heat Transfer and Fluid Flow*, Series in Computational Methods in Mechanics and Thermal Sciences, Hemisphere Pub. Corp. ; McGraw-Hill, Washington : New York.

Pennetier, O., William-Louis, M. and Langlet, A. (2015). Numerical and reduced-scale experimental investigation of blast wave shape in underground transportation infrastructure, *Process Safety and Environmental Protection* **94**(Supplement C): 96–104.

Post, D., Visser, C., Richardella, R., Martin, M. and Elam, C. (2015). Energy Systems Integration Facility: Hazard Analysis Review, *Technical report*, National Renewable Energy Laboratory.

Roberts, A. (1981). Thermal radiation hazards from releases of LPG from pressurised storage, *Fire Safety Journal* **4**(3): 197–212.

Rodionov, A., Wilkening, H. and Moretto, P. (2011). Risk assessment of hydrogen explosion for private car with hydrogen-driven engine, *International Journal of Hydrogen Energy* **36**(3): 2398–2406.

Rodríguez, R., Lombardía, C. and Torno, S. (2010). Prediction of the air wave due to blasting inside tunnels: Approximation to a 'phonometric curve', *Tunnelling and Underground Space Technology* **25**(4): 483–489.

Shen, C., Ma, L., Huang, G., Wu, Y., Zheng, J., Liu, Y. and Hu, J. (2018). Consequence assessment of high-pressure hydrogen storage tank rupture during fire test, *Journal of Loss Prevention in the Process Industries* **55**: 223–231.

Shentsov, V., Cirrone, D., Makarov, D. and Molkov, V. (2016). Simulation of Fireball and Blast Wave from a Hydrogen Tank Rupture in a Fire, *in* A. M. Starik and S. M. Frolov (eds), *NONEQUILIBRIUM PROCESSES IN PHYSICS AND CHEMISTRY Volume 2 Combustion and Detonation*, Vol. 2, Torus Press, Moscow, pp. 139–146.

Shentsov, V., Kim, W., Makarov, D. and Molkov, V. (2016). Numerical Simulations of Experimental Fireball and Blast Wave from a High-Pressure Tank Rupture in a Fire, *Proc. of the Eighth International Seminar on Fire & Explosion Hazards (ISFEH8).*

Shentsov, V., Makarov, D. and Dery, W. (2019). Stand-Alone Hemisphere-Tank Rupture in Tunnel Fire: Effect of Hydrogen Inventory on Blast Wave Strength in Far Field, *Proc. of the Ninth International Seminar on Fire & Explosion Hazards (ISFEH9)*, St. Petersburg, Russia.

Shentsov, V., Makarov, D. and Molkov, V. (2018). Blast wave after hydrogen storage tank rupture in a tunnel fire, *International Symposium on Tunnel Safety and Security 2018*, Borås, Sweden.

Silvestrini, M., Genova, B. and Leon Trujillo, F. J. (2009). Energy concentration factor. A simple concept for the prediction of blast propagation in partially confined geometries, *Journal of Loss Prevention in the Process Industries* **22**(4): 449–454.

Sinha, J. and Yang, Y. (2010). Direct hydrogen PEMFC manufacturing cost estimation for automotive applications, *2010 DOE Annual Merit Review, Washington, DC* .

Skacel, R., Janovsky, B., Dostal, L. and Svihovsky, J. (2013). Small-scale physical explosions in shock tubes in comparison with condensed high explosive detonations, *Journal of Loss Prevention in the Process Industries* **26**(6): 1590–1596.

Skjeltorp, A. (1968). One-Dimensional Blast Wave Propagation, *Technical Report FORTIFIKATORISK NOTAT-48/69*, NORWEGIAN DEFENCE CONSTRUCTION SERVICE OSLO OFFICE OF TEST AND DEVELOPMENT.

Skjeltorp, A. T. (1975). Airblast Propagation through Tunnels and the Effects of Wall Roughness, *Technical Report FORTIFIKATORISK*, NORWEGIAN DEFENCE CONSTRUCTION SERVICE OSLO OFFICE OF TEST AND DEVELOPMENT.

Staff, E. (2017). Nuclear Detonations In Urban And Surburban Areas, http://www.militarystory.org/nuclear-detonations-in-urban-and-suburban-areas/. (accessed 2018-06-08).

Steinar, H. and Gretler, W. (1994). The propagation of spherical and cylindrical shock waves in real gases, *Physics of Fluids* **6**(6): 2154.

Stoffen, P. G. (2005). Guidelines for quantitative risk assessment, *Ministerie van Volkshuisvesting Ruimtelijke Ordening en Milieu. CPR E* **18**.

Sunderland, P. B. (2008). Pressure relief devices for hydrogen vehicles, *Third European Summer School on Hydrogen Safety* .

Tamura, Y., Takabayashi, M. and Takeuchi, M. (2014). The spread of fire from adjoining vehicles to a hydrogen fuel cell vehicle, *International Journal of Hydrogen Energy* **39**(11): 6169–6175.

Tamura, Y., Takahashi, M., Maeda, Y., Mitsuishi, H., Suzuki, J. and Watanabe, S. (2006). Fire Exposure Burst Test of 70MPa Automobile High-pressure Hydrogen Cylinders, *Society of Automotive Engineers of Japan Annual Autum Congress*, Sapporro.

The Highway Agency, The Scottish Executive Development Department, The National Assembly for Wales Cynulliad Cenelaethol Cymru and Department of the Environment for Northern Ireland (1999). Design of Road Tunnels.

Thibault, P. A., Penrose, J. D., Shepherd, J. E., Benedick, W. and Ritzel, D. (1987). Blast Waves Generated by Planar Detonations, *Proceedings of the Sixteenth International Symposium on Shock Tubes and Waves.*, Aachen, West Germany, pp. 765–771.

Tolias, I. C., Giannissi, S. G., Venetsanos, A. G., Keenan, J., Shentsov, V., Makarov, D., Coldrick, S., Kotchourko, A., Ren, K., Jedicke, O., Melideo, D., Baraldi, D., Slater, S., Duclos, A., Verbecke, F. and Molkov, V. (2018). Best practice guidelines in numerical simulations and CFD benchmarking for hydrogen safety applications, *International Journal of Hydrogen Energy* **44**(17): 9050–9062.

Toyota Mirai Technical Specifications vs FCHV-Adv (2014). http://blog.toyota.co.uk/toyota-mirai-technical-specifications-vs-fchv-adv. (accessed 2018-05-31).

Tschirschwitz, R., Krentel, D., Kluge, M., Askar, E., Habib, K., Kohlhoff, H., Krüger, S., Neumann, P. P., Rudolph, M., Schoppa, A., Storm, S.-U. and Szczepaniak, M. (2019). Hazards from failure of CNG automotive cylinders in fire, *Journal of Hazardous Materials* **367**: 1–7.

Tu, J., Yeoh, G. H. and Liu, C. (2018). *Computational Fluid Dynamics: A Practical Approach*, third edition edn, Butterworth-Heinemann, Oxford ; Cambridge, MA.

UK HSE (2010). Methods of approximation and determination of human vulnerability for offshore major accident hazard assessment (Supporting document to SPC/Tech/OSD/30 Version 3.), http://www.hse.gov.uk/foi/internalops/hidcircs/technicalosd/spctechosd30/spctecosd30.pdf. (accessed 2018-01-23).

Uystepruyst, D. and Monnoyer, F. (2015). A numerical study of the evolution of the blast wave shape in rectangular tunnels, *Journal of Loss Prevention in the Process Industries* **34**(Supplement C): 225–231.

Varma, A. K., Chatwani, A. U. and Bracco, F. V. (1986). Studies of premixed laminar hydrogen-air flames using elementary and global kinetics models, *Combustion and Flame* **64**(2): 233–236.

Verfondern, K. (2008). *Safety Considerations on Liquid Hydrogen*, number Bd. 10 in *Schriften Des Forschungszentrums Jülich Reihe Energie & Umwelt*, Forschungszentrum, Zentralbibliothek, Jülich.

Vickers, M. (2017). *Northern California Coastal Bridges: Picturesque and Distinctive Spans*, Marquis Publishing.

Waite, P. (2012). CASE FOR SAFETY - RELATIVE FREQUENCY OF FAILURE MODES, http://h2safe.com/case_safety.html. (accessed 2018-01-18).

Wang, K., Liu, Z., Qian, X. and Huang, P. (2017). Long-term consequence and vulnerability assessment of thermal radiation hazard from LNG explosive fireball in open space based on full-scale experiment and PHAST, *Journal of Loss Prevention in the Process Industries* **46**: 13–22.

Warnatz, J., Maas, U. and Dibble, R. W. (2006). *Combustion: Physical and Chemical Fundamentals, Modeling and Simulation, Experiments, Pollutant Formation*, 4th ed edn, Springer, Berlin ; New York.

Wengle, H. and Werner, H. (1993). Large-eddy Simulation of Turbulent Flow Over Sharp-edged Obstacles in a Plate Channel, *in* K. Gersten (ed.), *Physics of Separated Flows — Numerical, Experimental, and Theoretical Aspects: DFG Priority Research Programme 1984–1990*, Notes on Numerical Fluid Mechanics (NNFM), Vieweg+Teubner Verlag, Wiesbaden, pp. 192–199.

Westbrook, C. and Dryer, F. L. (1981). Simplified Reaction Mechanisms for the Oxidation of Hydrocarbon Fuels in Flames, *Combustion Science and Technology* **27**(1-2): 31–43.

Weyandt, N. (2005). Analysis of Induced Catastrophic Failure Of A 5000 psig Type IV Hydrogen Cylinder, *Technical Report 01.06939.01.001*, Southwest Research Institute report for the Motor Vehicle Fire Research Institute.

Weyandt, N. (2006). Vehicle bonfire to induce catastrophic failure of a 5,000-psig hydrogen cylinder installed on a typical SUV, *Technical report*, Southwest Research Institute report for the Motor Vehicle Fire Research Institute.

Wolanski, P. and Wojcicki, S. (1973). Investigation into the mechanism of the diffusion ignition of a combustible gas flowing into an oxidizing atmosphere, *Fourteenth Symposium (International) on Combustion*, Pennsylvania: The Combustion Institute, Pennsylvania State University, p. 1217.

Wong, J. (2009). CNG and Hydrogen Tank Safety, R&D, and Testing.

Yan, L., Yue, G. and He, B. (2015). Development of an absorption coefficient calculation method potential for combustion and gasification simulations, *International Journal of Heat and Mass Transfer* **91**: 1069–1077.

Yan, Q. and Du, X. (2015). Forecasting research of overpressure of explosive blast in subway tunnels, *Journal of Vibroengineering* **17**(6): 3380–3391.

Yang, J., Sudik, A., Wolverton, C. and Siegel, D. J. (2010). High capacity hydrogenstorage materials: Attributes for automotive applications and techniques for materials discovery, *Chem. Soc. Rev.* **39**(2): 656–675.

Zalosh, R. (2007). Blast waves and fireballs generated by hydrogen fuel tank rupture during fire exposure, *5th International Seminar on Fire and Explosion Hazards*, Edinburgh, UK.

Zalosh, R. G. (2003). *Industrial Fire Protection Engineering*, Wiley, West Sussex, England ; Hoboken, NJ.

Zalosh, R. and Weyandt, N. (2005). Hydrogen Fuel Tank Fire Exposure Burst Test, *SAE Paper* **2005-01-1886**.

Zheng, J., Liu, X., Xu, P., Liu, P., Zhao, Y. and Yang, J. (2012). Development of high pressure gaseous hydrogen storage technologies, *International Journal of Hydrogen Energy* **37**(1): 1048–1057.

Zipf, R. K. and Cashdollar, K. L. (2015). Effects of blast pressure on structures and human body, http://www.docslides.com/calandra-battersby/explosions-and-refuge-chambers. (accessed 2018-01-22).

Züttel, A. (2003). Materials for hydrogen storage, *Materials Today* **6**(9): 24–33.